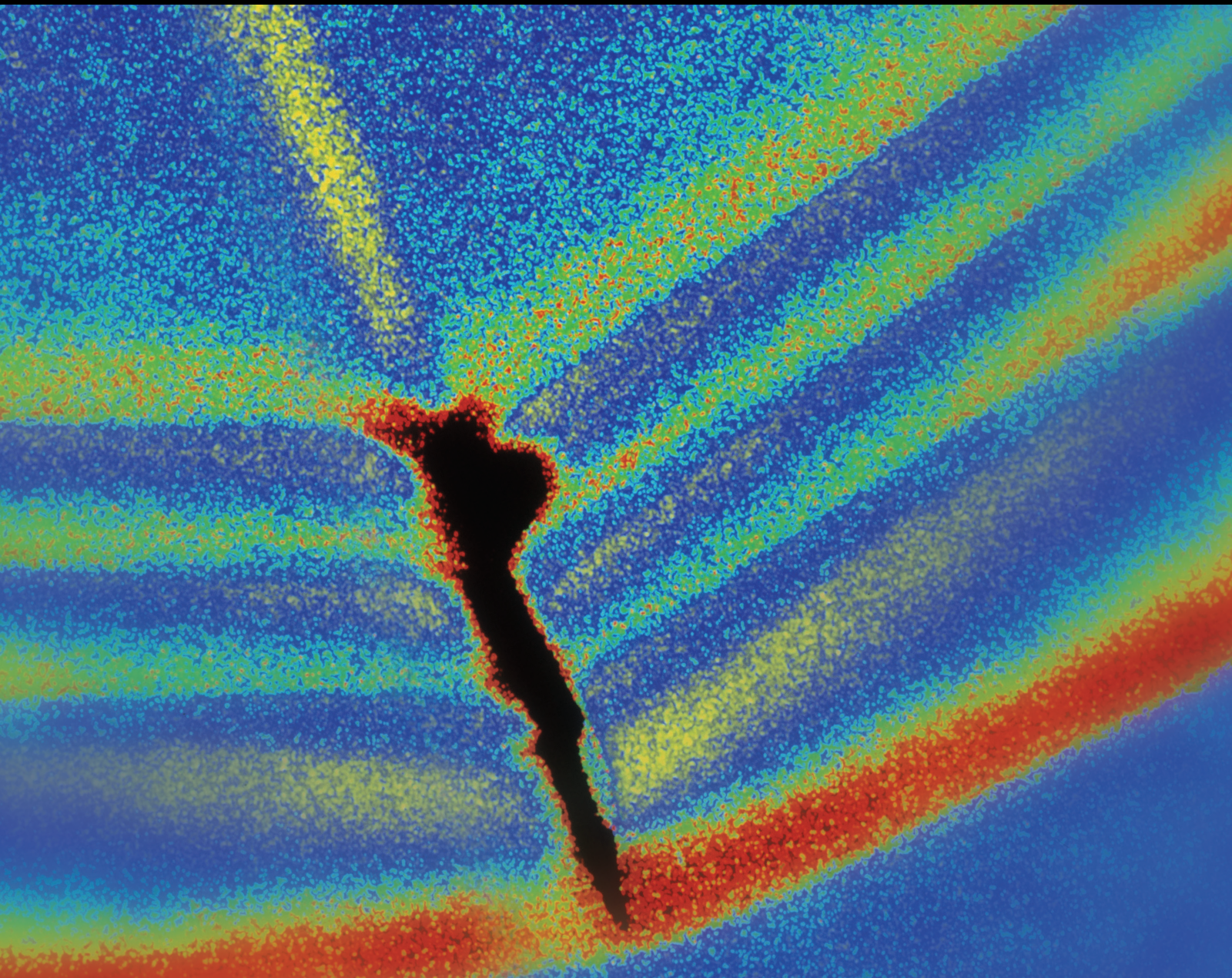


Rockburst Induced by Geological Structure and Dynamic Load in Deep Mines

Lead Guest Editor: Caiping Lu

Guest Editors: Longjun Dong and Hongwei Yang





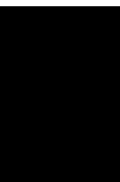
Rockburst Induced by Geological Structure and Dynamic Load in Deep Mines

Shock and Vibration

**Rockburst Induced by Geological
Structure and Dynamic Load in Deep
Mines**

Lead Guest Editor: Caiping Lu

Guest Editors: Longjun Dong and Hongwei Yang



Copyright © 2021 Hindawi Limited. All rights reserved.

This is a special issue published in "Shock and Vibration." All articles are open access articles distributed under the Creative Commons Attribution License, which permits unrestricted use, distribution, and reproduction in any medium, provided the original work is properly cited.

Chief Editor

Huu-Tai Thai , Australia


Associate Editors

Ivo Calìo , Italy
Nawawi Chouw , New Zealand
Longjun Dong , China
Farzad Ebrahimi , Iran
Mickaël Lallart , France
Vadim V. Silberschmidt , United Kingdom
Mario Terzo , Italy
Angelo Marcelo Tusset , Brazil

Academic Editors

Omid A. Yamini , Iran
Maher Abdelghani, Tunisia
Haim Abramovich , Israel
Desmond Adair , Kazakhstan
Manuel Aenlle Lopez , Spain
Brij N. Agrawal, USA
Ehsan Ahmadi, United Kingdom
Felix Albu , Romania
Marco Alfano, Italy
Sara Amoroso, Italy
Huaming An, China
P. Antonaci , Italy
José V. Araújo dos Santos , Portugal
Lutz Auersch , Germany
Matteo Aureli , USA
Azwan I. Azmi , Malaysia
Antonio Batista , Brazil
Mattia Battarra, Italy
Marco Belloli, Italy
Francisco Beltran-Carbajal , Mexico
Denis Benasciutti, Italy
Marta Berardengo , Italy
Sébastien Besset, France
Giosuè Boscato , Italy
Fabio Botta , Italy
Giuseppe Brandonisio , Italy
Francesco Bucchi , Italy
Rafał Burdzik , Poland
Salvatore Caddemi , Italy
Wahyu Caesarendra , Brunei Darussalam
Baoping Cai, China
Sandro Carbonari , Italy
Cristina Castejón , Spain

Nicola Caterino , Italy
Gabriele Cazzulani , Italy
Athanasios Chasalevris , Greece
Guoda Chen , China
Xavier Chimentin , France
Simone Cinquemani , Italy
Marco Civera , Italy
Marco Cocconcelli , Italy
Alvaro Cunha , Portugal
Giorgio Dalpiaz , Italy
Thanh-Phong Dao , Vietnam
Arka Jyoti Das , India
Raj Das, Australia
Silvio L.T. De Souza , Brazil
Xiaowei Deng , Hong Kong
Dario Di Maio , The Netherlands
Raffaella Di Sante , Italy
Luigi Di Sarno, Italy
Enrique Lopez Droguett , Chile
Mădălina Dumitriu, Romania
Sami El-Borgi , Qatar
Mohammad Elahinia , USA
Said Elias , Iceland
Selçuk Erkaya , Turkey
Gaoliang Fang , Canada
Fiorenzo A. Fazzolari , United Kingdom
Luis A. Felipe-Sese , Spain
Matteo Filippi , Italy
Piotr Fołga , Poland
Paola Forte , Italy
Francesco Franco , Italy
Juan C. G. Prada , Spain
Roman Gabl , United Kingdom
Pedro Galvín , Spain
Jinqiang Gan , China
Cong Gao , China
Arturo García García-Perez, Mexico
Rozaimi Ghazali , Malaysia
Marco Gherlone , Italy
Anindya Ghoshal , USA
Gilbert R. Gillich , Romania
Antonio Giuffrida , Italy
Annalisa Greco , Italy
Jiajie Guo, China

Amal Hajjaj , United Kingdom
Mohammad A. Hariri-Ardebili , USA
Seyed M. Hashemi , Canada
Xue-qi He, China
Agustin Herrera-May , Mexico
M.I. Herreros , Spain
Duc-Duy Ho , Vietnam
Hamid Hosano , Japan
Jin Huang , China
Ahmed Ibrahim , USA
Bernard W. Ikuu, Kenya
Xingxing Jiang , China
Jiang Jin , China
Xiaohang Jin, China
MOUSTAFA KASSEM , Malaysia
Shao-Bo Kang , China
Yuri S. Karinski , Israel
Andrzej Katunin , Poland
Manoj Khandelwal, Australia
Denise-Penelope Kontoni , Greece
Mohammadreza Koopialipour, Iran
Georges Kouroussis , Belgium
Genadijus Kulvietis, Lithuania
Pradeep Kundu , USA
Luca Landi , Italy
Moon G. Lee , Republic of Korea
Trupti Ranjan Lenka , India
Arcanjo Lenzi, Brazil
Marco Lepidi , Italy
Jinhua Li , China
Shuang Li , China
Zhixiong Li , China
Xihui Liang , Canada
Tzu-Kang Lin , Taiwan
Jinxin Liu , China
Ruonan Liu, China
Xiuquan Liu, China
Siliang Lu, China
Yixiang Lu , China
R. Luo , China
Tianshou Ma , China
Nuno M. Maia , Portugal
Abdollah Malekjafarian , Ireland
Stefano Manzoni , Italy




Stefano Marchesiello , Italy
Francesco S. Marulo, Italy
Traian Mazilu , Romania
Vittorio Memmolo , Italy
Jean-Mathieu Mencik , France
Laurent Mevel , France
Letícia Fleck Fadel Miguel , Brazil
FuRen Ming , China
Fabio Minghini , Italy
Marco Miniaci , USA
Mahdi Mohammadpour , United Kingdom
Rui Moreira , Portugal
Emiliano Mucchi , Italy
Peter Múčka , Slovakia
Fehmi Najar, Tunisia
M. Z. Naser, USA
Amr A. Nassr, Egypt
Sundararajan Natarajan , India
Toshiaki Natsuki, Japan
Miguel Neves , Portugal
Sy Dzung Nguyen , Republic of Korea
Trung Nguyen-Thoi , Vietnam
Gianni Niccolini, Italy
Rodrigo Nicoletti , Brazil
Bin Niu , China
Leilei Niu, China
Yan Niu , China
Lucio Olivares, Italy
Erkan Oterkus, United Kingdom
Roberto Palma , Spain
Junhong Park , Republic of Korea
Francesco Pellicano , Italy
Paolo Pennacchi , Italy
Giuseppe Petrone , Italy
Evgeny Petrov, United Kingdom
Franck Poisson , France
Luca Pugi , Italy
Yi Qin , China
Virginio Quaglini , Italy
Mohammad Rafiee , Canada
Carlo Rainieri , Italy
Vasudevan Rajamohan , India
Ricardo A. Ramirez-Mendoza , Mexico
José J. Rangel-Magdaleno , Mexico

Didier Rémond , France
Dario Richiedi , Italy
Fabio Rizzo, Italy
Carlo Rosso , Italy
Riccardo Rubini , Italy
Salvatore Russo , Italy
Giuseppe Ruta , Italy
Edoardo Sabbioni , Italy
Pouyan Roodgar Saffari , Iran
Filippo Santucci de Magistris , Italy
Fabrizio Scozzese , Italy
Abdullah Seçgin, Turkey
Roger Serra , France
S. Mahdi Seyed-Kolbadi, Iran
Yujie Shen, China
Bao-Jun Shi , China
Chengzhi Shi , USA
Gerardo Silva-Navarro , Mexico
Marcos Silveira , Brazil
Kumar V. Singh , USA
Jean-Jacques Sinou , France
Isabelle Sochet , France
Alba Sofi , Italy
Jussi Sopanen , Finland
Stefano Sorace , Italy
Andrea Spaggiari , Italy
Lei Su , China
Shuaishuai Sun , Australia
Fidelis Tawiah Suorineni , Kazakhstan
Cecilia Surace , Italy
Tomasz Szolc, Poland
Iacopo Tamellini , Italy
Zhuhua Tan, China
Gang Tang , China
Chao Tao, China
Tianyou Tao, China
Marco Tarabini , Italy
Hamid Toopchi-Nezhad , Iran
Carlo Trigona, Italy
Federica Tubino , Italy
Nerio Tullini , Italy
Nicolò Vaiana , Italy
Marcello Vanali , Italy
Christian Vanhille , Spain

Dr. Govind Vashishtha, Poland
F. Viadero, Spain
M. Ahmer Wadee , United Kingdom
C. M. Wang , Australia
Gaoxin Wang , China
Huiqi Wang , China
Pengfei Wang , China
Weiqiang Wang, Australia
Xian-Bo Wang, China
YuRen Wang , China
Wai-on Wong , Hong Kong
Yuanping XU , China
Biao Xiang, China
Qilong Xue , China
Xin Xue , China
Diansen Yang , China
Jie Yang , Australia
Chang-Ping Yi , Sweden
Nicolo Zampieri , Italy
Chao-Ping Zang , China
Enrico Zappino , Italy
Guo-Qing Zhang , China
Shaojian Zhang , China
Yongfang Zhang , China
Yaobing Zhao , China
Zhipeng Zhao, Japan
Changjie Zheng , China
Chuanbo Zhou , China
Hongwei Zhou, China
Hongyuan Zhou , China
Jiaxi Zhou , China
Yunlai Zhou, China
Radoslaw Zimroz , Poland



Contents

Mechanism and Procedure of Repeated Borehole Drilling Using Wall Protection and a Soft Structure to Prevent Rockburst: A Case Study

Yongliang He , Mingshi Gao , Xu Dong, and Xin Yu 

Research Article (15 pages), Article ID 6692543, Volume 2021 (2021)

Numerical and Field Investigations on Rockburst Risk Adjacent to Irregular Coal Pillars and Fault

Zhi-long He , Cai-ping Lu , Xiu-feng Zhang, Chao Wang, Bao-qi Wang, and Tao Zhou


Research Article (17 pages), Article ID 8830899, Volume 2021 (2021)

Precursory Indicator for Mode I Fracture in Brittle Rock through Critical Slowing Down Analysis

Zhenghu Zhang , Tao Chen , Ke Ma , Tiexin Liu , and Jianhui Deng 


Research Article (9 pages), Article ID 8820506, Volume 2020 (2020)

Research on Evaluation Index and Application of Rockburst Risk in Deep Strip Mining

Bangyou Jiang, Hongguang Ji, Long Fu, Shitan Gu , Tong Zou, and Jiaxin Lu


Research Article (10 pages), Article ID 8824323, Volume 2020 (2020)

Controlling Mechanism of Rock Burst by CO₂ Fracturing Blasting Based on Rock Burst System

Tianwei Lan, Chaojun Fan , Jun Han, Hongwei Zhang, and Jiawei Sun

Research Article (9 pages), Article ID 8876905, Volume 2020 (2020)

The Properties of a Coal Body and Prediction of Compound Coal-Rock Dynamic Disasters

Guwei Dong , Xuanming Liang, and Zhen Wang


Research Article (13 pages), Article ID 8830371, Volume 2020 (2020)

Experimental Study on the Influence of Specimen Shape on Rockburst Proneness of Red Sandstone

Jiajun Yang, Fengqiang Gong , Dongqiao Liu, and Zhixiang Liu


Research Article (17 pages), Article ID 4182861, Volume 2020 (2020)

Experimental Investigation of the Use of Expansive Materials to Increase Permeability in Coal Seams through Expansive Fracturing

Xiao Cui, Jiayong Zhang , Liwen Guo, and Xuemin Gong


Research Article (11 pages), Article ID 7925724, Volume 2020 (2020)

Discussions on the Complete Strain Energy Characteristics of Deep Granite and Assessment of Rockburst Tendency

Lu Chen and Lijie Guo 


Research Article (9 pages), Article ID 8825505, Volume 2020 (2020)

A New Method for Predicting Coal and Gas Outbursts

Guwei Dong , Xuanming Liang, and Qixiang Wang


Research Article (10 pages), Article ID 8867476, Volume 2020 (2020)

Dynamic Splitting Experimental Study on Sandstone at Actual High Temperatures under Different Loading Rates

Qi Ping , Mingjing Wu, Pu Yuan, Haipeng Su, and Huan Zhang

Research Article (12 pages), Article ID 8867102, Volume 2020 (2020)

Linkage Analysis between Solid-Fluid Coupling and the Strength Reduction Method for Karst Cave Water Inrush in Mines

Yanlin Zhao , Jian Liao, Qiang Liu, Yang Li, and Jianchao Cheng

Research Article (14 pages), Article ID 5415812, Volume 2020 (2020)

Research Article

Mechanism and Procedure of Repeated Borehole Drilling Using Wall Protection and a Soft Structure to Prevent Rockburst: A Case Study

Yongliang He ^{1,2}, Mingshi Gao ^{1,2}, Xu Dong^{1,2} and Xin Yu ^{1,2}

¹School of Mines, China University of Mining and Technology, Xuzhou, Jiangsu 221116, China

²State Key Laboratory of Coal Resource and Safe Mining, China University of Mining and Technology, Xuzhou, Jiangsu 221116, China

Correspondence should be addressed to Mingshi Gao; cumt_gms@cumt.edu.cn

Received 3 November 2020; Revised 19 February 2021; Accepted 10 March 2021; Published 26 March 2021

Academic Editor: Hongwei Yang

Copyright © 2021 Yongliang He et al. This is an open access article distributed under the Creative Commons Attribution License, which permits unrestricted use, distribution, and reproduction in any medium, provided the original work is properly cited.

With the increasing mining depth of coal mines, the occurrence of rockburst, especially in mine roadways, is becoming critical as a severe dynamic disaster. This paper explores the stability control of deep mine roadways and solves the contradiction between the support and pressure relief of roadways by studying the use of an internal steel pipe for wall protection and a soft structure for energy absorption during repeated borehole drilling. Numerical simulations are performed to examine the effects of active support technology on the support structure during repeated drilling. Internal steel pipes can effectively prevent the support structure from being damaged. When the soft structure cracks, the energy transmitted from the rockburst to the roadway is significantly reduced. According to the deformation and failure characteristics of the surrounding rock of the 21170 roadway, the combination of anchor active support, hydraulic lifting shed support, and soft structure energy absorption is proposed. An engineering case study shows that the support method can effectively maintain the stability of the surrounding rock and ensure the safe mining of the working face. The proposed control method can provide reference for the prevention and control of rockburst in mine roadways under similar geological conditions.

1. Introduction

A rockburst represents a severe dynamic disaster that affects the safety and efficient production in underground projects such as coal mines [1, 2]. With the increase in the depths of coal mines, the rockburst severity has considerably increased, especially in China [3]. As of June 2019, 121 coal mines in production in China were identified as rockburst prone mines [4].

The mechanism of rockburst in coal mines is highly complex because of the complexity of the mechanical properties of coal and rock and diversity of geological conditions. Many theories on rockburst mechanisms have been proposed, including the strength theory [5], energy theory [6–8], bursting liability theory [9, 10], and rigidity theory [11, 12]. In recent years, considerable research on the

mechanism of rockburst has been conducted in China, and notable results have been achieved through the rockburst research and engineering practice. Zhang [13] proposed the theory of rockburst instability. Qi et al. [14] proposed the “three-factor” mechanism of rockburst, based on the results of friction and sliding instability tests on coal and rock. Dou et al. [15] proposed the strength weakening theory for rockburst. Pan [16] established the theory of rockburst initiation. Moreover, Pan [17] proposed the instability theory for the rockburst-induced disturbance response in coal mines. Rockburst prevention and control can be achieved by regulating the stress state or decreasing the generation of high stresses in the coal/rock mass structure. To this end, the main measures include reasonable mining of the protective layer, water injection in coal seams [18], pressure relief through large-diameter coal seam drilling and

coal seam blasting, roof softening through deep hole blasting and hydraulic fracturing, and the use of directional hydraulic fracturing. These measures can considerably reduce the risk of rockburst and effectively prevent the occurrence of rockburst disasters. According to preliminary statistics, 90.8% of rockburst accidents occurred in coal mine roadways [19]. However, only a few studies have focused on the support of roadways to prevent/control rockburst. From the perspective of rigid or flexible supports, support concepts for mine roadways have been established. The combinations of support technology currently used in coal mines include anchor net + anchor cable + steel arch support technology, steel U-bolt support technology, anchor + metal net + shotcrete + steel U-bolt support technology, energy absorption support technology, coupled rigid and flexible support technology [20], and “three-level support” technology [21]. In the anchor net + anchor cable + steel arch support technology, steel U-bolt support technology, and anchor + metal net + shotcrete + steel U-bolt support technology, only the support of the roadway is strengthened, and the pressure relief of the high stress roadway is not considered. The reinforcement of the roadway support increases the support cost and process and does not considerably influence the support effect of the roadway with rock burst. The energy absorption support technology, coupled rigid and flexible support technology, and “three-level support” technology involve filling a layer of energy absorbing material and adding energy absorbing materials with a weak stiffness between the surrounding rock and support, which can absorb a considerable amount of the impact energy and reduce the damage of the impact load on the support structure. However, this type of support can passively absorb only a small amount of energy, and if a large energy rockburst is encountered, the roadway may be critically damaged. The new support method proposed in this paper solves the contradiction between strong active support, pressure relief, and antiscour in rockburst roadway and can enhance the support and pressure relief effect of the rockburst roadway. Moreover, this approach can effectively maintain the strength and integrity of the surrounding rock of the roadway, thereby protecting it from damage; increase the stability of the surrounding rock of roadway wall, as the soft structure may crack again after high stress compaction; and protect the inner strong small structure from secondary damage of the borehole.

Rockburst occurrence changes the stress state in the coal and rock masses and may alter the generation of high stresses by transferring and releasing stress. In this study, focused on providing roadway support through energy absorption by soft structures, relevant technical measures are adopted to realize the stress transfer and stress release from coal and rock masses in mine roadways and effectively prevent the occurrence of rockburst. The anchor (cable)- + hydraulic lifting support + soft structure energy absorption technology is adopted. The technology of repeated borehole drilling and soft structure cracking is researched, and the contradiction between the support and pressure relief of a roadway under impact loading is coordinated, thereby enhancing the roadway performance.

2. Engineering Background of the Changcun Coal Mine

2.1. Geological Conditions. The Yima coal field, which is located in Yima, China (Mianchi County, Henan Province), is a thick coal field from the Mesozoic era. This region contains the Changcun, Yuejin, Qianqiu, Gengcun, and Yangcun coal mines. The coal seam in the Yima coal field is the middle Jurassic Yima formation, which contains 5 coal seams, among which the No. 2⁻¹ and 2⁻³ coal seams are generally minable. The mining depth of each coal seam is generally greater than 600 m, and the maximum depth is 1060 m. The lithologies of the coal seam roof and floor mainly include mudstone, sandstone, and conglomerate. The direct roof is generally mudstone, above which lies a sand conglomerate/argillaceous interbedded sandstone (average thickness = 166 m) layer, followed by an extremely thick gravel layer of the upper Jurassic period. Mining results in brittle fractures of the overlying hard plate, which easily cause dynamic disturbances in the roof. The F16 fault is a regional compressional and torsional thrust fault with a strike of approximately 110° (nearly east-west in orientation), an extension of approximately 45 km, a dip angle of 15–35° in the deep part and 75° in the shallow part, and a fault throw of approximately 50–500 m. The F16 fault connects with the Qianqiu mine in the north and extends into the Yangcun and Gengcun mines to the west and Changcun and Yuejin mines to the east, as shown in Figure 1.

2.2. Roadway Support. In the Yima mining area, the No. 2⁻³ coal seam is mainly mined. The mining roadway is generally arranged in the coal seam, 0.5 m of coal is reserved in the floor, and the section of the mine roadway is generally arched. A three-level support mode including an anchor net cable, 36 steel U-bolts, and a single hydraulic prop is generally adopted during the excavation of the mine roadway. The single hydraulic support is replaced by a hydraulic lifting frame or roadway supports during mining. A schematic and photograph of the three-level support system are shown in Figure 2.

2.3. Changcun Coal Mine. The surface of the Changcun coal mine is mostly covered with Quaternary loess. The ground elevation is 415–580 m, and the F16 reverse fault is a regional reverse fault that developed in the southeast region of the mine field. The direct roof of the coal seam is mudstone with a thickness of 16–45 m. The roof is mainly composed of conglomerate, fine sandstone, and mudstone, which can be permeated by water. The bottom of the coal seam is carbonaceous mudstone with a thickness of 0.5–6.0 m and a coal seam with a hardness of 1.5–2.0. The geological formations in the coal seam are presented in Figure 3.

During service, the 21170 working face is affected by the mining-induced dynamic pressure of the adjacent face. The west side consists of the three descending coal pillars of the 21 mining area, and the east side is the coal pillar of the F16 fault. The upper part of the working face is the 21150

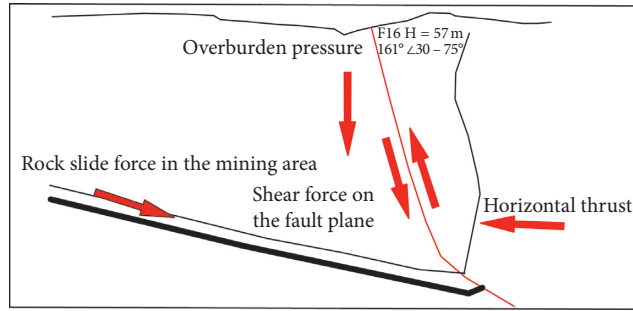
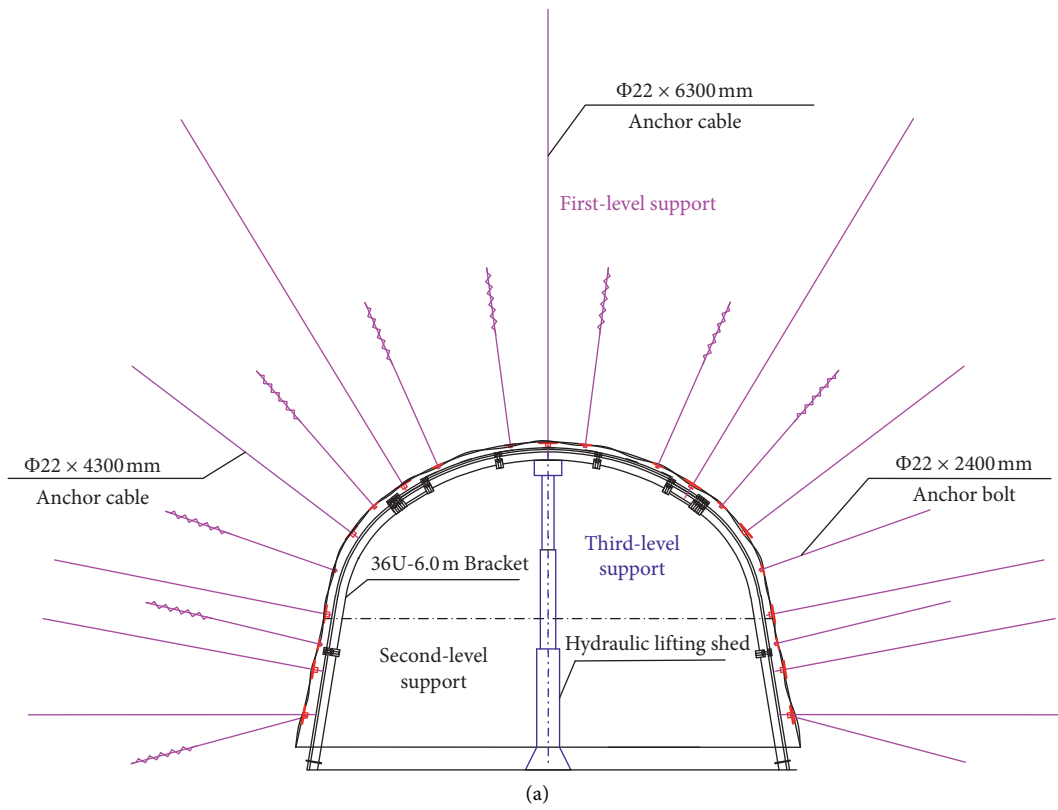


FIGURE 1: F16 fault diagram.



(a)



(b)

FIGURE 2: Three-level support of the surrounding rock. (a) Schematic. (b) Photograph.

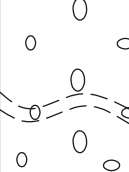
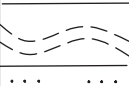
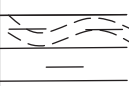
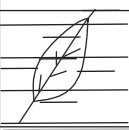

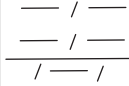
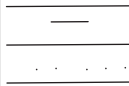
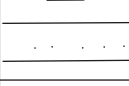
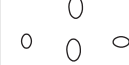
Drill hole	Depth (m)	Thickness (m)	Geological formation	Lithology name	Lithological characteristics
Roof	700.1	430		Conglomerate	Purplish red quartzite, quartz sandstone, gray green brown red igneous rock, with different diameters and sizes, argillaceous sand basement cemented, mixed with layered brown red siltstone
	720.6	23.5		Fine sandstone	Light gray spinning rock strip, wavy cross bedding, containing more nodular pyrite nodules, distributed along the layer, with dolomite broken in the section
	763.7	40.1		Mudstone	Plant fossils, partially carbonized, coarse-grained, dense and uniform below, with more siderite bands, horizontal bedding, and schistose pyrite at the bottom
	768.5	4.8		Mudstone	Muscovite sheet, containing siltstone locally, containing plant fragments and lamellibranchial fossils
Coal	779.7	12.0		Coal	Fibrous structure, light weight, mixed with carbonaceous mudstone and gangue
Floor	782.8	3.1		Mudstone	Black. High carbon content
	807.8	30.0		Argillite	Sandy claystone, containing angular quartzite small gravel and siderite, containing more plant root fossils. Slightly larger proportion
				Fine sandstone	Sandy claystone
812.9	5.1		Conglomerate	Quartz sandstone, shaly component, basal cementation	

FIGURE 3: Geological formations.

working face that has been stopped, and the lower part is the 21190 working face that has not been designed. The rock surrounding the roadway is mainly mudstone, which is easily weathered and broken, resulting in the rapid deformation of the roadway. The surrounding rock develops rapidly in the early stage of excavation. In addition to long-term creep, the overall deformation is large, and the roadway needs to be repaired after excavation. The deformation of the roadway mainly consists of two sides moving and floor heave. The 21170 working face is shown in Figure 4.

3. Borehole Wall Protection

Cracking of the soft structure is mainly caused by repeated drilling, blasting, water pressure [22], and air pressure [23, 24]. The complete rock mass is split into a loose state by an artificial method. The strength of the surrounding rock and support structure considerably influences the support of the roadway. Pressure relief or soft structure cracking

technology, such as drilling and blasting, transfers the stress from the roadway and weakens the strength of the roadway surrounding rock. After cracking, the structural integrity of the support structure is diminished, which deteriorates the stability of the roadway support. To protect the support structure from damage, the support structure is protected by an internal steel pipe. The control effect of the support structure and the internal steel pipe used for borehole protection on the strength of the surrounding rock and integrity of the support structure is analysed through numerical simulations; moreover, the stress and plastic zone of the surrounding coal and rock mass are investigated.

According to the geological conditions of the 21170 roadways, after the support of the roadway is completed, large-diameter pressure relief holes are drilled in the roadway. The drilling is performed perpendicular to the two sides of the roadway. The diameter of the hole is 110 mm, and the length and distance are 10 m and 1 m, respectively. The simulated roadway and support parameters are

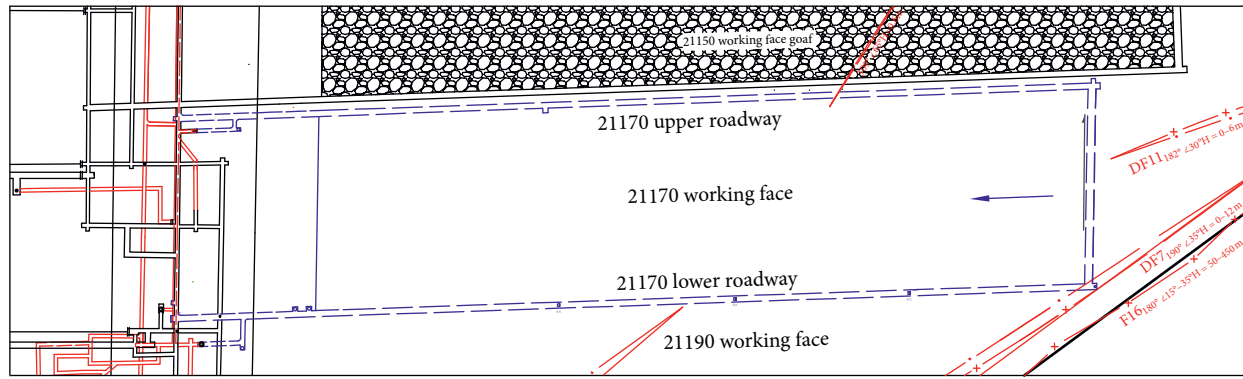


FIGURE 4: 21170 working face.

consistent with those on site. The steel pipe adopts a linear elastic constitutive model, with an elastic modulus of 210 GPa and wall thickness of 0.05 m. The steel pipe is modelled with cylindrical shell elements, for which the grid is as uniform as possible, and the grid in which the steel pipe and coal body are in contact is consistent. A contact surface is provided between the steel pipe and coal, and a hollow cylindrical grid is implemented at the contact surface on the steel pipe side. Figure 5 shows the simulation of the pressure relief hole.

Figures 6–11 show the stress and displacement states under the Mohr–Coulomb criterion. Almost no displacement is observed around the steel pipe; however, the displacement in the area around the steel pipe is 20 times larger when no steel pipes are used. The results of the stress calculation show that the stress in the coal cannot be released in the case of drilling with steel pipes installed, and the value is similar to the stress before drilling; in contrast, the stress in the coal is released when no steel pipes are used. Figure 12 shows the creep relations of the roadway during drilling with and without steel pipes. The plastic zone is larger when the borehole does not have a steel pipe. Under the action of high stress and large creep, the fracture range of the plastic zone further increases, thereby affecting the stability of the roadway support structure.

After the calculation balance of the roadway excavation, the plastic failure area of the surrounding rock is redefined into a new group by fish language. The Burger creep model is used as the constitutive model. The maximum time step is 0.04, the calculation time is 200, and the corresponding site age is 200 d. The creep variation and creep rate of the roadway are recorded in the whole process. Figure 13 shows the relationship curve of the creep variable, creep rate, and time.

4. Using a Soft Structure to Prevent Rockburst

4.1. Energy Absorption of a Soft Structure. A rockburst is a shock wave produced by either fracturing hard, thick strata during the mining process, or the movement and fracture of strata during the blasting process. The stress wave is directly transmitted to the roadway or working surface, and it may exceed the ultimate bearing capacity of the surrounding rock. Cracks in the surrounding rock induce instability and

failure of the support structure. Therefore, a soft structure with an energy-absorption function can be set outside the support area. The shock wave is considerably weakened through the scattering and absorption provided by the soft structure, and, consequently, the stability of the support structure can be maintained. Figure 14 shows the soft structure used for the mine roadway [25, 26]. The soft structure is essentially a wave absorption zone [27, 28]. The loose coal or rock formed by fracturing is used to absorb the energy generated by the rockburst.

In the process of transmission, an impact-induced stress wave may destroy the coal and rock mass. The energy generated when the impact occurs is denoted as E , the energy consumed in the transmission of the outer strong structure is denoted as E_1 , and the energy absorbed by the middle soft structure is denoted as E_2 . Therefore, the remaining energy that reaches the support structure is $E_3 = E - E_1 - E_2$. The energy absorption provided by the soft structure mainly includes the energy absorbed by the loose blocks and spatial scattering and that through rotation and rock reflection [29, 30], as shown in Figure 12. Energy is absorbed by the loose blocks because the dynamic shock wave requires more time to propagate through a fractured coal/rock mass than through a dense coal/rock mass, which decreases the shock wave velocity and vibration wave velocity; thus, the impact energy is reduced. Rotational energy absorption refers to the rotation/movement of the fractured coal/rock induced by the transmission of the dynamic waves, which transforms a portion of the impact energy to kinetic energy. Spatial scattering energy absorption refers to the energy absorbed through the formation of a broken area including fractured coal and rock. As the dynamic wave propagates, it is scattered to the surrounding broken area and expands continuously through the loose particles, thereby decreasing the energy of the dynamic wave. Rock-reflected energy absorption refers to the reflection and transmission phenomena of the dynamic wave in the broken area. After reflection, the energy of the transmitted dynamic wave is reduced, and the wave is dispersed. Therefore, the impact energy of the dynamic wave propagating to the roadway is reduced.

4.2. Numerical Simulation Development. A numerical simulation in FLAC3D is performed to examine the energy absorption and stress distribution of the soft structure in the

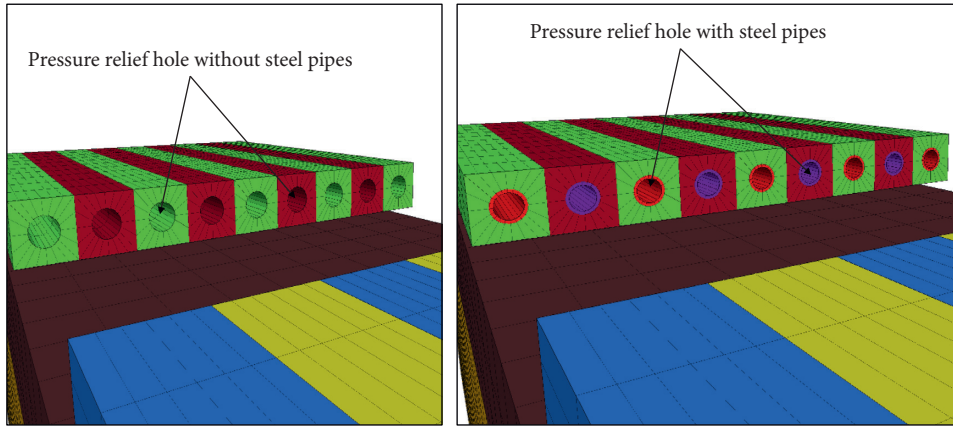


FIGURE 5: Pressure relief hole simulation.

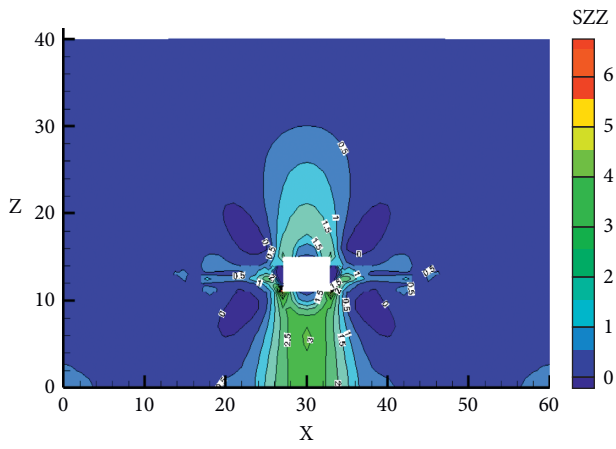


FIGURE 6: ZZ direction stress without steel pipes.

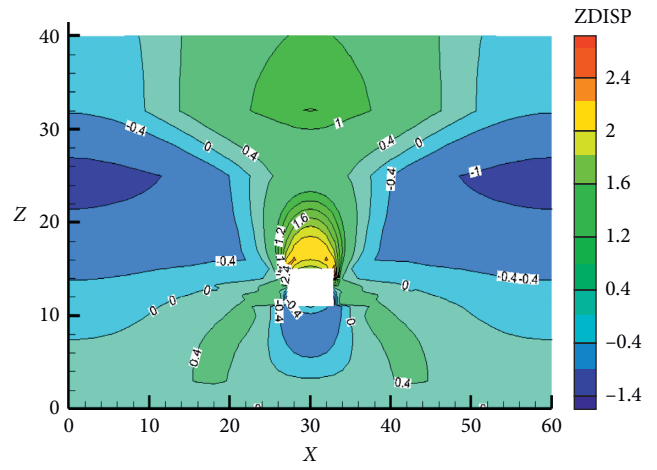


FIGURE 8: Z-displacement without steel pipes.

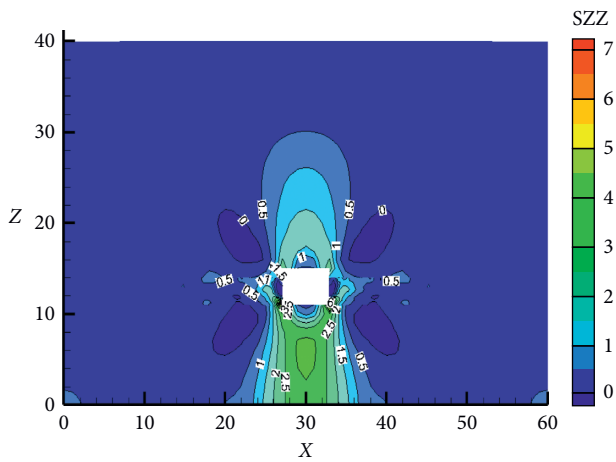


FIGURE 7: ZZ direction stress with steel pipes.

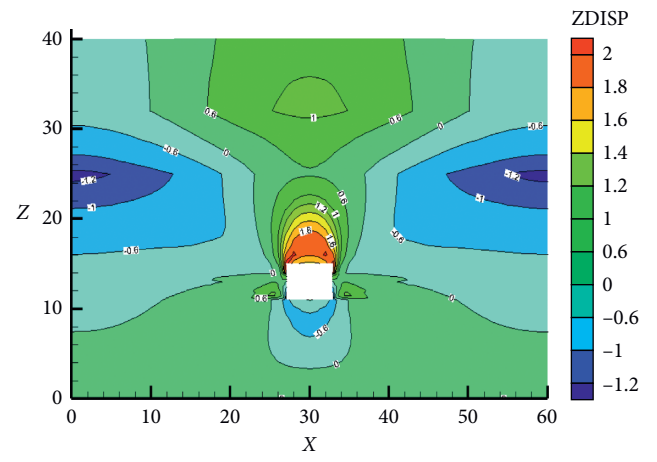


FIGURE 9: Z-displacement with steel pipes.

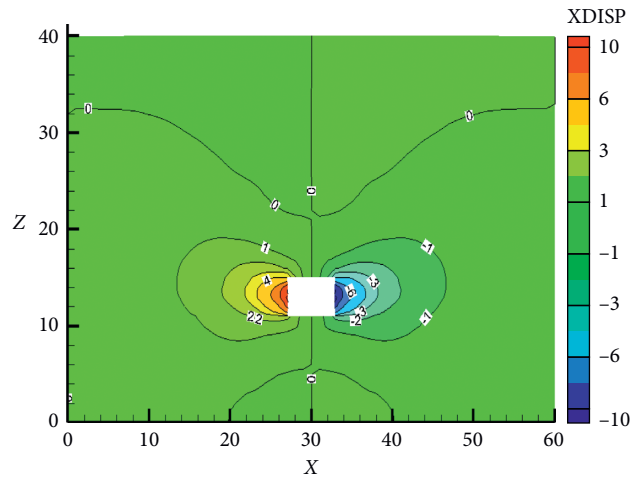


FIGURE 10: X-displacement without steel pipes.

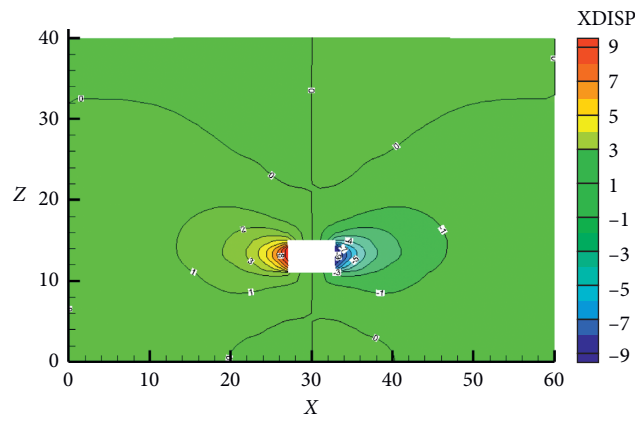


FIGURE 11: X-displacement with steel pipes.

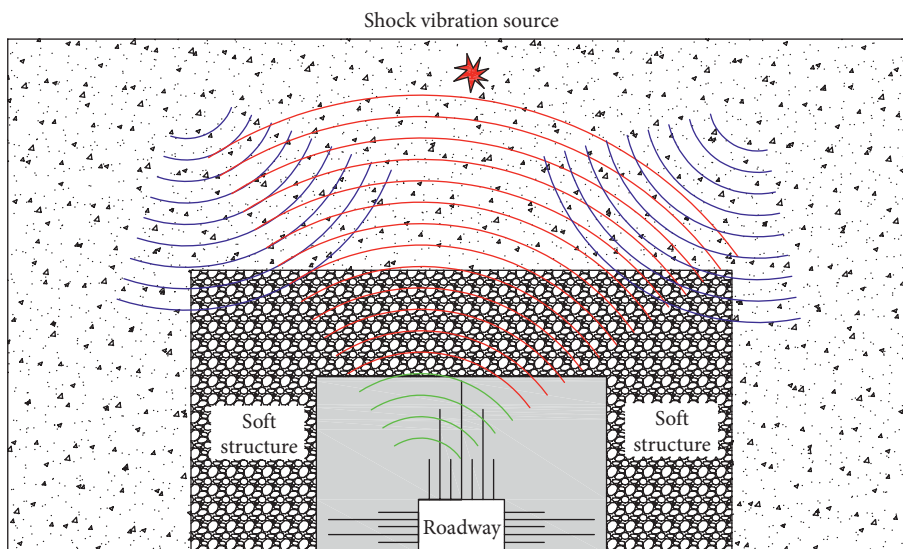


FIGURE 12: Soft structure used for a mine roadway.

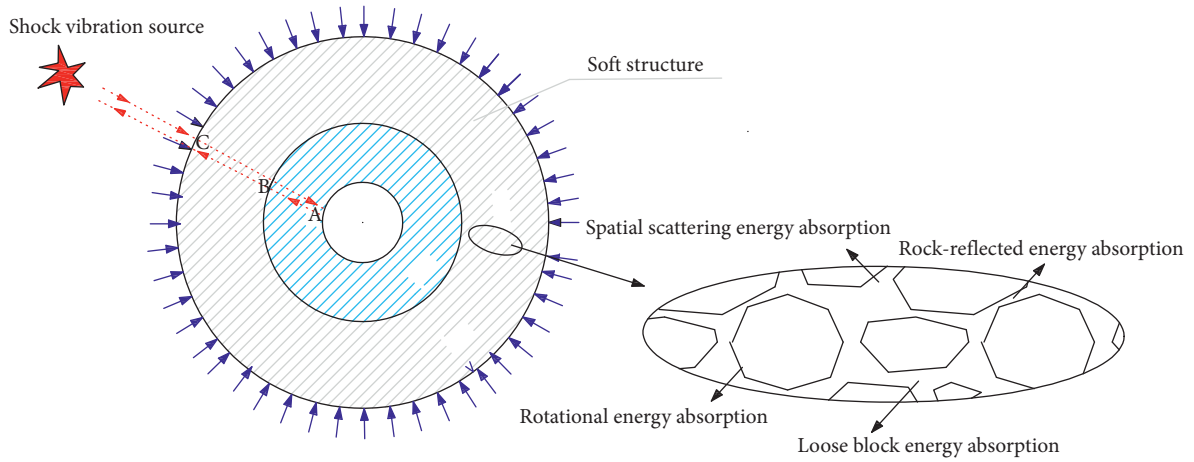


FIGURE 13: Roadway creep relations

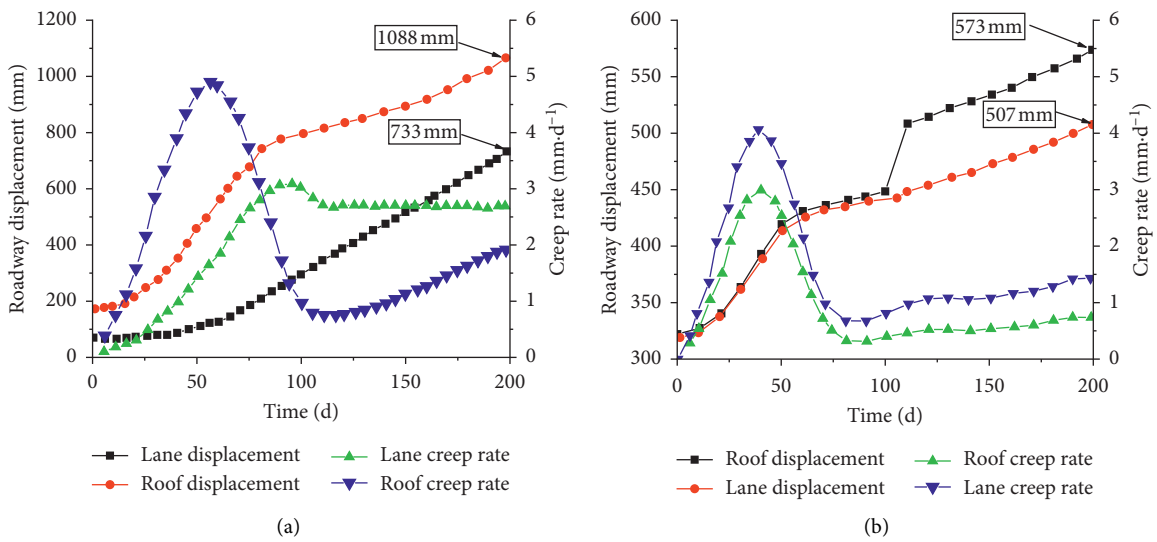


FIGURE 14: Roadway creep relations. (a) Roadway creep without steel pipes. (b) Roadway creep with steel pipes.

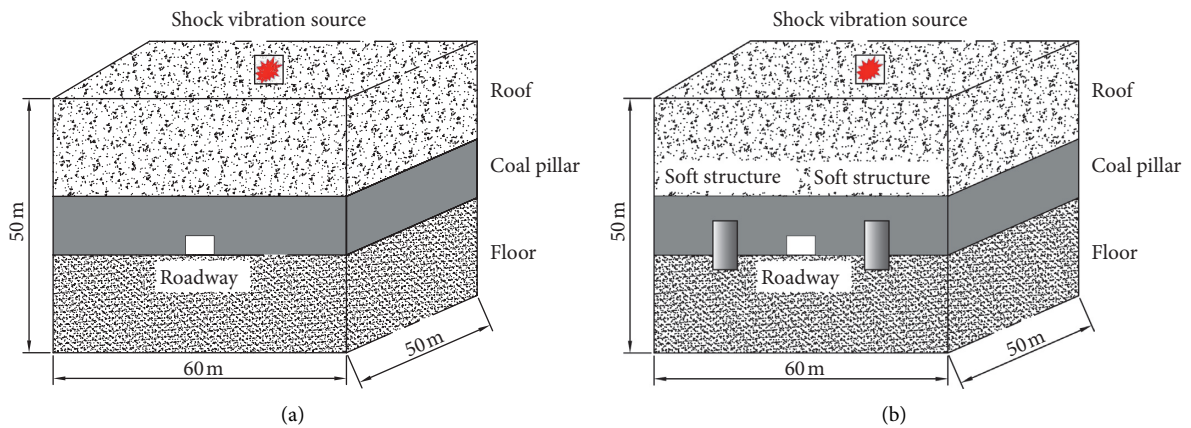


FIGURE 15: Numerical model. (a) Roadway without a soft structure. (b) Roadway with a soft structure.

roadway. According to the geological characteristics of the 21170 roadway, the numerical calculation model is as shown in Figure 15. This model has dimensions of $60\text{ m} \times 50\text{ m} \times 60\text{ m}$ ($X \times Y \times Z$), and a roadway with dimensions of $5.8\text{ m} \times 3.5\text{ m}$ is excavated in the centre of the model. According to the analysis of the soft structure with different widths and thicknesses, the soft structure is located 10 m outside the roadway support layer, with dimensions of $5\text{ m} \times 5\text{ m}$. The dynamic impact load is applied on the upper part of the model. The soft structure parameters can be set as 1% to 1/1000 of the rock parameters; we use 1% [31].

At the top of the model, a vertical stress of 17.5 MPa is applied to simulate the overburden. The horizontal and bottom sides are roller-constrained. The Mohr–Coulomb criterion is used to simulate the rock strata. Poisson's ratio of the coal and rock and the modulus of elasticity, cohesion, and tensile strength can be assumed to be 1.2–1.4 times and 0.1–0.25 times greater than those obtained through laboratory testing, respectively [32]. The average uniaxial compressive strength and average stiffness are 0.284 times and 0.469 times the values obtained in the laboratory [33]. According to the parameters determined experimentally, the distribution and mechanical parameters of the model are as shown in Table 1. The simulation involves the following steps. (1) Establish the model, set the boundary conditions, and balance the initial stress. (2) Excavate the roadway for static analysis. (3) Apply a dynamic load to simulate the effect of the roadway support without a soft structure. (4) Simulate the effect of the roadway support with a soft structure.

4.3. Impact Loading. The impact loading from a roof collapse on the roadway and time-history curve of the impact are shown in Figure 16. A roof collapse produces a dynamic load with an extremely short duration and high loading speed. The stress from this dynamic load has only a single peak, as it undergoes one loading and unloading action and later decays rapidly; no second stress wave occurs. The overall change trend is in the form of a pulse load. The maximum stress from the impact-induced dynamic load is 13.9 MPa, and the dynamic load duration is approximately 25 ms, of which the loading and unloading durations are 5 ms and 20 ms, respectively. The roof collapse rapidly produces a dynamic load greater than the static weight of the rock mass.

To describe the propagation of the stress wave in the model, the maximum grid width of the model is set as 1 m, which is less than 1/10 of the wavelength corresponding to the highest frequency of the wave. The boundary conditions are set as static boundaries, the mechanical resistance is Rayleigh damping, the minimum critical damping ratio is 0.005, and the minimum centre frequency is determined by the self-vibration frequency calculated using the model without damping under the action of gravity. The minimum centre frequency is calculated to be 8.0 Hz. The dynamic calculation time is 80 ms.

4.4. Numerical Simulation Effect. Before applying the dynamic load, the roadway strata are in a state of compressive stress, as shown in Figure 17. Because the dynamic loading wave is

reflected and refracted at the interface of the roadway strata during propagation, the reflected stress wave and unloading effect of the impact load are superposed, which transforms the vertical stress in the roadway from a compressive stress to a tensile stress. The low tensile strength of rock and action of the dynamic load can easily lead to tensile failure of the rock floor. After the soft structure cracks, the vertical stress is reduced, and the soft structure attenuates the stress wave and protects the roadway from damage. Figures 18 and 19 show the simulation results of the roadway displacement. The roadway displacement is large under the action of the dynamic load in the roadway without a soft structure. However, after the soft structure cracks, the soft structure absorbs the dynamic loading wave, and the roadway support structure is not damaged. Figure 20 shows the plastic zone under the impact load, in which the tensile and shear failures occurred in the roadway. Primarily existing shear and tension failure units can be observed around the roadway support without the soft structure; in contrast, existing and new shear failure units can be observed around the roadway with the soft structure.

The rockburst caused by the large-scale collapse of the rock mass on the roadway and the dynamic loading and stope pressure are superposed in the form of a vector. The result of this stress superposition causes oscillations in the roadway stress field. Since the stress state during dynamic loading shifts from compression to tension, when the tensile stress is greater than the tensile strength of the rock in the floor layer, cracks occur along the tensile surface. Under the superposition of the dynamic load and mining support pressure, the shear stress is concentrated, and the rock stratum is damaged by compression and shear. The impact of a large-scale rock mass promotes the development of fractures in the roadway strata, which causes a significant increase in the range and depth of damage in the roadway strata. The cracks created in the soft structure facilitate wave absorption and energy dissipation, as the formation and propagation of these cracks help absorb a portion of the energy from the dynamic wave.

5. Engineering Case Study

5.1. Roadway Support. As shown in Figure 21, $\Phi 22 \times 2500$ mm anchors are used for the roof, for which the individual spacing is 900 mm, and the row spacing is 800 mm; $\Phi 18.9 \times 5300$ mm anchor cables are arranged along the roadway, with an individual spacing of 1.5 m and row spacing of 1.6 m; and $\Phi 18.9 \times 8000$ mm anchor cables are arranged along the roadway, with an individual spacing of 2.5 m and row spacing of 1.6 m. Two rows of horizontal anchor cable beams are constructed in the middle of the two sides and near the bottom. The anchor cable has dimensions of $\Phi 18.9 \times 5300$ mm, the steel beam is 3.2 m long, and the hole spacing is 1.6 m. After installing the anchor and mesh support, a hydraulic lifting shed is built along the centre of the roadway to strengthen the support.

5.2. Soft Structure Cracking. The repeated cutting method is used to weaken the two sides of the roadway to create the “soft structure” to absorb the dynamic and static energy. The

TABLE 1: Mechanical parameters of the coal and rock used in the numerical model.

Rock strata	Thickness (m)	Density (kg/m^3)	Bulk modulus (GPa)	Shear modulus (GPa)	Cohesion (MPa)	Friction angle ($^\circ$)
Conglomerate	5	2440	3.06	1.66	2.1	34
Fine sandstone	20	2540	4.5	2.8	2.5	23.25
Carbon mudstone	2	2600	4.2	0.47	3.5	32
Coal	12	1350	0.433	0.2	7.0	33
Fine sandstone	3	2570	1.01	0.70	2.6	26
Mudstone	40	2450	2.82	0.57	3.5	32

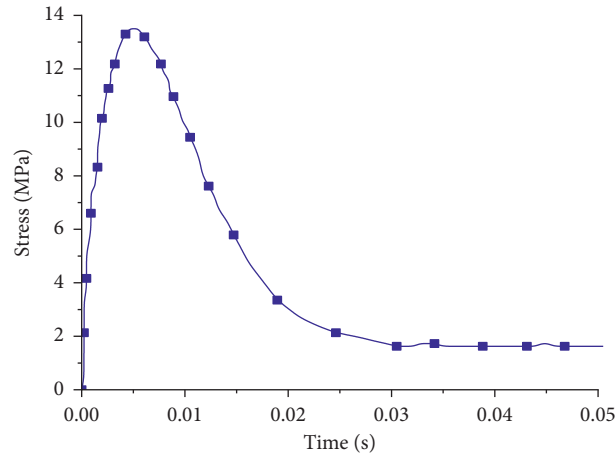


FIGURE 16: Time-history curve of the impact load.

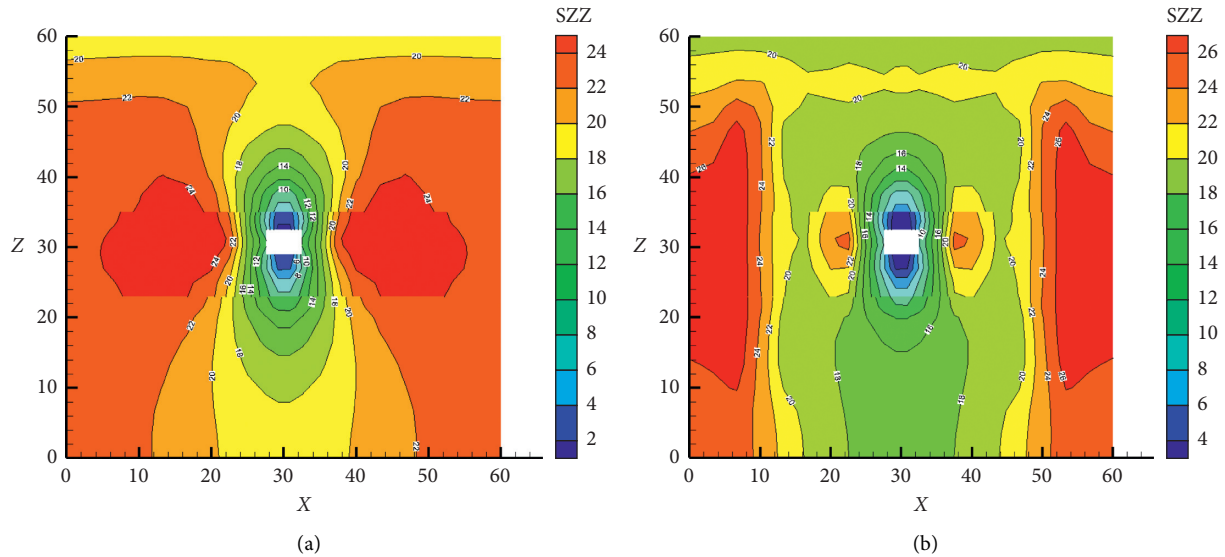


FIGURE 17: Stress field analysis. (a) Roadway without a soft structure. (b) Roadway with a soft structure.

drilling machine prepares several pressure-relief holes in the designated positions of the coal and rock on the left and right sides of the roadway. The diameter of the drilling hole is 110 mm, and the spacing between the openings of the pressure-relief holes is 3 m. A 10 m steel pipe is inserted in the borehole to protect the strong structure from damage, which helps strengthen the strong structure in the roadway. We continue drilling from the pressure relief borehole inside

the steel tube and crack the coal and rock in the roadway by using the drill pipe deep in the pressure relief borehole. After the cracking, the coal and rock are interconnected to form the soft anti-impact structure of the two sides of the roadway. After the two sides of the roadway are compacted under the action of the pressure of coal and rock mass, the coal and rock masses are cracked and relieved through repeated cycles of inserting steel tubes without destroying

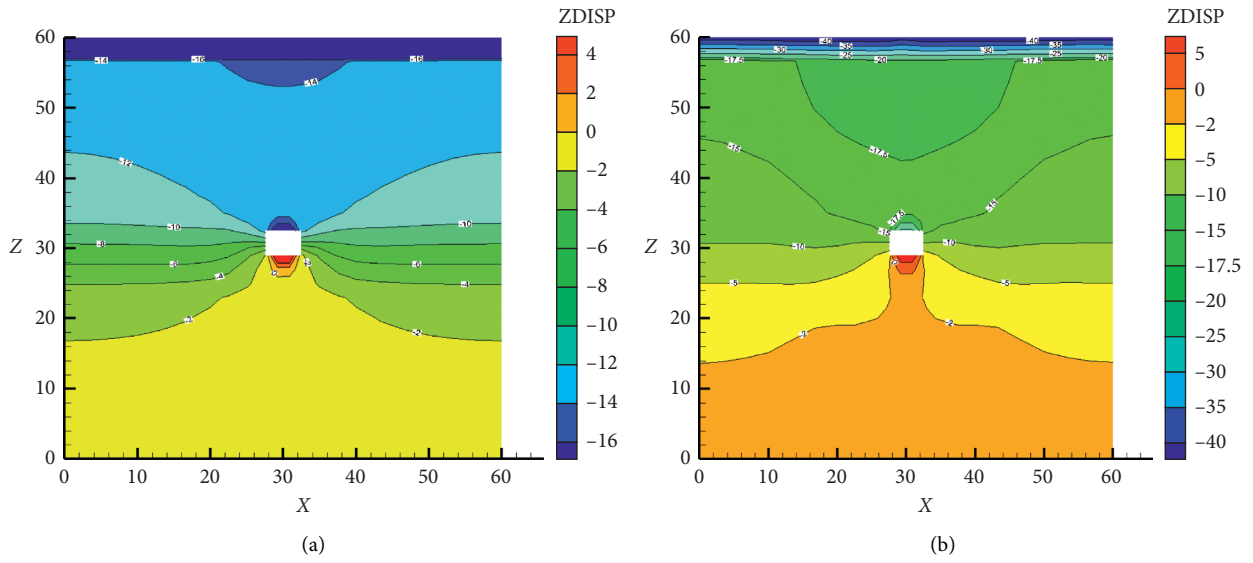


FIGURE 18: Z-displacement analysis. (a) Roadway without a soft structure. (b) Roadway with a soft structure.

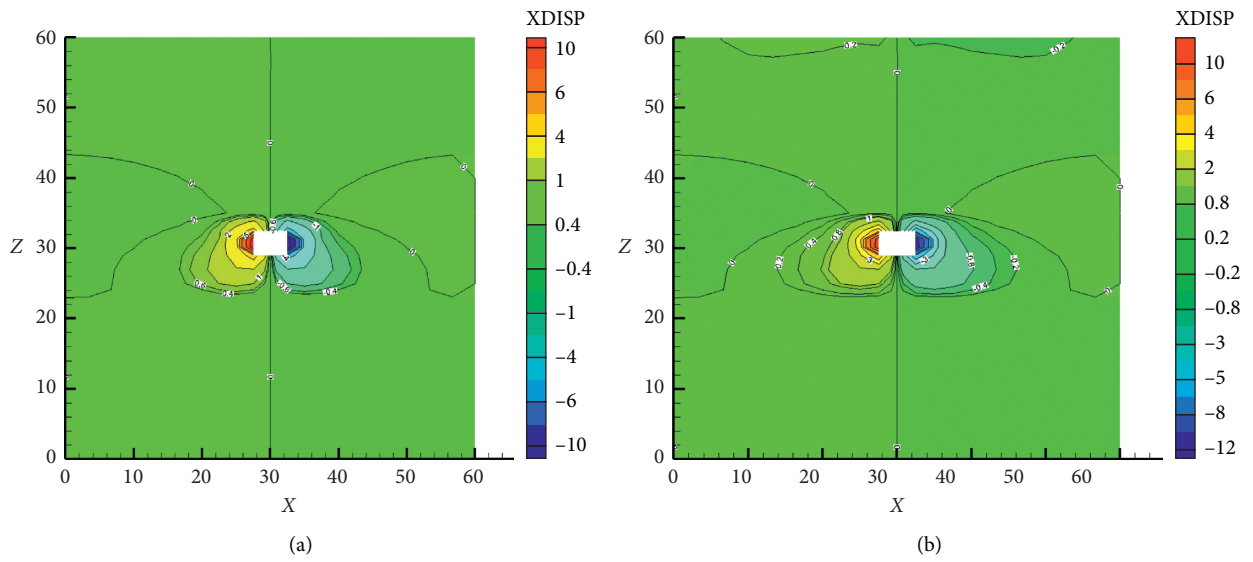


FIGURE 19: X-displacement analysis. (a) Roadway without a soft structure. (b) Roadway with a soft structure.

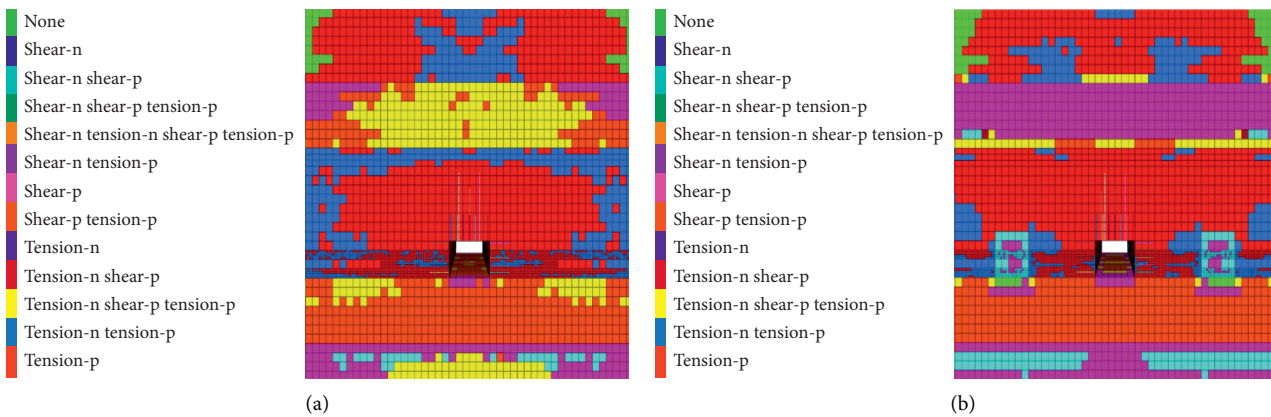


FIGURE 20: Plastic zone. (a) Roadway without a soft structure. (b) Roadway with a soft structure.

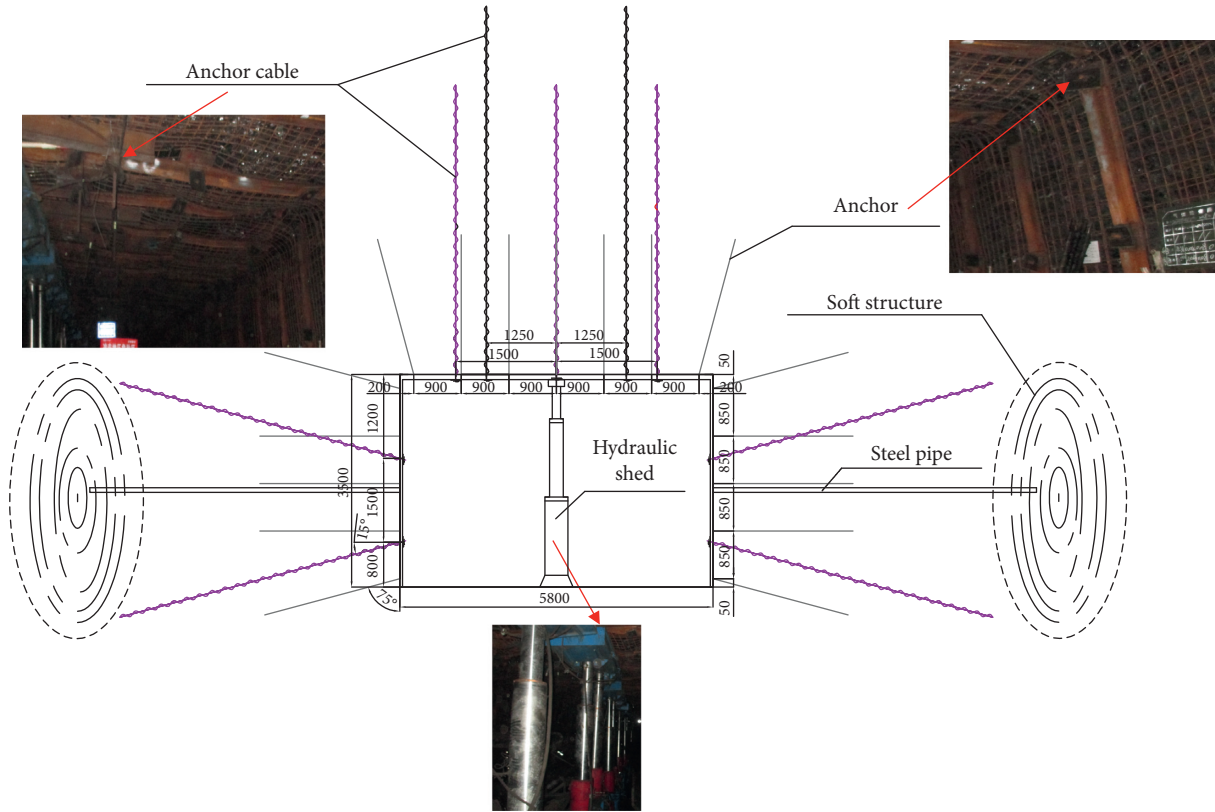


FIGURE 21: Roadway support parameters.

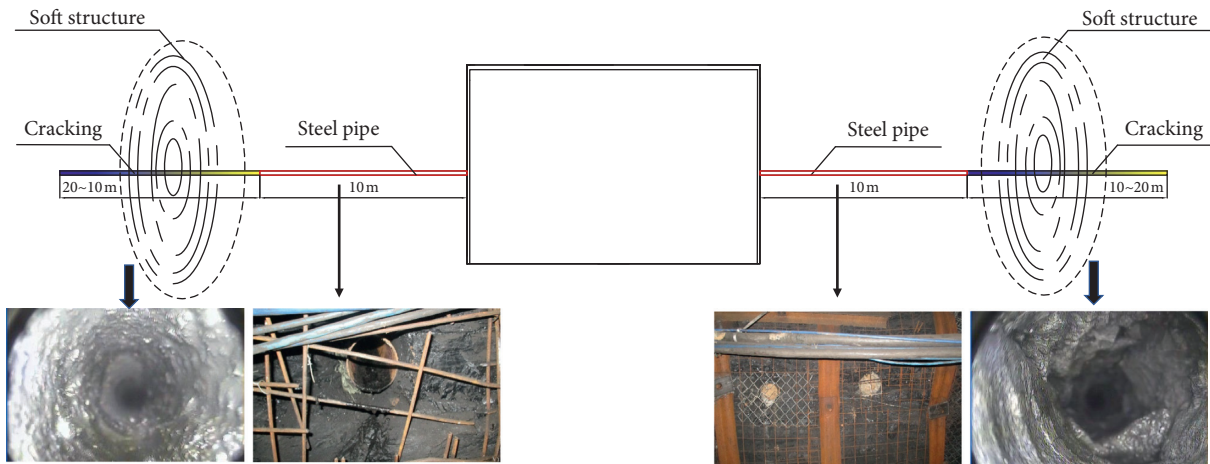


FIGURE 22: Soft structure construction.

the strong and small structures in the roadway. The support layer of the roadway does not enlarge the loose circle of the coal and rock mass under the action of pressure relief drilling.

According to the observation of the mine pressure, holes (depth and diameter of 20 m and 110 mm, respectively) are drilled on both sides of the roadway, and 10 m long steel pipes are placed in the holes. The steel pipe can be formed by the butt joint of a short steel pipe and screws. In the outer end of the steel pipe, the loose structure of coal is formed in the process of drilling. After the soft structures of the two

sides of the roadway are compacted under the pressure of the coal and rock mass, drilling is again performed through the steel pipe into the pressure relief borehole to crack the coal and rock mass of the roadway. According to the compaction of the soft structure of the two sides of the roadway, the coal and rock mass of the roadway is repeatedly cracked many times. In this process, the left and right sides of the roadway do not expand the loosening ring of the coal and rock mass under the action of pressure relief drilling, which protects the support structure while cracking the soft structure. The cracking of the soft structure is shown in Figure 22.

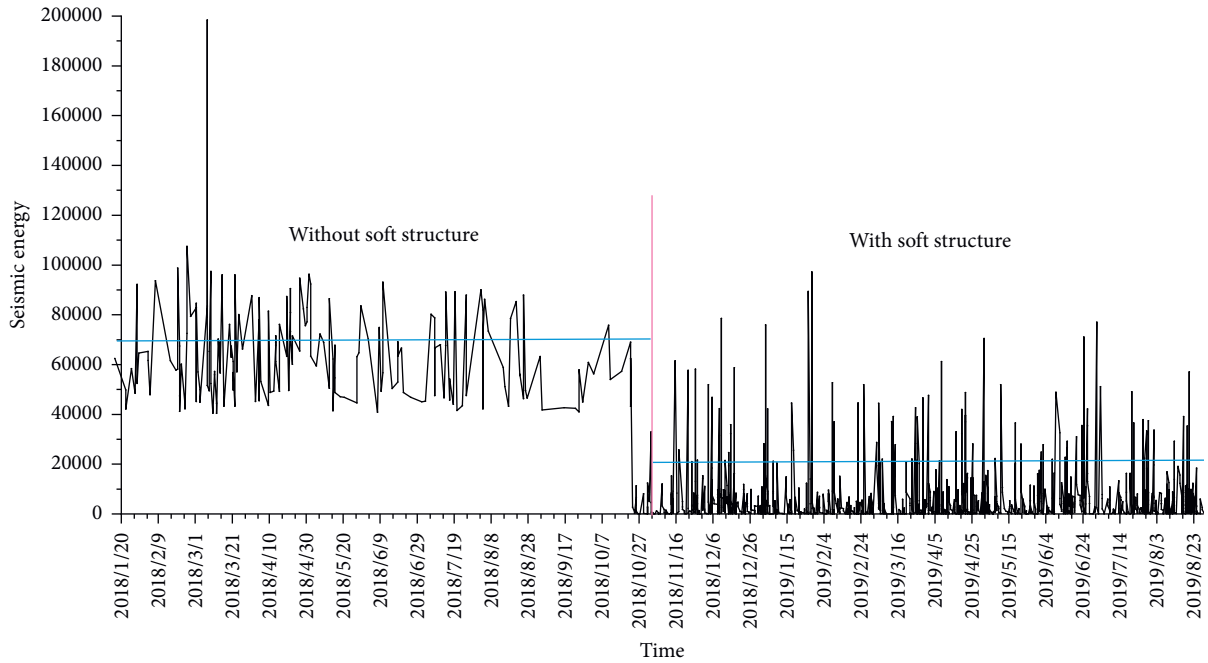


FIGURE 23: Microseismic energy monitoring before and after soft structure construction.

TABLE 2: Comparison of roadway supports.

	Previous	Present
Roof		
Roadway		
Overall		

Figure 23 shows the microseismic energy monitoring of the roadway before and after the soft structure cracking. It can be noted that the energy monitored is significantly reduced after the soft structure cracking. The stress in the coal body can be noted to be transferred or absorbed, which effectively reduces the roadway damage caused by the high stress and rockburst.

5.3. *Support Effect.* The active support of the stable anchorage bearing circle of the roadway support and pressure relief of the middle soft structure provide satisfactory stress support conditions for the roadway. The internal steel pipe used for borehole protection can repeatedly crack the middle soft structure while protecting the support structure from damage, which prevents not only the crack expansion of the

loosening circle of the support structure but also the overall instability of the support of the roadway, thereby solving the contradiction between the support and pressure relief of the roadway. Table 2 compares the roadway support effects. The support parameters significantly enhance the roadway support situation. The selection of the support parameters is reasonable, which effectively controls the roof separation and deformation of the rock surrounding the roadway.

6. Conclusions

The combination of internal steel pipe borehole protection, repeated borehole drilling, and soft structure cracking is studied. The soft structure can solve the contradiction between the support and pressure relief of roadways. Numerical simulations are performed to study the active support of the support structure and energy absorption of the soft structure. The internal steel pipe used for borehole protection effectively prevents the support structure from being damaged. When the soft structure cracks during drilling, the energy from a rockburst transmitted to the roadway is significantly reduced. The main conclusions are as follows:

- (1) The use of a soft structure for mine roadways is examined, the support structure mechanism of the surrounding rock is analysed, and the deformation of the rock surrounding the roadway is effectively controlled. The deformation and failure of the rock surrounding the roadway are closely related to the strength of the support structure.
- (2) The soft structure can transfer or absorb high stresses and high energy, thereby attenuating the shock wave. The energy absorption provided by the soft structures is analysed, which mainly includes loose block energy absorption, rotational energy absorption, spatial scattering energy absorption, and rock-reflected energy absorption.
- (3) The internal steel pipe used for borehole protection can protect the support structure from being weakened by pressure relief drilling. Under a high stress and large creep, the fracture range of the plastic zone in the roadway without a steel pipe increases to 1033 mm, according to the results of the numerical simulation. The soft structure facilitates wave absorption and energy dissipation and can mostly absorb the shock wave.
- (4) To control the stability of the surrounding rock in deep coal mines with high stresses, strong pressure relief and large creep under the condition of multifactor superposition, and failure mode coupling, the deformation and failure mechanism and failure characteristics of the surrounding rock in such roadways are studied. The combination of anchor active support + hydraulic lifting support + soft structure energy absorption is proposed. A steel pipe is embedded in the support structure to protect the structure from damage; this configuration can retain the integrity of the coal body in the roadway and ensure the support effect.

Data Availability

The data used to support the findings of this study are available from the corresponding author upon request.

Conflicts of Interest

The authors declare that they have no conflicts of interest regarding the publication of this study.

Acknowledgments

The authors would like to acknowledge the National Natural Science Foundation of China (Grant no. 51564044) and State Key Laboratory of Coal Resources and Safe Mining, China University of Mining and Technology (Grants nos. SKLCRSM15X02 and SKLCRSM18KF004).

References

- [1] W. D. Ortlepp and T. R. Stacey, "Rockburst mechanisms in tunnels and shafts," *Tunnelling and Underground Space Technology*, vol. 9, no. 1, pp. 59–65, 1994.
- [2] C. Wu, L. Dou, and M. Zhang, "A fuzzy comprehensive evaluation methodology for rock burst forecasting using microseismic monitoring," *Tunnelling and Underground Space Technology*, vol. 80, pp. 232–245, 2018.
- [3] Y. Jiang, Y. Zhao, and H. Wang, "A review of mechanism and prevention technologies of coal bumps in China," *Journal of Rock Mechanics and Geotechnical Engineering*, vol. 9, pp. 180–194, 2017.
- [4] Q. Qi, L. I. Yizhe, S. Zhao et al., "Seventy years development of coal mine rockburst in China: establishment and consideration of theory and technology system," *Coal Science and Technology (in Chinese)*, vol. 47, no. 9, pp. 1–40, 2019.
- [5] A. N. Romashov and S. S. Tsygankov, "Generalized model of rock bursts," *Journal of Mining Science*, vol. 28, no. 5, pp. 420–423, 1993.
- [6] N. G. W. Cook, "The failure of rock," *International Journal of Rock Mechanics and Mining Sciences & Geomechanics Abstracts*, vol. 2, pp. 389–403, 1965.
- [7] AV. Lovchikov, "Difference in rockburst hazard in ore and coal mines," *Iop Conference*, vol. 134, pp. 12–17, 2018.
- [8] Y. Xu and M. Cai, "Influence of strain energy released from a test machine on rock failure process," *Canadian Geotechnical Journal*, vol. 55, pp. 777–791, 2018.
- [9] A. Kidybiński, "Bursting liability indices of coal," *International Journal of Rock Mechanics and Mining Sciences*, vol. 18, no. 4, pp. 295–304, 1981.
- [10] J.-A. Wang and H. D. Park, "Comprehensive prediction of rockburst based on analysis of strain energy in rocks," *Tunnelling and Underground Space Technology*, vol. 16, no. 1, pp. 49–57, 2001.
- [11] T.-H. Ma, C.-A. Tang, S.-B. Tang et al., "Rockburst mechanism and prediction based on microseismic monitoring," *International Journal of Rock Mechanics and Mining Sciences*, vol. 110, pp. 177–188, 2018.
- [12] Z. H. Chen, C. A. Tang, and R. Q. Huang, "A double rock sample model for rockbursts," *International Journal of Rock*

- Mechanics and Mining Sciences*, vol. 34, no. 6, pp. 991–1000, 1997.
- [13] M. Zhang, “Instability theory and mathematical model for coal rock bursts,” *Chinese Journal of Rock Mechanics and Engineering*, vol. 6, no. 3, pp. 197–204, 1987.
- [14] Q. Qi, Y. Shi, and T. Liu, “Mechanism of instability caused by viscous sliding in rock burst,” *Journal of China Coal Society (in Chinese)*, vol. 21, no. 2, pp. 34–38, 1997.
- [15] L. Dou, C. Lu, Z. Mou et al., “Intensity weakening theory for rockburst and its application,” *Journal of China Coal Society (in Chinese)*, vol. 30, no. 6, pp. 690–694, 2005.
- [16] J. Pan, “Theory of rockburst start-up and its complete technology system,” *Journal of China Coal Society (in Chinese)*, vol. 44, no. 1, pp. 173–182, 2019.
- [17] Y. Pan, “Disturbance response instability theory of rockburst in coal mine,” *Journal of China Coal Society (in Chinese)*, vol. 43, no. 8, pp. 2091–2098, 2018.
- [18] Yi Xue, Z. Cao, and W. Shen, “Destabilization and energy characteristics of coal pillar in roadway driving along gob based on rockburst risk assessment,” *Royal Society Open Science*, vol. 6, pp. 1–20, 2019.
- [19] Y. Jiang and Y. Zhao, “State of the art: investigation on mechanism, forecast and control of coal bumps in China,” *Chinese Journal of Rock Mechanics and Engineering*, vol. 34, no. 11, pp. 2188–2204, 2015.
- [20] Y. Pan, X. Liu, and Z. Li, “The Model of energy-absorbing coupling support and its application in rock burst roadway,” *Journal of Mining and Safety Engineering*, vol. 28, no. 1, pp. 6–10, 2011.
- [21] Q. Qi, Y. Pan, L. Shu et al., “Theory and technical framework of prevention and control with different sources in multi-scales for coal and rock dynamic disasters in deep mining of coal mines,” *Journal of China Coal Society*, vol. 43, no. 7, pp. 1801–1810, 2018.
- [22] A. Pak and D. H. Chan, “Numerical modeling of hydraulic fracturing in oil sands,” *Scientia Iranica*, vol. 15, no. 5, pp. 516–535, 2008.
- [23] Z. Huang, S. Zhang, R. Yang et al., “A review of liquid nitrogen fracturing technology,” *Fuel*, vol. 266, pp. 1–15, 2020.
- [24] F. Bagheri, “Regulation of hydraulic fracturing of shale gas formations in the United States,” *Pepperdine Policy Review*, vol. 6, pp. 1–13, 2013.
- [25] M. Gao, L. Dou, and N. Zhang, “Strong-soft-strong mechanical model for controlling roadway surrounding rock subjected to rock burst and its application,” *Rock and Soil Mechanics*, vol. 29, no. 2, pp. 359–364, 2008.
- [26] Y. He, M. Gao, H. Zhao, and Y. Zhao, “Behaviour of foam concrete under impact loading based on SHPB experiments,” *Shock and Vibration*, vol. 2019, Article ID 2065845, 13 pages, 2019.
- [27] M. Gao, H. Zhao, Y. Zhao, X. Gao, and X. Wang, “Investigation on the vibration effect of shock wave in rock burst by in situ microseismic monitoring,” *Shock and Vibration*, vol. 2018, pp. 1–14, Article ID 8517806, 2018.
- [28] M. Gao, Y. Zhao, and X. Chen, “Destruction mechanism of rock burst in mine roadways and their prevention,” *Disaster Advances*, vol. 6, no. 5, pp. 34–43, 2013.
- [29] Y. Wu, F. Gao, J. Chen, and J. He, “Experimental study on the performance of rock bolts in coal burst-prone mines,” *Rock Mechanics and Rock Engineering*, vol. 52, no. 10, pp. 3959–3970, 2019.
- [30] L. Dai, Y. Pan, and A. Wang, “Study of the energy absorption performance of an axial splitting component for anchor bolts under static loading,” *Tunnelling and Underground Space Technology*, vol. 81, no. 81, pp. 176–186, 2018.
- [31] M.-S. Gao, *Strong-soft-strong Control Principle for Controlling Roadway Surrounding Rock Subjected to Rock burst*, China University of Mining and Technology Press, Xuzhou, China, 2011.
- [32] Z.-L. Li, X.-Q. He, L.-M. Dou, D.-Z. Song, and G.-F. Wang, “Numerical investigation of load shedding and rockburst reduction effects of top-coal caving mining in thick coal seams,” *International Journal of Rock Mechanics and Mining Sciences*, vol. 110, pp. 266–278, 2018.
- [33] N. Mohammad, D. J. Reddish, and L. R. Stace, “The relation between in situ and laboratory rock properties used in numerical modelling,” *International Journal of Rock Mechanics and Mining Sciences*, vol. 34, no. 2, pp. 289–297, 1997.

Research Article

Numerical and Field Investigations on Rockburst Risk Adjacent to Irregular Coal Pillars and Fault

Zhi-long He ¹, Cai-ping Lu ¹, Xiu-feng Zhang,² Chao Wang,² Bao-qi Wang,³ and Tao Zhou³

¹School of Mining Engineering, Key Laboratory of Deep Coal Resource Mining (Ministry of Education), China University of Mining and Technology, Xuzhou, Jiangsu 221116, China

²Centre of Rockburst Prevention Research, Yankuang Group Co., Ltd., Jining 250000, Shandong, China

³Zhaolou Coal Mine, Yankuang Group Co., Ltd., Heze 274000, Shandong, China

Correspondence should be addressed to Cai-ping Lu; cplucumt@126.com

Received 15 May 2020; Revised 23 November 2020; Accepted 24 December 2020; Published 4 February 2021

Academic Editor: Hongwei Yang

Copyright © 2021 Zhi-long He et al. This is an open access article distributed under the Creative Commons Attribution License, which permits unrestricted use, distribution, and reproduction in any medium, provided the original work is properly cited.

Irregular coal pillars are often reserved in the upper coal seam in multiseam mining due to the limitation of geological conditions and mining methods. Diffused and transmitted stress in the pillars will form the stress concentrated areas in the lower coal seam and will increase the risk of rockburst. Based on the upper irregular pillars and fault encountered in the 7301 working face of the Zhaolou coal mine, this paper studies the evolution of stress and energy when the working face passed through the area affected by pillars. The adopted methods include numerical simulations and field monitoring. The change in stress concentration factor and stress gradient because of the mining activities in lower coal seam was analyzed by numerical simulation, indicating that the stress gradient reaches a peak when the working face is closed to the area under the edge and junction of pillars, which has the high risk of inducing rockburst. The sources' location, variation rule of microseismic (MS) total energy and events, frequency spectrum distributions, and source parameters are discussed, respectively, based on the field monitoring data. The main conclusions were obtained as follows: (1) The total energy and event counts reach the peak when working face is close to the area under the edge and the junction of pillars. (2) The dominant frequency transfers from high frequency to low frequency, the stress drop reaches the peak value, the energy index decreases sharply, and the cumulative apparent volume increases sharply, which all are obvious precursory characteristics before rockburst.

1. Introduction

Most coal exists in the state of multiple coal seams. With the increase of the mining intensity, an increasing number of underground coal mines have begun to exploit coal seams with close distance to each other [1–5]. Due to the limitation of the geological conditions and the layout of the mining area, pillars are often left in the upper coal. The coal pillar is affected by the overburden of the goaf, which produces the stress concentration and transfers it downward, causing the stress redistribution of the lower coal seam [6–8]. When the lower layer coal mining enters area affected by pillars, the abutment pressure and the additional stress transferred by

pillars are superposed, which greatly increases the risk of rockburst.

Problems of residual pillars in multiseam mining have been studied by many researchers, and the subject has been well discussed in the literature. Regarding the strength characteristics of pillars, Wattimena et al. [9] utilized logistic regression to calculate the probability that a particular pillar of a given geometry (width-to-height ratio) and a known stress condition (strength-to-stress ratio) will be stable. Khanal et al. [10] investigated the effects that seam separation distances, mining offset, panel layout, and panel orientation each have on surface subsidence and chain pillar stress magnitude taking numerical simulation. Mohan et al. [11] showed the results of numerical modelling of failed and stable cases of pillars from Indian coal

mines using FLAC3D in the strain-softening mode. Kaiser et al. [12] explored the limitations and potential opportunities in pillar design and considered pillar designs based on current empirical rules may be inadvertently conservative. Alber et al. [13] discussed the failure behavior of pillar using the theory of fracture mechanics. Esterhuizen et al. [14] proposed a method of estimating the pillar strength and selecting a safety factor for design based on observations of stable and failed pillars, supplemented by numerical models. These researches lay a foundation for further understanding the strength characteristics of pillars.

With respect to the stress redistribution under coal pillar, Suchowerska et al. [15] attempted to identify the variables that affect stress redistribution in the strata under the supercritical longwall panels in the way of Wilson's equations in conjunction with finite element modelling. Yan et al. [16] calculated the depth of the strata affected by the concentrated stress imparted by established gob coal pillars and the effective range of energy density concentration. Liu et al. [17] analyzed the diffusion angle of the pillar floor by using UDEC and proposed the optimization suggestions for roadway layout. Zhu et al. [18] carried on FLAC3D numerical simulation of vertical stress field and deformation field under different coal pillar width in order to investigate the protected layer pressure relief effect under the influence of different width of coal pillar. Yang et al. [19] calculated the stress of strata under pillars with linear load by the calculation method for uniform load. Yu et al. [20] evaluated the performance of coal pillars under weak roof based on stress and deformation field monitoring.

The studies mentioned above make a great contribution to stress redistribution under coal pillar. But these studies mainly focus on the stress distributions under a single regular coal pillar. When there are irregular and multiple residual pillars, the stress distribution will become more complex due to stress superposition of adjacent pillars. At the same time, most of the above researches are based on the simplified theoretical model and numerical simulation, which may be not applicable to irregular pillars due to the lack of the support of field monitoring data. Microseism, a technology by receiving the elastic wave in the process of fracture and deformation of coal and rock, has a wide range of monitor in space and time and has wide application in rockburst prediction. By comprehensive analysis of the received waveform and a series of source parameters [21–25], the location, time, energy, and even the failure form of rock mass of the microseism can be obtained, thus profoundly revealing the whole process of the rockburst from its initiation to outbreak. The purpose of this paper is to discuss the influence of the residual pillars and fault on the mining of the lower coal seam. Therefore, through numerical simulation and field monitoring, we explore the stress redistribution of the pillars and the lower working face, as well as the characteristics of MS source location, energy, and frequency variation. The conclusions of this research can provide references for the safe mining of working face under the similar geological conditions.

2. Field Conditions

As shown in Figure 1, the average buried depth of 7301 working face in the Zhaolou coal mine is approximately 1000 m, where the fully mechanized top-coal caving mining technique is adopted. The mining width of the working face is 230 m, and the lengths of the headentry and tailentry are 1691 and 1664 m, respectively. The #3 coal seam with relatively simple structure is mainly mined, the thickness is 6.8–9.0 m with the average of 7.8 m, and the dip angle is 1–13° with the average of 3.5°. The immediate roof is composed of sandstone and mudstone with 2.93 m in thickness, the main roof consists of 9.61 m-thick fine sandstones, and the immediate floor is composed of tone and mudstone with 10.85 m-thick mudstone. The headentry is adjacent to the FZ14 thrust reverse fault with 50–70 m throw in the northern direction; meanwhile, the #3 mining area adjoining to the 7301 working face has been mined out. The irregular coal pillars are expected to lead to complex stress distributions in 7301 working face.

From Figure 1, it appears that irregular pillars are close to headentry, the minimum horizontal distance between them is only 60 m, and the vertical distance is 50–70 m. As a result, the vertical stress will increase in the headentry side of the working face due to the imposed extravertical load by pillars. At the same time, the tectonic stress near the FZ14 fault will also affect the working face. The rockburst may be induced by the superposition of the abutment pressure, additional stress transmitted by pillars, and tectonic stress near the fault with the advance of the working face.

3. Numerical Simulation

3.1. Modelling. As it is difficult to monitor the stress variation in the field in real time, numerical simulation is a proper method at the current stage to study stress characteristics at different mining stages. Based on the actual geological conditions of the Zhaolou coal mine, a simplified numerical model is established in FLAC3D software as shown in Figure 2. The length, width, and height of the model are 2000 m, 1000 m, and 260 m, respectively. The model includes a total of 1.06 million elements. The bottom boundary of the model is fixed in the vertical direction, and the four boundaries are fixed in the horizontal direction; the top is free. The buried depth of the bottom of the model is 1000 m, and the gravity gradient is 0.025 MPa/m; the vertical z -axis σ_z of -20.5 MPa is loaded on the top boundary. The lateral pressure coefficient is set to 1.5; therefore, the horizontal x -axis σ_x of -27.75 MPa and the horizontal y -axis σ_y of -27.75 MPa are loaded on the four sides of the boundary. The Mohr–Coulomb model is chosen to determine elements' strength failure. The mechanical parameters are determined according to the geological surveys and the rock tests conducted in the laboratory. The uniaxial compressive strength (UCS), elastic modulus, and Poisson's ratio are obtained based on uniaxial compression test, the tensile strength is obtained from Brazilian splitting test, and the cohesion and internal frictional angles are obtained from the shear test. Figure 3 shows the photos before and after the test, and the obtained mechanical parameters are shown in Table 1.

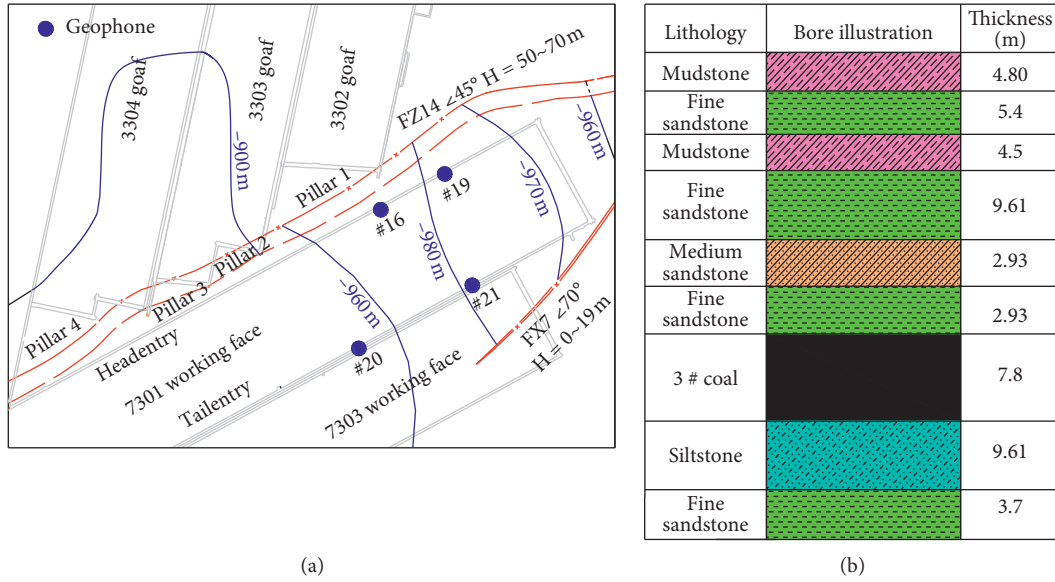


FIGURE 1: The plane layout of the 7301 working face and lithology of coal and rock strata. (a) The plane layout of the 7301 working face. (b) Lithology of coal and rock strata.

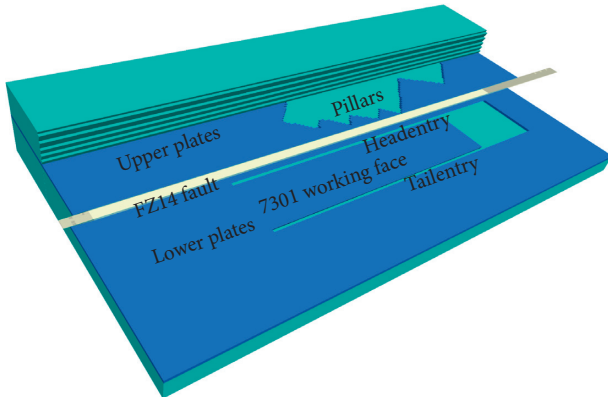


FIGURE 2: 3D numerical model.

3.2. *Fault Setting.* Generally speaking, in FLAC3D, mechanical properties of faults can be represented in two different ways: the interface element without thickness and the solid element with different mechanical properties. Compared with the real geological conditions, if the size of the fault in the numerical model can be ignored, then interface representation is probably more appropriate [26].

Different constitutive models are assigned in solid elements with specific thickness to reflect the characteristics of faults. The ubiquitous-joints model is found to be a representative choice. This model accounts for the presence of an orientation of weakness (weak plane) in a FLAC3D Mohr–Coulomb model. The criterion for failure on the plane, whose orientation is given, consists of a composite Mohr–Coulomb envelope with tension cutoff. The strongly anisotropic mechanical behavior can be reflected due to the

existence of weak plane. The advantage of using the ubiquitous-joints model is able to account for the heterogeneity of faults and the mechanical interaction between the weak plane and the intermediate matrix. At the same time, Frederic Cappa [26] pointed out the same results can be obtained when the fault is simulated by the ubiquitous-joints model as by the interface, and the premise is the same Coulomb strength parameters are used. The FZ14 fault shown in Figure 1 is distributed almost along the whole strike, and its average thickness is about 40 m. The thickness of the fault will affect the relative position of the pillars and the working face in the horizontal direction, and then affect the stress distribution of the lower coal seam. Therefore, the size of fault cannot be ignored for the key problems studied. It is a more suitable choice to use the solid elements with the ubiquitous-joint model.

The mechanical parameters used to simulate faults are presented in Table 1. Considering that the existence of weak matrix and weak planes in the fault will reduce its elastic modulus, the elastic modulus is set to a lower value (one tenth of siltstone) [27]. Relatively lower values of tensile strength and cohesion are used to represent the features of low fault strength. The direction of weak planes is parallel to dip of fault.

The plan of excavation simulation is as follows: (1) when numerical model reaches equilibrium, the #3 mining area is excavated to form irregular pillars. The stress distribution of each pillar and lower coal seam were observed. (2) During mining of the 7301 working face, the evolution of vertical stress of the area under the pillars is investigated.



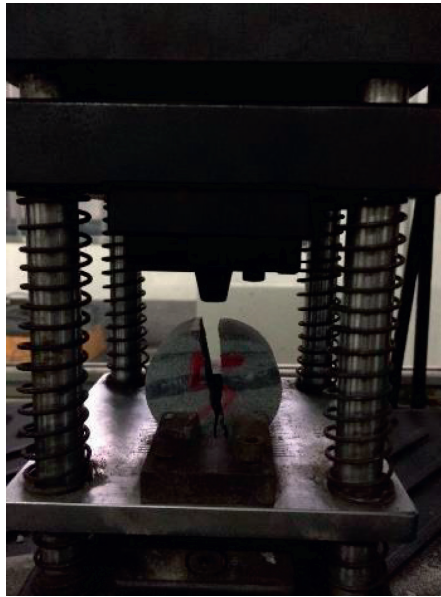
(a)



(b)



(c)



(d)

FIGURE 3: Continued.

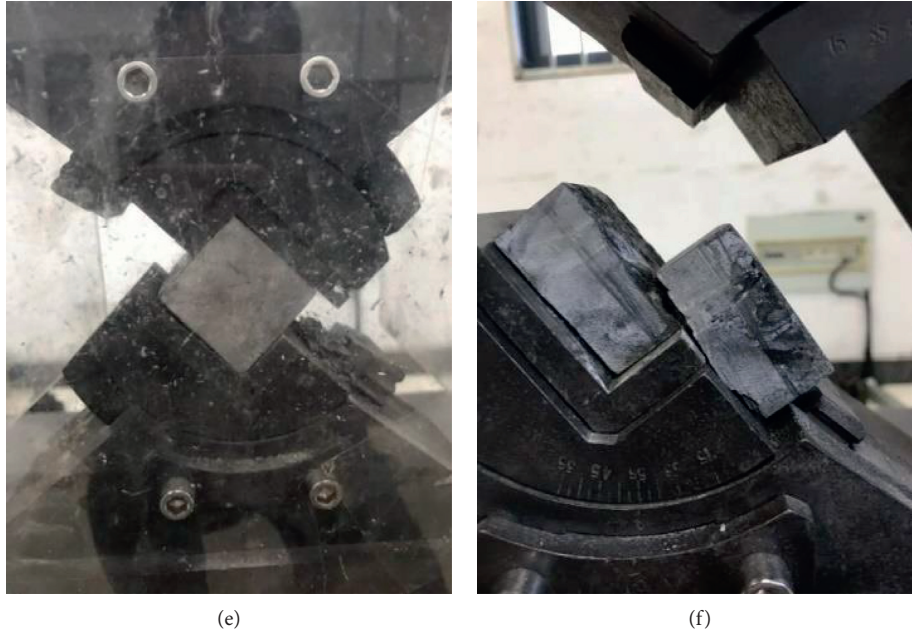


FIGURE 3: Experimental photos in the laboratory. (a) Before uniaxial compression test. (b) After uniaxial compression test. (c) Before Brazilian splitting test. (d) After Brazilian splitting test. (e) Before shear test. (f) After shear test.

TABLE 1: Mechanical parameters of the model.

Mineral	UCS (MPa)	Elastic modulus (GPa)	Poisson's ratio	Cohesion (MPa)	Internal frictional angle (°)	Tensile strength (MPa)	Density (kg/m ³)
Mudstone	32	17.7	0.26	1.2	32	0.58	2500
Fine sandstone	45	25	0.2	2.75	38	1.84	2700
#3 coal	18	5.3	0.32	1.25	28	0.15	1350
Siltstone	68	33.4	0.23	3.2	42	1.29	2500
Medium sandstone	30	10.85	0.18	2.45	38	2.01	2600
Fault	—	3.3	0.25	0.32	25	0.12	2200

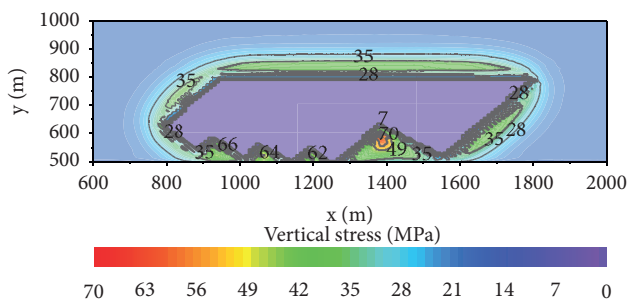


FIGURE 4: The vertical stress distribution of pillars.

3.3. Vertical Stress Distribution of the Pillars and Working Face. The vertical stress distribution in pillars is shown as Figure 4. After the coal is extracted, the abutment pressure will form on one side of the pillar, and then the abutment pressure on both sides will superpose, which causes a high stress concentration area to form in the center of each pillar. Besides, it can be clearly seen in Figure 4 that the maximum value of the stress of the pillars is closely related to its size.

The maximum vertical stress of pillar 1 reaches 70 MPa; however, that of coal pillars 2, 3, and 4 are only about 62, 64, and 66 MPa, respectively. Compared to other three pillars, the width of goafs on both sides of pillar 1 is wider, the caving height of overlying strata is higher after mined, and the hanging area of broken strata is larger, which causes higher concentrated stress to form in pillar 1. In general, the whole area of irregular pillars presents stress concentration in various degrees and redistribution of the lower coal seam stress.

Figure 5 shows the vertical stress distribution in 7301 working face. It is clearly shown that the vertical stress in the headentry side rises sharply, indicating that the stress transfer from pillars is obvious. The vertical stress in area under pillar 1 is the maximum, i.e., the peak value located at the headentry side reaches 36 MPa, and the peak vertical stress in area under coal pillars 2, 3, and 4 is 31–32 MPa, which is located at the middle of the working face. The width and stress concentration of the pillars is responsible for these differences. The concentrated stress in pillar 1 is the highest,

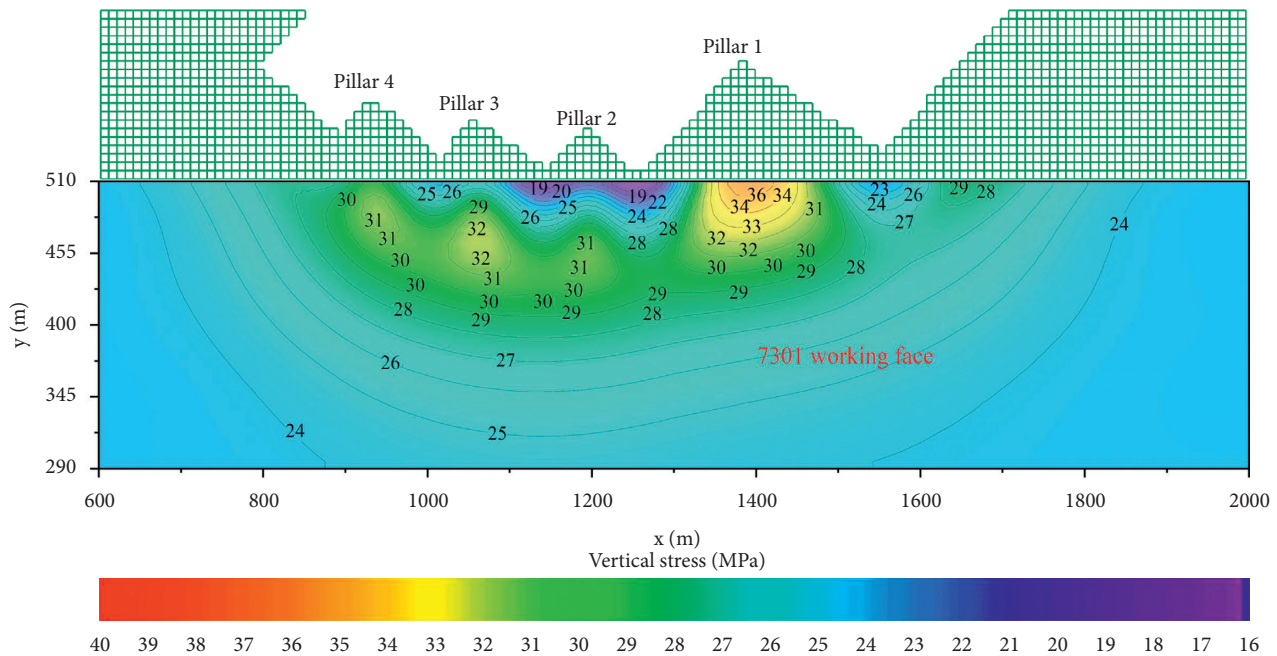


FIGURE 5: The vertical stress distribution of working face with influence of pillars.

as the transferred additional stress in working face is larger accordingly.

The formation of goafs on both sides will lead to the formation of stress concentration area near the sharp corner in the triangular coal pillar due to the superposition of abutment pressure on each side. The distance from the peak of abutment pressure to the coal wall is generally 5–30 m. Therefore, if the width of the pillar is smaller, the distance between the stress concentration area of pillar and the working face is smaller in the horizontal direction, but the corresponding influence on the working face is greater. In order to study the relationship between the width of pillars and the additional stress transferred to the lower coal seam, the profile of the model is made along the middle of each pillar, as shown in Figure 6. The additional stress is equal to the difference between the vertical stress of the lower coal seam after the pillar is formed and in situ stress (23 MPa).

In Figure 6, the lower additional stress (less than 5 MPa) is plotted in red to clearly observe the range of additional stress growth in lower coal seam caused by pillars. Among the pillars, the vertical stress in pillar 1 is the largest, but the width of pillar 1 in the profile is also the largest (182 m), thus the area with the peak stress is further away from the lower coal seam, and the corresponding range of additional stress is the smallest, only 57 m. For coal pillar 2, although the width is the minimum only 50 m, the area with the peak stress is the closest to the lower coal seam. However, the peak stress is the lowest, and the range of the larger additional stress in lower coal seam is smaller compared with that in pillars 3 and 4, but larger than that of pillar 1. To sum up, it can be seen that the peak stress in pillars and the horizontal distance between the pillars and the lower coal seam are the main factors affecting the stress distribution in the working face. When the peak stress in pillars is low or far

from the working face, the affected area of working face is relatively small.

3.4. Stress Variation with Advancing of the Working Face.

The high stress concentration area formed in the center of every pillar contributes to the appearance of multiple stress peaks at the working face along the strike. With the gradually advancing to underneath pillars, the abutment pressure will overlap with the additional stress, which causes the vertical stress in working face to rise sharply, and the increasing risk of rockburst. The stress evolution described above is shown as Figure 7.

Figure 8 shows the evolution of vertical stress in the lower coal seam before and after passing through the affected area. It can be seen from Figure 8 that the location and distribution of the peak vertical stress change obviously. When mining area is not affected by pillars (Figures 8(a) and 8(f)), the additional stress in the front of the working face is small, and the peak value of the vertical stress is mainly the abutment pressure, about 50.98–52.69 MPa. When mining in the pillars affecting area, due to the superposition of additional stress and abutment pressure, the maximum vertical stress value reaches 73.17 MPa (Figure 8(d)).

Figure 9 shows the variation of vertical stress concentration factor and stress gradient (with interval of 20 m) in different mining stages when mining under the pillars. It can be seen that the stress concentration factor increases obviously with the face advancing to area under pillars. Among pillars, the stress concentration factor achieves the maximum when working face is under pillar 3, the second is under pillar 2 and coal pillar 4, and the minimum is under pillar 1. The stress gradient varying curve shows that the

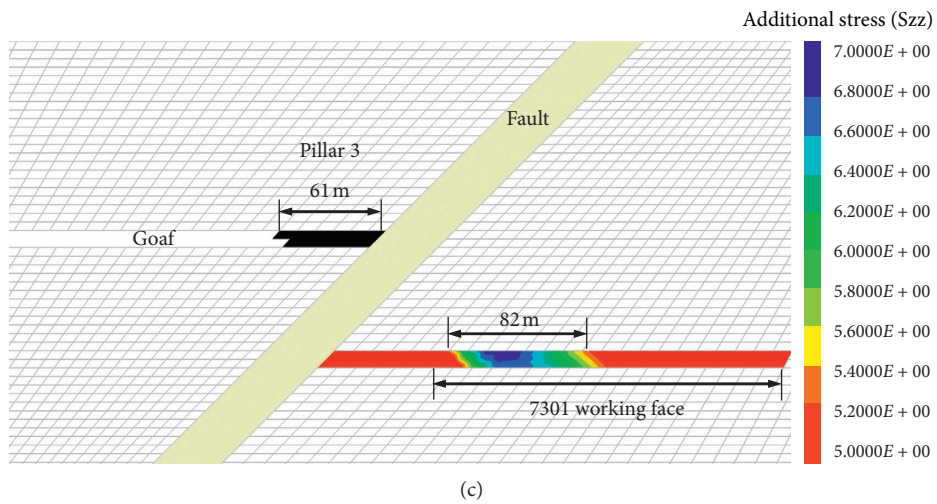
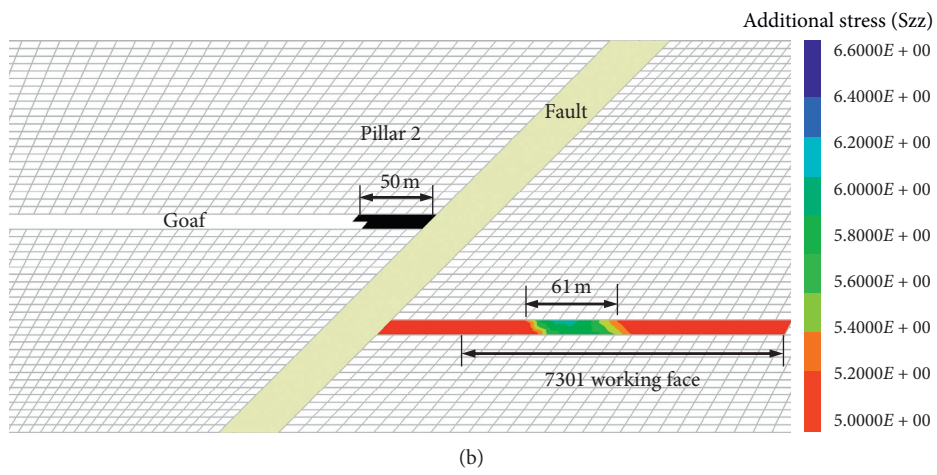
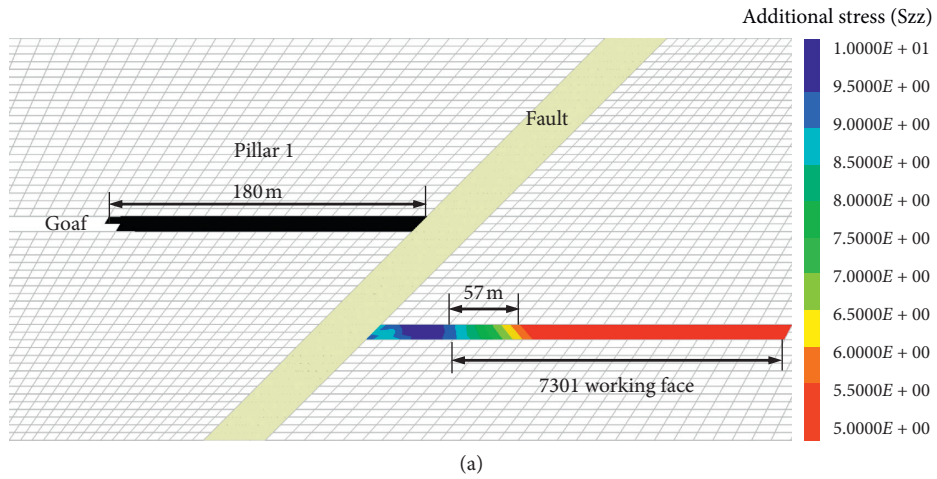


FIGURE 6: Continued.

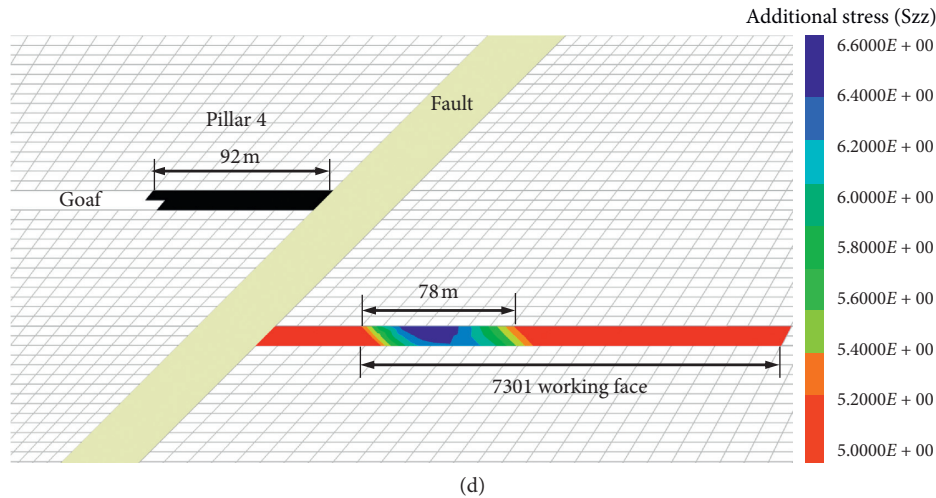


FIGURE 6: The width of pillars in the profile and corresponding distribution range of additional stress. (a) The profile along the middle of pillar 1. (b) The profile along the middle of pillar 2. (c) The profile along the middle of pillar 3. (d) The profile along the middle of pillar 4.

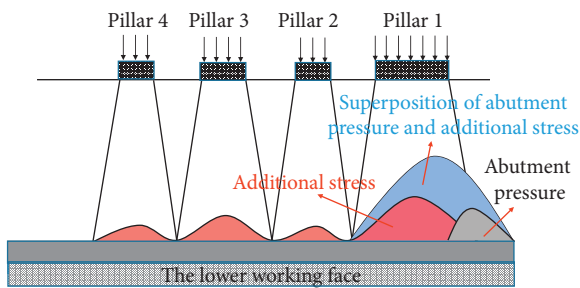


FIGURE 7: The superposition of additional stress and abutment pressure.

gradient stress reaches the peak when the working face is close to the area under the edge of pillar 1, the edge of pillar 4, and 100 m from the junction of pillar 1 and pillar 2, respectively. This indicates that the risk of rockburst is the highest when the working face begins to approach the areas under the edge and junction of pillars due to the sharp stress change.

4. MS Characteristics during Mining under the Pillars

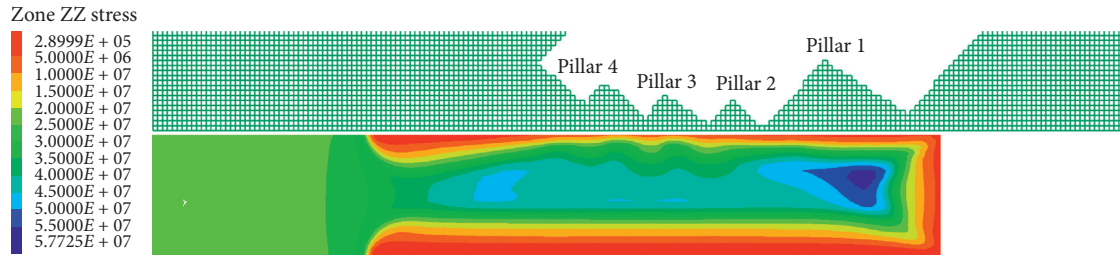
4.1. Source Locations. The SOS MS monitoring system designed and manufactured by the Institute of Mining Seismology, Polish General Institute of Mining Research is installed in the Zhaolou coal mine. The MS monitor can receive the microearthquake with energy larger than 100 J and the frequency between 1 and 600 Hz. A total of 4 geophones were installed in the headentry and tailentry of 7301 working face with 2 geophones in each entry, as shown in Figure 1. Figure 10 shows the plan of the MS sources located in the surroundings of the 7301 working face during mining periods underneath pillars 1 and 2 (from August 2019 to February 2020).

Before the working face entering the area affected by pillars (Figure 10(a)), the MS events in front of the coal wall

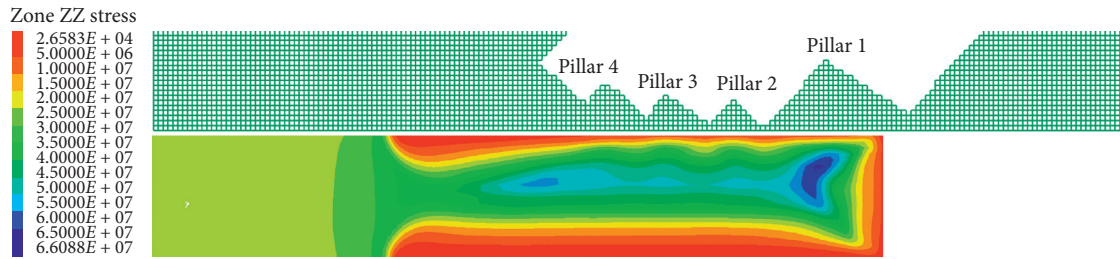
are mainly caused by the abutment pressure. In this period, the energy of most MS events are small (less than 10^3 J), which tends to be evenly distributed along the whole working face without obvious concentration trend. With face continued to advance to the area under the pillar 1 (Figure 10(b)), the number of large energy events (larger than 10^3 J) increases sharply, and the MS events tend to concentrate obviously in the area under pillars 1 and 2, indicating the formation of a high stress concentration area due to the superposition of additional stress and abutment pressure under coal pillars 1 and 2. As the face advancing to the area under the pillar 2 (Figure 10(c)), the number of large energy events continue to increase, the sources are clustered in the area under the pillar 3 and 4, indicating the concentrated stress in front of the working face rises further, the additional stress transmitted by pillars 3 and 4 is higher than pillars 1 and 2.

In addition, the distribution range of large energy MS events is consistent with the stress concentration of lower coal seam. According to the comparison of Figures 10(a)–10(c), the distance between the farthest MS events and coal wall increases from 206 m to 426 m as the face gradually advances to the high stress area. This may be due to the fact that even a slight disturbance is enough to cause the fracture of coal when the coal seam under the pillars has high stress concentration. At the same time, the larger energy sources under pillars 1 and 2 are mainly concentrated on the edge of the working face and close to the headentry side (Figure 10(b)). In comparison, the larger energy sources under pillars 3 and 4 almost distribute in the whole working face-inclined direction (Figure 10(c)). In terms of the scope of the area affected by pillars in lower working face, pillars 3 and 4 are larger than pillars 1 and 2. The simulation results in Figure 6 are consistent with the conclusion.

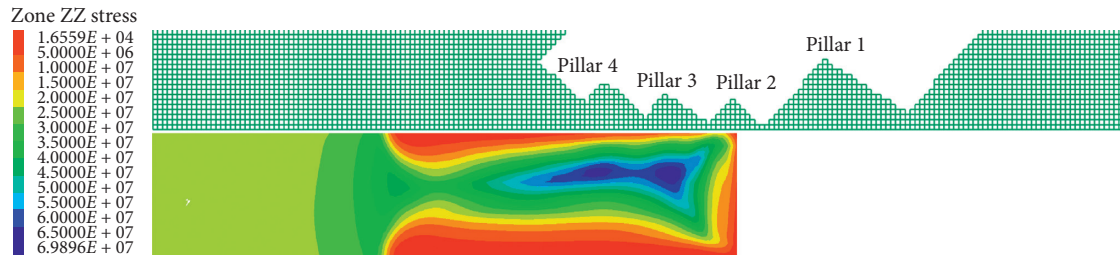
4.2. Variation of Total Energy and Events. Until February 2020, the working face has entered the area under pillar 2. Figure 11 shows the change rule of total energy and event



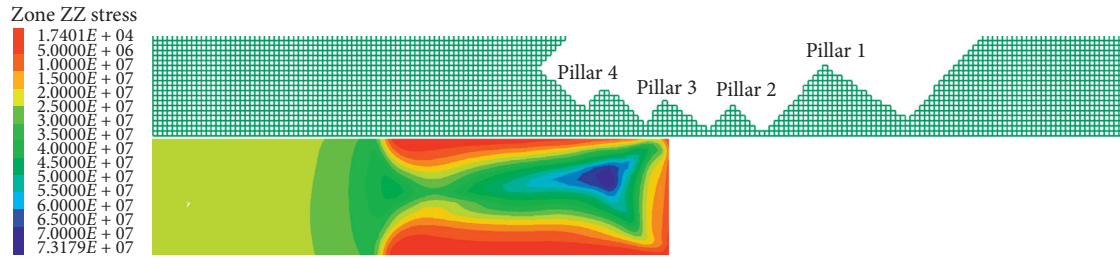
(a)



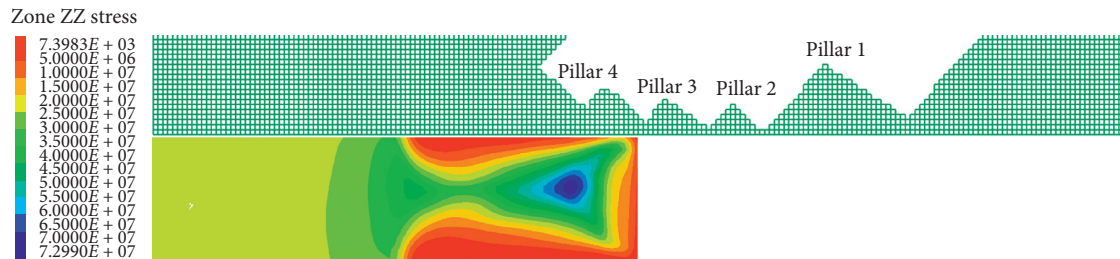
(b)



(c)



(d)



(e)

FIGURE 8: Continued.

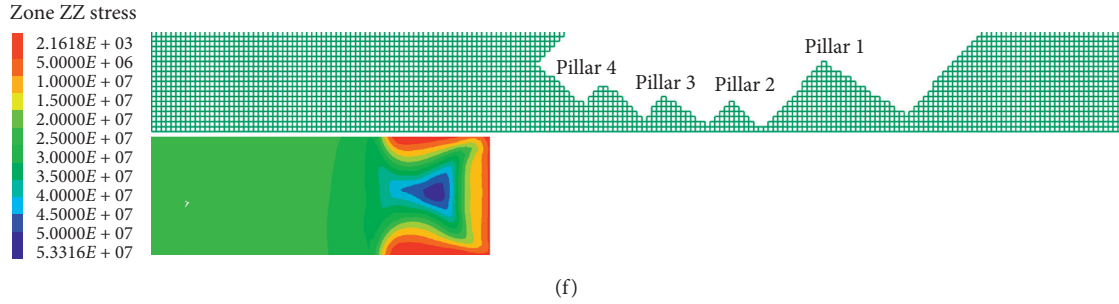


FIGURE 8: Vertical stress distribution in different mining stages. (a) Before entering the area under pillars. (b) Advancing to the area under pillar 1. (c) Advancing to the area under pillar 2. (d) Advancing to the area under pillar 3. (e) Advancing to the area under pillar 4. (f) After passing through the affected area by pillars.

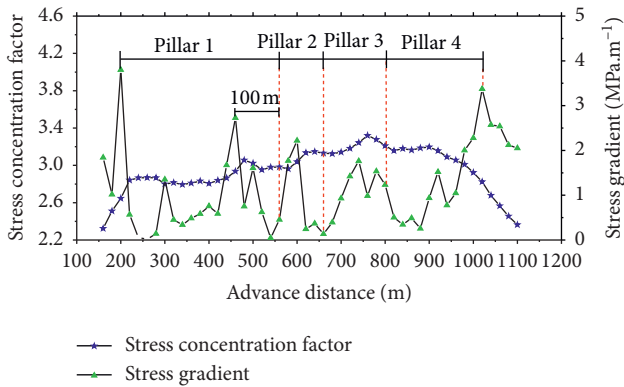


FIGURE 9: Varying curve of vertical stress in different mining stages.

counts of microseisms per day before or after the face passing through underneath pillar 1. The total energy and event counts reach the peak when face is close to the edge and middle of pillar 1, and the junction of pillar 1 and pillar 2, respectively. These three positions all correspond to the corner part of the triangular pillar. This may be attributed to the irregular shape of the pillar corner, leading to the sharp change of the gradient stress in the lower working face, and inducing a large number of coal fractures. The change regulation is consistent with the simulation results presented in Figure 9. It shows that the gradient stress of working face under the edge of pillar will change rapidly, which will increase the risk of rockburst during mining.

4.3. MS Frequency Spectrum Evolution before and after Strong Mining-Induced Tremors. A large number of laboratory tests and field observations [28–32] indicate that a series of microfractures will occur in coal and rock mass before the occurrence of large fractures and the frequency spectrum distribution of MS events will switch from chaotic mixed high frequency to obvious low frequency. At 15:18:50 on December 2, 2019, when face advanced to the middle of pillar 1, a strong mining-induced shock bump with energy of 6.53×10^3 J was received, which was located in the area under the junction of pillar 1 and pillar 2. The value of stress sensor at the corresponding position rose rapidly from 5.6 MPa to 16.4 MPa (variable growth rate of 10.8 MPa), reaching the

red alert, and a strong coal burst occurred in the field. Figure 12 shows the frequency spectrum distributions of the five MS events before and after the strong mining-induced earthquake, as recorded by three geophones close to the source.

It is shown in Figure 12 that before the occurrence of the strong tremor, the frequency spectrum distributions have the characteristics of wide frequency distribution, high central frequency, and low frequency spectrum. It indicates a series of microfractures and a small energy release occurring in coal induced by mining activities. With the continued face advancing, the frequency spectrum increases sharply when the strong mining-induced earthquake occurs at 15:18:50, and the dominant frequencies shift to the low frequency, which indicated that the high stress caused by the superposition of mining stress and additional stress results in the large coal cracks and the release of a large amount of energy. After the strong mining-induced shock bump, the frequency spectrum decreased obviously, the frequency distribution converted from concentration to dispersion, and the dominant frequency changed from low frequency to high frequency. It shows that after the energy release, the stress concentration decreases and only microfracture occurs in the coal. Therefore, the high frequency spectrum, concentrated frequency distribution, and obvious and low dominant frequency can be regarded as the characteristics of strong mining-induced shock bump in high stress concentration area.

4.4. Source Parameters Evolution Mining through the Pillars.

The mining-induced tremor is similar to nature earthquake, which all are the phenomenon that the elastic energy is released in the form of wave due to rock break. Thus, the seismology has been applied to the coal mine MS monitoring to predict rockburst. The static stress drop, cumulative apparent volume, and energy index are commonly used parameters to estimate the occurrence of rockburst. The stress difference between stress before and after the rock break is the static stress drop, which reflects stress level in seismic source region and is defined as follows:

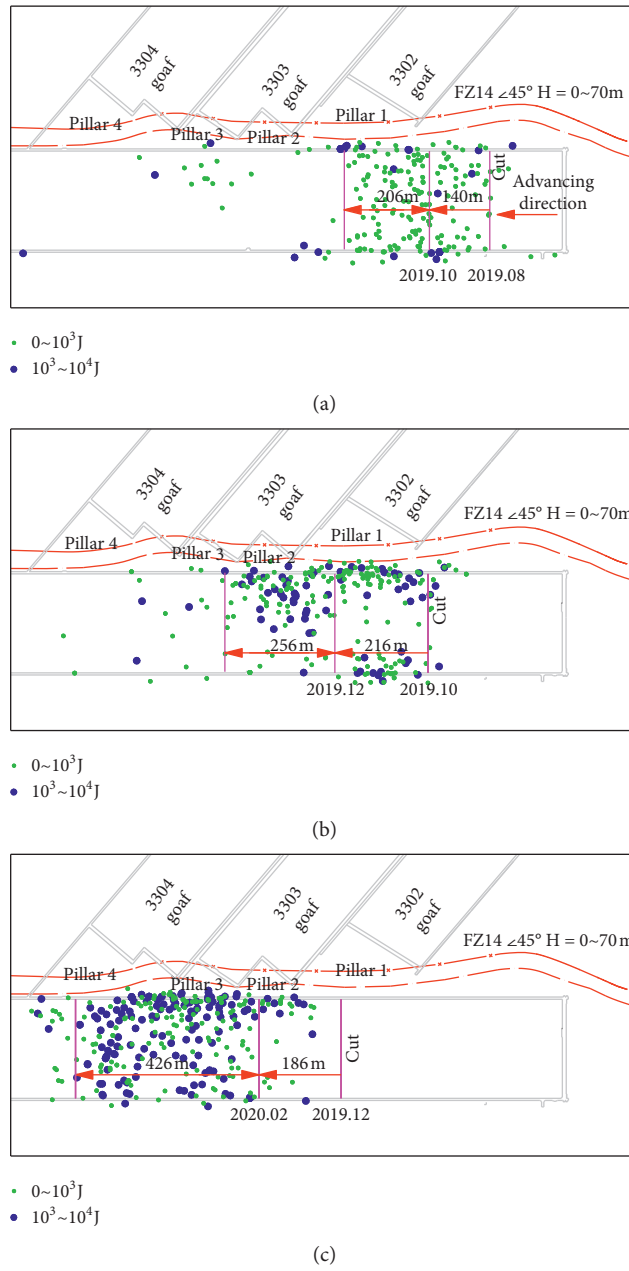


FIGURE 10: The MS sources location from August 2019 to February 2020. (a) Sources location before entering under the pillars from August to October 2019. (b) Sources location when advancing under the pillar 1 from October to December 2019. (c) Sources location when advancing under the pillar 2 from December 2019 to February 2020.

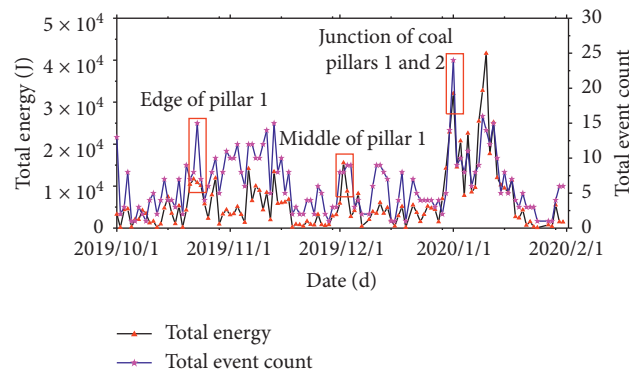
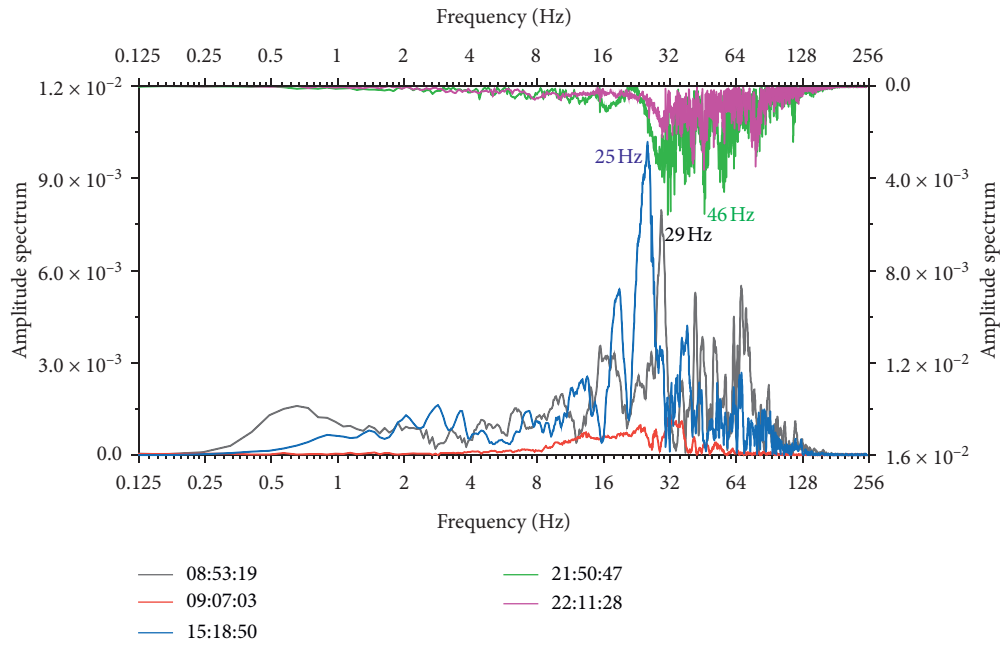
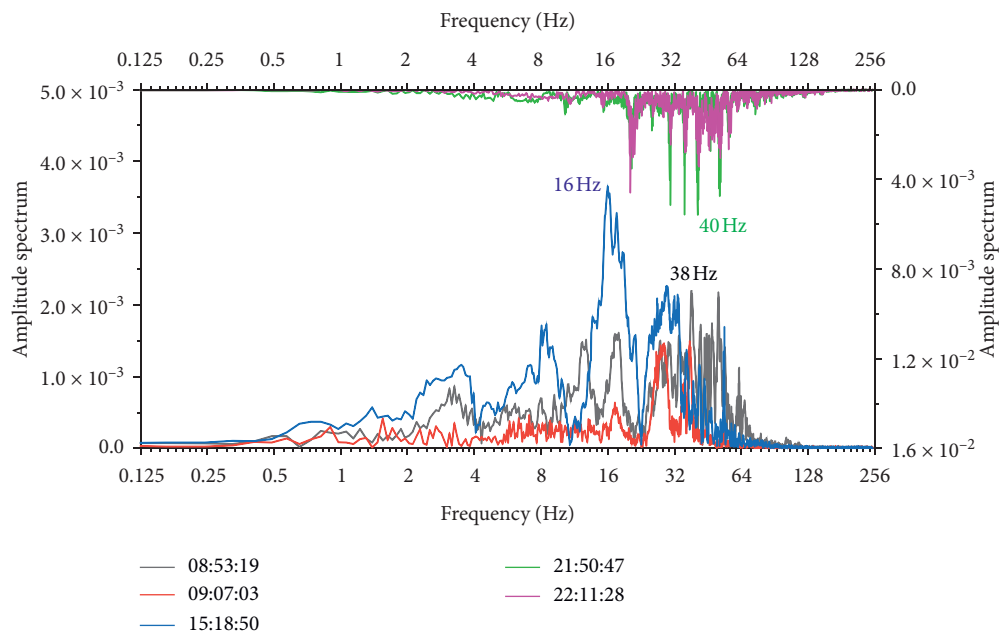


FIGURE 11: Varying curve of total energy and event counts of MS with face under pillars.



(a)



(b)

FIGURE 12: Continued.

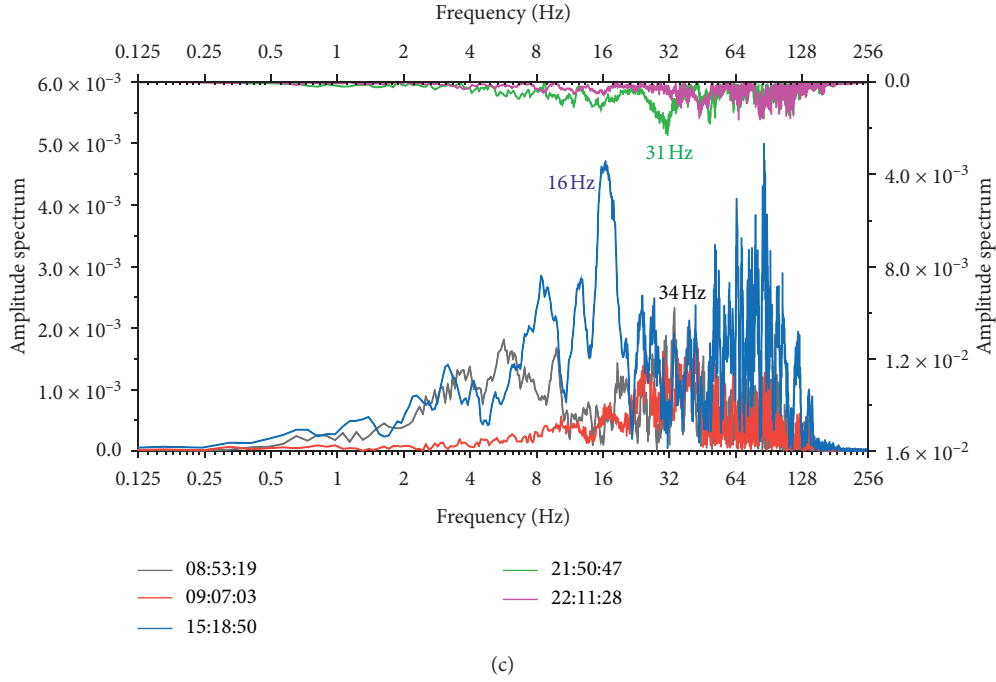


FIGURE 12: Frequency spectrum evolution of the MS events. (a) #16 geophone. (b) #19 geophone. (c) #21 geophone.

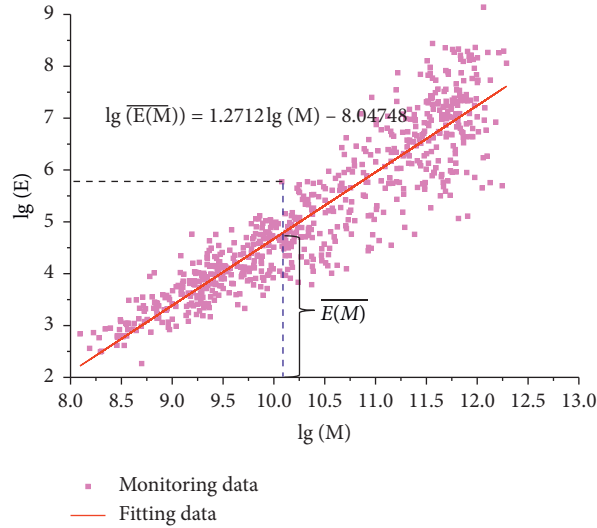


FIGURE 13: Relationship between the energy and seismic moment of the MS events.

$$\Delta\sigma = \frac{7M}{16R^3}, \quad (1)$$

where M_0 is the seismic moment, R is the radius of microseismic source, and $\Delta\sigma$ is the static stress drop.

The apparent volume [33] is the volume of a rock mass that experiences inelastic strain. Cumulative apparent volume is the sum of apparent volume in time. The sharp

increase of cumulative apparent volume indicates rock failure, which is defined as follows:

$$v_A = \frac{M^2}{2\mu E}, \quad (2)$$

where μ is the rigidity of the rock, E is the radiated seismic energy of an even, and v_A is the apparent volume.

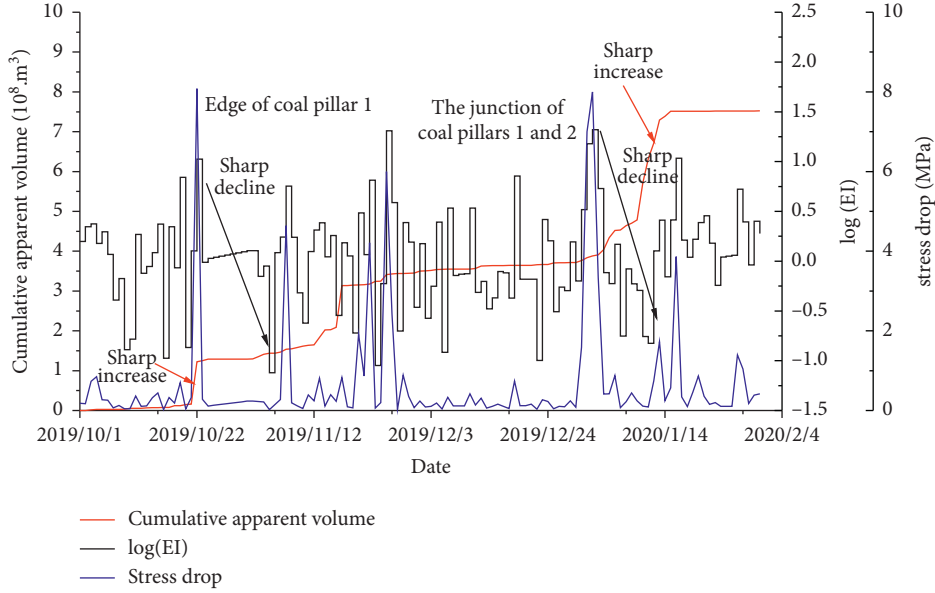


FIGURE 14: Stress drop, cumulative apparent volume, and energy index curves.

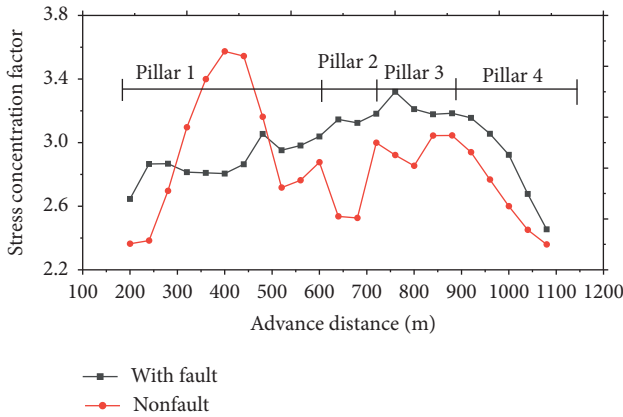


FIGURE 15: The stress concentration factor curves with setting or not setting fault.

The energy index of an event [34] is the ratio of the radiated seismic energy of that event to the average radiated seismic energy of events with the same seismic moment, which is defined as follows:

$$EI = \frac{E}{\overline{E(M)}} \quad (3)$$

where $\overline{E(M)}$ is the average radiated seismic energy for a given seismic moment and EI is the energy index. Average source radiation energy $\overline{E(M)}$ can be obtained from the relationship between $\lg E$ and $\lg E(M)$ for areas monitored. The relationship between them is shown as follows:

$$\lg E = c + d \lg \overline{E(M)}, \quad (4)$$

where c and d are the constants that can be obtained to make a linear fit between $\lg E$ and $\lg E(M)$, as shown in Figure 13. The energy index and cumulative apparent volume can be used to describe evolution of stress within rock. Based on the

stress-strain curve of rock failure, when the energy index increases gradually and the cumulative apparent volume increases slowly, the rock can be regarded as stable and in the state of energy accumulation; when the energy index decreases sharply and the cumulative apparent volume increases quickly, the rock is broken and in the state of strain softening.

A total of 695 effective MS events were received before and after the working face pushed through the area under pillar 1 (October 2019 to February 2020). First, filtering is applied to the waveform of these events to remove noise signals, then the seismic moment (M) and radiated seismic energy (E) of each event can be calculated based on the waveform characteristics. Finally, the change of the static stress drop, cumulative apparent volume, and energy index with time are obtained according to the formulas (1), (2), (3), and (4) which is shown in Figure 14.

It can be seen from Figure 14, before working face advances to the area under edge of coal pillar 1, the stress drop and energy index fluctuate at a small range, cumulative apparent volume increases slowly, which means that rock mass in the monitoring area is in the state of energy accumulation. On October 22, 2019, the stress drop of events reaches a peak; correspondingly, the MS sources mainly concentrate at area under the edge and middle of pillar 1; the stress drop reflects the stress level in seismic source region, and the high stress drop indicates the static high stress concentration. Meanwhile, the energy index declines sharply and cumulative apparent volume increases quickly, and it is the typical potential damage of rock mass and strain-softening stage. It indicates the surrounding rock has been broken with strength decrease and the deformation increase. Similarly, the same change is followed by stress drop, energy index, and cumulative apparent volume when the working face advances to the area under junction of coal pillars 1 and 2. From January 1 to January

10, 2020, the working face is gradually pushed through the area under the junction of pillar 1 and pillar 2. During this period, the stress drop reaches a peak value, the energy index decreases significantly, and the cumulative apparent volume increases rapidly, indicating that the rock mass failure in the monitoring area is gradually increasing. As a consequence of the above points, when the working face is close to the area under edge and junction of pillars, the stress drop will reach the peak value, the energy index decreases sharply, and the cumulative apparent volume increases sharply, and the risk of rockburst will increase. This is consistent with the results of numerical simulation in Figure 9.

5. Discussion

Fault is the initial fracture of stratum and formed in the process of tectonic movement. The discontinuity of the fault blocks the stress transfer in the stratum (the nonuniform stress distributions in the stratum) and causes the tectonic stress concentration near the fault. The superposition of the tectonic stress near the FZ14 fault, the additional stress transferred by pillars, and the abutment pressure will greatly improve the risk of rockburst in the 7310 working face. Figure 15 shows the stress concentration factor curves of the two cases setting or not setting faults in the numerical model, respectively. It can be seen from Figure 15, excepting when face is under coal pillar 1, the stress concentration factor with fault is generally higher than that without fault, indicating the tectonic stress near the fault has significant impact on the mining. However, the reasons that the stress concentration factor behaves differently when face is under pillar 1 may be as follows: compared with setting fault, without fault, the peak stress in pillar 1 is closer to the working face, and the peak stress in pillar 1 is the highest; thus the additional stress will increase greatly, and the influence of that on the working face is greater than the tectonic stress when fault is set. It also shows that it is necessary to consider the thickness of fault in this numerical simulation.

6. Conclusions

- (1) Among pillars, the width of the goaf on both sides of pillar 1 is wider, which leads to the higher caving of the stratum and the larger area of the suspended roof. Therefore, the concentration stress in pillar 1 is higher, and additional stress transferred by pillar 1 is larger at the working face. But there is more distance between the areas with the peak stress and working face; thus the area affected by pillar 1 is smaller. Contrary to pillar 1, the stress peaks of pillars 2, 3, and 4 are closer to the working face, so the area affected by pillars 2, 3, and 4 in the working face is larger.
- (2) The numerical simulation results show that the gradient stress reaches the peak value when face is close to the area under the edge of coal pillar 1, the

edge of coal pillar 4, and junction of pillars 1 and 2. At the same time, the field MS monitoring data also show that the total energy and event counts reach the peak when face is close to the area under the edge of pillar 1, the middle of pillar 1, and the junction of pillar 1 and coal pillar 2, respectively. It can be concluded that the area under the edge and the junction of pillars are stress concentration areas, which leads to the sharp change of the gradient stress in lower working face and very likely induce rockburst.

- (3) The increase of the concentrated stress in the coal seam under the pillars will lead to strong coal fracture and induce high energy MS events; meanwhile, the corresponding frequency spectrum distributions converts from dispersed to concentrate, and the dominant frequency gradually becomes obvious and transfers from high frequency to low frequency. These are the characteristics of the occurrence of strong mining-induced shock bump
- (4) Source parameters monitoring based on seismology can be used to predict rockburst. The evolution of static stress drop, cumulative apparent volume, and energy index before and after the working face pushed through the area under pillar 1 are analyzed. Results indicate that when the working face is close to the area under edge and junction of pillars, the stress drop reaches the peak value, the energy index decreases sharply, the cumulative apparent volume increases sharply, and the risk of rockburst increases.
- (5) The FZ14 fault also affects the safety of working face. The superposition of the tectonic stress near the FZ14 fault, the additional stress transferred by pillars, and the abutment pressure formed in the mining process greatly improve the risk of rockburst at the working face.

Data Availability

The data in this manuscript are available from the authors.

Conflicts of Interest

The authors declare that there are no conflicts of interest regarding the publication of this paper.

Acknowledgments

The authors gratefully wish to acknowledge the collaborative funding support from the National Natural Science Foundation of China (51574225), the Fundamental Research Funds for the Central Universities (YC150001), and a project funded by the Priority Academic Program Development of Jiangsu Higher Education Institutions (PAPD).

References

- [1] R. Howarth and N. R. Monger, "Multi-seam working," *Australian Coal Mining Practice-Monograph 12 - 3rd ed. AusIMM*, pp. 376-391, 2009.
- [2] Q. X. Huang, Y. P. He, and J. Cao, "Experimental investigation on crack development characteristics in shallow coal seam mining in China," *Energies*, vol. 12, no. 7, pp. 1-16, 2019.
- [3] H. Guo, L. Yuan, B. Shen, Q. Qu, and J. Xue, "Mining-induced strata stress changes, fractures and gas flow dynamics in multi-seam longwall mining," *International Journal of Rock Mechanics and Mining Sciences*, vol. 54, pp. 129-139, 2012.
- [4] A. M. S. Iwanec, J. P. Carter, and J. P. Hambleton, "Geomechanics of subsidence above single and multi-seam coal mining," *Journal of Rock Mechanics and Geotechnical Engineering*, vol. 8, no. 3, pp. 304-313, 2016.
- [5] B. Ghabraie, G. Ren, and J. V. Smith, "Characterising the multi-seam subsidence due to varying mining configuration, insights from physical modelling," *International Journal of Rock Mechanics and Mining Sciences*, vol. 93, pp. 269-279, 2017.
- [6] J. W. Cassie, P. B. Cartwright, R. Altounyan et al., "Coal pillar behaviour from underground stress measurements," in *Proceedings of the 9th International Congress on Rock Mechanics*, pp. 1347-1354, Paris, France, August 1999.
- [7] H. Wagner, "Pillar design in coal mines," *Journal of the South African Institute of Mining & Metallurgy*, vol. 80, no. 1, pp. 37-45, 1980.
- [8] S. Jayanthu, T. N. Singh, and D. P. Singh, "Stress distribution during extraction of pillars in a thick coal seam," *Rock Mechanics and Rock Engineering*, vol. 37, pp. 171-192, 2004.
- [9] R. K. Wattimena, S. Kramadibrata, I. D. Sidi, and M. A. Azizi, "Developing coal pillar stability chart using logistic regression," *International Journal of Rock Mechanics and Mining Sciences*, vol. 58, pp. 55-60, 2013.
- [10] M. Khanal, D. Adhikary, C. Jayasundara, and R. Balusu, "Numerical study of mine site specific multiseam mining and its impact on surface subsidence and chain pillar stress," *Geotechnical and Geological Engineering*, vol. 34, no. 1, pp. 217-235, 2015.
- [11] G. Murali Mohan, P. R. Sheorey, and A. Kushwaha, "Numerical estimation of pillar strength in coal mines," *International Journal of Rock Mechanics and Mining Sciences*, vol. 38, no. 8, pp. 1185-1192, 2001.
- [12] P. K. Kaiser, B. Kim, R. P. Bewick, and B. Valley, "Rock mass strength at depth and implications for pillar design," *Mining Technology*, vol. 120, no. 3, pp. 170-179, 2011.
- [13] M. Alber and J. Heiland, "Investigation of a limestone pillar failure Part 2: stress history and application of fracture mechanics approach," *Rock Mechanics and Rock Engineering*, vol. 34, pp. 187-199, 2001.
- [14] G. S. Esterhuizen, D. R. Dolinar, and J. L. Ellenberger, "Pillar strength in underground stone mines in the United States," *International Journal of Rock Mechanics and Mining Sciences*, vol. 48, pp. 42-50, 2001.
- [15] A. M. Suchowerska, R. S. Merifield, and J. P. Carter, "Vertical stress changes in multi-seam mining under supercritical longwall panels," *International Journal of Rock Mechanics and Mining Sciences*, vol. 61, pp. 306-320, 2013.
- [16] J. X. Yang, C. Y. Liu, B. Yu, and F. F. Wu, "The effect of a multi-gob, pier-type roof structure on coal pillar load-bearing capacity and stress distribution," *Bulletin of Engineering Geology and The Environment*, vol. 74, no. 4, pp. 1267-1273, 2014.
- [17] X. Liu, X. M. Li, and W. D. Pan, "Analysis on the floor stress distribution and roadway position in the close distance coal seams," *Arabian Journal of Geosciences*, vol. 9, no. 83, pp. 1-8, 2016.
- [18] H. Z. Zhu, L. Ping, and Z. Y. Tong, "Numerical simulation research and application on protected layer pressure relief affection under different coal pillar width," *Procedia Engineering*, vol. 84, pp. 818-825, 2014.
- [19] J.-X. Yang, C.-V. Liu, B. Yu, and F.-F. Wu, "Calculation and analysis of stress in strata under gob pillars," *Journal of Central South University*, vol. 22, no. 3, pp. 1026-1036, 2015.
- [20] B. Yu, Z. Zhang, T. Kuang, and J. Liu, "Stress changes and deformation monitoring of longwall coal pillars located in weak ground," *Rock Mechanics and Rock Engineering*, vol. 49, no. 8, pp. 3293-3305, 2016.
- [21] R. X. Xue, Z. Z. Liang, N. W. Xu, and L. L. Dong, "Rockburst prediction and stability analysis of the access tunnel in the main powerhouse of a hydropower station based on microseismic monitoring," *International Journal of Rock Mechanics and Mining Sciences*, vol. 126, pp. 1-13, 2020.
- [22] Y. Zhao, T. Yang, P. Zhang, J. Zhou, Q. Yu, and W. Deng, "The analysis of rock damage process based on the microseismic monitoring and numerical simulations," *Tunnelling and Underground Space Technology*, vol. 69, pp. 1-17, 2017.
- [23] G. K. Ghosh and C. Sivakumar, "Application of underground microseismic monitoring for ground failure and secure longwall coal mining operation: a case study in an Indian mine," *Journal of Applied Geophysics*, vol. 150, pp. 21-39, 2018.
- [24] G. Cheng, T. Ma, C. Tang, H. Liu, and S. Wang, "A zoning model for coal mining - induced strata movement based on microseismic monitoring," *International Journal of Rock Mechanics and Mining Sciences*, vol. 94, pp. 123-138, 2017.
- [25] T.-H. Ma, C.-A. Tang, S.-B. Tang et al., "Rockburst mechanism and prediction based on microseismic monitoring," *International Journal of Rock Mechanics and Mining Sciences*, vol. 110, pp. 177-188, 2018.
- [26] P. M. Benson, S. Vinciguerra, P. G. Meredith, and R. P. Young, "Spatio-temporal evolution of volcano seismicity: a laboratory study," *Earth and Planetary Science Letters*, vol. 291, no. 1-2, pp. 315-323, 2010.
- [27] A. I. Sainoki and H. S. Mitri, "Simulating intense shock pulses due to asperities during fault-slip," *Journal of Applied Geophysics*, vol. 103, pp. 71-81, 2018.
- [28] H. Spetzler, C. Sondergeld, G. Sobolev, and B. Salov, "Seismic and strain studies on large laboratory rock samples being stressed to failure," *Tectonophysics*, vol. 144, no. 1-3, pp. 55-68, 1987.
- [29] Y. Liu, C.-P. Lu, B. Liu, H. Zhang, and H.-Y. Wang, "Experimental and field investigations on seismic response of joints and beddings in rocks," *Ultrasonics*, vol. 97, pp. 46-56, 2019.
- [30] C.-P. Lu, B. Liu, B. Liu, Y. Liu, H.-Y. Whang, and H. Zhang, "Anatomy of mining-induced fault slip and a triggered rockburst," *Bulletin of Engineering Geology and the Environment*, vol. 78, no. 7, pp. 5147-5160, 2019.
- [31] H. Wang, A. Dyskin, E. Pasternak, P. Dight, and M. Sarmadivaleh, "Effect of the intermediate principal stress on 3-D crack growth," *Engineering Fracture Mechanics*, vol. 204, pp. 404-420, 2018.
- [32] F. Cappa and J. Rutqvist, "Modeling of coupled deformation and permeability evolution during fault reactivation induced by deep underground injection of CO₂," *International Journal of Greenhouse Gas Control*, vol. 5, no. 2, pp. 336-346, 2010.

- [33] A. J. Mendecki, R. P. Young, Real time quantitative seismicity in mines," in *Proceedings of Sixth International Symposium on Rockburst and Seismicity in Mines*, pp. 287–296, A. A. Balkema, Rotterdam, Netherland, August 1993.
- [34] V. A. Aswegen and A. G. Butler, R. P. Young, Application of quantitative seismology in South African gold mines," in *Proceedings of the 3rd International Symposium on Rockbursts and Seismicity in Mines*, pp. 261–266, A. A. Balkema, Rotterdam, Netherland, August 1993.

Research Article

Precursory Indicator for Mode I Fracture in Brittle Rock through Critical Slowing Down Analysis

Zhenghu Zhang ^{1,2}, Tao Chen ³, Ke Ma ¹, Tiexin Liu ⁴, and Jianhui Deng ²

¹School of Civil Engineering, Dalian University of Technology, Dalian 116024, China

²State Key Laboratory of Hydraulics and Mountain River Engineering, Sichuan University, Chengdu 610065, China

³Bureau of Housing and Urban-Rural Development of Dongxihu District, Wuhan 430030, China

⁴Department of Civil Engineering, Dalian Maritime University, Dalian 116026, China

Correspondence should be addressed to Ke Ma; mark1983@dlut.edu.cn

Received 16 April 2020; Revised 28 October 2020; Accepted 19 November 2020; Published 1 December 2020

Academic Editor: Hongwei Yang

Copyright © 2020 Zhenghu Zhang et al. This is an open access article distributed under the Creative Commons Attribution License, which permits unrestricted use, distribution, and reproduction in any medium, provided the original work is properly cited.

The abrupt rock-related hazards, such as landslide, rock burst, and collapse, seriously threaten the safety and service life of engineering works. Precursory information on critical transitions preceding sudden fracture is of great significance in rock mechanics and engineering. This study investigates the critical slowing down feature of acoustic emission (AE) signals and precursory indicators during the mode I fracture process of brittle rock. Cracked chevron notched Brazilian disc (CCNBD) specimens were utilized, accompanied by acoustic emission monitoring. The principle of critical slowing down was introduced to study AE count sequences, and the variance and autocorrelation coefficient versus loading time curves were analyzed. The results show critical slowing down phenomenon exists during mode I rock fracture. The variance and autocorrelation coefficient of AE counts grow significantly prior to rock fracture, and thus, the significant growth of variance and autocorrelation coefficient of AE signals can act as the precursory indicator of rock fracture. Compared to the autocorrelation coefficient, the precursors determined by the variance are more remarkable. The time interval between the precursory indicator using the critical slowing down theory and fracture moment ranges from 2% to 15% of the entire loading time. The findings in this study could facilitate better understandings on the rock fracture process and early-warning technique for rock fracture-related geological disasters.

1. Introduction

The stability of rock structures is important in extensive engineering fields, such as coal mining, tunnel excavation, water resources, and hydropower engineering. By contrast, rock failure and instability during the engineering construction and performance periods may cause a series of geological disasters, including landslide, rock burst, collapse, and large deformation of the tunnel, which seriously threatens the safety and service life of engineering works. Therefore, it is of great significance to study the precursory information and early-warning technology of rock fracture.

A rock inevitably contains preexisting defects, e.g., microcracks, cavities, and pores. When the rock is subjected to external forces, the stress concentrations are generated

around preexisting defects and the rapid release process of localized strain energy is accompanied by acoustic emission (AE) phenomena [1–3]. Since German scientist Kaiser [4] verified the acoustic emission phenomenon of common engineering materials, the AE technique has been widely used in rock mechanics and engineering [5–7]. Many scholars investigated the characteristics and precursory information of AE signals during the rock deformation and damage process, e.g., the remarkable increase in the number and release rate of AE counts or events [8, 9], the change of seismic *b*-value [10–12], the variation of spatial correlation length [13, 14], frequency spectrum characteristics [15, 16], and fractal characteristics [17–21].

The critical slowing down phenomenon exists in a complicated dynamical system as the system shifts suddenly

from one stable state to another contrasting one, which has attracted widespread attention in many fields [22–25]. Dakos et al. [22] and Wu et al. [26] assumed that slowing down could be viewed as a precursor for upcoming catastrophic climate change. The literature [27–29] investigated the critical slowing down phenomenon preceding a bifurcation from a stable equilibrium to a chaotic state in the ecosystem. Yan et al. [30] stated that the critical slowing down characteristics are a possible early sign for upcoming earthquakes. Ren and Watts [31] showed statistical measures occur in the energy supply infrastructure upon reaching abrupt large-scale disruptions in the electrical system. Obviously, the critical slowing down theory provides a new sight to identify whether a dynamical system is undergoing a critical transition.

Although the critical transition feature has been widely studied in extensive fields [23, 25], spanning from the ecosystem to the climate and seismic systems, the critical slowing down characteristics of AE signals preceding rock failure are in their infancy. Kong et al. [32] and Wei et al. [33] analyzed the early signs of AE counts in coal and sandstone during uniaxial compression tests. Zhang et al. [34] investigated the critical slowing down characteristics of electric potential (EP) generated during the sandstone failure process subjected to compression. However, the critical slowing down feature of AE signals during the rock damage process under other types of loading, especially mode I fracture, is still absent.

The purpose of this paper is to study the critical slowing down feature of acoustic emission (AE) signals and reveal the early-warning information during the mode I fracture process of brittle rock. The mode I fracture tests were carried out using cracked chevron notched Brazilian disc (CCNBD) specimens, which is a suggested method for determining mode I fracture toughness [35]. Real-time acoustic emission monitoring was conducted during the loading process. Variances and autocorrelation coefficients of AE count sequences with loading time were investigated through the critical slowing down theory. The average time intervals between the precursory indicator and rock fracture point for brittle rock were statistically analyzed. Finally, the critical transition characteristics of rock fracture were revealed.

2. Critical Slowing Down Theory

The critical transition can be characterized and predicted by the changes of some statistical parameters when a complex dynamical system undergoes sudden transition from a stable state to another contrasting one. As a concept in statistical physics, critical slowing down describes the fluctuation phenomenon when the system approaches the critical point. Specifically, critical slowing down refers to the phenomenon that the fluctuation duration is lengthened, the recovery rate decreases, and the ability to return to the previous state declines [23, 27]. Critical slowing down phenomenon can be statistically characterized by the variance and autocorrelation coefficient.

The variance (δ) is the deviation of sample data to its mathematical expectation, expressed as follows:

$$\delta = S^2 = \frac{1}{N} \sum_{i=0}^N (x_i - E(x_i))^2, \quad (1)$$

where S and $E(x_i)$ represent the standard deviation and mathematical expectation, respectively, and x_i and N are the i^{th} data and the number of data, respectively.

Autocorrelation coefficient statistically describes the correlation between different periods of the same variable. The autocorrelation coefficient ($\beta(k)$) of the variable x_i with lag length k can be denoted as follows:

$$\beta(k) = \sum_{i=1}^{N-k} \left(\frac{x_i - E(x_i)}{S} \right) \left(\frac{x_{i+k} - E(x_i)}{S} \right). \quad (2)$$

It is assumed that the state variable has a repeated disturbance after each period (Δt). The return to equilibrium is approximately exponential during the perturbation process with a certain recovery rate (α). This can be described in an autoregressive (AR) model as follows [23]:

$$u_{n+1} = e^{\alpha \Delta t} u_n + S \omega_n, \quad (3)$$

$$u_n = x_n - E(x_n), \quad (4)$$

where u_n denotes the deviation of the state variable from equilibrium and ω_n is a random quantity from a normal distribution.

If the recovery speed (α) and period (Δt) are independent of the deviation (u_n), this model can be simplified into an AR (1) model:

$$u_{n+1} = \beta u_n + S \omega_n. \quad (5)$$

The autocorrelation coefficient $\beta = e^{\alpha \Delta t}$ is approximately one for red noise and zero for white noise. The variance of the AR (1) model (equation (5)) is found to be

$$\text{Var}(u_{n+1}) = E(u_n^2) + (E(u_n))^2 = \frac{\delta}{1 - \beta^2}. \quad (6)$$

The recovery rate of small amplitude disturbances is increasingly lower when the system approaches the critical point [22, 23]. The variance will approximate infinity and the autocorrelation coefficient will approach 1 as the recovery rate approaches 0. Therefore, the significant increase of variance and autocorrelation coefficient of one system parameter can be regarded as the precursor close to the critical point [30–34]. Here refers to the AE count of marble samples during the mode I fracture process.

3. Experimental Setup

The cracked chevron notched Brazilian disc (CCNBD) specimens are suggested for determining mode I fracture toughness by the International Society for Rock Mechanics (ISRM) [35]. The CCNBD marble specimens were prepared according to the requirements of the suggested method, as shown in Figure 1. The radius (R) and thickness (B) of marble specimens are 50 mm and 32 mm. The dimensions of the final chevron notched crack length (a_1) and initial

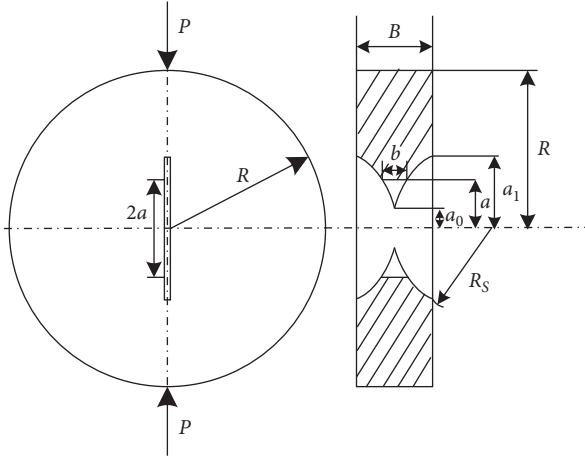


FIGURE 1: Sample geometry parameters of the CCNBD specimen (ISRM, 1995) [35].

chevron notched crack length (a_0) are 38 mm and 13 mm on average. The density of marble specimens is $2.68 \times 10^3 \text{ kg/m}^3$ on average. The average uniaxial compression strength (UCS) and tensile strength are 53.85 and 4.05 MPa. Mineral composition analysis showed that white marble is constituted by only a single mineral, namely, calcite. The force-controlled loading mode was adopted in this study. The loading rate was constant at 1 kN/min. In total, there are 7 CCNBD marble specimens for mode I fracture tests.

A rock mechanics testing system (model: MTS815 Flex Test GT) with a maximum normal load of 4600 kN was used to carry out mode I fracture tests. The force, displacement, and crack opening displacement were recorded during the tests. Force was measured by force sensors with a range of 0 to 1000 kN, while displacement and crack opening displacement were measured by linear variable differential transducers (LVDTs) with a range of ± 2.5 mm and crack opening displacement meter (COD) with a range of -2 mm to 5 mm, respectively. This configuration used in this study is according to the suggested method by ISRM [35]. An acoustic emission monitoring system (model: PCI-2), produced by American Physical Acoustics Corporation, was utilized to automatically monitor AE signals during the whole loading process. The experimental setup of acoustic emission monitoring is shown in Figure 2. Eight Micro30 sensors, which have a good sensitivity to AE signals, were equally distributed on the surface of each CCNBD specimen symmetrically with respect to the loading direction. Vaseline was used to guarantee good connections between AE sensors and rock sample. The threshold level was set as 35 dB in the experiments. The sampling rate was 1 MHz and the pre-amplification was set as 40 dB. The Micro30 sensor has a wide frequency response [36].

To analyze the critical slowing down feature of AE signals, the variances and autocorrelation coefficients of AE counts with loading time were calculated through a batch program written by MATLAB software.

4. Results

4.1. Mechanical Properties of Marble under Mode I Fracture.

Figure 3 shows the typical CCNBD sample after mode I fracture tests. According to the recommended method by ISRM, the mode I fracture toughness (K_{IC}) of specimen can be determined by the following equation [35]:

$$K_{IC} = \frac{P_{\max}}{B\sqrt{D}} Y_{\min}^* \quad (7)$$

where Y_{\min}^* refers to the critical dimensionless stress intensity for the CCNBD specimen, which is calculated by geometry dimensions of specimen only. P_{\max} refers to the peak force recorded during the experiments. The symbols B and D are the thickness and diameter of the disc specimen, respectively.

The mode I fracture toughness of marble specimens was calculated by equation (7), as listed in Table 1. The mode I fracture toughness is $0.636 \text{ MPa} \times \text{m}^{1/2}$ on average, ranging from 0.447 to $0.797 \text{ MPa} \times \text{m}^{1/2}$. The number of AE hits released during the rock fracture process is on average 20479 with a range of 13659 to 27321.

According to the ISRM suggested method [35], the minimum valid diameter (D_{\min}) of CCNBD specimens can be estimated as follows:

$$D_{\min} = 8.88 + 1.4744 \cdot \left(\frac{K_{IC}}{\sigma_t} \right)^{-2}, \quad (8)$$

where σ_t denotes the tensile strength of rock specimens.

The minimum valid diameter (D_{\min}) for marbles in this study is approximately 68.6 mm calculated by equation (8). The diameter of marble specimens is 100 mm, which is much greater than D_{\min} . Therefore, the mode I fracture toughness in this study is valid and accurate.

The typical force-crack opening displacement curve of the specimens is shown in Figure 4. Obviously, the crack opening displacement grows slowly with the increasing force at the initial loading stage. The crack opening displacement increases significantly after the applied force reaches the peak, while the applied force on the CCNBD specimens remains approximately constant at this stage.

4.2. Characteristics of AE Signals Released during Mode I Fracture Process. The typical spatial distribution of AE signals is presented in Figure 5. Note that black line represents the boundary of rock specimen and red lines refer to macroscopic cracks distributed in rock specimens. It can be found that the spatial distribution of AE sources agrees well with macroscopic failure pattern of rock specimens subjected to mode I fracture loading. Figure 6 shows typical acoustic emission count curve versus loading time during the mode I fracture test. Note that red dotted line in Figure 6 refers to the force-loading time curve during mode I rock fracture. On the left vertical axis is AE count while on the right vertical axis is force in kN. There are few AE signals produced by the specimen at the initial stage. This is because the external force at this loading stage is too small to cause microcrack initiation and propagation in rocks. At this stage, AE signals result from the closure of preexisting cracks. Subsequently, the AE counts increase gradually with

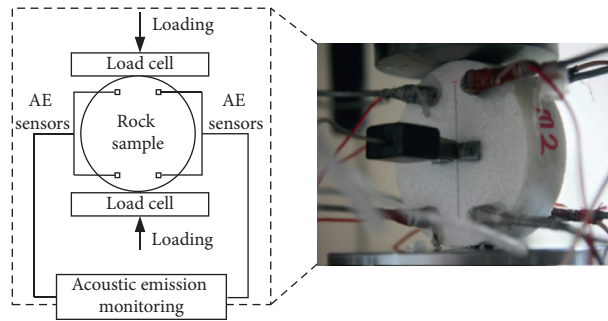


FIGURE 2: Schematic diagram of acoustic emission monitoring.

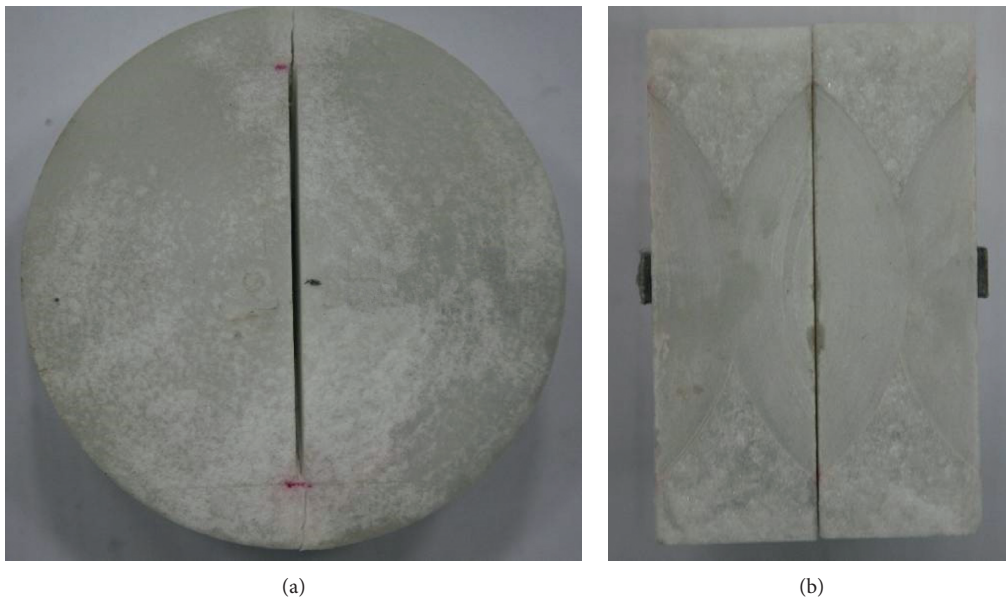


FIGURE 3: Typical CCNBD sample after the mode I fracture test.

TABLE 1: Fracture toughness and total AE hit of specimens.

Specimen no.	Mode I fracture toughness (MPa \times m ^{1/2})	AE hit total
M1	0.797	21101
M2	0.734	13659
M3	0.527	19071
M4	0.783	25153
M5	0.596	20347
M6	0.569	16699
M7	0.447	27321
Average	0.636	20479

increasing force, which reflects the onset and propagation of microcracking. Significant growth of AE counts occurs as the applied force approaches the peak. Formation and penetration of macroscopic cracks occur at this stage. The release of AE counts is consistent with the rock fracture process.

4.3. Critical Slowing Down Feature during Mode I Fracture Process. To investigate the critical slowing down feature, appropriate window length and lag step length need to be

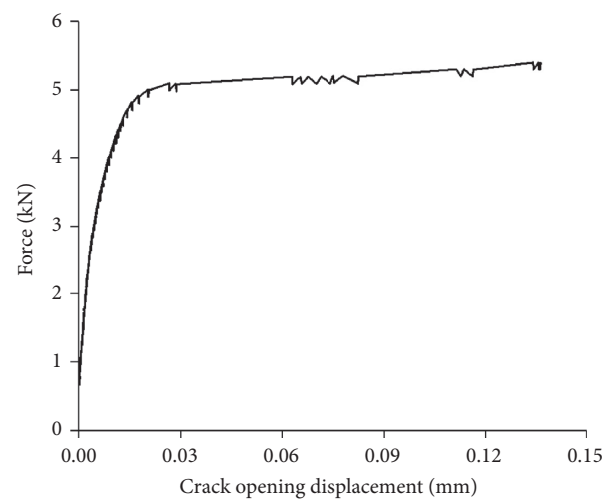


FIGURE 4: Typical force versus crack opening displacement curve of rock sample.

adopted to determine the variance and autocorrelation coefficient of AE counts. Window length is the basic unit of sequence analysis and refers to the number of data in each

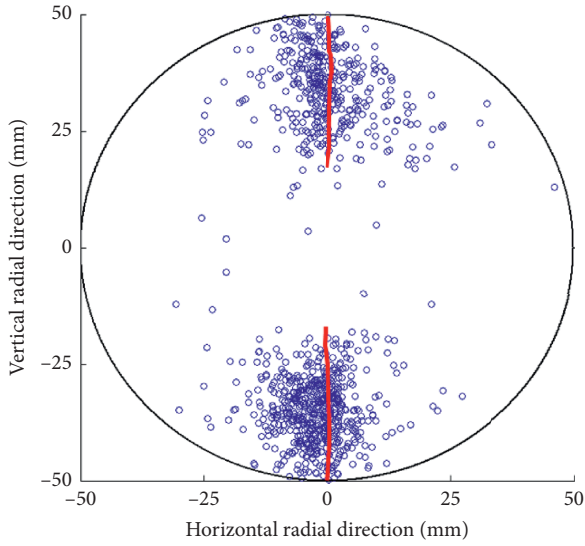


FIGURE 5: Typical spatial distribution of AE signals. Note that black line represents the boundary of rock specimen and red lines refer to macroscopic cracks distributed in rock specimens.

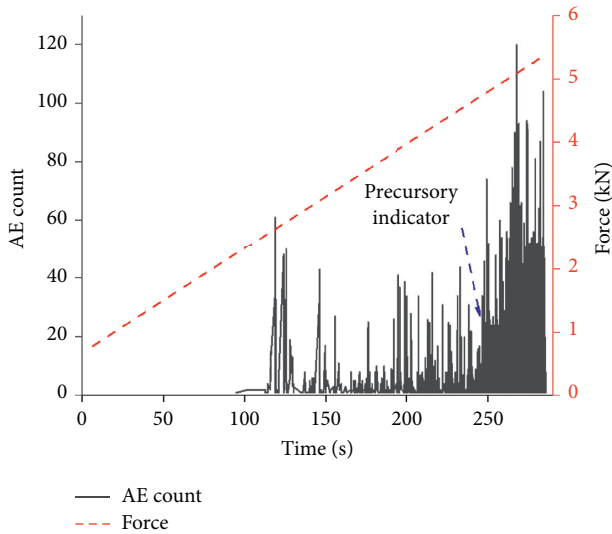


FIGURE 6: Typical AE count curve with loading time under mode I fracture.

sequence selected from the total data. The lag step length refers to the lag length from the sequence of a specific window length to another new identical sequence. Hence, the effect of different window lengths and lag step lengths on the results was analyzed. Figure 7 shows the variance and autocorrelation coefficient curves of AE counts under the same lag step length of 50 with different window lengths of 80, 100, and 120. For different window lengths, the overall trend of variance and autocorrelation coefficient curves is almost the same although there are differences in their magnitude. The variance and autocorrelation coefficient curves of AE counts with different lag step lengths under the same window length are presented in Figure 8. The window length was set constant at 100, and the lag step length was set as 20, 50, and 80, respectively. When the window length

remains constant, the variance curves are consistent for different lag step lengths, while the lag step length influences autocorrelation coefficient curves. Overall, the window length and lag step length have a little effect on the results, especially the trend of variance and autocorrelation coefficient curves. The window length of 100 with a lag step length of 50 was adopted in the following analysis.

Figure 9 shows the variance and autocorrelation coefficient curves of AE counts with loading time. Obviously, there are sudden and significant increases in the variance and autocorrelation coefficient curves preceding rock fracture. This indicates the critical slowing down phenomenon exists during the rock fracture process. By comparing Figures 9(a) and 9(b), the precursory indicator is easier to identify in the variance curve compared to the autocorrelation coefficient curve. The critical slowing down feature characterized by variances is more remarkable than autocorrelation coefficients. This is due to differences between the mathematical meaning and range of the two parameters. The variance is the deviation of sample data to its mathematical expectation, while autocorrelation coefficient statistically describes the correlation between different periods of the same variable. The variance can be a very large value, whereas the range of autocorrelation coefficient is from -1 to 1 . Thus, the change of variance is more remarkable compared to autocorrelation coefficient. According to the critical slowing down feature of AE counts, the sudden and significant growth of variance and autocorrelation coefficient, especially variance, can be viewed as the precursory indicator for imminent rock fracture. The precursory indicator is automatically identified by the magnitude and gradient of changes.

Time intervals between the precursory indicator and failure moment for different specimens are shown in Figure 10. The time intervals between the precursory indicator and failure moment range from 3.36 to 42.94 seconds with an average of 13.68 seconds.

To study the relationship between the precursory indicator and the loading process, ratios of precursory indicator to failure moment in time and force are shown in Table 2. The average ratios of the precursory indicator to failure moment in time and load are 95.69% and 95.62%, respectively. The ratios of the precursory indicator to failure moment range from approximately 85% to 98% in terms of both time and force. In other words, the period between precursory signal and fracture time of marble specimens occupies 2%–15% of the fracture time after analysis of critical slowing down feature. Therefore, the critical slowing down theory has great potential for predicting rock fracture.

5. Discussion

According to analysis results, the phenomenon of critical slowing down exists during the mode I rock fracture process, which is a new method to identify whether a rock is approaching fracture. This further verifies that the critical slowing down feature is ubiquitous for complex dynamical systems in nature, spanning from ecosystems to seismic systems [27, 29, 30]. The time intervals between the

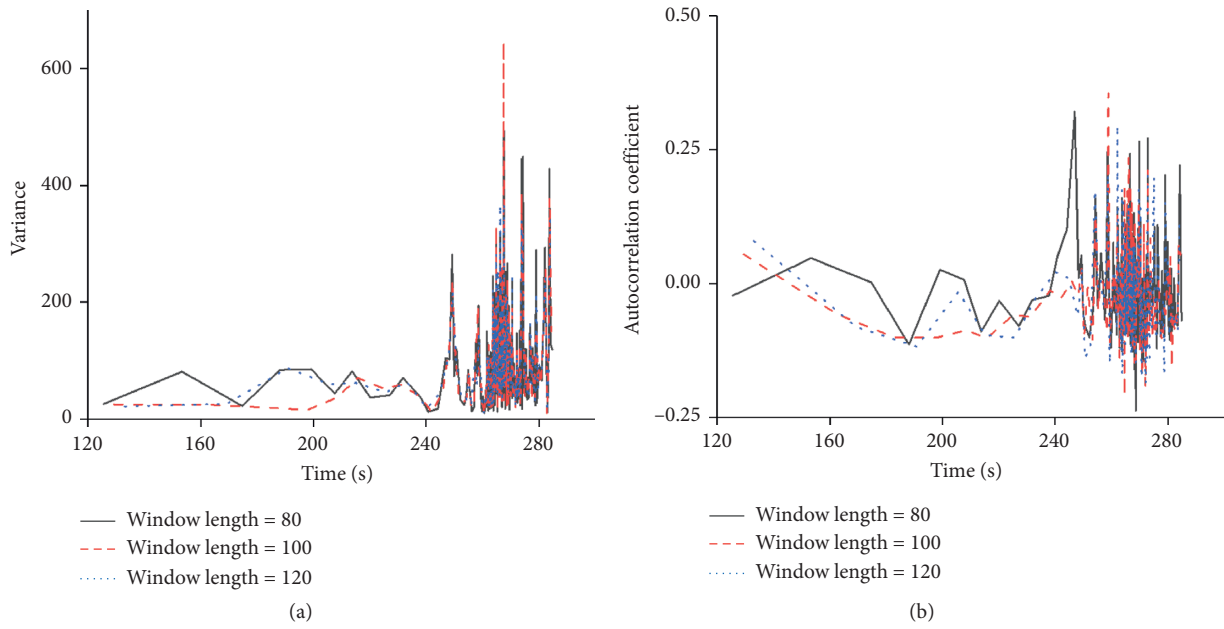


FIGURE 7: Variance and autocorrelation coefficient curves of AE counts with different window lengths under the same lag step length: (a) variance; (b) autocorrelation coefficient.

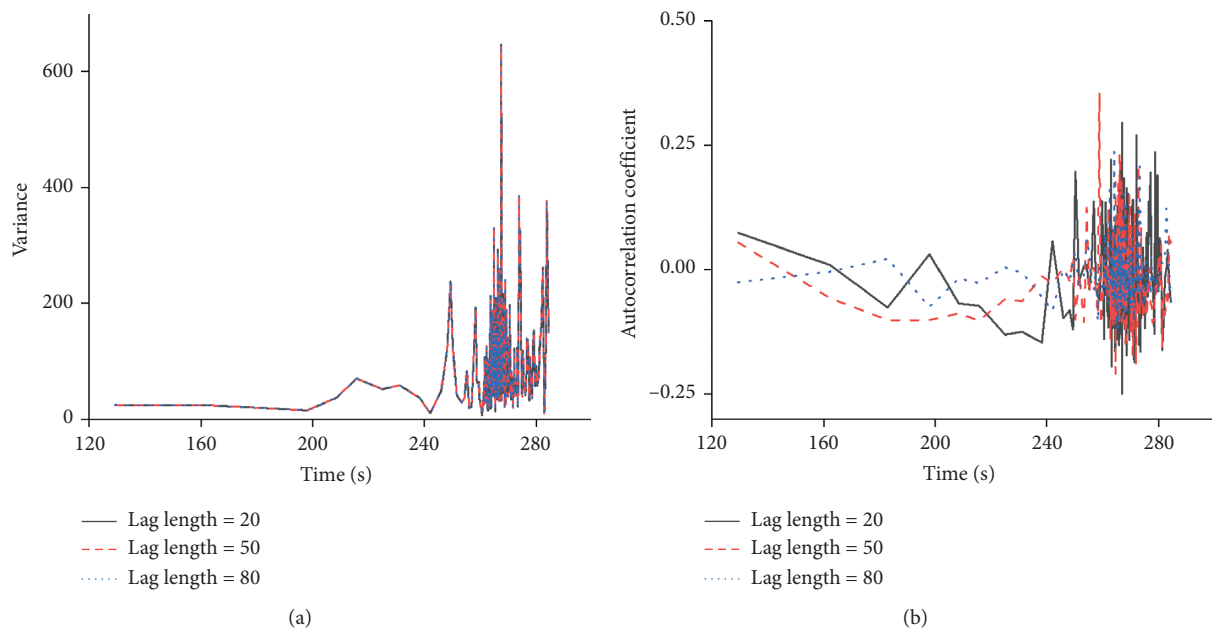


FIGURE 8: Variance and autocorrelation coefficient curves of AE counts with different lag step lengths under the same window length: (a) variance; (b) autocorrelation coefficient.

precursory indicator using critical slowing down theory and fracture moment (averagely 4% with a range of 2%–15%) are not very short or long compared to total loading time. This is of great significance for early-warning sudden fracture of rock because it is meaningless if the early-warning time is too short or too long. The findings in this study could facilitate better understandings on the rock fracture process and early-warning technique of rock fracture-related geological disasters.

As shown in Section 4.3, the range of time intervals between the precursory indicator and failure moment is from 3.36 to 42.94 seconds, and the period between precursory signal and fracture time of marble specimens occupies 2%–15% of the loading time. It can be found that there are differences between the results of different marble specimens. The differences may be attributed to the discrepancy between microstructure of specimens although white marble is constituted by only calcite. The spatial

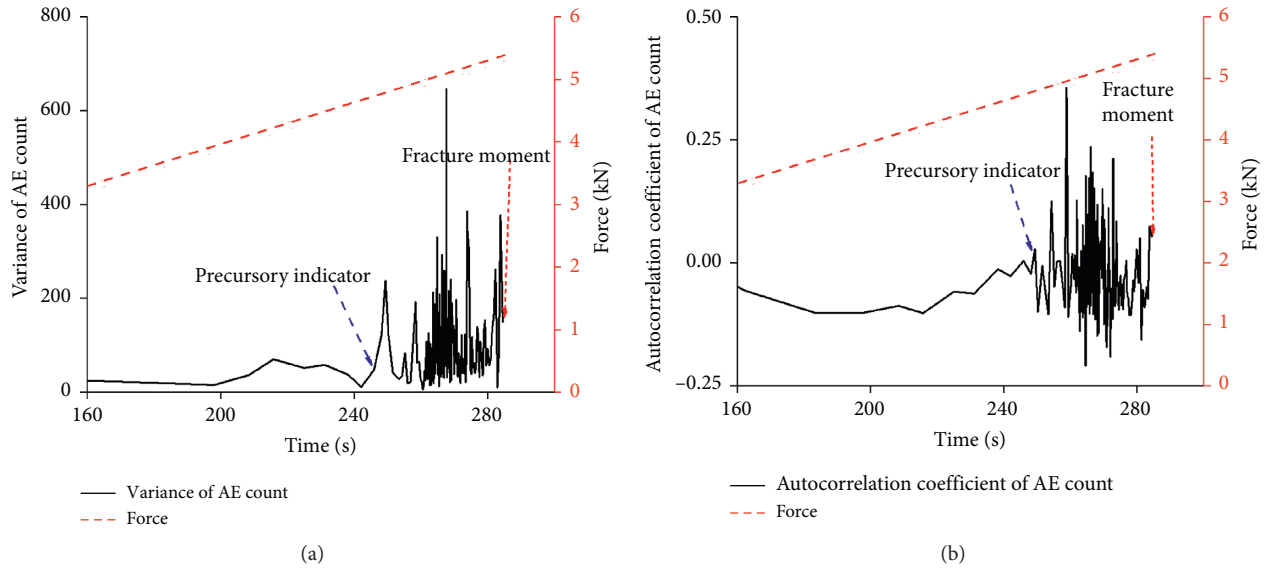


FIGURE 9: Variance and autocorrelation coefficient curves of AE counts with the loading time: (a) variance; (b) autocorrelation coefficient.

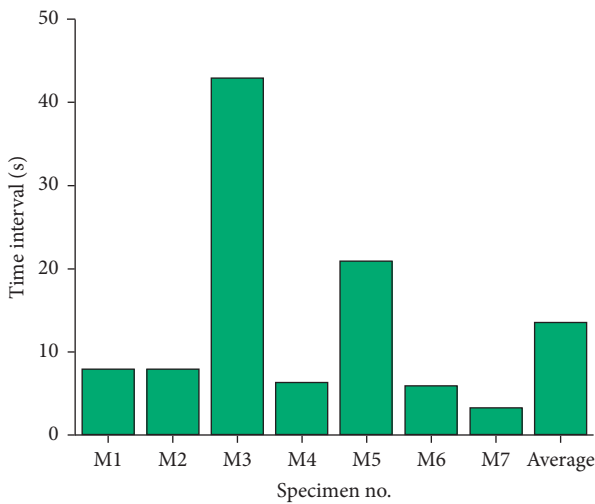


FIGURE 10: Time intervals between the precursory indicator and failure moment.

TABLE 2: Ratios of the precursory indicator to failure moment in time and force.

Specimen no.	Ratio of the precursory indicator to failure moment (%)	
	Time	Force
M1	98.21	98.00
M2	97.87	97.46
M3	85.13	86.14
M4	98.49	98.19
M5	93.45	93.74
M6	98.12	97.86
M7	98.59	97.98
Average	95.69	95.62

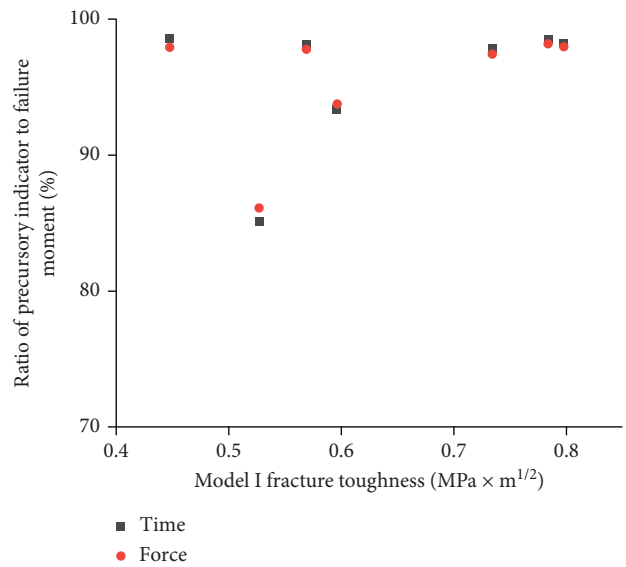


FIGURE 11: Scatter diagram between the ratios of the precursory indicator to failure moment and mode I fracture toughness of marble specimens.

distribution and quantity of preexisting defects, e.g., preexisting microcracks, pores, and cleavage, affect the rock fracture process subjected to external load.

A comparison was made between the precursory point obtained by the AE count curve directly and that of variance and autocorrelation coefficient, as shown in Figures 6 and 9. It is found that the precursory indicator through the variance and autocorrelation coefficient of AE counts approximates that obtained by the AE count curve directly. However, compared to the direct determination of the precursory indicator through AE response, i.e., the remarkable growth in AE counts [8, 9], the precursory indicator through critical

slowing down analysis is more precise and recognizable. Furthermore, compared to seismic b -value, which is also applied to analyze the rock failure process [10–12], the change of the variance and autocorrelation coefficient preceding rock fracture is easier to identify. This advantage is crucial for engineers.

To discuss whether there is a certain relationship between the ratio of the precursory indicator to failure moment and mode I fracture toughness, a comparison was made among different marble specimens. Scatter diagram between the ratios of the precursory indicator to failure moment and mode I fracture toughness of marble specimens is shown in Figure 11. The ratios of the precursory indicator to failure moment in terms of time and force are relatively stable when the mode I fracture toughness of rock specimens varies.

Acoustic emission response can reflect the influence of preexisting defects on the rock failure process indirectly. However, direct measurement of preexisting defects through three-dimensional CT scanning or other methods would be much more convincing. Further study on the effect of preexisting defects on the critical slowing down characteristics is needed. Furthermore, the present study investigated the precursory information for mode I fracture of rock based on the critical slowing down theory. Further study on mode II and mixed-mode loading conditions is needed.

6. Conclusions

The study investigated the precursory indicator of AE signals during mode I rock fracture through critical slowing down analysis. The following conclusions are drawn:

- (1) The critical slowing down phenomenon exists during mode I rock fracture. The variance and autocorrelation coefficient of AE count sequences grow significantly preceding rock fracture.
- (2) The significant growth of variance and autocorrelation coefficient of AE signals can be viewed as the precursory indicator of rock fracture. Compared to autocorrelation coefficient, the precursors determined by variance are more remarkable.
- (3) The time interval between the precursory indicator using critical slowing down theory and fracture moment ranges from 2% to 15% of the loading time.
- (4) The difference between different specimens may be attributed to the discrepancy between microstructure of specimens, especially the spatial distribution and quantity of preexisting defects.

Data Availability

The data used to support the findings of this study are available from the corresponding author upon request.

Conflicts of Interest

The authors declare that they have no conflicts of interest.

Acknowledgments

This study was financially supported by the National Natural Science Foundation of China (nos. 51909026, 51974055, 51774064, and 41941018), the Fundamental Research Funds for the Central Universities (Grant no. DUT20GJ216), and the National Key Research and Development Program of China (no. 2018YFC1505301).

References

- [1] M. Ohtsu, "Simplified moment tensor analysis and unified decomposition of acoustic emission source: application to in situ hydrofracturing test," *Journal of Geophysical Research: Solid Earth*, vol. 96, no. B4, pp. 6211–6221, 1991.
- [2] Z.-H. Zhang, J.-H. Deng, J.-B. Zhu, and L.-R. Li, "An experimental investigation of the failure mechanisms of jointed and intact marble under compression based on quantitative analysis of acoustic emission waveforms," *Rock Mechanics and Rock Engineering*, vol. 51, no. 7, pp. 2299–2307, 2018.
- [3] D. G. Aggelis, "Classification of cracking mode in concrete by acoustic emission parameters," *Mechanics Research Communications*, vol. 38, no. 3, pp. 153–157, 2011.
- [4] J. Karsner, *A Study of Acoustic Emission Phenomena in Tensile Tests*, Technische Hochschule Munchen, Munich, Germany, 1950.
- [5] M. Ohnaka and K. Mogi, "Frequency characteristics of acoustic emission in rocks under uniaxial compression and its relation to the fracturing process to failure," *Journal of Geophysical Research*, vol. 87, no. B5, pp. 3873–3884, 1982.
- [6] R. Prikryl, T. Lokajiček, C. Li, and V. Rudajev, "Acoustic emission characteristics and failure of uniaxially stressed granitic rocks: the effect of rock fabric," *Rock Mechanics and Rock Engineering*, vol. 36, no. 4, pp. 255–270, 2003.
- [7] K.-H. Li, P. Cao, K. Zhang, and Y.-F. Zhong, "Macro and meso characteristics evolution on shear behavior of rock joints," *Journal of Central South University*, vol. 22, no. 8, pp. 3087–3096, 2015.
- [8] T. Shiotani, M. Ohtsu, and K. Ikeda, "Detection and evaluation of AE waves due to rock deformation," *Construction and Building Materials*, vol. 15, no. 5-6, pp. 235–246, 2001.
- [9] M. Cai, H. Morioka, P. K. Kaiser et al., "Back-analysis of rock mass strength parameters using AE monitoring data," *International Journal of Rock Mechanics and Mining Sciences*, vol. 44, no. 4, pp. 538–549, 2007.
- [10] C. H. Scholtz, "The frequency-magnitude relation of microfracturing in rock and its relation to earthquakes," *Bulletin of the Seismological Society of America*, vol. 58, no. 1, pp. 399–415, 1968.
- [11] X. Lei, K. Masuda, O. Nishizawa et al., "Detailed analysis of acoustic emission activity during catastrophic fracture of faults in rock," *Journal of Structural Geology*, vol. 26, no. 2, pp. 247–258, 2004.
- [12] Z. Zhang, R. Zhang, H. Xie, J. Liu, and P. Were, "Differences in the acoustic emission characteristics of rock salt compared with granite and marble during the damage evolution process," *Environmental Earth Sciences*, vol. 73, no. 11, pp. 6987–6999, 2015.
- [13] Y. H. Li, J. P. Liu, X. D. Zhao, and Y. J. Yang, "Experimental studies of the change of spatial correlation length of acoustic emission events during rock fracture process," *International Journal of Rock Mechanics and Mining Sciences*, vol. 47, no. 8, pp. 1254–1262, 2010.

- [14] Z. Zhang, E. Wang, N. Li, X. Li, X. Wang, and Z. Li, "Damage evolution analysis of coal samples under cyclic loading based on single-link cluster method," *Journal of Applied Geophysics*, vol. 152, pp. 56–64, 2018.
- [15] M. C. He, J. L. Miao, and J. L. Feng, "Rock burst process of limestone and its acoustic emission characteristics under true-triaxial unloading conditions," *International Journal of Rock Mechanics and Mining Sciences*, vol. 47, no. 2, pp. 286–298, 2010.
- [16] L. R. Li, J. H. Deng, L. Zheng, and J. F. Liu, "Dominant frequency characteristics of acoustic emissions in white marble during direct tensile tests," *Rock Mechanics and Rock Engineering*, vol. 50, no. 5, pp. 1337–1346, 2017.
- [17] T. Hirata, T. Satoh, and K. Ito, "Fractal structure of spatial distribution of microfracturing in rock," *Geophysical Journal International*, vol. 90, no. 2, pp. 369–374, 1987.
- [18] H. P. Xie, J. F. Liu, Y. Ju, J. Li, and L. Z. Xie, "Fractal property of spatial distribution of acoustic emissions during the failure process of bedded rock salt," *International Journal of Rock Mechanics and Mining Sciences*, vol. 48, no. 8, pp. 1344–1351, 2011.
- [19] R. Zhang, F. Dai, M. Z. Gao, N. W. Xu, and C. P. Zhang, "Fractal analysis of acoustic emission during uniaxial and triaxial loading of rock," *International Journal of Rock Mechanics and Mining Sciences*, vol. 79, pp. 241–249, 2015.
- [20] X. Kong, E. Wang, X. He, D. Li, and Q. Liu, "Time-varying multifractal of acoustic emission about coal samples subjected to uniaxial compression," *Chaos, Solitons & Fractals*, vol. 103, pp. 571–577, 2017.
- [21] S. W. Zhang, K. J. Shou, X. F. Xian, J. P. Zhou, and G. J. Liu, "Fractal characteristics and acoustic emission of anisotropic shale in Brazilian tests," *Tunnelling and Underground Space Technology*, vol. 71, pp. 298–308, 2018.
- [22] V. Dakos, M. Scheffer, E. H. Van Nes, V. Brovkin, V. Petoukhov, and H. Held, "Slowing down as an early warning signal for abrupt climate change," *Proceedings of the National Academy of Sciences*, vol. 105, no. 38, pp. 14308–14312, 2008.
- [23] M. Scheffer, J. Bascompte, W. A. Brock et al., "Early-warning signals for critical transitions," *Nature*, vol. 461, no. 7260, pp. 53–59, 2009.
- [24] V. Dakos and J. Bascompte, "Critical slowing down as early warning for the onset of collapse in mutualistic communities," *Proceedings of the National Academy of Sciences*, vol. 111, no. 49, pp. 17546–17551, 2014.
- [25] E. A. Gopalakrishnan, Y. Sharma, T. John, P. S. Dutta, and R. I. Sujith, "Early warning signals for critical transitions in a thermoacoustic system," *Nature*, vol. 6, pp. 1–10, 2016.
- [26] H. Wu, W. Hou, and P. C. Yan, "Using the principle of critical slowing down to discuss the abrupt climate change," *Acta Physica Sinica*, vol. 62, no. 3, pp. 1–10, 2013, in Chinese.
- [27] E. H. Van Nes and M. Scheffer, "Slow recovery from perturbations as a generic indicator of a nearby catastrophic shift," *The American Naturalist*, vol. 169, no. 6, pp. 738–747, 2007.
- [28] R. A. Chisholm and E. Filotas, "Critical slowing down as an indicator of transitions in two-species models," *Journal of Theoretical Biology*, vol. 257, no. 1, pp. 142–149, 2009.
- [29] K. K. Beck, M.-S. Fletcher, P. S. Gadd et al., "Variance and rate-of-change as early warning signals for a critical transition in an aquatic ecosystem state: a test case from Tasmania, Australia," *Journal of Geophysical Research: Biogeosciences*, vol. 123, no. 2, pp. 495–508, 2018.
- [30] R. Yan, C. Jiang, and L. Zhang, "Study on critical slowing down phenomenon of radon concentrations in water before the Wenchuan MS8.0 earthquake," *Chinese Journal of Geophysics*, vol. 54, no. 7, pp. 1817–1826, 2011, in Chinese.
- [31] H. Ren and D. Watts, "Early warning signals for critical transitions in power systems," *Electric Power Systems Research*, vol. 124, pp. 173–180, 2015.
- [32] X. Kong, E. Wang, S. Hu et al., "Critical slowing down on acoustic emission characteristics of coal containing methane," *Journal of Natural Gas Science and Engineering*, vol. 24, pp. 156–165, 2015.
- [33] Y. Wei, Z. Li, X. Kong et al., "The precursory information of acoustic emission during sandstone loading based on critical slowing down theory," *Journal of Geophysics and Engineering*, vol. 15, no. 5, pp. 2150–2158, 2018.
- [34] X. Zhang, Z. Li, Y. Niu, F. Cheng, M. Ali, and S. Bacha, "An experimental study on the precursory characteristics of EP before sandstone failure based on critical slowing down," *Journal of Applied Geophysics*, vol. 170, pp. 1–10, 2019.
- [35] ISRM Testing Commission and R. J. Fowell, "Suggested method for determining mode I fracture toughness using cracked chevron notched Brazilian disc (CCNBD) specimens," *International Journal of Rock Mechanics and Mining Sciences & Geomechanics Abstracts*, vol. 32, pp. 57–64, 1995.
- [36] Z. H. Zhang and J. H. Deng, "A new method for determining the crack classification criterion in acoustic emission parameter analysis," *International Journal of Rock Mechanics and Mining Sciences*, vol. 130, Article ID 104323, 2020.

Research Article

Research on Evaluation Index and Application of Rockburst Risk in Deep Strip Mining

Bangyou Jiang,^{1,2} Hongguang Ji,³ Long Fu,⁴ Shitan Gu ,^{1,2} Tong Zou,^{1,2} and Jiaxin Lu^{1,2}

¹State Key Laboratory of Mining Disaster Prevention and Control Co-Founded by Shandong Province and the Ministry of Science and Technology, Shandong University of Science and Technology, Qingdao 266590, China

²College of Energy and Mining Engineering, Shandong University of Science and Technology, Qingdao 266590, China

³School of Civil and Resource Engineering, University of Science and Technology Beijing, Beijing 100083, China

⁴School of Photovoltaics Engineering, Shandong Polytechnic College, Jining 272067, China

Correspondence should be addressed to Shitan Gu; chinasdgt@163.com

Received 11 March 2020; Revised 22 June 2020; Accepted 8 July 2020; Published 8 September 2020

Academic Editor: Hongwei Yang

Copyright © 2020 Bangyou Jiang et al. This is an open access article distributed under the Creative Commons Attribution License, which permits unrestricted use, distribution, and reproduction in any medium, provided the original work is properly cited.

The practice shows that deep strip mining induces rockburst disaster easily. Accurately evaluating rockburst risk of the strip coal pillar is of great significance for ensuring the safety of deep strip mining. In this paper, the catastrophe mechanics model was used to analyze the abrupt instability condition of strip coal pillar. And the three indicators that are the medium stiffness ratio (k) of the elastic and plastic zone in the coal pillar, the plastic zone width ratio (a_V), and the elastic deformation index (U_q) of core zone were put forward with considering the geometry size of coal pillar. Based on the 3202 panel of Gucheng Coal Mine, the evolution characteristics of rockburst risk of coal pillar under different mining widths and coal pillar widths were studied by numerical simulation. The evaluation result shows that the strip coal pillar of the 3202 panel is in danger of strong rockburst, which is more in line with the actual situation than the results of the traditional rockburst tendency identification test and comprehensive index method. These three indicators can be regarded as important indicators to evaluate the rockburst risk in the strip mining engineering field. Based on that, the design principle of strip mining in Gucheng Coal Mine was put forward, which is considered an important reference for similar cases.

1. Introduction

In recent years, with the increasing depletion of shallow coal resources in China, in order to improve mining rate of coal resources and prolong mine life, many mining areas increase the exploitation of coal under buildings, railways, and water bodies, especially in the eastern part of China [1–5]. Strip mining is one of the common mining methods of coal under buildings, railways, and water bodies, which can effectively alleviate the surface subsidence of the coal mining area. Strip mining is widely used in the old eastern mining areas of China, which is one of the research hotspots in the Green Mining of Coal Resources in China. However, under mining disturbance, the high concentrated stress of the strip coal pillar is easy to induce dynamic disasters such as rockburst, which seriously affects the safety production of the working face [6–10].

As a complex nonlinear dynamic disaster, the occurrence of rockburst in coal and rock mass needs to meet certain physical conditions, such as the burst risk of coal and rock mass [11, 12]. It is of great significance for the prevention and control of rockburst to accurately evaluate the risk of rockburst [13]. In order to quantitatively measure the burst risk of coal and rock, domestic and overseas scholars have proposed a variety of impact propensity indexes based on energy storage, dynamic failure time, deformation, and stiffness of coal and rock and put forward corresponding discrimination indexes [14–16]. Pan et al. [17] put forward three new indexes: impact energy velocity index considering time effect, critical softening region coefficient, and critical stress coefficient. Jiang et al. [18–22] studied the influence of mining supporting pressure and structural stress on the rockburst and adopted a multiparameter early warning

method to evaluate the rockburst risk of the working face. Lu et al. [23, 24] revealed the mining-induced fault slip mechanism and proposed the multiparameter precursors of a rockburst induced by the fault slip. Zhao et al. [25] established the prediction model of rockburst induced by roof. Yang et al. [26] studied the mechanism of rockburst from the vertical stress of coal pillar. Tan et al. [27] established a cusp catastrophe model for the instability of narrow coal pillars between mining tunnels and strip coal pillars and analyzed the instability mechanism and engineering stability conditions of the coal pillar system of Wongawilli mining. The above studies were based on the characteristics of stress, structure, and roof to establish the rockburst risk assessment model, mainly considering the influence of geological and mining factors on the occurrence of rockburst. However, there are relatively few studies on the dynamic instability characteristics and the main control factors of the strip coal pillar. The existing evaluation methods do not consider the special stress characteristics and instability conditions of the strip coal pillar and lack of pertinence in the evaluation of the rockburst risk of strip mining.

In this study, the medium stiffness ratio of the elastic and plastic zone in coal pillar, the plastic zone width ratio, and the elastic deformation index of kernel zone were put forward based on catastrophe theory, which could be used to guide the prevention and control of rockburst of deep strip working face.

2. Cusp Catastrophe Model of Strip Coal Pillar

Rockburst in the coal mine is characterized by abruptness, concealment, no forewarning, and heavy casualties and economic loss [28]. Rockburst is essentially a discontinuous process of sudden instability of the system. Therefore, catastrophe theory can be used to study the process of stope impact instability [29]. For strip coal pillar, with the increase of the width of goaf, the side abutment pressure increases significantly. Under the concentrated load, the coal pillar shows strain softening and remains in a stable position at the initial stage. With the compression deformation of the coal pillar, the deformation energy in the coal pillar gradually accumulates and gradually reaches the unstable critical state. Under the external disturbance, the critical system suddenly jumps to the corresponding stable equilibrium point. The jump phenomenon of the coal pillar system can be considered as the occurrence of rockburst [30].

In order to explore the process of coal pillar rockburst, Tan et al. [27] established the mechanical model of the coal pillar system as shown in Figure 1. In Figure 1, m is the mining thickness of the coal seam, a is the reserved width of the coal pillar, and b is the mining width of the working face, all of which are in meters.

According to the stress-strain curve of the coal pillar, the constitutive relationship between elastic core and plastic zone of coal pillar is different. In order to simplify the calculation, the elastic core of the coal pillar is regarded as linear elastic, the stress-strain curve is a straight line, and the slope of the straight line is the elastic modulus of the coal seam. The plastic zone constitutive relation is approximately

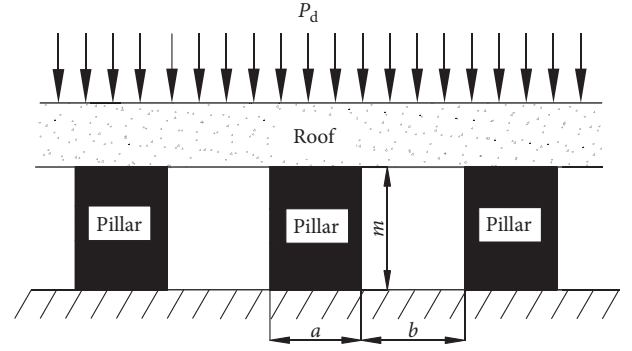


FIGURE 1: Mechanical model of the coal pillar system.

replaced by the strain-softening constitutive relation of coal. The stress-strain relationship of coal pillar can be expressed as

$$\sigma = \begin{cases} E\varepsilon, & (\varepsilon < \varepsilon_c), \\ E\varepsilon e^{-(\varepsilon/\varepsilon_c)}, & (\varepsilon \geq \varepsilon_c), \end{cases} \quad (1)$$

where E is the elastic modulus of the coal seam, ε is the strain of coal pillar, and ε_c is the strain corresponding to the peak stress.

The width of the plastic zone of the coal pillar is defined as Y , and then the width of the elastic core of the coal pillar is $a - 2Y$. Considering the influence of coal pillar size, the medium stiffness of the elastic core and the plastic zone of the coal pillar can be expressed as follows:

$$\begin{cases} k_e = \frac{E(a - 2Y)}{m}, \\ k_s = \frac{2EY}{m} e^{-(u/u_c)}, \end{cases} \quad (2)$$

where k_e is the medium stiffness in the elastic core of the strip coal pillar, k_s is the medium stiffness in the plastic zone of the strip coal pillar, u is the deformation value of the coal pillar, and u_c is the deformation value of the coal pillar under peak load. Since the height of the coal pillar is m , there is $u_c = m\varepsilon_c$.

According to the research results of Tan et al. [27], the expression of total potential energy function of the system, denoted by V , can be expressed as follows:

$$V = V_s + V_e - V_p = \frac{EY}{m} u^2 e^{-(u/u_c)} + \frac{E(a - 2Y)}{2m} u^2 - \gamma H \left[a + \frac{b}{2} \left(2 - \frac{b}{0.6H} \right) \right] u, \quad (3)$$

where V_s is the strain energy of the plastic zone of the strip coal pillar, V_e is the elastic potential energy in the elastic nuclear region, and V_p is the gravitational potential energy of the overlying strata.

The first derivative of equation (3) is expanded by Taylor series at $u = u_1 = (3 - \sqrt{3})u_c$, the cubic term is extracted, and the following is obtained:

$$\begin{aligned}
V' = & \frac{\sqrt{3}EY}{3mu_c^2} e^{(\sqrt{3}-3)} (u - u_1)^3 \\
& + \left[(2 - 2\sqrt{3}) \frac{EY}{m} e^{(\sqrt{3}-3)} + \frac{E(a-2Y)}{m} \right] (u - u_1) \\
& + \frac{EY}{m} e^{(\sqrt{3}-3)} (4\sqrt{3} - 6)u_c + \frac{E(a-2Y)}{m} (3 - \sqrt{3})u_c \\
& - \gamma H \left[a + \frac{b}{2} \left(2 - \frac{b}{0.6H} \right) \right] = 0.
\end{aligned} \quad (4)$$

Then, the standard equation of the cusp catastrophe equilibrium surface is obtained and can be expressed as equation (5). Point $u = u_1 = (3 - \sqrt{3})u_c$ is the mutation point of the following equation [27]:

$$V'(x) = x^3 + px + q = 0. \quad (5)$$

In equation (5), x is the state variable, p and q are control variables, and thus

$$x = u - u_1, \quad (6)$$

$$p = (2\sqrt{3} - 6)u_c^2 + \sqrt{3}u_c^2 k, \quad (7)$$

$$q = \sqrt{3}u_c^2 \left[(4\sqrt{3} - 6)u_c + (3 - \sqrt{3})u_c k - \frac{P_d}{k_s} \right], \quad (8)$$

where k is the ratio of the medium stiffness k_e in the elastic core to the medium stiffness k_s in the plastic zone of the coal pillar, which is stiffness ratio for short.

According to the mutation theory, only when $p \leq 0$, the system will mutate [31]. So the necessary condition for the system mutation is

$$\begin{aligned}
p &= (2\sqrt{3} - 6)u_c^2 + \sqrt{3}u_c^2 k \leq 0, \\
k &\leq 2\sqrt{3} - 2 \approx 1.46.
\end{aligned} \quad (9)$$

The critical compression of coal pillar before rockburst is denoted by u_q and can be expressed as follows:

$$u_q = \left(3 - \sqrt{3} - \sqrt{2 - \frac{2}{3}\sqrt{3} - \frac{\sqrt{3}}{3}k} \right) u_c. \quad (10)$$

According to equations (9) and (10), the internal cause of strip pillar rockburst is the stiffness ratio of the elastic-plastic zone which is less than 1.46 caused by strain softening. And the external cause of the coal pillar rockburst is that the deformation energy accumulation caused by the compression deformation of the coal pillar reaches the instability, and the compression of the elastic core of coal pillar reaches or approaches to the critical value. The strain-softening state reflects the failure degree of the coal pillar under load, while the elastic deformation index reflects the magnitude of energy accumulation. Therefore, it is feasible to evaluate the rockburst risk of the coal pillar by using the indexes of strain-softening degree and compression deformation.

3. Rockburst Risk Evaluation Index of Strip Coal Pillar

3.1. Medium Stiffness Ratio of Elastic and Plastic Zones in Strip Coal Pillar. At present, the commonly used stiffness ratio index for rockburst risk evaluation of coal and rock is the preyield to postyield stiffness ratio on the stress-strain curve of the coal and rock specimen, denoted by K_{CF} , which reflects the strain-softening degree of the specimen after yield [32]. According to the literature [32], when $K_{CF} < 1$, there is rockburst tendency, and when $K_{CF} > 1$, there is no rockburst tendency, and the detailed division is as follows: $K_{CF} \geq 1$, no rockburst tendency; $0.5 < K_{CF} < 1$, weak and medium rockburst tendency; $K_{CF} < 0.5$, strong rockburst tendency. However, this stiffness ratio index ignores the influence of strip coal pillar size effect, and the evaluation result of rockburst risk is not accurate.

Based on the old stiffness ratio index of rockburst risk evaluation and considering the influence of coal pillar geometry size, this paper proposes a new index, the medium stiffness ratio of the elastic and plastic zone in strip coal pillar, which is denoted by k . The physical significance of this index is the ratio of the medium stiffness in the elastic core and the medium stiffness in the plastic zone of the loaded strip coal pillar, which indicates the degree of strain-softening during the loading process of the strip coal pillar. The smaller the k of coal pillar, the greater the rockburst risk. The k can be expressed as follows:

$$k = \frac{k_e}{k_s} = \frac{E(a-2Y)/m}{(2EY/m)e^{(\sqrt{3}-3)}}. \quad (11)$$

According to calculation results of equations (9) and (10), referring to K_{CF} index, the classification standard of plasticity zone width ratio index is as follows: $k \leq 0.73$, strong rockburst tendency; $0.73 < k < 1.46$, medium rockburst tendency; $k \geq 1.46$, no rockburst tendency.

3.2. Plastic Zone Width Ratio of Strip Coal Pillar. According to equation (11), it can be predicted that the field application of the stiffness ratio index in the elastic-plastic zone of strip coal pillar is complicated.

By changing the form of equation (11), the necessary condition for rockburst of the strip coal pillar can be obtained as follows:

$$\frac{Y}{a} \geq 0.354, \quad (12)$$

where Y is the plastic zone width of strip coal pillar and a is the width of strip coal pillar.

In the field application, the width of the plastic zone of the strip coal pillar can be measured by the drilling cuttings method. The larger the width ratio of the plastic zone is, the greater the rockburst risk is. The width ratio of the plastic zone is denoted by a_Y , which can be expressed as follows:

$$a_Y = \frac{Y}{a}. \quad (13)$$

The classification standard of the plasticity zone width ratio index is as follows: $a_Y \geq 41.5\%$, strong rockburst tendency; $35.4\% < a_Y < 41.5\%$, medium rockburst tendency; $a_Y \leq 35.4\%$, no rockburst tendency.

3.3. Elastic Deformation Index of the Strip Coal Pillar Core Zone. The elastic deformation index is also one of the commonly used evaluation indexes of rockburst risk of coal and rock. The old elastic deformation index is obtained by the ratio of the elastic deformation to the total deformation under the cyclic loading and unloading test, and the test loading is not less than 80% of the peak strength of coal and rock [33]. This index reflects the influence of the elastic deformation degree of the specimen on the burst failure. The detailed classification standard of the elastic deformation index which is usually denoted by K_i is as follows: $K_i > 0.83$, strong rockburst tendency; $0.7 \leq K_i \leq 0.83$, medium rockburst tendency; $K_i < 0.7$, no rockburst tendency. However, this index is aimed at small size specimens of coal and rock, and the impact of strip coal pillar geometric size on the rockburst risk is also not considered, resulting in its little significance in the application of strip coal pillar rockburst risk assessment.

Based on the old elastic deformation index and considering the influence of coal pillar geometry size on rockburst risk, this paper proposes a new elastic deformation index of strip coal pillar core zone, which is denoted by U_q . U_q is the ratio of elastic core compression to critical core area compression of loaded strip coal pillar. The elastic deformation index is directly related to the accumulation of deformation energy, which indirectly reflects the relationship between the deformation energy accumulation of strip coal pillar and the critical state of rockburst. The larger elastic deformation index of strip coal pillar core zone, the greater the rockburst risk of strip coal pillar. When the compression amount of strip coal pillar core zone exceeds the critical compression amount of impact instability, it can be considered that the rockburst has occurred. The new elastic deformation index can be expressed as

$$U_q = \frac{u_0}{u_q}, \quad (14)$$

where u_0 is the compression of the elastic core of strip coal pillar and u_q is the rockburst critical compression of strip coal pillar core zone.

According to the old elastic deformation index of coal and rock, the classification standard of the new elastic deformation index of strip coal pillar core zone is as follows: $U_q \leq 0.7$, no rockburst tendency; $0.7 < U_q < 0.83$, medium rockburst tendency; $0.83 < U_q < 1$, strong rockburst tendency; $1 \leq U_q$, rockburst has occurred.

4. Application of Rockburst Risk Evaluation

4.1. Mining and Geological Condition. The Gucheng Coal Mine is located in Jining city, Shandong Province, China. The average overburden depth of Gucheng Coal Mine is 1070 m, which is a typical deep mine. The current mining

seam is #3 coal seam. The average thickness and dip angle of the coal seam are 8.83 m and 7.5° , respectively. The Protodyakonov scale of hardness, Poisson's ratio, and elastic modulus of the coal seam are 3.0, 0.22, and 6.72 GPa, respectively. The rock strata above the coal seam are, in order, sandy mudstone with 1.88 m thick and medium sandstone with 18.7 m thick. This study involves mining panel 3202, which is approximately 116 m in a strike. A fully mechanized longwall top coal caving method is used for #3 coal extraction in this working face, with a mechanized mining height of 3.0 m. The top-coal caving height is 5.83 m. 3202 panel is located at the east of the mining area 3203 panel with the width 120 m, where the coal has been extracted. The width of the strip coal pillar between the 3203 panel and the 3202 panel is 120 m, as shown in Figure 2.

4.2. Evaluation of Rockburst Risk. According to Section 3 of this paper, rockburst risk evaluation indexes of strip coal pillar are listed in Table 1.

According to A. H. Wilson progressive failure theory, the plastic zone width of strip coal pillar can be expressed as

$$Y = 0.0049mH, \quad (15)$$

where Y is the plastic zone width of strip coal pillar, m is the height of the strip coal pillar, and H is the mining depth.

For the 3202 panel, the height of the strip coal pillar is 8.83 m, the mining depth is 1070 m, while the width of the strip coal pillar is 120 m. Therefore, the plastic zone width of the coal pillar calculated by equation (15) is 46.3 m, and the a_Y is 38.6%. According to the evaluation index of a_Y in Table 1, the coal pillar of the 3202 panel is of medium rockburst tendency.

Further, k_e and k_s calculated by equation (9) are 2.11×10^{10} and 1.018×10^{11} N/m, respectively, and the medium stiffness ratio k is 0.207. According to the evaluation index of k in Table 1, the coal pillar of the 3202 panel is of strong rockburst tendency.

According to the test results, the strain corresponding to the peak load of the coal seam under uniaxial compression is 0.013. So u_c is 0.115 m. Further, the critical compression of the strip coal pillar u_q calculated by equation (8) is 0.086 m. However, according to equation (12), u_0 is still unknown, which needs to be obtained by numerical simulation.

4.3. Numerical Simulation for the Elastic Deformation Index

4.3.1. Numerical Model Generation. The FALC3D was used to construct a numerical model. According to the geological conditions of the 3202 working face, the FALC3D was used to construct the numerical calculation model. Considering the influence of boundary effect, coal pillars of 30 m in width are reserved at the boundary along the direction of length and width, and the dimensions of the model are $222 \text{ m} \times 158 \text{ m} \times 69.5 \text{ m}$. The horizontal displacements of the four vertical planes of the model were restricted in the normal direction, and the vertical displacement at the base of the model was set to zero. The top surface of the model is allowed to move freely. Vertical stress of 26.875 MPa is

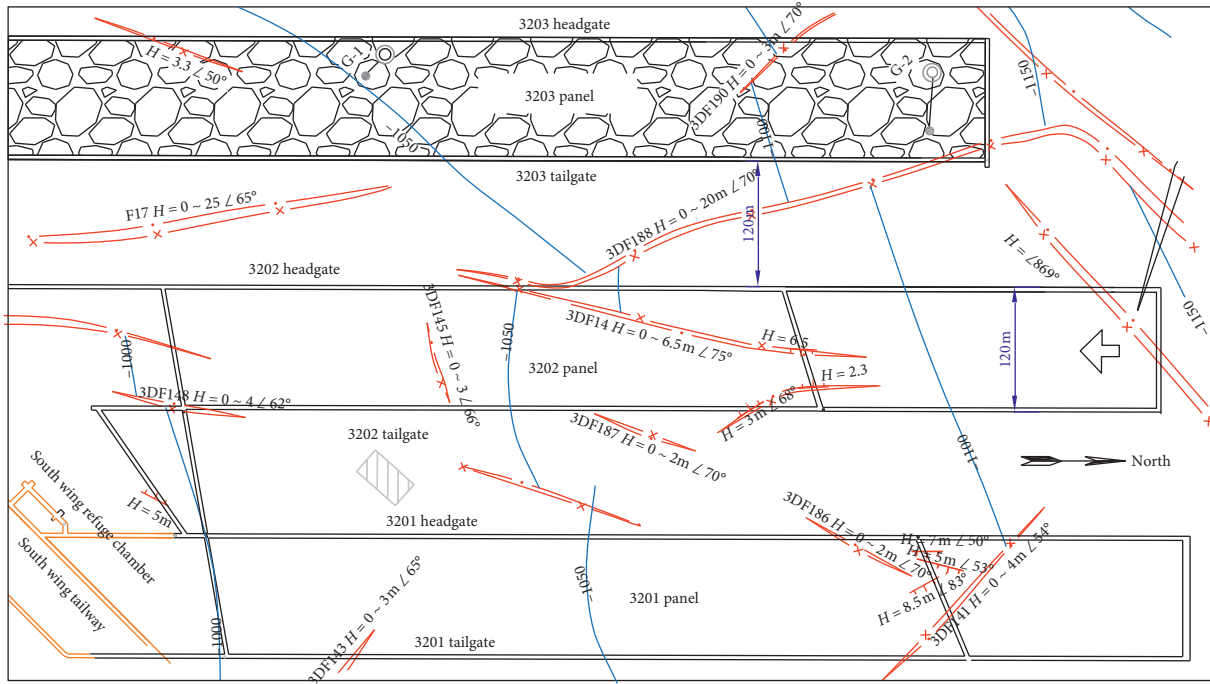


FIGURE 2: Layout of the 3202 panel.

TABLE 1: Rockburst risk indexes of strip coal pillar.

Index	Risk classification standard		
	No rockburst tendency	Medium rockburst tendency	Strong rockburst tendency
Medium stiffness ratio of the elastic and plastic zone, k	$k \geq 1.46$	$0.7 < K < 1.46$	$k \leq 0.73$
Plastic zone width ratio, a_Y	$a_Y \leq 35.4\%$	$35.4\% < a_Y < 41.5\%$	$a_Y \geq 41.5\%$
Elastic deformation index of the core zone, U_q	$U_q \leq 0.7$	$0.7 < U_q < 0.83$	$0.83 \leq U_q < 1$

applied to the top boundary of the model to simulate the self-weight of the overburden, and the horizontal side pressure coefficient is 0.5.

The model uses Mohr–Coulomb constitutive relations, and the mechanical properties applied in the model are listed in Table 2.

4.3.2. Evaluation of the Plastic Zone Width Ratio. When the width of the strip coal pillar is 120 m and the mining width of the 3202 panel varies from 76 m to 136 m, the plastic zone width ratio of the coal pillar is shown in Figure 3.

As shown in Figure 3, when the mining width of the working face is 76 m and 96 m, the plastic zone width of the strip coal pillar is 40 m and a_Y is 33.3%. When the mining width of the working face is 116 m and 136 m, the plastic zone width of the coal pillar is 44 m and 56 m, respectively, and a_Y is 36.7% and 46.7%, respectively.

The relationship between a_Y and mining width is shown in equation (16). When the width of the strip coal pillar is fixed, a_Y increases exponentially with the increase of mining width:

$$a_Y = 0.323 + 0.000031e^{0.0062a}, \quad (16)$$

$$R^2 = 0.989.$$

According to equation (16), when the mining width is less than 112 m, there is no rockburst tendency for the strip coal pillar; when the mining width is between 112 m and 128 m, there is medium rockburst tendency for the strip coal pillar; and when the mining width is greater than 128 m, there is strong rockburst tendency for the strip coal pillar.

When the mining width of the 3202 panel is 116 m and the width of the strip coal pillar varies from 60 m to 120 m, the plastic zone width ratio of the coal pillar is shown in Figure 4. When the width of the strip coal pillar is 60 m, the whole coal pillar has a plastic failure and a_Y is 100%. When the mining width is fixed, the plastic zone of strip coal pillar decreases with the increase of the width of the coal pillar. When the width of the strip coal pillar is 80 m, 100 m, and 120 m, the plastic zone width of the coal pillar is 60 m, 44 m, and 44 m, respectively, and a_Y is 75.0%, 44.0%, and 36.7%, respectively.

As shown in Figure 4, the relationship between a_Y and the width of the strip coal pillar is shown in equation (17).

TABLE 2: Physical and mechanical parameters of the rock mass.

Lithology	Thickness (m)	Bulk modulus (GPa)	Shear modulus (GPa)	Cohesion (MPa)	Tensile strength (MPa)	Friction angle (°)
Siltstone	17	7.3	5.1	3.2	2.8	27
Fine sandstone	15	9.2	7.7	3.5	3.2	29
Sandy mudstone	3.4	4.7	2.83	2.7	2.21	31.4
Fine sandstone	5	9.2	7.7	3.5	3.2	29
Medium sandstone	19	11.8	8.1	4.3	4.84	34.1
Sandy mudstone	2	4.7	2.83	2.7	2.21	31.4
#3 coal	9	2.1	1.78	1.8	1.25	25
Sandy mudstone	2.3	4.7	2.83	2.7	2.21	31.4
Medium sandstone	21	11.8	8.1	4.3	4.84	34.1

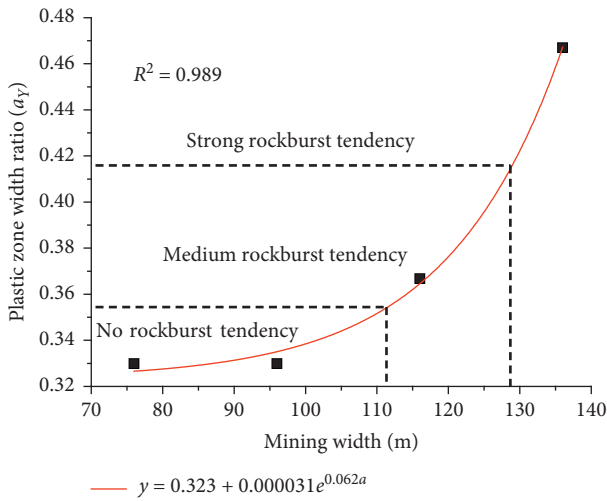


FIGURE 3: Fitting relationship of plastic zone width ratio and mining width.

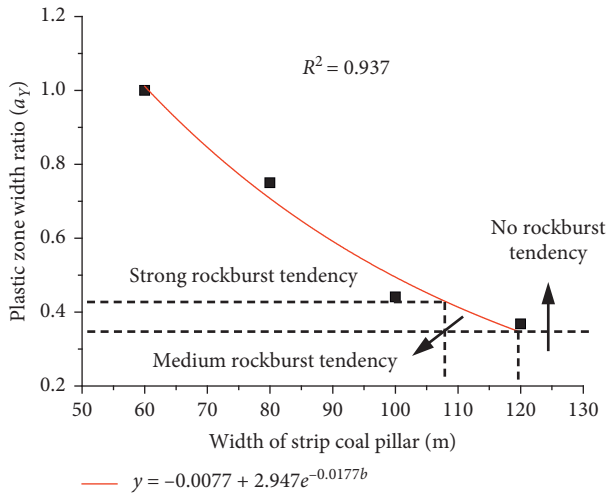


FIGURE 4: Fitting relationship of plastic zone width ratio and strip coal pillar.

When the mining width of the 3202 panel is fixed, a_Y decreases exponentially with the increase of the coal pillar width:

$$a_Y = -0.0077 + 2.947e^{-0.0177b}, \quad (17)$$

$$R^2 = 0.937.$$

According to equation (17), when the width of strip coal pillar is less than 108 m, there is strong rockburst tendency for the strip coal pillar; when the width of strip coal pillar is between 108 m and 120 m, there is medium rockburst tendency for the coal pillar; and when the width of strip coal pillar is greater than 120 m, there is no rockburst tendency for the coal pillar.

4.3.3. Evaluation of the Elastic Deformation Index. In the numerical simulation, the compression of the strip coal pillar is obtained by measuring the subsidence of the coal pillar roof. When the width of the strip coal pillar is 120 m, the compression of the coal pillar with different mining widths is shown in Figure 5.

It can be seen from Figure 5 that with the increase of mining width, the compression of the coal pillar keeps increasing gradually.

When the mining width is 76 m, 96 m, and 116 m, respectively, U_0 is 0.061 m, 0.066 m, and 0.072 m, respectively, and U_q is 0.709, 0.767, and 0.837, respectively. When the mining width is 136 m, u_0 reaches 0.129 m, and U_q increases to 1.5. As shown in Figure 6, the relationship between the U_q and the mining width is shown in

$$U_q = 0.725 + 0.0000022e^{0.094a}, \quad (18)$$

$$R^2 = 0.993.$$

According to equation (18), when the mining width is less than 76 m, there is no rockburst tendency for the coal pillar; when the mining width is between 76 m and 116 m, there is medium rockburst tendency for the coal pillar; when the mining width is between 116 m and 126 m, there is strong rockburst tendency for the coal pillar; and when the mining width is greater than 126 m, the rockburst has occurred, and U_q increases rapidly which can be shown in Figure 6.

When the mining width of the 3202 panel is 116 m and the width of the strip coal pillar varies from 60 m to 120 m, the compression of the coal pillar is shown in Figure 7.

It can be seen from Figure 7 that with the decrease of the width of strip coal pillar, the compression of the coal pillar keeps increasing gradually. When the width of the strip coal

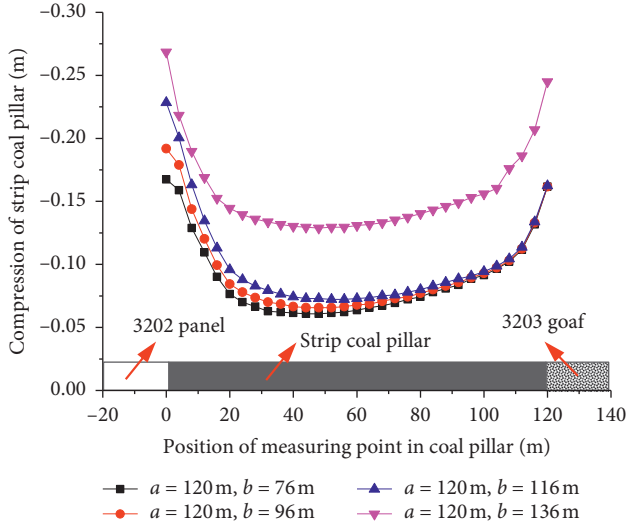


FIGURE 5: Compression of strip coal pillar under different mining widths.

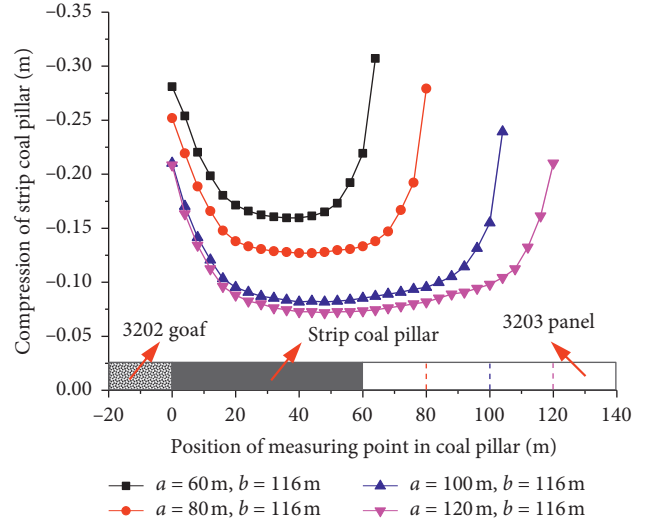


FIGURE 7: Compression of strip coal pillar under different coal pillar widths.

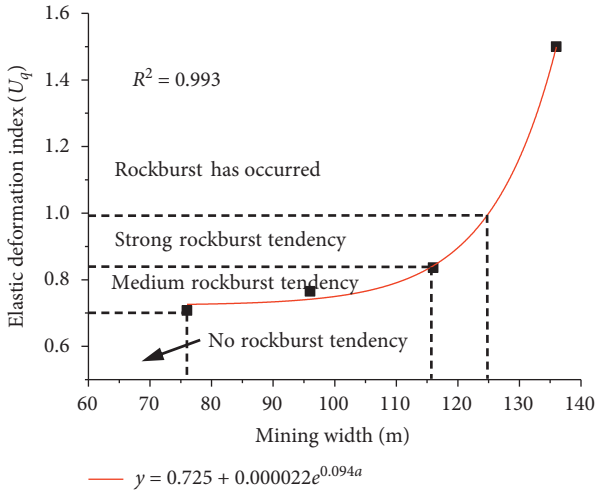


FIGURE 6: Fitting relationship of elastic deformation index of kernel zone and mining width.

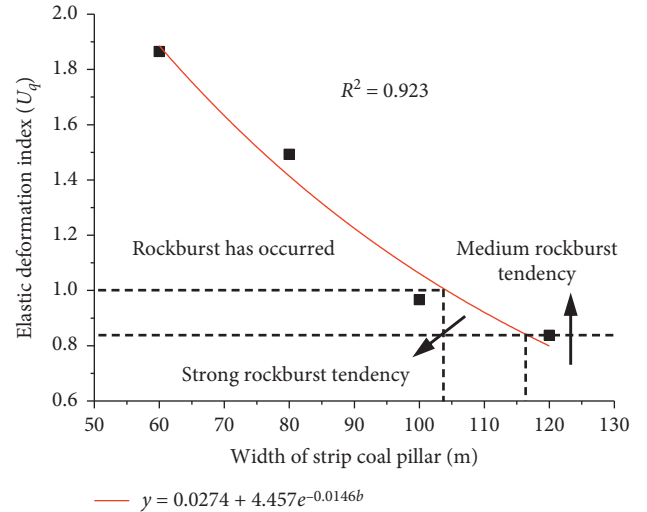


FIGURE 8: Fitting relationship of U_q and the width of the coal pillar.

pillar is 120 m and 100 m, respectively, u_0 is 0.072 m and 0.083 m, respectively, and U_q is 0.837 and 0.965, respectively. When the width of the coal pillar is 80 m and 60 m, respectively, u_0 is 0.128 m and 0.160 m, respectively, and U_q is 1.49 and 1.86, respectively. As shown in Figure 8, the relationship between U_q and the width of the coal pillar is shown in

$$U_q = 0.0274 + 4.457e^{-0.0146b}, \quad (19)$$

$$R^2 = 0.923.$$

According to equation (19), when the width of strip coal pillar is greater than 114 m, there is medium rockburst tendency for the coal pillar; when the width of strip coal

pillar is between 98 m and 114 m, there is strong rockburst tendency for the coal pillar; and when the width of strip coal pillar is less than 98 m, the rockburst has occurred, and U_q increases rapidly.

4.4. Comprehensive Evaluation Results. According to the above simulation results, the rockburst risk of strip coal pillar under different mining widths and the width of coal pillar conditions is shown in Figure 9. The results of rockburst risk evaluation in this paper are compared with those of the traditional rockburst tendency identification test in the laboratory, as shown in Table 3.

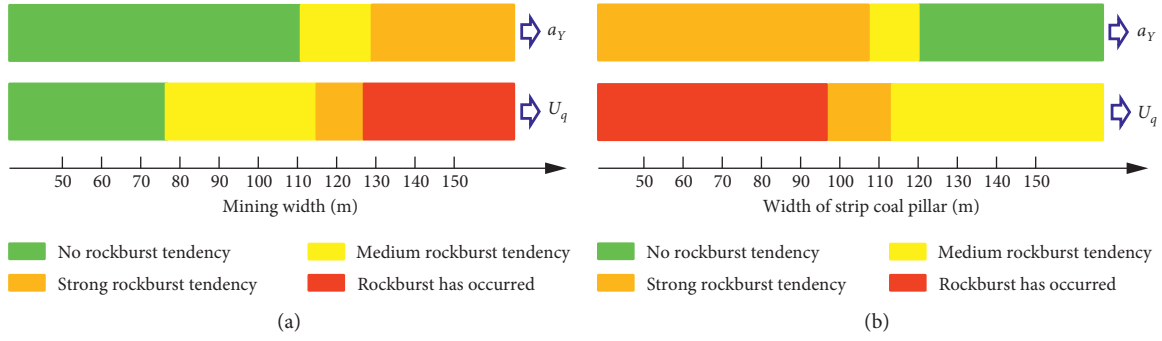


FIGURE 9: Rockburst risk under different mining widths and the width of strip coal pillar: (a) width of strip coal pillar is fixed as 120 m; (b) mining width is fixed as 120 m.

TABLE 3: Rockburst risk evaluation results of 3202 panel.

Classification	Index	Value	Evaluation conclusion
Traditional rockburst tendency identification test	Dynamic failure time, DT (ms)	56	Weak rockburst tendency
	Impact energy index, W_{ET}	5.32	Strong rockburst tendency
	Elastic energy index, K_E	4.65	Weak rockburst tendency
	Uniaxial compressive strength, R_C (MPa)	13.5	Weak rockburst tendency
Theoretical calculation results in this paper	k	0.207	Strong rockburst tendency
	a_Y	38.45%	Medium rockburst tendency
Numerical simulation results in this paper	a_Y	36.7%	Medium rockburst tendency
	U_q	0.837	Strong rockburst tendency

It can be seen from Figure 9 and Table 3 that under the same mining width and width of the coal pillar, the rockburst risk obtained by U_q is higher than the evaluation result of a_Y . For the sake of safety, the evaluation result of U_q is adopted. So, the strip coal pillar of the 3202 panel has a strong rockburst tendency.

As shown in Table 3, the result of the traditional rockburst tendency identification test of #3 coal in Gucheng Coal Mine is a weak rockburst tendency. Moreover, the comprehensive index method [34] is used to evaluate the rockburst risk of the 3202 panel, and the evaluation result shows that the 3202 panel is of medium rockburst tendency. However, the field monitoring results [35] showed that the deformation of the roadway on the side of the strip coal pillar was very serious, the maximum deformation was more than 1100 mm, large energy microseismic events gather relatively, and the rockburst risk of the coal pillar was high. It can be seen that the rockburst risk evaluation result in this paper is more in line with the actual situation. Therefore, the rockburst risk evaluation indexes of strip coal pillar proposed in this paper are more accurate and reasonable.

According to Figure 9, from the perspective of reducing the rockburst risk, for the strip mining of Gucheng Coal Mine, when the mining width of the working face is 116 m, the width of strip coal pillar cannot be less than 98 m. The width of strip coal pillar of the 3202 panel is 120 m, which meets the above requirements. Therefore, the rockburst risk of the coal pillar of the 3202 panel is relatively low.

5. Conclusions

- (1) The traditional test method of coal and rockburst risk ignores the influence of coal pillar geometry size, and the evaluation results have little significance for the field guidance of deep strip mining. Considering the influence of mining width and coal pillar width in strip mining, three new indexes were put forward to evaluate the rockburst risk of deep strip mining, namely, the medium stiffness ratio (k) of the elastic and plastic zone in coal pillar, the plastic zone width ratio (a_Y), and the elastic deformation index (U_q) of the core zone.
- (2) The stiffness ratio index (k) of the elastic-plastic zone indicates the degree of strain-softening during the loading process of strip coal pillar. The plastic zone width ratio (a_Y) of strip coal pillar can be measured by the drilling cutting method, which has strong field operability. And the elastic deformation index (U_q) indirectly reflects the relationship between the deformation energy accumulation of strip coal pillar and the critical state of rockburst. For these three indexes, the larger the index value is, the greater the rockburst risk is.
- (3) According to the new evaluation indexes of this paper, the strip coal pillar of the 3202 panel of Gucheng Coal Mine is in danger of strong rockburst. Compared with the results of the traditional

rockburst tendency identification test and comprehensive index method, the evaluation result in this paper is more in line with the actual situation.

- (4) From the point of view of prevention and control of rockburst, the design principle of strip mining in Gucheng Coal Mine is put forward; that is, when the mining width of the working face is 116 m, the width of the strip coal pillar cannot be less than 98 m.

Data Availability

All data supporting this study are included within the article.

Conflicts of Interest

The authors declare no conflicts of interest.

Acknowledgments

This work was supported by the Shandong Provincial Natural Science Foundation, China (ZR2019BEE001, ZR2018MEE009) and Key Research and Development Projects of Shandong Province, China (2019GSF111038).

References

- [1] Z. Wen, E. Xing, S. Shi, and Y. Jiang, "Overlying strata structural modeling and support applicability analysis for large mining-height stopes," *Journal of Loss Prevention in the Process Industries*, vol. 57, pp. 94–100, 2019.
- [2] S. Hu, Y. Tan, H. Zhou et al., "Anisotropic modeling of layered rocks incorporating planes of weakness and volumetric stress," *Energy Science & Engineering*, vol. 8, no. 3, pp. 789–803, 2020.
- [3] N. Jiang, C. Wang, H. Pan, D. Yin, and J. Ma, "Modeling study on the influence of the strip filling mining sequence on mining-induced failure," *Energy Science & Engineering*, vol. 8, no. 6, pp. 2239–2255, 2020.
- [4] Y. Wang, B. Liu, and Y. Qi, "A risk evaluation method with an improved scale for tunnel engineering," *Arabian Journal for Science and Engineering*, vol. 43, no. 4, pp. 2053–2067, 2018.
- [5] W. P. Huang, C. Li, L. W. Zhang, Q. Yuan, Y. S. Zheng, and Y. Liu, "In situ identification of water-permeable fractured zone in overlying composite strata," *International Journal of Rock Mechanics and Mining Sciences*, vol. 105, pp. 85–97, 2018.
- [6] F. X. Jiang, J. L. Wen, W. S. Bai, G. L. Wang, and M. Li, "Rock burst risk in surrounding abscission layer of overlying high key strata in deep strip mining mines," *Journal of China University of Mining and Technology*, vol. 47, no. 1, pp. 40–47, 2018.
- [7] J. Wang, P. Qiu, J. Ning, L. Zhuang, and S. Yang, "A numerical study of the mining-induced energy redistribution in a coal seam adjacent to an extracted coal panel during longwall face mining: a case study," *Energy Science & Engineering*, vol. 8, no. 3, pp. 817–835, 2020.
- [8] Q. Liu, J. Chai, S. Chen, D. Zhang, Q. Yuan, and S. Wang, "Monitoring and correction of the stress in an anchor bolt based on pulse pre-pumped Brillouin optical time domain analysis," *Energy Science & Engineering*, vol. 8, no. 6, pp. 2011–2023, 2020.
- [9] G. C. Zhang, Z. J. Wen, S. J. Liang et al., "Ground response of a gob-side entry in a longwall panel extracting 17 m-thick coal seam: a case study," *Rock Mechanics and Rock Engineering*, vol. 53, no. 2, pp. 497–516, 2020.
- [10] G. C. Zhang, L. J. Chen, Z. J. Wen et al., "Squeezing failure behavior of roof-coal masses in a gob-side entry driven under unstable overlying strata," *Energy Science and Engineering*, vol. 8, no. 1, 2020.
- [11] T.-B. Zhao, W.-Y. Guo, Y.-L. Tan, C.-P. Lu, and C.-W. Wang, "Case histories of rock bursts under complicated geological conditions," *Bulletin of Engineering Geology and the Environment*, vol. 77, no. 4, pp. 1529–1545, 2018.
- [12] P. X. Zhao, S. G. Li, C. Ho, H. F. Lin, and R. S. Zhuo, "Crack propagation and material characteristics of rocklike specimens subject to different loading rates," *Journal of Materials in Civil Engineering*, vol. 31, no. 7, pp. 1–17, 2019.
- [13] Y. D. Jiang and Y. X. Zhao, "State of the art: investigation on mechanism, forecast and control of coal bumps in China," *Chinese Journal of Rock Mechanics and Engineering*, vol. 34, no. 11, pp. 2188–2204, 2015.
- [14] Y. Tan, D. Fan, X. Liu, S. Song, X. Li, and H. Wang, "Numerical investigation of failure evolution of the surrounding rock of a super-large section chamber group in a deep coal mine," *Energy Science & Engineering*, vol. 7, no. 6, pp. 3124–3146, 2019.
- [15] J. M. Yao, Y. Y. Yan, S. Z. Li, J. W. Yang, and X. Wang, "Damage index of coal seam rock burst proneness," *Journal of China Coal Society*, vol. 36, no. S2, pp. 353–357, 2011.
- [16] C. D. Su, B. B. Gao, R. F. Yuan, and J. Yang, "Outburst-proneness index and their correlation analysis of coal seams in Pingdingshan mine area," *Journal of China Coal Society*, vol. 39, no. S1, pp. 8–14, 2014.
- [17] Y. S. Pan, L. Geng, and Z. H. Li, "Research on evaluation indices for impact tendency and danger of coal seam," *Journal of China Coal Society*, vol. 35, no. 12, pp. 1975–1978, 2010.
- [18] B. Y. Jiang, L. G. Wang, Y. L. Lu, C. Q. Wang, and D. Ma, "Combined early warning method for rockburst in a deep island, fully mechanized caving face," *Arabian Journal of Geosciences*, vol. 9, no. 20, p. 743, 2016.
- [19] Z. Zhang, M. Deng, J. Bai, X. Yu, Q. Wu, and L. Jiang, "Strain energy evolution and conversion under triaxial unloading confining pressure tests due to gob-side entry retained," *International Journal of Rock Mechanics and Mining Sciences*, vol. 126, Article ID 104184, 2020.
- [20] T. B. Zhao, W. Zhang, and W. Y. Guo, "Digital image correlation analysis of displacement based on corrected three surface fitting algorithm," *Complexity*, vol. 2019, Article ID 4620858, 9 pages, 2019.
- [21] J. Wang, J. G. Ning, J. Q. Jiang, and T. T. Bu, "Structural characteristics of strata overlying of a fully mechanized longwall face: a case study," *Journal of the Southern African Institute of Mining and Metallurgy*, vol. 118, pp. 1195–1204, 2018.
- [22] J. Wang, J. G. Ning, P. Q. Qiu, S. Yang, and H. F. Shang, "Microseismic monitoring and its precursory parameter of hard roof collapse in longwall faces: a case study," *Geomechanics and Engineering*, vol. 17, no. 4, pp. 375–383, 2019.
- [23] C.-P. Lu, Y. Liu, N. Zhang, T.-B. Zhao, and H.-Y. Wang, "In-situ and experimental investigations of rockburst precursor and prevention induced by fault slip," *International Journal of Rock Mechanics and Mining Sciences*, vol. 108, pp. 86–95, 2018.
- [24] C.-P. Lu, B. Liu, B. Liu, Y. Liu, H.-Y. Wang, and H. Zhang, "Anatomy of mining-induced fault slip and a triggered rockburst," *Bulletin of Engineering Geology and the Environment*, vol. 78, no. 7, pp. 5147–5160, 2019.

- [25] T. B. Zhao, Y. C. Yin, and Y. L. Tan, "Safe mining and new prediction model in coal seam with rock burst induced by roof," *Disaster Advances*, vol. 5, no. 4, pp. 691–695, 2012.
- [26] W. L. Yang, F. X. Jiang, J. L. Wen, Y. Liu, and Q. D. Wei, "Study on mechanisms of rock burst induced by a left coal pillar and prevention technology," *Journal of Mining and Safety Engineering*, vol. 31, no. 6, pp. 876–880, 2014.
- [27] Y. Tan, W. B. Guo, and Y. H. Zhao, "Engineering stability and instability mechanism of strip Wongawilli coal pillar system based on catastrophic theory," *Journal of China Coal Society*, vol. 41, no. 7, pp. 1667–1674, 2016.
- [28] B.-Y. Jiang, S.-T. Gu, L.-G. Wang, G.-C. Zhang, and W.-S. Li, "Strainburst process of marble in tunnel-excavation-induced stress path considering intermediate principal stress," *Journal of Central South University*, vol. 26, no. 4, pp. 984–999, 2019.
- [29] Q. L. Zhang, X. G. Cao, Y. L. Wang, and L. H. Qiang, "Stability analysis of stope roof-pillar based on cusp catastrophe model," *China Safety Science Journal*, vol. 21, no. 10, pp. 52–57, 2011.
- [30] Y. L. Tan, C. X. Liu, and T. B. Zhao, *On Nonlinear Rock Mechanics*, China Coal Industry Publishing House, Beijing, China, 2008.
- [31] Y. S. Pan and M. T. Zhang, "The study of coalburst by catastrophic theory," *Journal of Fuxin Mining Institute*, vol. 11, no. 1, pp. 12–18, 1992.
- [32] Q. X. Qi and L. M. Dou, *Theory and Technology of Rockburst*, China University of mining and Technology Press, Xuzhou, China, 1997.
- [33] Q. X. Qi, Y. W. Peng, H. Y. Li, J. Q. Li, Y. G. Wang, and C. R. Li, "Study of bursting liability of coal rock," *Chinese Journal of Rock Mechanics and Engineering*, vol. 30, no. S1, pp. 2736–2742, 2011.
- [34] O. Y. Zhenhua, G. H. Zhang, H. Y. Qin, R. Peng, and X. H. Liu, "Improved comprehensive index evaluation method and its application on rockburst hazard of gas coal seam," *Coal Science and Technology*, vol. 46, no. 10, pp. 30–36, 2018.
- [35] J. L. Wen, *Rockburst Mechanism of Skip Mining in Deep Coal Mines and its Application*, Doctoral thesis, University of Science and Technology Beijing, Beijing, China, 2018.

Research Article

Controlling Mechanism of Rock Burst by CO₂ Fracturing Blasting Based on Rock Burst System

Tianwei Lan,^{1,2} Chaojun Fan ,¹ Jun Han,¹ Hongwei Zhang,¹ and Jiawei Sun¹

¹College of Mining, Liaoning Technical University, Fuxin 123000, China

²Key Laboratory of Mining Disaster Prevention and Control, Qingdao 266590, China

Correspondence should be addressed to Chaojun Fan; chaojunfan@139.com

Received 27 April 2020; Revised 28 July 2020; Accepted 5 August 2020; Published 27 August 2020

Academic Editor: Caiping Lu

Copyright © 2020 Tianwei Lan et al. This is an open access article distributed under the Creative Commons Attribution License, which permits unrestricted use, distribution, and reproduction in any medium, provided the original work is properly cited.

Rock burst induced by mining is one of the most serious dynamic disasters in the process of coal mining. The mechanism of a rock burst is similar to that of a natural earthquake. It is difficult to accurately predict the “time, space, and strength” of rock burst, but the possibility of rock burst can be predicted based on the results of microseismic monitoring. In this paper, the rock burst system under the tectonic stress field is established based on the practice of coal mining and the result of mine ground crustal stress measurement. According to the magnitude of microseismic monitoring, the amount of the energy and spatial position of the rock burst are determined. Based on the theory of explosion mechanics, aiming at the prevention and control of rock burst in the coal mine, the technique of liquid CO₂ fracturing blasting is put forward. By the experiment of blasting mechanics, the blasting parameters are determined, and the controlling mechanism of rock burst of liquid CO₂ fracturing blasting is revealed. The application of liquid CO₂ fissure blasting technology in the prevention and control of rock burst in Jixian Coal Mine shows that CO₂ fracturing blasting reduces the stress concentration of the rock burst system and transfers energy to the deeper part, and there is no open fire in the blasting. It is a new, safe, and efficient method to prevent and control rock burst, which can be applied widely.

1. Introduction

Rock burst is one of the most serious dynamic disasters in coal mining. Both rock burst and natural earthquake are dynamic disasters caused by the crack and instability of crustal rock mass, resulting in the release of energy. The occurrence mechanisms of the two are similar and they are difficult to be predicted [1–4]. The research on the mechanism of rock burst has always been an unsolved scientific problem that has been discussed for a long time in the fields of mining engineering and rock mechanics [5–10]. The application of CT scanning, 3D printing, big data, cloud computing, Internet of things, and other emerging technologies in the study of coal mine rock burst has become a hot topic in mining research [11–14]. The monitoring and warning methods of rock burst mainly include microseismic monitoring method, electromagnetic radiation method, AE method, mining stress monitoring method, and drilling cuttings method. Through the analysis of monitoring data,

the possibility of rock burst can be predicted, but the accuracy still needs to be further improved [15–19]. For the prevention of rock burst, there are two aspects: regional prevention and local risk relief, including protection layer mining, borehole pressure relief, coal seam water injection, pressure relief blasting, liquid CO₂ fracturing blasting, hydraulic fracturing, and other methods [20–23]. Through the implementation of risk relief measures, the risk of rock burst is reduced. But the exact location of the rock burst cannot be determined; it leads to the heavy workload and material consumption. If the structure and energy characteristics of coal and rock mass can be predicted and preventive measures can be taken according to the predicted results, the prevention level of rock burst will be improved and the cost of risk relief will be reduced.

The gestation and generation of rock burst can be affected by the stress concentration degree and energy storage size of the regional coal-rock mass structure system, and the coal-rock mass system should have a certain scale range

[24, 25]. In order to study the structure system and energy characteristics of rock mass under rock burst, a rock burst system based on the tectonic stress field is established. The energy magnitude and spatial location of rock burst system are determined by microseismic monitoring technology. Based on the established rock burst system, the liquid CO₂ fracturing blasting technology is put forward. The practice of preventing and controlling rock burst in coal mine shows that the CO₂ fracturing blasting reduces the stress concentration of the rock burst system and transfers the energy to the deeper part. It is a new, safe, and efficient technology to prevent rock burst.

2. Analysis of Energy in Rock Burst System

2.1. Establishment of Rock Burst System. The complexity of rock burst is related to the heterogeneity, anisotropy, and diversity of influencing factors of the structure system of coal and rock mass. The stress and energy of coal and rock mass system are the basic conditions, and the mining engineering activities are the induced conditions. More than 85% of the energy causing rock burst comes from surrounding rock. The coal mainly provides the medium condition for rock burst. The space of energy storage-exchange-release of coal and rock mass system with rock burst should have a certain scale, which cannot be infinitely great or infinitely small, and should be related to the structure, stress, and energy level in the coal and rock mass system. A model of rock burst system, which reflects the relation of the coal and rock mass system and rock burst, is established. The shape of the model is assumed to be spherical, hereinafter referred to as the rock burst system (Figure 1).

2.2. Analysis of Energy in Rock Burst System. According to the theory of elasticity, a representative element of rock mass at the depth H in the crustal rock mass is subjected to three-dimensional stress, and the unit body is in the state of elastic deformation (Figure 2). The elastic energy of unit volume accumulation under in situ stress field can be expressed by the following formula:

$$U_0 = \frac{1}{2E} [\sigma_1^2 + \sigma_2^2 + \sigma_3^2 - 2\mu(\sigma_1\sigma_2 + \sigma_2\sigma_3 + \sigma_1\sigma_3)], \quad (1)$$

where U_0 represents elastic energy accumulated in unit volume, J; σ_1 , σ_2 , and σ_3 represent principal stress in three directions of any unit, MPa; E represents modulus of elasticity, MPa; μ represents Poisson's ratio.

Then, the energy for the spherical rock burst system can be expressed:

$$U = \frac{1}{2E} [\sigma_1^2 + \sigma_2^2 + \sigma_3^2 - 2\mu(\sigma_1\sigma_2 + \sigma_2\sigma_3 + \sigma_1\sigma_3)] \frac{4}{3} \pi R^3, \quad (2)$$

where U represents the energy of rock burst system, J; R represents the radius of rock burst system, m.

According to the in situ stress measurement results of some rock burst mines in China, the stress fields in most (almost all) areas are horizontal compressive tectonic stress

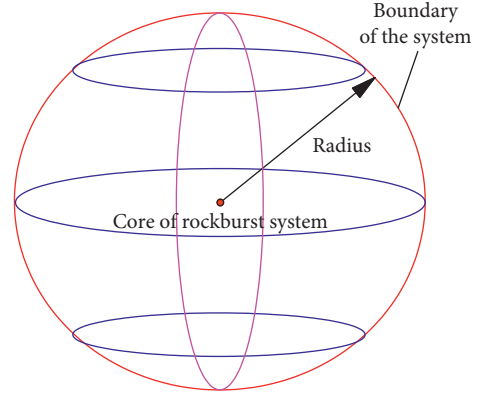


FIGURE 1: Schematic diagram of "spherical" type rock burst system.

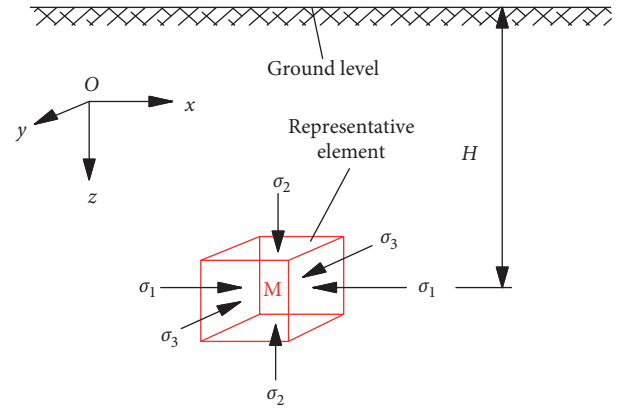


FIGURE 2: Representative element under the action of three-dimensional stress.

fields. The change of maximum principal stress direction and magnitude in most parts of China is due to the collision of the Chinese mainland plate by the India plate and Eurasian plate and the subduction of the eastern Pacific plate and the Philippines plate to Eurasia. In the vast majority of areas, the in situ stress is a three-dimensional unequal compressive stress field dominated by horizontal stress. The magnitude and direction of the three principal stresses vary with space and time, so they are unstable stress fields. The measured data show that the vertical stress is basically equal to the weight of overlying strata. The deviation between the vertical stress direction and the vertical direction is generally no more than 20°. The measured data show that there are two principal stresses in the horizontal or nearly horizontal plane in most (almost all) regions, and the angle between the two principal stresses and the horizontal plane is generally no more than 30°.

The dip angles of the maximum and minimum principal stresses σ_1 and σ_3 are near horizontal direction. The maximum horizontal stress σ_1 is generally larger than the vertical stress σ_2 , and there are certain linear relationships between σ_1 , σ_2 , and σ_3 and self-weight stress γH , and they are usually $\sigma_1 \approx 2\gamma H$, $\sigma_2 \approx \gamma H$, and $\sigma_3 \approx 0.7\gamma H$. The energy of rock burst system related to self-weight stress can be obtained by substituting them into formula (2).

$$U = \frac{2\pi}{3E} (5.49 - 8.2\mu)\gamma^2 H^2 R^3. \quad (3)$$

2.3. Analysis of Scale in Rock Burst System. When the energy stored in the rock burst system reaches the critical state of the energy required for the occurrence of the rock burst, mining engineering activities induce the instability of the rock burst system, and the instantaneous release of energy causes the rock burst. So, the rock burst is a nonlinear dynamic process of energy accumulation in steady state and energy release in a nonsteady state in the deformation process of rock burst system.

The energy of rock burst ΔU is provided by the rock burst system, which is usually determined by the difference between the energy of tectonic stress field U_G and the energy of gravity stress field U_Z . By calculation,

$$\begin{cases} U_Z = \frac{2\pi}{3E} \left(\frac{1-2\mu^2-\mu}{1-\mu} \right) \gamma^2 H^2 R^3, \\ U_G = \frac{2\pi}{3E} (5.49 - 8.2\mu) \gamma^2 H^2 R^3. \end{cases} \quad (4)$$

Then,

$$\Delta U = U_G - U_Z = \frac{2\pi(10.2\mu^2 - 12.69\mu + 4.49)\gamma^2 H^2 R^3}{3E(1-\mu)}. \quad (5)$$

Therefore, we can obtain the radius of the rock burst system as

$$R = \sqrt[3]{\frac{3E(1-\mu)\Delta U}{2\pi(10.2\mu^2 - 12.69\mu + 4.49)\gamma^2 H^2}}. \quad (6)$$

Rock burst and natural earthquake are both dynamic disasters caused by the crack and instability of crustal rock mass. It can also be considered that rock burst is an earthquake induced by mining. In seismology, the energy to produce an earthquake can be determined by Gutenberg's and Kanamori's empirical formulas of energy magnitude. The principle of microseismic monitoring is similar to that of earthquake prediction and has been widely used in the monitoring of rock burst in coal mines. By analyzing seismic wave signals, the position, magnitude, and energy of the rock burst can be determined. Therefore, according to the magnitude of microseismic monitoring, the relationship between energy and magnitude can be established, and the scale range of rock burst system can be determined.

$$\Delta U = 10^{1.695M_L+3.18}. \quad (7)$$

ΔU is the energy released by a rock burst, J ; M_L is magnitude.

$$R = \sqrt[3]{\frac{3E(1-\mu) \cdot 10^{1.695M_L+3.18}}{2\pi(10.2\mu^2 - 12.69\mu + 4.49)\gamma^2 H^2}}. \quad (8)$$

3. The Working Principle of Liquid CO₂ Fracturing Blasting

3.1. Structure of CO₂ Cracker. Liquid CO₂ fracturing blasting technology is mainly used in coal mines to increase the permeability of coal seams and gas extraction efficiency [26, 27]. It is rare to apply liquid CO₂ fracturing blasting technology to rock burst prevention and control. Compared with the traditional explosive technology, the liquid CO₂ fracturing technology has no open fire and can be relatively safe in the process of blasting, and the pressure relief effect is remarkable. The CO₂ cracker is mainly composed of a filling valve, a heating pipe, the main pipe, a sealing gasket, a shearing piece, and an energy release head (Figure 3).

3.2. The Working Principle of Liquid CO₂ Fracturing Blasting. When the temperature of liquid CO₂ is lower than 31°C or the pressure is greater than 7.35 MPa, it usually exists in liquid form. When the temperature of liquid CO₂ is higher than 31°C, it begins to gasify. Taking advantage of the phase transition characteristics of CO₂, liquid CO₂ was filled in the main pipe of the cracker, and the heat pipe was rapidly excited by the detonator. Liquid CO₂ was instantly gasified and expanded to generate high pressure. When the pressure reached the ultimate strength of the constant pressure shearing piece, the shearing piece was broken, and the high-pressure gas was released from the energy release head and then acts on the coal and rock mass, thus realizing the directional fracturing blasting on the coal and rock mass (Figure 4). The crushing zone, fracture zone, and vibration zone were formed successively from the center of the explosion position, so as to complete the pressure relief (Figure 5).

4. Test and Research on Liquid CO₂ Fracturing Blasting

4.1. Test Purpose and Determination of Parameters. Based on the theory of explosion mechanics, in order to determine the blasting effect of liquid CO₂ fracturing device, reasonable blasting parameters were determined through the experimental research of blasting mechanics. Pressure tests were carried out on the basic parameters of the fracturing blasting in the laboratory to determine the matching relationship between the crackers and borehole diameters, the stress at different positions in the boreholes during the blastings, and the impact on the blasting effect after hole sealing, so as to reveal the controlling mechanism of rock burst of liquid CO₂ fracturing blasting and provide a basis for the prevention and control of rock burst.

The parameters and specifications of liquid CO₂ fracturing blasting test devices are shown in Tables 1 and 2. Different crackers are placed in three different specifications of test devices for blasting test; YE5853-4CH signal amplifier and YE6231 data collector are used in the experiment to collect the pressure of CO₂ released during blasting on the pipe wall, and YE7600 software is used to process the data. Finally, the blasting parameters are determined by comparing and analyzing the pressure data.



FIGURE 3: Structure of CO₂ cracker. 1, filling valve; 2, heating pipe; 3, main pipe; 4, sealing gasket; 5, shearing piece; 6, energy release head.

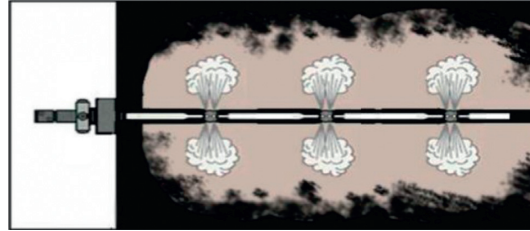


FIGURE 4: Sketch map of working principle of CO₂ cracker.

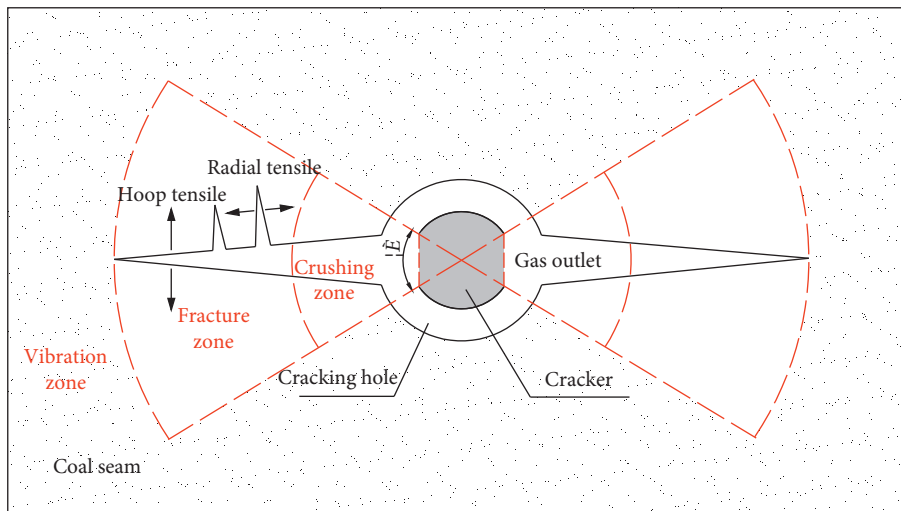


FIGURE 5: Sketch map of damage range of CO₂ cracker.

TABLE 1: Specifications and parameters of test devices.

	Bore (mm)	Length (mm)	Tube thickness (mm)
CSZZ-82/ 2500	82	2500	6.5
CSZZ-68/ 2500	68	2500	4.5
CSZZ-48/ 2500	48	2500	14.0

4.2. *Experiment Scheme and Design.* According to the purpose of the experiment, different specifications of crackers were selected and put into three different specifications of test devices for blasting test. Six experiment schemes were designed, and each scheme was tested three times. The design of the experiment scheme is shown in Table 3.

Before blasting, all the small holes in the pipe wall were opened, and the blasting power was controlled by controlling the strength of the shearing pieces. Sampling

frequency was set to 96 kHz, and pure cotton cloth was used to seal holes when the holes needed to be sealed. Force tests at different positions of the test device are shown in Figure 6.

4.3. *Analysis of Experiment Data.* According to the experimental schemes of liquid CO₂ fracturing blasting, ZLQ-38/300 was selected to blast in CSZZ-82/2500, and the strength of shearing piece in the cracker was 300 MPa. Four sensors were installed to test the force at different positions: the pressure sensor at point A is about 21 mm away from the energy release head of the cracker, which keeps level with the venting of the energy release head; the measuring points B and C were located at the top of the testing device, and the measuring point D was located at the tail of the testing device. The stress test data of different positions after liquid CO₂ blasting are shown in Figure 7.

Through the liquid CO₂ fracturing blasting test, it can be seen that the pressure at point A was the largest, and the pressure was above 200 MPa, which could meet the requirement of coal failure; the pressure at measuring points B,

TABLE 2: Specifications and parameters of liquid CO₂ crackers.

	Bore (mm)	Length of main pipe (mm)	Cartridge length (mm)	Material of shearing piece	Strength of shearing piece (MPa)	CO ₂ capacity (kg)
ZLQ-38/300	38	300	15	High strength alloy steel	200/300	0.234
ZLQ-38/600	38	600	15	High strength alloy steel	200/300	0.468

TABLE 3: Experiment schemes design.

Schemes	Specifications of test devices	Specifications of crackers	Sealed or not sealed	Number of sensors	Strength of shearing piece (MPa)	Spacing between hole wall and energy release head (mm)
No. 1	CSZZ-82/2500	ZLQ-38/300	Sealed	4	300	21
No. 2	CSZZ-82/2500	ZLQ-38/300	Sealed	2	300	21
No. 3	CSZZ-82/2500	ZLQ-38/300	No	2	300	21
No. 4	CSZZ-82/2500	ZLQ-38/300	Sealed	2	200	21
No. 5	CSZZ-68/2500	ZLQ-38/300	Sealed	2	200	17
No. 6	CSZZ-48/2500	ZLQ-38/300	Sealed	2	200	10

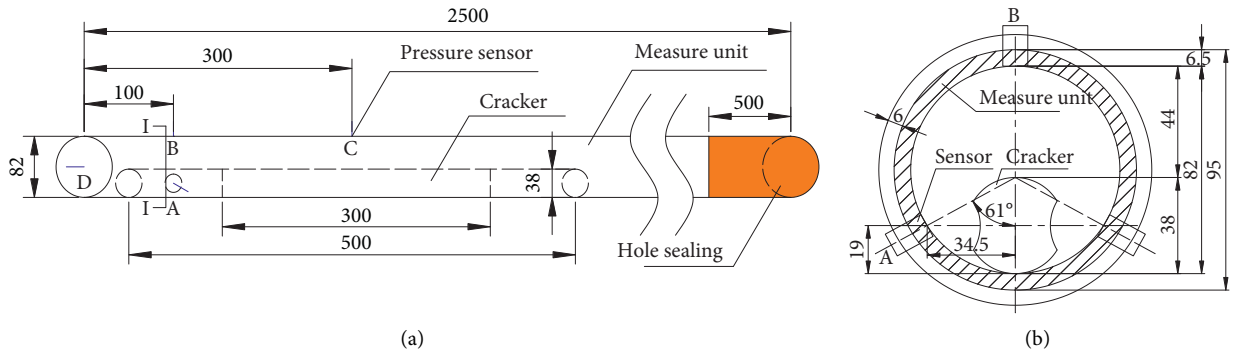
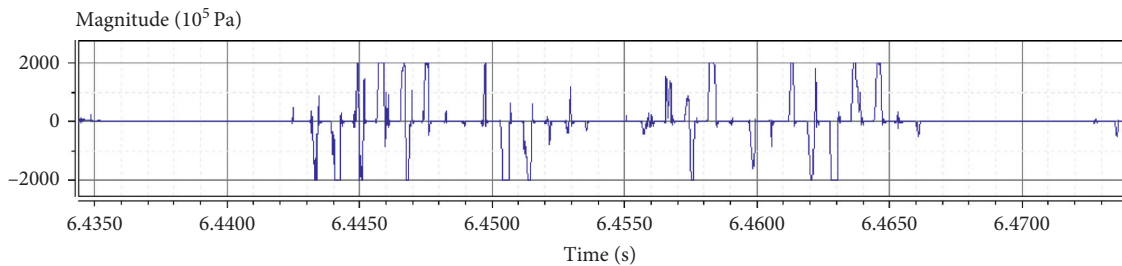
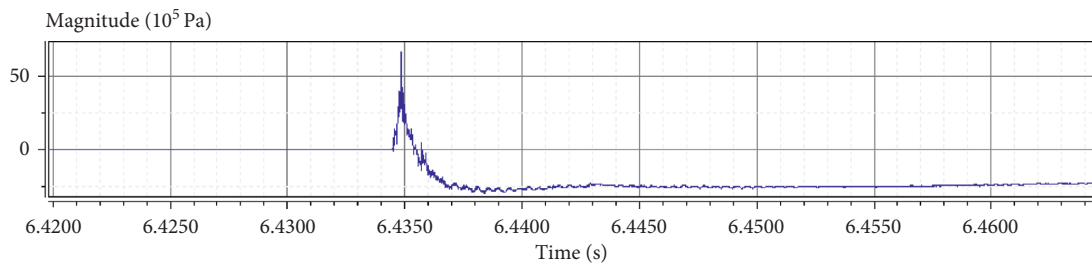


FIGURE 6: Diagram of force tests at different positions (length unit: mm).



(a)



(b)

FIGURE 7: Continued.

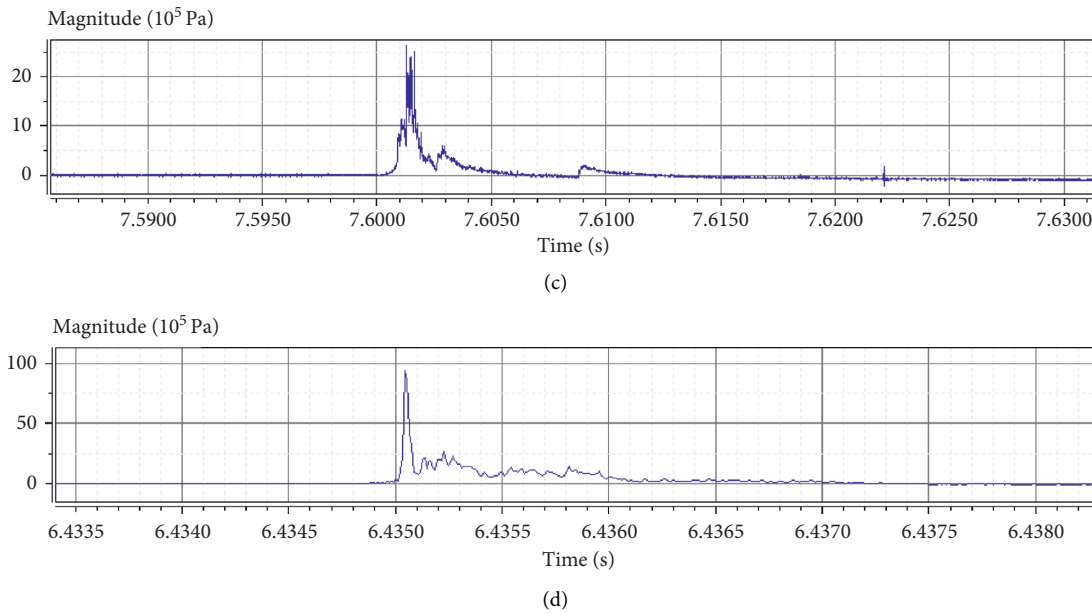


FIGURE 7: Waveforms of stress in different positions of CO₂ fracturing blasting. (a) The waveform of measuring point A (201.3 MPa). (b) The waveform of measuring point B (6.6 MPa). (c) The waveform of measuring point C (2.6 MPa). (d) The waveform of measuring point D (9.4 MPa).

C, and D was no more than 10 MPa, which did not meet the requirement of coal failure. Therefore, in the practice, the energy release head of the cracker should be directed to the risk relief area, and the radial level of the energy release head of the cracker must be maintained. It is suggested that the distance between the hole wall and the energy release head should be between 10 mm and 15 mm. For the area with a longer blasting range, multisection series blasting can be implemented.

5. Analysis of CO₂ Fracturing Blasting of Rock Burst System in Jixian Coal Mine

5.1. Analysis of Rock Burst System in Jixian Coal Mine. The rock burst in Jixian Coal Mine is serious, especially in the syncline axis of the No. 2 mining area in the deep mining area, where gas content is high, and multiple rock bursts occur continuously. The magnitude of rock burst monitored by microseism in the mine is mostly within the range of $M_L = 0.5-2.5$. On March 11, 2013, a rock burst with the magnitude of 1.5 occurred in the lower roadway of the left first working face in West No. 2 Mining Area. The rock burst caused the floor heave of the 15 m roadway outward from the coal wall of the working face. The range of 210 m to 270 m of the lower roadway was seriously damaged by the impact, and the adjacent working faces were all shocked. The rock burst location was vertically depth of $h = 700$ m from the surface, and the lithology of the floor was sandstone, $E = 21700$ MPa, and $\mu = 0.24$. According to formulas (5) and (6), the energy released by the “3.11” rock burst system in Jixian Coal Mine was $\Delta U = 5.3 \times 10^5$ J, and the radius of the rock burst system is 25.9 m (Figure 8).

When a rock burst occurs, after a period of energy transfer, exchange, supplement, and storage of the rock burst system, the energy reaches the critical energy of the next rock burst, and the rock burst will occur again under the influence of mining engineering. Therefore, in view of the “3.11” rock burst system of Jixian Coal Mine, the liquid CO₂ fracturing blasting method is chosen as the priority to relieve the pressure of rock burst system.

5.2. Analysis of CO₂ Fracturing Blasting Technology for Rock Burst System. According to the theoretical analysis of liquid CO₂ fracturing blasting and laboratory experiment results, multiple series blasting was carried out with crackers with specifications of ZLQ-38/300 and ZLQ-38/600. The weight of injected CO₂ was 0.17 kg and 0.26 kg, respectively, the diameter of the borehole was 50 mm, a total of 5 boreholes were constructed, the drilling spacing was 10 m, and the distance between the cracker and the borehole wall was 12 mm. Hole collapse occurred in the borehole after blasting. There were many broken coal blocks and the hole wall was rough, which contributed to the pressure relief for the rock burst pressure system (Figure 9).

The application of liquid CO₂ fracturing blasting technology in the prevention and control of rock burst in Jixian Coal Mine shows that CO₂ fracturing blasting reduces the stress concentration of rock burst system and transfers energy to the deeper part, and there is no open fire in blasting. It is a new, safe, and efficient technology to prevent rock burst, which can be applied widely.

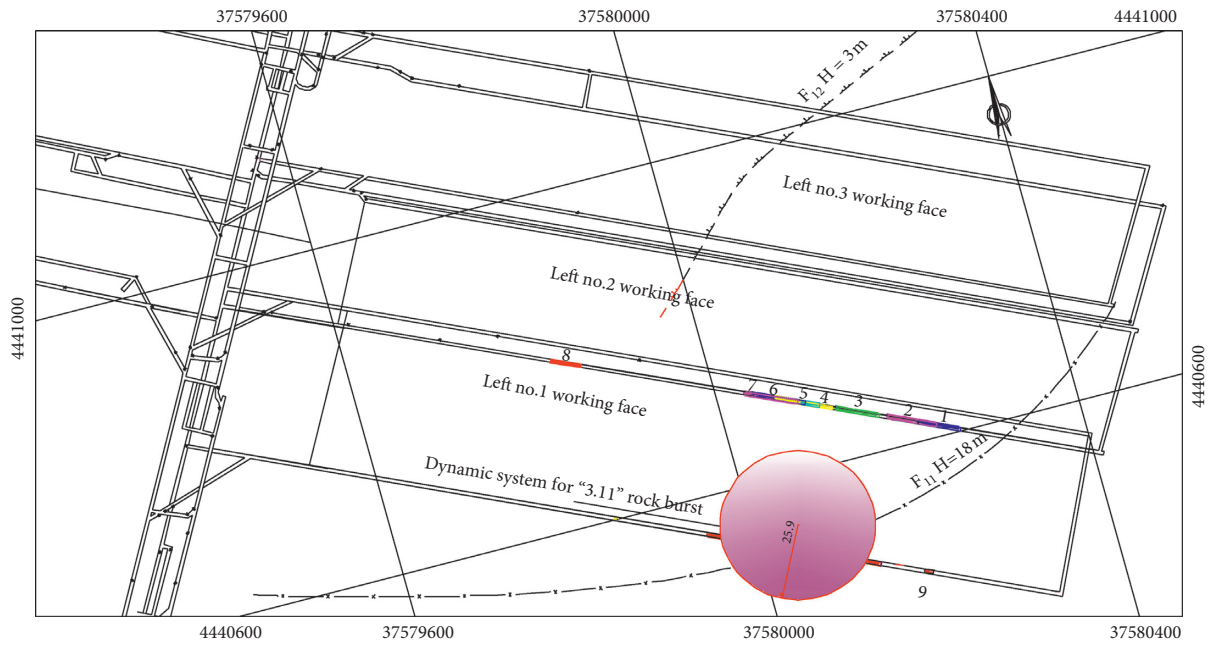


FIGURE 8: Dynamic system for "3.11" rock burst in Jixian Coal Mine.

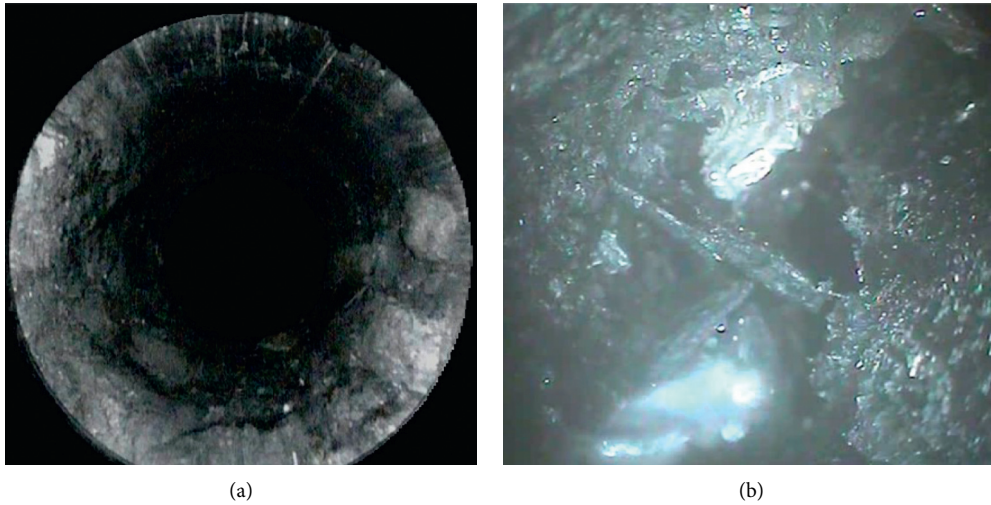


FIGURE 9: Borehole surface before and after liquid CO_2 fracturing blasting. (a) Before blasting. (b) After blasting.

6. Conclusions

- (1) It is difficult to accurately predict the "time, space, and intensity" of rock burst, but the possibility of rock burst can be predicted according to the results of microseismic monitoring. The relationship between rock burst and monitoring data of mine microseism is established.
- (2) The stress field of rock burst mine is mostly horizontal compression tectonic stress field. The rock burst system under the tectonic stress field is established. The energy criterion related to mining depth, system size, and medium properties of coal and rock mass is analyzed, and the critical energy condition is proposed.
- (3) According to the magnitude of microseismic monitoring, the relationship between the energy of rock burst and the radius of rock burst system is determined. It is revealed that the failure process of rock burst system is a nonlinear dynamic process of accumulating energy in stable state and releasing energy in unstable state.

- (4) The application of liquid CO₂ fracturing blasting technology in the prevention and control of “3.11” rock burst in Jixian Coal Mine shows that the application of liquid CO₂ fracturing blasting in the rock burst system reduces the stress concentration of the rock burst system and makes the energy transfer to the deeper part, and there is no open fire in the blasting process, which has a good pressure relief effect. It can be applied widely in the prevention and control of rock burst in coal mines.

Data Availability

The experimental data used to support the findings of this study are included within the article.

Conflicts of Interest

The authors declare no potential conflicts of interest with respect to the research, authorship, and/or publication of this article.

Acknowledgments

This research was funded by the Research Fund of Key Laboratory of Mining Disaster Prevention and Control (MDPC201926), the State Key Research Development Program of China (2017YFC0804209), and the National Natural Science Foundation of China (51604139).

References

- [1] H. Xie, J. Wang, G. Wang et al., “New ideas of coal revolution and layout of coal science and technology development,” *Journal of China Coal Society*, vol. 43, no. 5, pp. 1187–1197, 2018.
- [2] C. Fan, S. Li, D. Elsworth, J. Han, and Z. Yang, “Experimental investigation on dynamic strength and energy dissipation characteristics of gas outburst-prone coal,” *Energy Science & Engineering*, vol. 8, no. 4, pp. 1015–1028, 2020.
- [3] Q. Qi, H. Li, Z. Deng, S. Zhao et al., “Studying of standard system and theory and technology of rock burst in domestic,” *Coal Mining Technology*, vol. 22, no. 01, pp. 1–5, 2017.
- [4] L. Dou, “Induced shock and control of hard roof,” in *Proceedings of the 37th International Conference on Ground Control in Mining*, China, Xuzhou, July 2018.
- [5] T. Lan, C. Fan, H. Zhang et al., “Seepage law of injected water in the coal seam to prevent rock burst based on coal and rock system energy,” *Advances in Civil Engineering*, vol. 2018, Article ID 8687108, 9 pages, 2018.
- [6] Y. Pan, “Integrated study on compound dynamic disaster of coal-gas outburst and rockburst,” *Journal of China Coal Society*, vol. 41, no. 01, pp. 105–112, 2016.
- [7] Y. Jiang, Y. Pan, F. Jiang, L. Dou, and Ju Yang, “State of the art review on mechanism and prevention of coal bumps in China,” *Journal of China Coal Society*, vol. 39, no. 2, pp. 205–213, 2014.
- [8] Q. Qi, Z. Ouyang, H. Shankun, H. Li, X. Li, and N. Zhang, “Study on types of rock burst mine and prevention methods in China,” *Coal Science and Technology*, vol. 42, no. 10, pp. 1–5, 2014.
- [9] Y. Jiang and Y. Zhao, “State of the art: investigation on mechanism, forecast and control of coal bumps in China,” *Chinese Journal of Rock Mechanics and Engineering*, vol. 34, no. 11, pp. 2188–2204, 2015.
- [10] T. Lan, H. Zhang, J. Han, and W. Song, “Study on the rockburst mechanism based on geo-stress and rock mass energy principle,” *Journal of Mining & Safety Engineering*, vol. 29, no. 06, pp. 840–844, 2012.
- [11] Z. Ma, R. Gu, Z. Huang, G. Peng, L. Zhang, and D. Ma, “Experimental study on creep behavior of saturated disaggregated sandstone,” *International Journal of Rock Mechanics and Mining Sciences*, vol. 66, pp. 76–83, 2014.
- [12] M. Birk, R. Dapp, N. V. Ruiters, and J. Becker, “GPU-based iterative transmission reconstruction in 3D ultrasound computer tomography,” *Journal of Parallel and Distributed Computing*, vol. 74, no. 1, pp. 1730–1743, 2014.
- [13] Y. Ju, J. Zheng, M. Epstein, L. Sudak, J. Wang, and X. Zhao, “3D numerical reconstruction of well-connected porous structure of rock using fractal algorithms,” *Computer Methods in Applied Mechanics and Engineering*, vol. 279, pp. 212–226, 2014.
- [14] H. Zhao, L. Yang, Li Kun, and Y. Zhao, “Design and experimental research of a multifunctional loading system based on industrial CT,” *Machine Tool and Hydraulics*, vol. 46, no. 4, pp. 109–115, 2018.
- [15] L. Dong, J. Wesseloo, Y. Potvin, and X. Li, “Discrimination of mine seismic events and blasts using the Fisher classifier, naive bayesian classifier and logistic regression,” *Rock Mechanics and Rock Engineering*, vol. 49, no. 1, pp. 183–211, 2016.
- [16] F. Gan, X. Wang, M. Wang, and Y. Kang, “Experimental investigation of thermal cycling effect on fracture characteristics of granite in a geothermal-energy reservoir,” *Engineering Fracture Mechanics*, vol. 235, Article ID 107180, 2020.
- [17] G. Bai, X. Zeng, X. Li, X. Zhou, Y. Cheng, and J. Linghu, “Influence of carbon dioxide on the adsorption of methane by coal using low-field nuclear magnetic resonance,” *Energy & Fuels*, vol. 34, no. 5, pp. 6113–6123, 2006.
- [18] V. Frid, “Rockburst hazard forecast by electromagnetic radiation excited by rock fracture,” *Rock Mechanics and Rock Engineering*, vol. 30, no. 4, pp. 229–236, 1997.
- [19] M. Alber, R. Fritschen, M. Bischoff, and T. Meier, “Rock mechanical investigations of seismic events in a deep longwall coal mine,” *International Journal of Rock Mechanics and Mining Sciences*, vol. 46, no. 2, pp. 408–420, 2009.
- [20] M. Geng, Z. Ma, P. Gong et al., “Analysis of the effect on pressure relief by the pressure relieving hole layouts on high stress coal roadway,” *Journal of Safety Science and Technology*, vol. 11, pp. 5–10, 2012.
- [21] C. Fan, M. Luo, S. Li, H. Zhang, Z. Yang, and Z. Liu, “A thermo-hydro-mechanical-chemical coupling model and its application in acid fracturing enhanced coalbed methane recovery simulation,” *Energies*, vol. 12, no. 4, p. 626, 2019.
- [22] Z. Ouyang, “Application and mechanism of mine strata pressure pumping prevention with multi-stage blasting pressure releasing technology,” *Coal Science and Technology*, vol. 10, pp. 32–36, 2014.
- [23] P. Konicek, K. Soucek, L. Stas, and R. Singh, “Long-hole destress blasting for rockburst control during deep underground coal mining,” *International Journal of Rock Mechanics and Mining Sciences*, vol. 61, pp. 141–153, 2013.
- [24] T. Lan, C. Fan, S. Li et al., “Probabilistic prediction of mine dynamic disaster risk based on multiple factor pattern recognition,” *Advances in Civil Engineering*, vol. 2018, Article ID 7813931, 6 pages, 2018.

- [25] J. Liu, L. Xie, Y. Yao, Q. Gan, P. Zhao, and L. Du, "Preliminary study of influence factors and estimation model of the enhanced gas recovery stimulated by carbon dioxide utilization in shale," *ACS Sustainable Chemistry & Engineering*, vol. 7, no. 24, pp. 20114–20125, 2019.
- [26] C. Fan, D. Elsworth, S. Li, L. Zhou, Z. Yang, and Y. Song, "Thermo-hydro-mechanical-chemical couplings controlling CH₄ production and CO₂ sequestration in enhanced coalbed methane recovery," *Energy*, vol. 173, pp. 1054–1077, 2019.
- [27] X. Zhou, J. Men, D. Song et al., "Research on increasing coal seam permeability and promoting gas drainage with liquid CO₂ blasting," *China Safety Science Journal*, vol. 02, pp. 60–65, 2015.

Research Article

The Properties of a Coal Body and Prediction of Compound Coal-Rock Dynamic Disasters

Guowei Dong ^{1,2,3}, Xuanming Liang^{1,3} and Zhen Wang^{4,5}

¹School of Energy Engineering, Xi'an University of Science and Technology, Xi'an 710054, China

²The State Key Laboratory of Coal Resources and Safe Mining (CUMT), Xuzhou 221116, China

³Key Laboratory of Western Mine Exploitation and Hazard Prevention of the Ministry of Education, Xi'an 710054, China

⁴China Coal Technology and Engineering Group Corp Chongqing Research Institute, Chongqing 400039, China

⁵National Key Laboratory of Gas Disaster Monitoring, Preventing and Emergency Controlling, Chongqing 400039, China

Correspondence should be addressed to Guowei Dong; leng285@xust.edu.cn

Received 30 April 2020; Revised 28 June 2020; Accepted 27 July 2020; Published 20 August 2020

Academic Editor: Caiping Lu

Copyright © 2020 Guowei Dong et al. This is an open access article distributed under the Creative Commons Attribution License, which permits unrestricted use, distribution, and reproduction in any medium, provided the original work is properly cited.

Since the precise identification and prediction and early warning of compound coal-rock dynamic disaster remain difficult, a new coal characterisation and prediction method for compound coal-rock dynamic disasters was described based on theoretical analysis, laboratory experiment, field sampling, mathematical treatment, and industrial testing. The results implied that the physicochemical properties of coal in a compound coal-rock dynamic disaster are between those pertinent to a typical rock burst and a coal-gas outburst, i.e., with high crustal stress surrounding pressure, high gas pressure, low permeability, bump proneness, and outburst risk. The predicted drilling data indicate moderate gas desorption indices. The gas desorption velocity and permeability of compound coal-rock dynamic disaster coal decrease with the increase in crustal stress, while increase and decrease with the increase in gas pressure, respectively, at the same time, and they change little with increasing temperature. Gas extraction leads to the increase in coal mass brittleness and bump proneness. Based on the unique physical-mechanical properties of compound coal-rock dynamic disaster coal, a reasonably sensitive predictive index and critical value for Donglin Coal Mine were determined.

1. Introduction

Due to the prevailing demand for energy resources, the coal-based energy pattern of China will not change in the foreseeable future. The proportion of coal in the energy system will remain at around 50% in the long-term, and 80% of coal is mined from a deeper underground, especially in mideastern China. Due to deep mining, the features of coal-rock dynamic disasters become more complicated and diverse; thereby, a new compound coal-rock dynamic disaster occurs. Besides, in some middeep regions with abnormal gas geology, new compound coal-rock dynamic disasters also occur. This new compound coal-rock dynamic disaster presents a dual dynamic feature combining bump proneness and outburst risk; that is, the disaster exhibits the features of both typical coal-gas outburst and rock burst (Figure 1).

In recent years, some of China's coal mines such as those in the Pingdingshan mining areas, Huainan mining areas, Xinji mining areas, Fengcheng mining areas, Fuxin mining areas, and Fushun mining areas took the lead in deep mining, where some compound coal-rock dynamic disasters already occurred or are likely to occur.

At present, many scholars have studied the mechanism of compound coal-rock dynamic disasters, their prediction, early warning, and prevention: Petukhov [1], Zhang et al. [2], He et al. [3], Li et al. [4, 5], Li [6], Zhang et al. [7], Pan [8], Yin et al. [9], Dou et al. [10], and Dong et al. [11] have studied the occurrence mechanism of compound coal-rock dynamic disaster. Zhang and Li [12], Zhen et al. [13], Li et al. [14], Yuan [15], Li et al. [16], Qi et al. [17], Pan [8], Yin et al. [9], and Dou et al. [10] studied the occurrence conditions or types of compound coal-rock

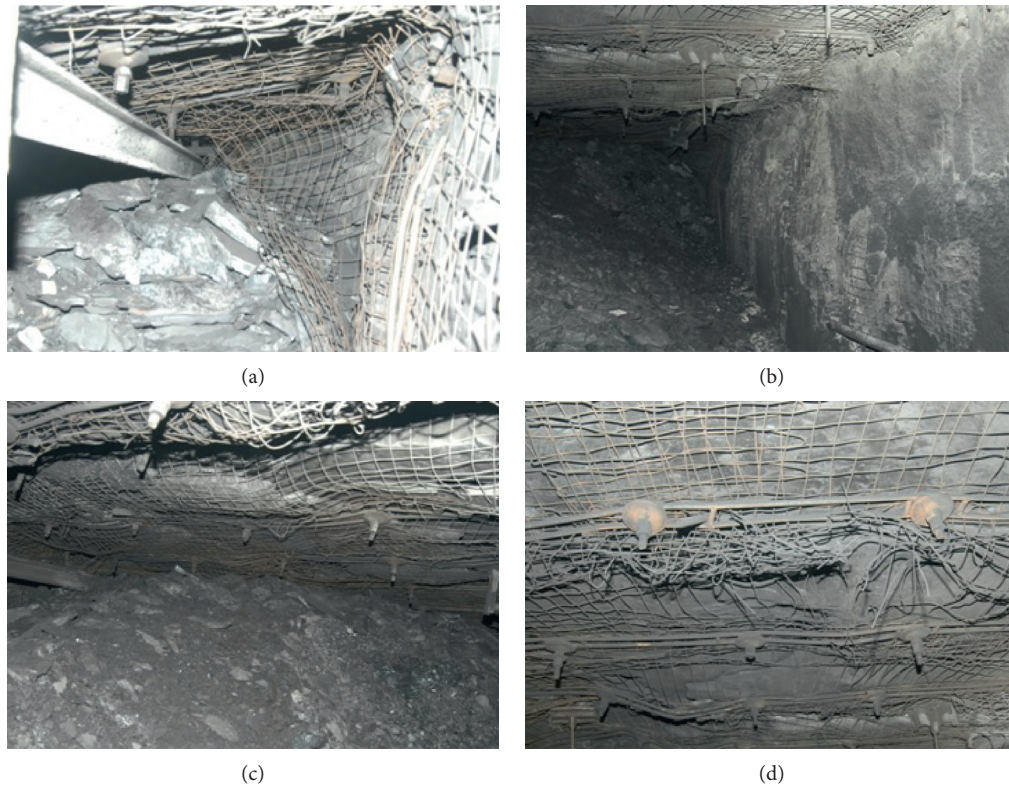


FIGURE 1: A compound coal-rock dynamic disaster accident: no. 12 coal mine, Pingdingshan Coal Group Co., Ltd.: (a) damage on the roadway supports; (b) the piling of coal flow; (c) the piling of coal flow; (d) normal supports of roadway.

dynamic disasters. Zhang [18], Yuan [15], Jianwei [19], Jiang et al. [20], Dong et al. [11], Sheng et al. [21], and Ouyang et al. [22] have studied the prediction, early warning, and evaluation of compound coal-rock dynamic disasters. Qi et al. [23] investigated the theory and technical framework of multiscale and multisource prevention and control of coal-rock dynamic disasters in deep coal mines. The prediction and early warning of a compound coal-rock dynamic disaster mainly relies on the direct or indirect parameters such as the amount of drilling cuttings [5–7, 10, 11, 15, 18, 20, 21, 23, 24], the size of the drilling cuttings [8, 23], the temperature of the drilling cuttings [8, 23], the desorption index of the drilling cuttings [5, 7, 11, 15, 18], the initial velocity of gas emission from boreholes [5, 7, 10, 11, 15, 18], the stress [7, 19, 20, 23], the displacement [23], the gas concentration extraction index [11, 20], coal temperature [8], coal charge [8], electromagnetic radiation [10], microseismic event count [10, 19, 20, 23, 25], acoustic emission event count [10, 11, 20, 21], shock wave CT [10], and seismic wave or elastic wave CT [10, 23]. However, the coal physical-mechanical characterisation and prediction method of a compound coal-rock dynamic disaster still contain many deficiencies; therefore, in this study, a new coal characterisation and prediction method of compound coal-rock dynamic disasters were studied, based on the actual occurrence data of compound coal-rock dynamic disasters.

2. Physicomechanical Properties of Coal in a Compound Coal-Rock Dynamic Disaster

2.1. Physical Properties

2.1.1. Experimental Study of the Coal-Gas Desorption Regularity of Compound Coal-Rock Dynamic Disaster. The instantaneous desorption (from the initial desorption to steady state) features of gas in coal samples after artificial unloading under different mining conditions were analysed via laboratory experiments. These experimental results are the foundation for the further study of different action mechanisms of stress, gas, and temperature on the risk of a disaster occurring.

Under certain confining pressure (CP) and gas pressure (GP) conditions, the desorption features of gas at different temperatures were analysed to reveal the controlling effect of temperature on gas desorption. Under a specific confining pressure and temperature conditions, the influence of gas pressure on the coal desorption regularity was discussed. The influence of confining pressure on the gas desorption behaviour was also studied under specific pore pressure and temperature conditions.

During the experiment, the Darcy steady flow method and triaxial penetration test device were used. The outlet pressure is the atmospheric pressure, while the inlet pressure is adjustable. The desorption and penetration experiments of coal samples under different gas pressures, temperatures,

and confining pressure conditions were conducted. The main device and experimental system used are displayed in Figure 2.

By using a customised rock coring and detection device, the raw coal was cut into cylinders measuring $\Phi 50 \text{ mm} \times 100 \text{ mm}$. After that, the samples were ground using an electric grinder, to meet test requirements. Experimental results and trend analyses are demonstrated in Figures 3–6.

- (1) Variation regularity of raw coal-gas desorption velocity (GDV) with confining pressure

The gas desorption velocity curves under different confining pressures are shown in Figure 3. During the test, the gas adsorption pressure is 2 MPa, and the temperature is 35°C. As shown in Figure 3, when the confining pressure is 6 MPa, the gas desorption velocity is greater than those under confining pressures of 10 and 12 MPa, in both the initial stage and steady stage. Meanwhile, the gas desorption velocities under confining pressures of 10 MPa and 12 MPa remain similar.

As shown in Figure 4, when the confining pressure increases from 6 to 8 MPa, the gas desorption velocity (after entering the steady stage) sharply decreases from 2.72 to 1.51 cm³/s. Meanwhile, the gas desorption velocities at 10 MPa and 12 MPa are 1.31 cm³/s and 1.22 cm³/s, respectively. That is, under specific gas pressure and temperature conditions, the influence of confining pressure on the gas desorption velocity decreases gradually, after it increases to a certain value.

- (2) Variation in raw coal-gas desorption velocity with gas adsorption pressure

The gas desorption velocity curves under different gas pressures are shown in Figure 5. During the test, the confining pressure is 6 MPa, and the temperature is 35°C. As displayed in Figure 5, when the gas adsorption pressure reaches 4 MPa, the gas desorption velocity is beyond the range of the instrumentation used, so its values are not illustrated in the figure. Hence, no matter in the initial stage or the steady stage, the gas desorption velocity increases with the improvement of gas adsorption pressure.

- (3) Variation in raw coal-gas desorption velocity with temperature

The gas desorption velocity curves under different temperature conditions are shown in Figure 6. During the test, the gas adsorption pressure is 1 MPa, and the confining pressure is 6 MPa. As illustrated in Figure 6, in the initial stage, the raw coal-gas desorption velocity at low temperatures is higher than that at high temperatures. Meanwhile, the final desorption velocity at low temperatures is lower than that at high temperatures.

2.1.2. Experimental Study of the Coal-Gas Permeability in a Compound Coal-Rock Dynamic Disaster. The variation in coal permeability (gas permeability coefficient) under

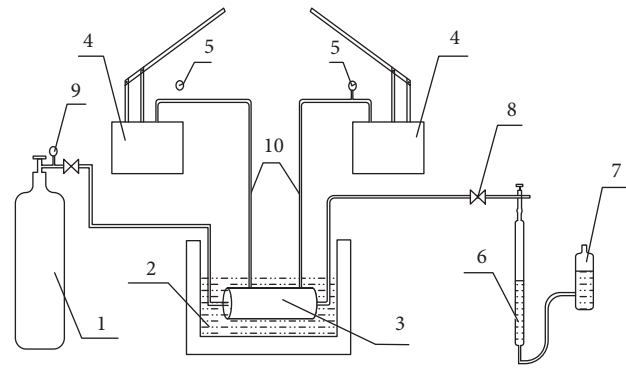


FIGURE 2: Schematic of the experimental system. 1, high-pressure gas cylinder; 2, thermostatic water bath; 3, triaxial osmoscope; 4, manual hydraulic pump; 5, oil pressure gauge; 6, burette; 7, levelling bottle; 8, valve; 9, reducing valve; 10, hydraulic tube.

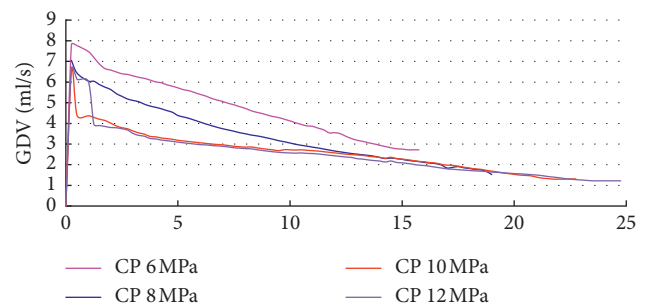


FIGURE 3: Gas desorption velocity curves under different confining pressure conditions.

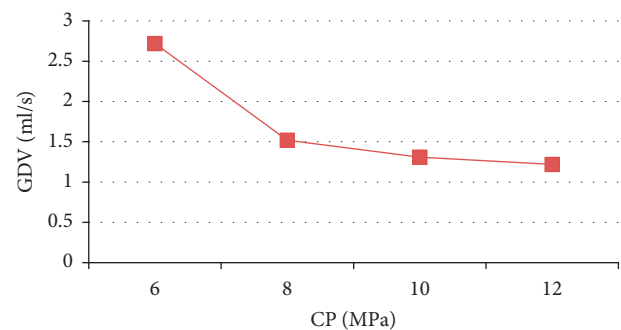


FIGURE 4: Change in gas desorption velocity with confining pressure.

different conditions was characterised. The main device and experimental system used are displayed in Figure 2.

- (1) Variation in raw coal permeability with changing confining pressure

The variation in permeability during continuous unloading is shown in Figures 7–10. As shown in the figure, the coal permeability gradually increases during unloading and the rate of increase also increases. In the initial unloading stage, i.e., high confining pressure stage (high burial depth), the

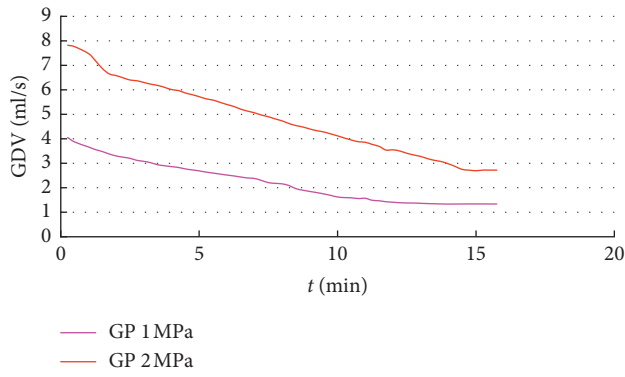


FIGURE 5: Gas desorption velocity under different gas pressure conditions.

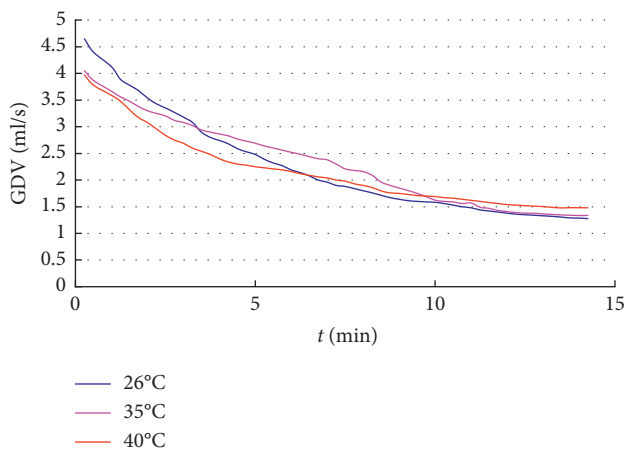


FIGURE 6: Gas desorption velocity curves under different temperature conditions.

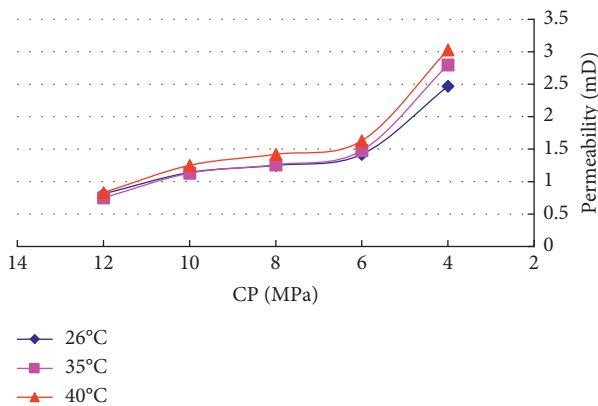


FIGURE 7: Variation in permeability during confining pressure unloading at a gas pressure of 1 MPa.

permeability rises slowly during the unloading of confining pressure. Meanwhile, in the mid-late stage, i.e., low confining pressure stage (low burial depth), the increase rate of coal permeability is accelerated during unloading. For example, when the adsorption pressure is 1 MPa, the rate of increase increased under confining pressures is lower than 6 MPa. Meanwhile, when the

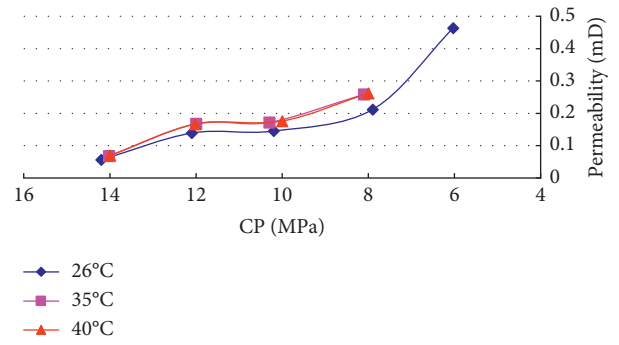


FIGURE 8: Variation in permeability during confining pressure unloading at a gas pressure of 4 MPa.

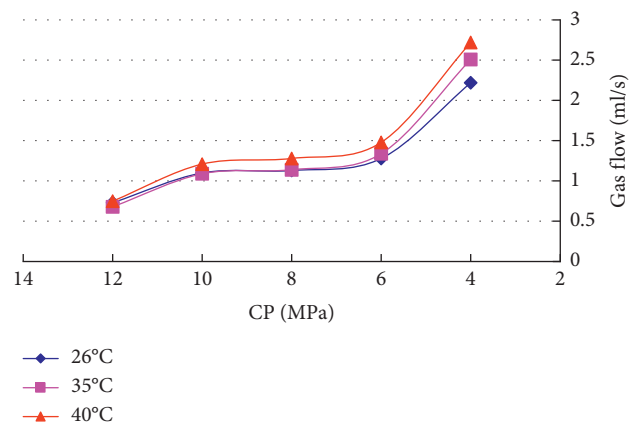


FIGURE 9: Variation in gas flow during confining pressure unloading at a gas pressure of 1 MPa.

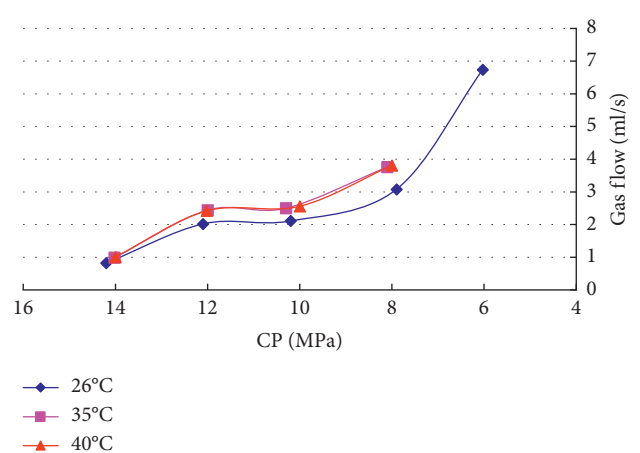


FIGURE 10: Variation in gas flow during confining pressure unloading at a gas pressure of 4 MPa.

adsorption pressure is 4 MPa, the rate of increase rate is increased under confining pressures is lower than 8 MPa. In a word, the variation in permeability is closely related to the initial confining pressure (burial depth or tectonic stress) and gas pressure.

According to the above analysis, when the adsorption pressure and temperature are constant, upon the reduction of confining pressure, the permeability increases gradually; in the initial stage of unloading, i.e., the high confining pressure stage, the increasing amplitude of permeability is relatively small; meanwhile, in the later stage of unloading, i.e., the low confining pressure stage, the rate of increase of permeability is increased; the gas flow changes in a way similar to the permeability.

(2) Variation in raw coal permeability with gas pressure changing

The permeability of the same sample under different gas adsorption pressures was characterised. The results indicate that, with the increase in gas adsorption pressure, the permeability decreases. On the contrary, the gas desorption velocity; i.e., the gas flow increases accordingly (Figures 11 and 12).

(3) Variation in raw coal permeability with changing temperature

Figures 13–15 show the variation between the sample permeability and temperature under different confining pressures when the gas adsorption pressure is 1 MPa and 4 MPa, respectively. As shown, the coal permeability increases with increasing temperature because as the temperature rises, the activity and internal energy of gas molecules increase. Some of the adsorbed gas is desorbed. The seepage channels expand. The diffusion of gas molecules is accelerated; thus, the permeability of coal gas increases accordingly. Under high confining pressure conditions, the increase in permeability with temperature is relatively small yet becomes more significant at low confining pressure. In particular, when the gas adsorption pressure is 4 MPa, the seepage flow velocity exceeds the measuring range of equipment and cannot be precisely determined.

According to the above analysis, when the adsorption pressure and confining pressure are constant, with the increase in temperature, the coal permeability rises slightly, but the variation is smooth (Figures 13 and 14); under high confining pressure, the increase in permeability as the temperature rises is relatively small (a trend that strengthens under low confining pressure conditions, as shown in Figure 14); when the gas adsorption pressure is 4 MPa, the seepage flow velocity and permeability (confining pressure of 6 MPa and temperatures of 35°C and 40°C) exceed the measuring range of equipment and cannot be accurately measured. Meanwhile, Figure 15 indicates that the variation in gas flow is similar to that of the permeability.

2.2. Coal Mechanical Properties in a Compound Coal-Rock Dynamic Disaster. By using gas-tight equipment [26], the approximate-uniaxial test method for the characterisation of gas-containing coal mechanical properties was developed.

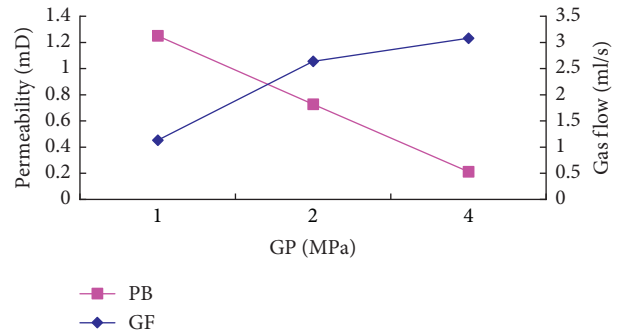


FIGURE 11: At 26°C.

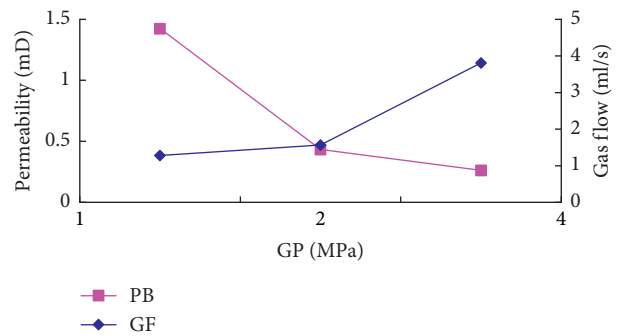


FIGURE 12: At 40°C.

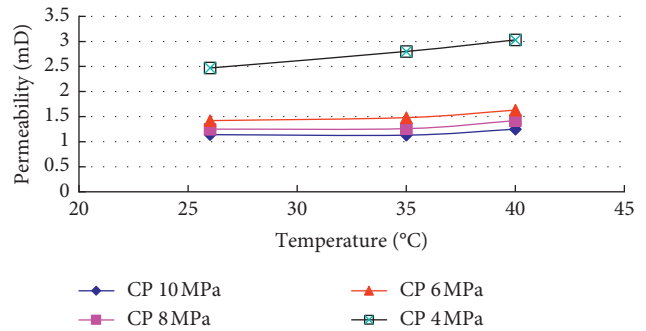


FIGURE 13: Variation in permeability with increasing temperature at a gas pressure of 1 MPa.

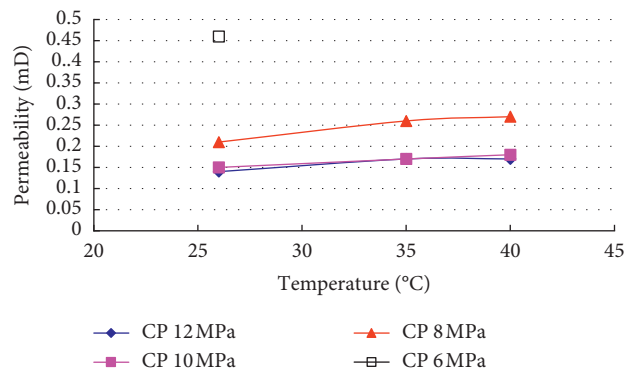


FIGURE 14: Variation in permeability with increasing temperature at a gas pressure of 4 MPa.

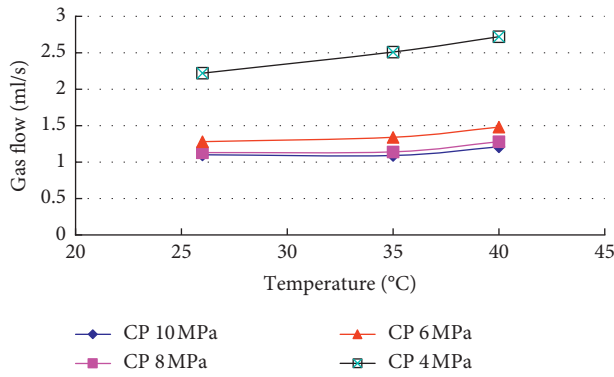


FIGURE 15: Variation in gas flow with increasing temperature at a gas pressure of 1 MPa.

Based on experiment, the influence of gas on the coal mechanical properties and mechanical response under zero effective confining pressure condition was obtained.

2.2.1. Stress-Strain Curves of Coal Samples under Uniaxial Compression. In uniaxial compression tests, the gas pressures were set to 0 MPa, 1 MPa, and 2 MPa, respectively. Under each condition, at least three samples were characterised. The experimentally obtained stress-strain curves and related data are displayed in Figures 16 and 17.

Figure 16 shows the uniaxial compression stress-strain curve of coal samples without gas being present. As shown in the figure, although the samples are cut from the same coal block, the uniformity of bedding direction is ensured, so some discreteness of measured data is unavoidable. Figure 17 demonstrates the stress-strain curves of coal samples uniaxially compressed under various gas pressure conditions. The gas in pores and fissures not only changes the mechanical properties and mechanical response of the coal body in the plastic deformation stage and after peak strength deformation stage but also affects the elastic deformation of the coal body; i.e., mechanical properties such as elastic modulus no longer remain constant. In other words, the gas pressure changes the mechanical response features of coal in all deformation stages, including its elastic deformation stage.

2.2.2. Influence of Adsorbed Gas on Coal Mechanical Properties. Within the coal, gas exists in the free and adsorbed states. Under specific temperature and pressure conditions, a dynamic equilibrium is reached. The physicommechanical properties of coal containing gas are affected by these two gas states. The free gas affects the mechanical properties of coal via pore pressure which affects the volumetric strain. Meanwhile, adsorbed gas changes the mechanical properties and mechanical response of coal via the adsorption and desorption processes, which further affect the constitutive relationship of the coal.

- (1) Elastic modulus (EM) decreases with the increase in gas pressure

As shown in Figure 18, the elastic modulus decreases with the increase in gas pressure. Gas molecules

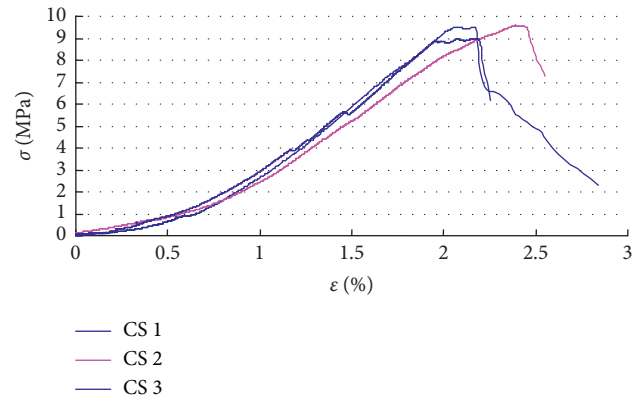


FIGURE 16: Stress-strain curves of coal samples (CS) compressed under no-gas conditions.

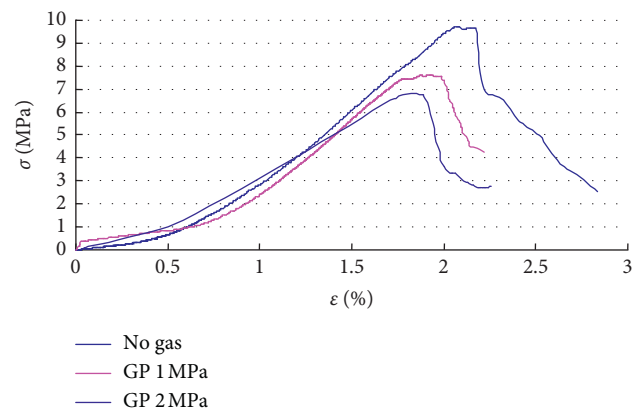


FIGURE 17: Stress-strain curves of coal samples compressed under different gas conditions.

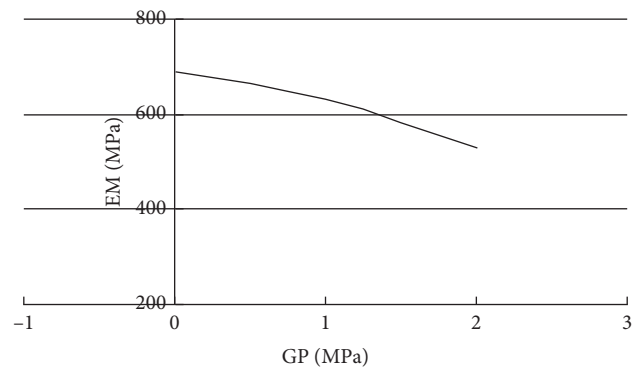


FIGURE 18: Variation in elastic modulus with changing gas pressure.

adsorbing on the coal particle surface and inter-particle space will reduce the cohesion of the coal samples, so the macroscopic deformation resistance of coal sample is decreased; i.e., the elastic modulus is reduced.

- (2) Plastic deformation at the peak point decreases with the increase in gas pressure

As shown in Figure 19, at the peak point stage, the plastic deformation of coal sample gradually decreases with the increase in gas pressure.

(3) Influence of gas on the bump proneness index

Experimental results of coal bump proneness index under different gas pressures are listed in Table 1.

As shown in Figure 20, the dynamic fracture time, i.e., the time required for the occurrence of brittle fracture, increases with the increase in gas pressure.

The bump energy index and elastic energy index both decrease with the increase in gas pressure. Comparing to coal body skeleton frame bearing load alone, the coal body skeleton frame and gas bear the external load together after gas adsorption. Thus, the elastic deformation energy accumulated within the coal body is significantly reduced, making it difficult for the formation of coal body bump burst. Besides, according to the method used for calculation of bump energy index and elastic energy index, the reduction of uniaxial compressive strength and elastic modulus will result in the reduction of bump energy index and elastic energy index with the increase in gas pressure, as shown in Figures 21 and 22.

Based on above analyses, as the mine gets deeper, the gas extraction is likely to increase the bump proneness of coal with the increase in coal strain energy. Thus, the risk of compound coal-rock dynamic disaster is increased.

(4) Brittleness decreases with the increase in gas pressure

As shown in Figures 16 and 17, the presence of gas makes the postpeak curve more shallow; in particular, the brittle fracture, that stage with a sharp instant reduction in strength, is less significant. This is mainly attributed to the existence of gas increasing the ductility of coal and reduces the possibility of brittle fracture. As shown in Figure 23, after the fracture of samples without gas adsorption effect, the sample fractures into a relatively complete split line; meanwhile, for samples affected by gas adsorption, they fragment, exhibiting poor completeness after fracture.

Also, it can also be found that the trend in coal mechanical properties and mechanical response slows as the gas pressure increases. In other words, under the uniaxial compression condition with zero confining pressure, the influence of gas on the coal mechanical properties and mechanical response gradually diminishes when the gas adsorption reaches saturation. Gas extraction will increase the risk of compound a coal-rock dynamic disaster.

3. Prediction Used in a Case Study of a Compound Coal-Rock Dynamic Disaster

3.1. Mine Overview: Contorted Fold Structure Characteristics and Compound Coal-Rock Dynamic Disaster Condition of Donglin Coal Mine. Donglin Coal Mine is located in

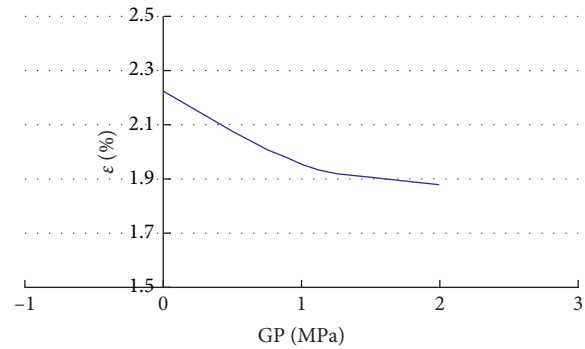


FIGURE 19: Variation in peak point plastic deformation for changing gas pressure.

Wansheng District, Chongqing City; it is a coal-gas outburst mine and adopts the vertical multilevel partition mining method. It mainly exploits the No. 4 and No. 6 coal seams in the Permian Longtan formation. The types of coal are coking coal, lean coal, meagre coal, and fat coal. Donglin Coal Mine lies along the Ganjiaping syncline shaft. Folds in the mine are classified as secondary folds of the Bamianshan syncline. Secondary tectonics include the Ganjiaping syncline, Maoyan anticline, Yaqueyan syncline, Heiqiyan torsion, and Yaqueyan torsion, as shown in Figure 24.

Contorted fold structures are folds transiting from normal incline to inverted incline or compress shear and noncylindrical folds caused by trend transition and increasing dip angle. According to the formation area and morphological features of contorted fold structures, the fold structures can be classified into reverse or kinked structures.

The Heiqiyan contorted fold band in Donglin Mine is distributed approximately north to south, with a total length of 4 km, and Heiqiyan Matong marks the transition point. Its south trend is 1.5 km. The deep stratum trend transits into S30°W, and the incline is W (i.e., the east wing of the Ganjiaping syncline); the band trend between the north of Matong and boundary is 2.5 km. The stratum overturns into an east incline of 30°. Its shallow seam trend is N10°W, while the deep seam trend is N10°E. The ground elevation is +310 m, and the production level is -100 m. The initial crustal stress is 56.3 MPa. The initial gas pressure is 1.8 MPa. The initial bump proneness indices of coal seam are such that the dynamic fracture time DT is 323 ms, elastic energy index W_{ET} is 2.16, bump energy index K_E is 1.64, and the uniaxial compressive strength R_c is 4.3 MPa, thus indicating bump proneness.

Donglin Coal Mine is located at the intersection of the north-east secondary fold and the north-south structure. Due to stress imbalance, contorted fold structures are formed in Heiqiyan.

During the formation of contorted fold structures in Donglin Coal Mine, severe damage to the coal body structure and intensive changes in coal attitude are caused by compression and interformational sliding. Furthermore, the contorted fold structures also form a closed structural unit with favourable gas occurrence: these geological factors lead to the serious compound coal-rock dynamic disaster accidents that have occurred in Donglin Coal Mine.

TABLE 1: Experimental results of coal bump proneness index under different gas pressure conditions.

Type name	1-type without gas	2-type gas pressure of 1 MPa	3-type gas pressure of 2 MPa	
Bump proneness index	Dynamic fracture time (ms)	280	630	640
		260	480	460
	Average	320	570	720
		287	560	607
		2.33	1.87	1.77
	Elastic energy index (EEI)	3.21	1.76	1.52
		2.90	1.69	1.43
	Average	2.81	1.77	1.57
		1.92	1.62	1.23
	Bump energy index (BEI)	1.74	1.51	1.35
		1.81	1.38	1.56
	Average	1.82	1.50	1.41

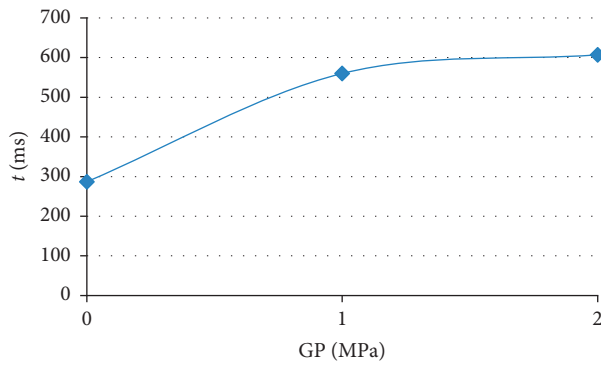


FIGURE 20: Variation in dynamic fracture time with changing gas pressure.

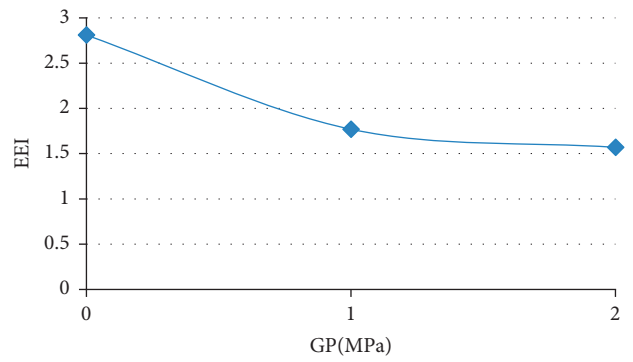


FIGURE 22: Variation in elastic energy index with changing gas pressure.

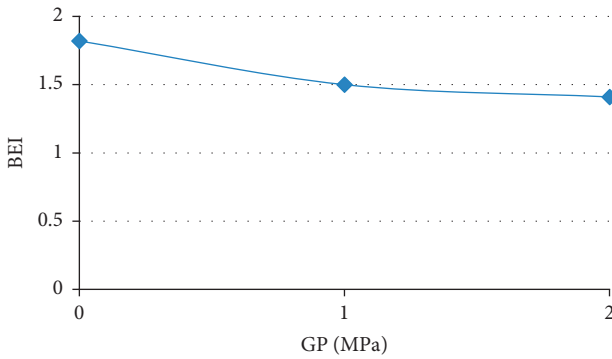


FIGURE 21: Variation in bump energy index with changing gas pressure.

To date, about 200 compound coal-rock dynamic disasters have occurred in Donglin Coal Mine, with an average intensity of 72.8 t each. The maximum intensity reached 3500 t, and the maximum gas emission was 200,000 m³. Altogether, 92 people have died in such gas accidents. As for the No. 4 coal seam, the maximum intensity was 3500 t, while that for the No. 6 coal seam was 160 t. The parameters of compound coal-rock dynamic disasters in Donglin Coal Mine are summarised in Table 2.

3.2. Study of the Prediction Index for Compound Coal-Rock Dynamic Disasters in Donglin Coal Mine. In this study, the

prediction indices of compound coal-rock dynamic disaster are studied mainly focusing on the No. 6 coal seam in the north wing of Donglin Coal Mine, via laboratory tests and field investigation.

3.2.1. Laboratory Study. Soft coal samples were collected in the 2607-50 heading face and 2609-90 heading face. Risk parameters of compound coal-rock dynamic disaster were measured in the laboratory, with the results listed in Table 3. In the table, 0.5 MPa, 0.74 MPa, and 1.1 MPa are the assumed gas pressures used.

The risk parameters of a compound coal-rock dynamic disaster include initial gas emission velocity ΔP and the consistency coefficient of coal f . The K_1 - P relationship was fitted according to related experimental data. As shown in Table 3, coal samples were collected at different sites in the No. 6 coal seam. The critical value of K_1 was determined to be 0.10 to 0.23 based on the minimum gas pressure method. The gas parameters and mechanical parameters of compound coal-rock dynamic disaster were mainly decided by laboratory investigation. The critical gas desorption index K_1 was determined based on the critical gas pressure of 0.74 MPa and the theoretical gas pressure of 1.1 MPa calculated according to the consistency coefficient.

3.2.2. Field Investigation. Some 70 prediction cycles were carried out in the 2607-50 heading face and 2609-90 heading

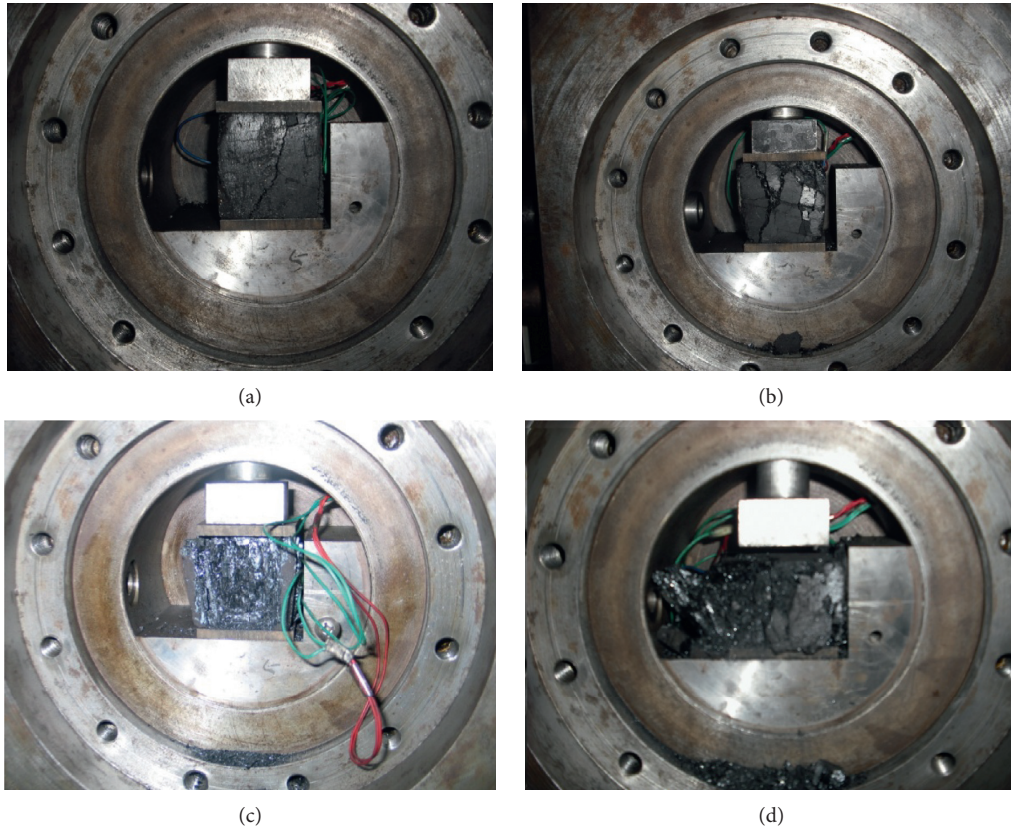


FIGURE 23: Fracture patterns of coal samples compressed under different gas pressures: (a) without gas effect; (b) under the influence of 1 MPa gas pressure; (c) under the influence of 2 MPa gas pressure.

face during the study, with 58 sets of prediction data collected.

Among the 58 sets of data, on more than 26 occasions, the prediction rate of compound coal-rock dynamic disaster reached 45%. The averaged maximum values of K_1 and S in the 58 sets of data are $0.16 \text{ ml/g}\cdot\text{min}^{1/2}$ and 14.3 kg/m , respectively. A check on the result cycle was conducted after 25 events (i.e., a check rate of 32%). The per-metre cuttings desorption index of prediction cycle, and the distribution of the maximum prediction cycle and check cycle values of this index, is listed in Tables 4–6, corresponding to Figures 25–28.

According to Tables 4 and 5, the maximum average value of per-metre drilling index K_1 is $0.08 \text{ ml/g}\cdot\text{min}^{1/2}$, while the maximum average value of S is 8.2 kg/m .

Based on the above field measurements, it is implied that the following relationship exists between the desorption index of cuttings, kinetic phenomena, hole depth, and coal seam occurrence: for $K_{1\text{max}} < 0.2$, no spray hole phenomenon has been reported. When the coal body is relatively hard (failure type II and consistency coefficient of 0.7) and no drill jamming or coal-gunning occurs, the maximum drilling chip amount index S is usually around 6.0 kg/m . When the coal body is relatively hard (failure type II and firmness of 0.7) and there is drill jamming or coal-gunning, the maximum drilling chip amount index S is usually above 15 kg/m . For soft coal (failure types III and IV and consistency coefficient of 0.2) with drill jamming or

coal-gunning, the maximum drilling chip amount index S is even greater.

The prediction or check cycle drill hole depth should be controlled to within 10 m; the maximum drilling chip amount index S occurs within a hole depth of 6 m, so the maximum index K_1 value occurs within a hole depth of 9 m.

In areas with significant coal seam occurrence (average seam thickness) variation, hole collapse, drill jamming, and coal-gunning occur frequently.

In ordinary mines, the occurrence rate of compound coal-rock dynamic disaster is between 5% and 10%. By considering a safety factor of three, the critical value of the compound coal-rock dynamic disaster prediction was theoretically determined; i.e., the number of an index exceeding a certain value accounts for 30% of the total number of statistical items of data. As shown in Table 6 and Figures 27 and 28, the ranges of different K_1 and S were obtained via statistical analysis of data obtained through 58 field tests.

According to the range of $K_{1\text{max}}$ obtained via 58 field tests, the maximum value of K_1 exceeding 30% is $0.2 \text{ mL}/(\text{g}\cdot\text{min}^{1/2})$, the proportion of which is 31% overall. As implied by field investigation results, when $K_1 < 0.2 \text{ mL}/(\text{g}\cdot\text{min}^{1/2})$, no spray hole phenomenon has been reported. With the increase in K_1 , the possibility of occurrence of kinetic phenomena including spray hole development increases.

According to the range of the prediction cycle drilling chip amount index S_{max} obtained through 58 field tests, the

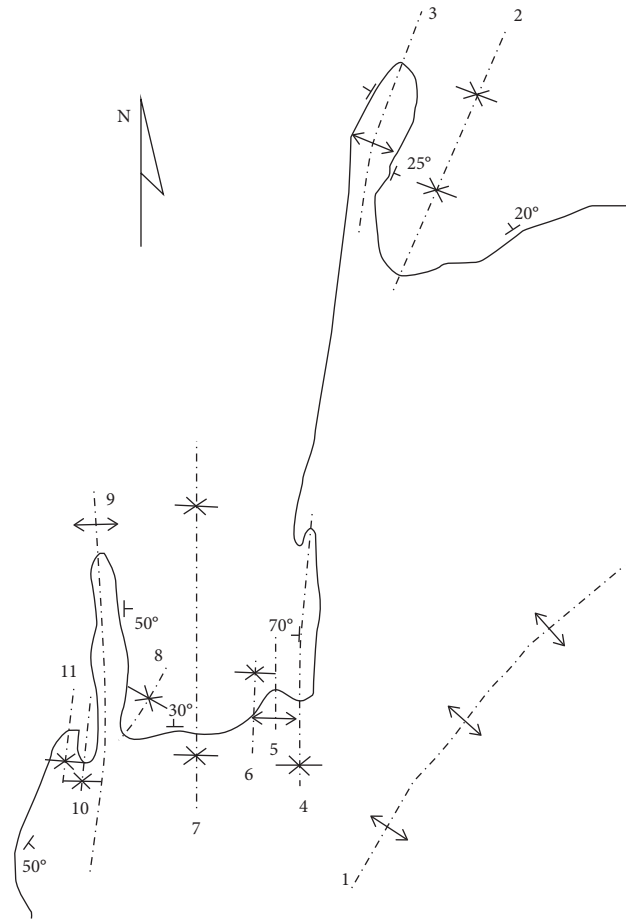


FIGURE 24: Tectonic outline map of the Nantong Coal Mine Zone. 1, Longguxigeo anticline; 2, Conglingou syncline; 3, Xianjiaping anticline; 4, Ganjiaping syncline; 5, Maoyan anticline; 6, Yaqueyan syncline; 7, Bamianshan syncline; 8, Wangjiaba syncline; 9, Wuguishan anticline; 10, Pingtu syncline; 11, Miaoding syncline.

TABLE 2: Compound coal-rock dynamic disasters in Donglin Coal Mine.

		Parameters
Times	No. 4 coal seam	152
	No. 6 coal seam	41
Maximum strength (t)	No. 4 coal seam	3500
	No. 6 coal seam	160

TABLE 3: Gas parameters of coal found by laboratory investigation.

Sampling site	Initial gas emission velocity ΔP	Firmness coefficient of soft coal f	K_1 - P relational model, $K_1 = AP^B$					
			A	B	0.50 MPa	0.60 MPa	0.74 MPa	1.10 MPa
2607-50 heading face	6	0.27	0.1472	0.5582	$K_1 = 0.10$	$K_1 = 0.11$	$K_1 = 0.12$	$K_1 = 0.16$
2607-50 heading face	5	0.26	0.1902	0.7115	$K_1 = 0.12$	$K_1 = 0.14$	$K_1 = 0.15$	$K_1 = 0.20$
2609-90 heading face	8	0.29	0.2196	0.6989	$K_1 = 0.14$	$K_1 = 0.15$	$K_1 = 0.18$	$K_1 = 0.23$

TABLE 4: Prediction cycle cuttings desorption index K_1 with changing hole depth.

Prediction hole depth (m)	1	2	3	4	5	6	7	8	9	10
Prediction times	9	93	30	82	27	66	23	55	18	33
K_{1max} (ml/g.min ^{1/2})	0.06	0.34	0.22	0.37	0.3	0.35	0.21	0.46	0.21	0.33
K_{1min} (ml/g.min ^{1/2})	0.01	0	0.01	0	0.02	0	0.01	0.02	0.01	0
Average value of K_1 (ml/g.min ^{1/2})	0.03	0.08	0.07	0.08	0.08	0.07	0.06	0.07	0.08	0.07

TABLE 5: Prediction cycle drilling chip amount index S with changing hole depth.

Prediction hole depth (m)	1	2	3	4	5	6	7	8	9	10
Prediction times	107	122	115	112	94	94	79	76	56	47
S_{\max} (kg/m)	18.5	64	36	26	42	73	48	40	42	30
S_{\min} (kg/m)	0.6	0.8	0.6	1.2	1.8	1.8	2.2	1.6	1	1.2
Average value of S (kg/m)	2.4	3.4	4.8	4.7	5.6	7.1	7.7	7.8	8.2	7.4

TABLE 6: Prediction cycle percentage-based statistics of cuttings desorption index.

$K_{1\max}$ (ml/g·min ^{1/2})	Total times/58	Percentage (%)	S_{\max} (kg/m)	Total times/58	Percentage (%)
≥ 0.05	55	95	≥ 6	42	72
≥ 0.1	39	67	≥ 10	27	47
≥ 0.15	26	45	≥ 12	23	40
≥ 0.2	18	31	≥ 15	16	28
≥ 0.25	8	14	≥ 20	12	21
≥ 0.3	6	10	≥ 25	9	16
≥ 0.35	4	7	≥ 30	7	12
≥ 0.4	1	2	≥ 35	1	2

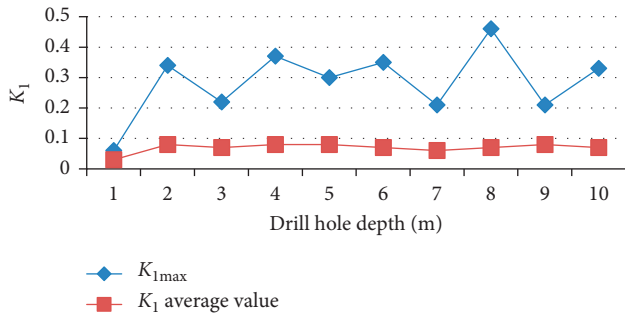


FIGURE 25: Distribution of 58 sets prediction cycle cuttings desorption index K_1 at different hole depths.

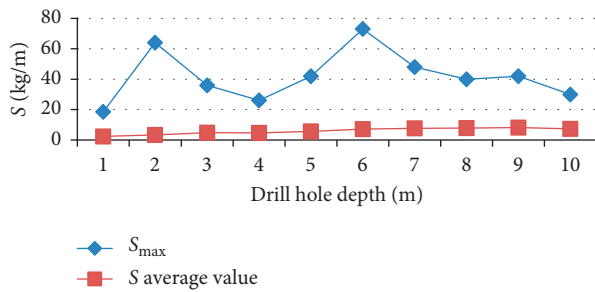


FIGURE 26: Distribution of 58 sets of prediction cycle drilling chip amount index S at different hole depths.

maximum value of S exceeding 30% is 15 kg/m, the proportion of which is 28% overall. When S_{\max} exceeds 15 kg/m, kinetic phenomena including drill jamming, coal-gunning, and collapse occur frequently.

3.2.3. Prediction Index and Critical Value of the No. 6 Coal Seam of Compound Coal-Rock Dynamic Disasters in Donglin Coal Mine. In combination with laboratory investigation, field data statistics, and field kinetic phenomena, the cuttings desorption index K_1 is taken as the gas prediction index, with a critical value of 0.2 ml/(g·min^{1/2}).

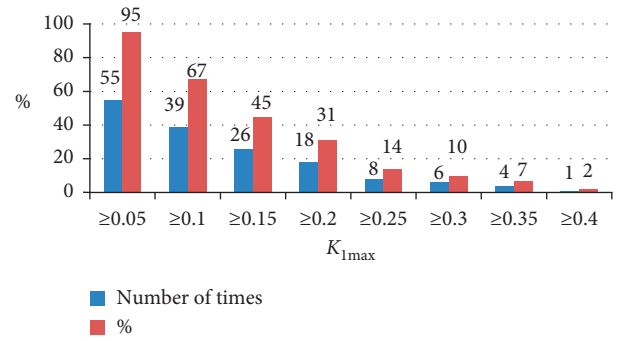


FIGURE 27: Distribution of 58 sets of prediction cycle cuttings desorption index $K_{1\max}$.

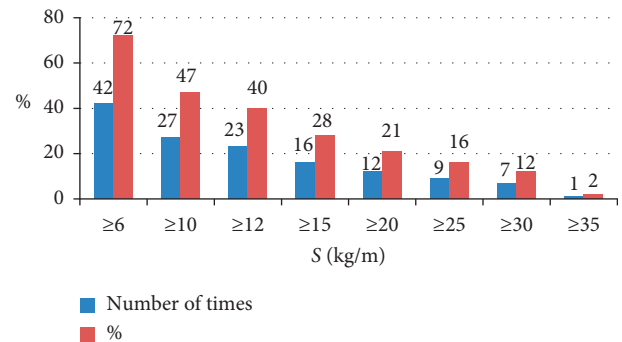


FIGURE 28: Distribution of 58 sets of prediction cycle drilling chip amount index $S_{1\max}$.

Based on the field test data statistics and actual kinetic phenomenon, the drilling chip amount S can be determined as the crustal stress index of compound coal-rock dynamic disaster for the No. 6 seam in the contorted fold structure band of Donglin Coal Mine, with a critical value of 15 kg/m.

According to these prediction indices and critical values, 85 sets of prediction data and check cycle analysis were adopted during extensive field application. During the

excavation of a 257.5 m long roadway, no compound coal-rock dynamic disaster occurred.

4. Conclusion

- (1) The areas of occurrence of compound coal-rock dynamic disasters are those with high crustal stress confining pressure, high gas pressure, and low permeability; the coal mechanical properties of compound coal-rock dynamic disaster exhibit bump proneness and outburst risk.
- (2) The gas desorption velocity and permeability reduce with the increase in crustal stress, while increase and decrease with increasing gas pressure, respectively. A temperature variation within 30°C has limited influence on the gas desorption velocity.
- (3) As the mining depth increases, the crustal stress and gas pressure both increase. At the same time, compared to the gas pressure, the increase amplitude and velocity of crustal stress increase, resulting in the increase in coal strain energy, elastic modulus, bump energy index, and elastic energy index. Meanwhile, the dynamic fracture time is reduced. Gas extraction leads to the increase in bump energy index and elastic energy index, while reducing the dynamic fracture time; thus, the risk of compound coal-rock dynamic disaster is significantly increased.
- (4) Based on the actual geological conditions of Donglin Coal Mine, the prediction sensitivity index and critical value of compound coal-rock dynamic disaster were investigated. The cuttings desorption index K_1 and drilling chip amount S were set as the sensitivity index, with critical values of 0.2 mL/(g·min^{1/2}) and 15 kg/m, respectively.

Data Availability

The data used to support the findings of this study are included within this article.

Conflicts of Interest

The authors declare that there are no conflicts of interest.

Authors' Contributions

Dong G and Wang Z conceived and designed the experiments. Wang Z performed the experiments. Wang Z and Liang X analysed the data. Dong G wrote the paper.

Acknowledgments

This work was funded by the National Key Research and Development Programme of China (Grant no. 2016YFC0801402), National Science and Technology Major Project of the Ministry of Science and Technology of China in the 13th Five-Year Period (Grant no. 2016ZX05045-004), One Hundred Youth Talents Project of Shaanxi Province of China, Shaanxi Natural Science Foundation of China (Grant no. 2020JM-519), and the Research

Fund of the State Key Laboratory of Coal Resources and Safe Mining, CUMT (Grant no. SKLCRSM18KF017).


References

- [1] I. M. Petukhov, "Theory and Practice in rock burst prevention," in *Proceedings of the 22nd International Conference on Mining Safety*, Beijing, China, 1987.
- [2] M. Zhang, Z. Xu, and Y. Pan, "A united instability theory on coal (rock) burst and outburst," *Journal of China Coal Society*, vol. 16, no. 4, pp. 48–52, 1991.
- [3] M. He, H. Xie, S. Peng, and Y.-D. Jiang, "Study on rock mechanics in deep mining engineering," *Chinese Journal of Rock Mechanics and Engineering*, vol. 24, no. 16, pp. 2803–2813, 2005.
- [4] T. Li, M. Cai, J. Wang et al., "Discussion on relativity between rock burst and gas in deep exploitation," *Journal of China Coal Society*, vol. 30, no. 5, pp. 562–567, 2005.
- [5] T. Li, T. Mei, G. Li et al., "Mechanism study of coal and gas outburst induced by rockburst in "three-soft" coal seam," *Chinese Journal of Rock Mechanics and Engineering*, vol. 30, no. 6, pp. 1283–1288, 2011.
- [6] Z. Li, *Rock-Burst Mechanism and Application of High-Methane Coal-Seam*, Liaoning Technical University, Fuxin, China, 2007.
- [7] H. Zhang, Jun, W. Song et al., *Geology Dynamic Division*, Coal industry Press, Beijing, China, 2009.
- [8] Y.-S. Pan, "Integrated study on compound dynamic disaster of coal-gas outburst and rockburst," *Journal of China Coal Society*, vol. 41, no. 1, pp. 105–112, 2016.
- [9] G. Yin, L. Xing, J. Lu, and M. Li, "Disaster-causing mechanism of compound dynamic disaster in deep mining under static and dynamic load conditions," *Journal of China Coal Society*, vol. 42, no. 9, pp. 2316–2326, 2017.
- [10] L. Dou, X. He, T. Ren et al., "Mechanism of coal-gas dynamic disasters caused by the superposition of static and dynamic loads and its control technology," *Journal of China University of Mining & Technology*, vol. 47, no. 1, pp. 48–59, 2018.
- [11] G. Dong, H. Jin, Q. Hu et al., *Compound Coal-Rock Dynamic Disaster Forecasting and Early Warning and its Application*, China University of Mining and Technology Press, Xuzhou, China, 2017.
- [12] F. Zhang and T. Li, "Cognizance on compound dynamic disaster of coal and gas in deep mining," *Zhongzhou Coal*, vol. 4, pp. 73–76, 2009.
- [13] W. Zhen, Y. Guangzhi, H. Qianting et al., "Study on induced transformation conditions of rock burst and outburst in high gassy seams," *Journal of Mining and Safety Engineering*, vol. 27, no. 4, pp. 572–580, 2010.
- [14] H. Li, J. Han, Z. Xiong et al., "Analysis and prevention of complex dynamic phenomena in deep mining," *Coal Engineering*, vol. 7, no. 4, pp. 40–41, 2010.
- [15] R. Yuan, "Features of dynamic disasters combined rockburst and gas outburst in deep coal mine and its preventive measures," *Coal Science and Technology*, vol. 47, no. 8, pp. 6–10, 2013.
- [16] H. Li, L. Qi, X. Chen et al., "The influence of gas pressure on mobile mechanism of coal rock burst," *Safety in Coal Mines*, vol. 44, no. 9, pp. 1–4, 2013.
- [17] L. Qi, X. Chen, G. Cheng et al., "Research on the burst triggering mechanism under the coupling action of higher stress and gas pressure," *Journal of North China Institute of Sci-Ence and Technology*, vol. 11, no. 2, pp. 18–21, 2014.
- [18] T.-G. Zhang, "Prediction and control of coal and gas outburst in Pingdingshan Mining Area," *Journal of China Coal Society*, vol. 26, no. 2, pp. 172–177, 2001.

- [19] G. Jianwei, *Hazard Assessment and Monitoring Technology of Com-Pound Dynamic Disaster in Mine*, China University of Mining and Technology, Xuzhou, China, 2013.
- [20] F. Jiang, G. Yang, W. Quande et al., "Study and prospect on coal mine composite dynamic disaster real-time prewarning platform," *Journal of China Coal Society*, vol. 43, no. 2, pp. 333–339, 2018.
- [21] L. Sheng, H. Yang, M. Luo et al., "Improved comprehensive index evaluation method and its application on rockburst hazard of gas coal seam," *Coal Science and Technology*, vol. 13, no. 11, pp. 34–40, 2017.
- [22] Z. Ouyang, G. Zhang, H. Qin et al., "Improved comprehensive index evaluation method and its application on rockburst hazard of gas coal seam," *Coal Science and Technology*, vol. 46, no. 10, pp. 30–36, 2018.
- [23] Q. Qi, Y. Pan, L. Shu et al., "Theory and technical framework of prevention and control with different sources in multi-scales for coal and rock dynamic in deep mining of coal mines," *Journal of China Coal Society*, vol. 43, no. 7, pp. 1801–1810, 2018.
- [24] C. Wang, X. Li, C. Xu et al., "Study on factors influencing and the critical value of the drilling cuttings weight: an index for outburst risk prediction," *Process Safety and Environmental Protection*, vol. 140, pp. 356–366, 2020.
- [25] C.-P. Lu, G.-J. Liu, Y. Liu, N. Zhang, J.-H. Xue, and L. Zhang, "Microseismic multi-parameter characteristics of rockburst hazard induced by hard roof fall and high stress concentration," *International Journal of Rock Mechanics and Mining Sciences*, vol. 76, pp. 18–32, 2015.
- [26] G. Dong, X. Ren, and Z. Wang, "A novel early warning method for atypical outbursts disasters in mines: extraction of indexes from gas concentration data for the early warning of atypical outbursts," *Arabian Journal of Geosciences*, vol. 12, no. 24, p. 796, 2019.

Research Article

Experimental Study on the Influence of Specimen Shape on Rockburst Proneness of Red Sandstone

Jiajun Yang,¹ Fengqiang Gong ,^{1,2,3} Dongqiao Liu,² and Zhixiang Liu¹

¹School of Resources and Safety Engineering, Central South University, Changsha 410083, China

²State Key Laboratory for Geomechanics and Deep Underground Engineering, China University of Mining and Technology, Beijing 100083, China

³School of Civil Engineering, Southeast University, Nanjing 211189, China

Correspondence should be addressed to Fengqiang Gong; fengqiangg@126.com

Received 9 February 2020; Revised 24 June 2020; Accepted 28 July 2020; Published 17 August 2020

Academic Editor: Caiping Lu

Copyright © 2020 Jiajun Yang et al. This is an open access article distributed under the Creative Commons Attribution License, which permits unrestricted use, distribution, and reproduction in any medium, provided the original work is properly cited.

To investigate the specimen shape effect on rockburst proneness of rock materials, a string of conventional and single-cycle loading-unloading uniaxial compression tests was performed with cylindrical and cuboid red sandstone specimens. Despite similar development paths on stress-strain curves for the specimens with two shapes, the cuboid specimens generally show a higher uniaxial compressive strength than the cylindrical specimens. The energy evolution laws inside the two shaped specimens were explored. The results show that the input energy density (IED), elastic energy density (EED), and dissipated energy density (DED) of the two shaped specimens increased in a quadratic relationship with the increment of unloading level. Moreover, the linear relationships between the EED, DED, and IED were further confirmed for two shaped specimens, which were defined as the linear energy storage and dissipation laws, respectively. The energy storage coefficients and energy dissipation coefficients (the slopes of the linear relationships between the EED, DED, and IED, respectively) are almost independent of the specimen shape. According to the linear energy storage and dissipation laws, the peak EED and peak DED of every specimen can be calculated accurately. Finally, combining the failure process of rock specimens recorded by a high-speed camera, the elastic energy index (W_{ET}), the residual elastic energy index (A_{EF}), and the far-field ejection mass ratio (M_F) of each specimen were adopted to assess the rockburst proneness of the red sandstone sampled in cylindrical and cuboid. The results show that cuboid specimens exhibited stronger rockburst proneness than cylindrical ones, which favorably agreed with the actual failure phenomena.

1. Introduction

With the underground engineering developing to the deeper crustal areas, rockburst phenomena appear with a growing trend which pose a vast risk to mining operations and result in production losses [1–7]. Hence, scholars in mounting number begin to focus on rockburst problems [8–13], and the rockburst proneness turned into one of the vital research sites [14–16]. Moreover, because the deformation and failure of rock are accompanied by energy conversion, rockburst is often caused by energy release [17]. Some scholars analyzed the rockburst proneness of rock materials from an energy perspective, and many rockburst proneness criteria were proposed and developed. For example, Kidybiński [18]

introduced the strain energy storage index W_{ET} with the single-cycle loading-unloading uniaxial compression (SCLUC) test, which has been widely used to assess the rockburst proneness of rock materials [19–23]; Wang and Park [20] investigated and predicted the intensity of the rockburst proneness of Linglong gold mine in China adopting the elastic strain energy PES; Based on the linear energy storage law, Gong et al. [16, 24] presented the peak-strength strain energy storage index W_p^{ET} and the residual elastic energy index A_{EF} . Among the above references, all of these rockburst proneness criteria were obtained with cylindrical specimens. However, in many cases, cuboid specimens were often used when investigating rock behavior under complex stress states such as biaxial and true triaxial

compression tests [25, 26]. Although several researchers have revealed the shape effect on the mechanical properties of rock specimens under the conventional uniaxial compression (UC) tests [27, 28], the studies on rockburst proneness of cuboid specimens were relatively rare.

In this paper, to investigate the effect of specimen shape on rockburst proneness, the SCLUC tests were implemented with the specimens of two shapes (cylinder and cuboid), and the input energy density (IED), elastic energy density (EED), and dissipated energy density (DED) were calculated by the graphical integration according to the stress-strain curves at different unloading points. According to the test results, the energy evolution laws inside the two shaped specimens were attained. Meanwhile, combined with the bursting processes of specimens accorded by a high-speed camera, the rockburst proneness of the cylindrical and cuboid specimens was compared by the elastic energy index (W_{ET}), the residual elastic energy index (A_{EF}), and the far-field ejection mass ratio (M_F).

2. Specimens and Methods

2.1. Specimen Preparation. The red sandstone block collected from the Shandong Province of China was used for testing. To compare the effect of specimen shape on the determination of rockburst proneness, the cylindrical and cuboid specimens with sizes of $\Phi 50 \times 100$ mm and of $50 \times 50 \times 100$ mm were prepared according to the guidelines of International Society for Rock Mechanics (ISRM). The cylindrical specimens were named as RS-CL, such as RS-CL-1; the cuboid specimens were named as RS-CB, such as RS-CB-1. The basic parameters of specimens were measured and are presented in Table 1.

2.2. Test Methods and Procedures. To acquire the IED, EED, and DED inside specimens at different unloading points (see Figure 1), a series of SCLUC tests were conducted on an Instron1346 testing machine. The test procedures, using the stress-strain curve of specimen RS-CB-4 as an example, were as follows:

- (1) To attain the uniaxial compressive strength (UCS) of specimens and further to determine the unloading points for SCLUC tests, the UC test was first carried out, and the loading rate was 150 kN/min (1.00 MPa/s) under the force control.
- (2) According to the UCS attained from the first test, five stress unloading points $i\sigma_c^{CB}$ (i represented the setting unloading level, $i = 0.1, 0.3, 0.5, 0.7, 0.9$; σ_c^{CB} represented the UCS of the cuboid specimen in the UC test) were generally set for five specimens, respectively. Then, the SCLUC tests were conducted. As Figure 1 shows, the stress was initially loaded to the unloading point and then unloaded to a minor value of “0.02 $i\sigma_c^{CB}$ ” (due to the restriction of equipment characteristics, the achievable stress minimum for unloading operation was unable to be “0”). After that, the stress was loaded once again from the minor value, until the specimen failed.

Therein, the loading rate and unloading rate were both controlled at 150 kN/min.

- (3) The UCS of the cuboid specimen in the SCLUC tests was denoted by σ_c^{iCB} , then the actual unloading level (i_a^{CB}) can be calculated as follows:

$$i_a^{CB} = \frac{i\sigma_c^{CB}}{\sigma_c^{iCB}} \quad (1)$$

In terms of the cylindrical specimens, a similar test procedure was employed referring to that of the cuboid specimens, except for the loading rate as well as the unloading rate at 120 kN/min (1.02 MPa/s), were adopted. Besides, for the distinction, σ_c^{CL} and σ_c^{iCL} were used to represent the UCS of the cylindrical specimens in the UC and SCLUC tests, respectively.

2.3. Calculation Method of Energy inside Rock Specimens. Considering the specimen volume in test results, the energy density was used as an investigation value in this study. During testing, the energy densities including IED, EED, and DED were commonly utilized to describe failure process of rock specimens. According to the law of thermodynamics which states there is no energy conversion between the rock specimens and the environment during the loading and unloading process [29], the relationship existing among energy densities is described as follows:

$$u_o = u_e + u_d, \quad (2)$$

where u_o is the IED, u_e is the EED, and u_d is the DED.

In this study, different stress unloading points were preset for the SCLUC tests. The initial loading curve and the unloading curve can be precisely determined according to the experimental data at each unloading point, and the energy densities were calculated by the graphical integration according to these curves. As Figure 2(a) shows, at the unloading point, the IED was described as the area enclosed by the loading curve and horizontal axis, and the EED as the area within the unloading curve and horizontal axis. The DED can be determined by subtracting the EED from IED further. Moreover, the calculation methods of IED at the peak point (peak IED) and failure energy density (FED) are shown in Figure 2(b), wherein the FED represented the additional energy provided by further compression of the rock specimen after the peak point. The peak IED was described as the area enclosed by the envelope curve of the two loading curves and horizontal axis, and the FED as the area enveloped by the post-peak curve and horizontal axis.

$$u_o^i = \int_0^{\varepsilon_2} f_1(\varepsilon) d\varepsilon, \quad (3)$$

$$u_e^i = \int_{\varepsilon_1}^{\varepsilon_2} f_2(\varepsilon) d\varepsilon, \quad (4)$$

$$u_d^i = u_o^i - u_e^i, \quad (5)$$

TABLE 1: Basic parameters of specimens.

Specimen shape	Specimen ID	Diameter or width (mm)	Height (mm)	Weight (g)	Density (g·cm ⁻³)	Longitudinal wave velocity (m·s ⁻¹)
Cylinder	RS-CL-1	48.73	100.80	457	2.43	3360.00
	RS-CL-2	48.72	99.65	455	2.45	3349.58
	RS-CL-3	48.70	99.73	455	2.45	3329.88
	RS-CL-4	48.72	100.33	456	2.44	3305.77
	RS-CL-5	48.70	100.33	458	2.45	3424.23
	RS-CL-6	48.70	100.03	456	2.45	3419.83
Cuboid	RS-CB-1	50.23	100.10	622	2.46	3309.09
	RS-CB-2	50.27	100.19	629	2.48	3295.72
	RS-CB-3	50.30	100.20	629	2.48	3206.40
	RS-CB-4	50.53	100.57	636	2.48	3357.60
	RS-CB-5	50.07	100.31	622	2.47	3378.41
	RS-CB-6	50.18	100.32	625	2.47	3429.74
	RS-CB-7	50.25	100.12	621	2.46	3354.10

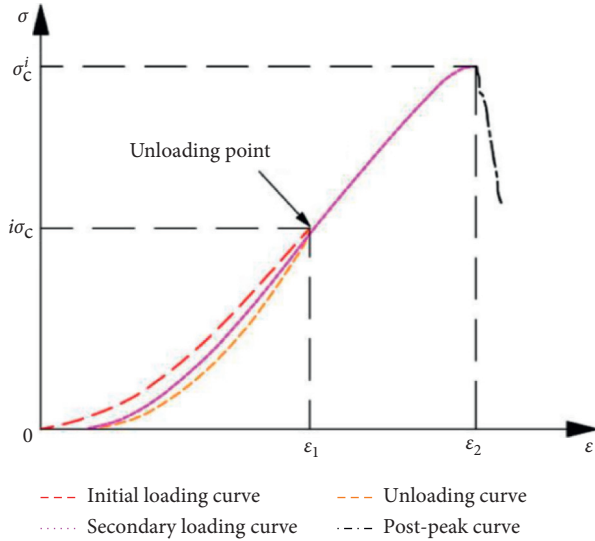


FIGURE 1: Stress-strain path of the SCLUC test.

$$U_o = \int_0^{\varepsilon_1} f_3(\varepsilon) d\varepsilon, \quad (6)$$

$$U_a = \int_{\varepsilon_1}^{\varepsilon_2} f_4(\varepsilon) d\varepsilon, \quad (7)$$

where u_o^i , u_c^i , u_d^i denoted the IED, EED, and DED at the unloading point, respectively; U_o denoted the peak IED, U_a denoted the FED; $f_1(\varepsilon)$, $f_2(\varepsilon)$ denoted the functions of loading and unloading curves, respectively; $f_3(\varepsilon)$ denoted the function of the envelope before peak point; and $f_4(\varepsilon)$ denoted the function of the post-peak curve.

3. Test Results

3.1. Stress-Strain Curves and UCS. To ensure that the measured strain only comes from the specimen, we have subtracted the strain of the stiff pad when drawing the stress-strain curve. The stress-strain curves of cylindrical and cuboid specimens at each unloading level are illustrated in

Figure 3. All the curves were in favourable consistency and generally consisted of a crack closure phase, linear elastic deformation and stable fracture propagation phase, unstable fracture propagation phase, and postfracture phase [30]. Meanwhile, as the stress-strain curves show, the initial loading curves did not coincide with the unloading curves, which was caused by the irreversible permanent deformation occurred in the loading-unloading process [31, 32]. Furthermore, the cuboid specimen possesses a more obvious nonlinear phase near the peak point of the stress-strain curve than the cylindrical specimens.

The UCS of the cylindrical and cuboid specimens in UC and SCLUC tests is shown in Table 2 and Figure 4. The UCS of the cuboid specimens was higher than that of the cylindrical specimens in general and approximately 12 MPa higher on average. Some scholars reported similar results, i.e., the cuboid specimen had a slightly higher strength than the cylindrical specimen by the laboratory test and numerical study [27, 28].

Zhao et al. [27] carried out the UC tests with cuboid specimens (at a size of $50 \times 50 \times 100$ mm, the cross-sectional area was 2500 mm^2) and cylindrical specimens (at a size of $\Phi 50 \times 100$ mm, the cross-sectional area was 1963 mm^2), and the result showed the UCS of the cuboid specimens was approximately 4 MPa higher than that of the cylindrical ones. Based on the basic parameters and sizes of the rock specimen adopted from the laboratory test of Zhao et al., Xu and Cai conducted a numerical simulation with cuboid and cylindrical specimens [28]. The simulation result was consistent with the laboratory test result, namely, the UCS of the cuboid specimens was higher than that of the cylindrical specimens. In such a case, if the cross-section of the cuboid specimen was equivalent to a circle, the equivalent diameter of this circle was 56.4 mm, which was significantly larger than the diameter of the cross-section of the cylindrical specimen. Therefore, a further numerical simulation, where the side length of the cuboid specimen was 44 mm (the cross-sectional area was 1936 mm^2), was conducted, and the result showed a close UCS for the specimens with two shapes. Hence, it can be understood that the cross-sectional areas may exert an influence on the UCS of the two shaped

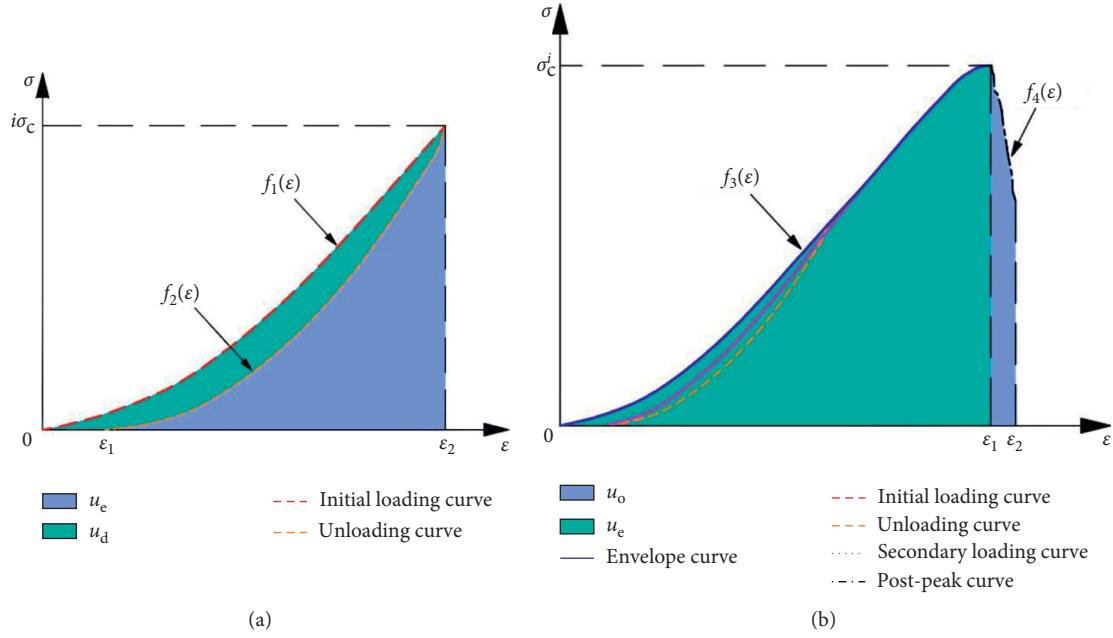


FIGURE 2: Calculation method of energy density. (a) Calculation of energy density at unloading point. (b) Calculation of energy density at peak point.

specimens, and the difference in UCS for the two shaped specimens can be narrowed via equalizing the cross-sectional areas. Xu and Cai confirmed that the end effect controlled the strength of the specimen according to the simulation model [28].

3.2. Energy Evolution Laws inside Specimens. In the rock test, the deformation and failure of the specimen under the action of external force are continuously transformed with the external energy, and the energy distribution and transformation run through the whole process. In recent years, the study of rock failure from an energy viewpoint has become a new research trend, and a host of advances have been obtained [16, 24, 33–36]. Rockburst hazard is one of the dynamic failure phenomena. To more effectively evaluate the rockburst proneness degree of the cylindrical and cuboid specimens further, the energy evolution characteristics inside specimens were explored. According to the energy calculation method in Figure 2(a), the energy densities at different unloading points are calculated in Table 3.

Figure 5 shows the mutual relationship among the IED (u_o^{CL} and u_o^{CB}), EED (u_e^{CL} and u_e^{CB}), DED (u_d^{CL} and u_d^{CB}), and the actual unloading level for cylindrical and cuboid specimens. Figure 5(a) displays the distinctly quadratic relationships between the three types of energy densities and the actual unloading level. For each of the shaped specimens, as the actual unloading level increases, the EED shows a quicker growing rate than the DED, which implies that the energy stored in the specimens was higher than the dissipated energy before the specimens failed. In addition, the fitting functions are displayed in Table 4, and all the fitting correlation coefficients were in excess of 0.9840.

Figures 5(b) and 5(c) display the linear relationships between the three types of energy densities. The largest correlation coefficient was up to 0.9999, which suggested the prominent linearity between the EED, DED, and IED. In addition, no matter what the fitting lines described the relationship between the IED and EED or between the IED and DED, these fitting lines of the two shaped specimens almost coincided. The uniform fitting functions of the linear relationships between the EED, DED, and the IED are as follows:

$$\begin{aligned} u_e &= Au_o + c, \\ u_d &= Bu_o - c, \\ A + B &= 1, \end{aligned} \quad (8)$$

where the A , B , and c are the fitting parameters. According to the fitting functions between the EED (or DED) and IED, we observed that the intercept (c) was 3 orders of magnitude smaller than the corresponding slope (A or B), so the effect of intercept on the linear relationships can be ignored, and the result of the fitting function was chiefly determined by the fitting slope. Of these, the linear relationships were defined as linear energy storage and dissipation laws; the slopes (A and B) of the linear energy storage and dissipation laws were defined as energy storage coefficient and energy dissipation coefficient, respectively, which were indicated the energy storage and dissipation capacities of rocks, respectively [16, 24]. In this study, the energy storage coefficients were 0.7596 and 0.7486, and the energy dissipation coefficients were 0.2404 and 0.2514 for cylindrical and cuboid specimens, respectively, which had little change. Namely, the change of specimen shape had a rare effect on the energy storage and dissipation

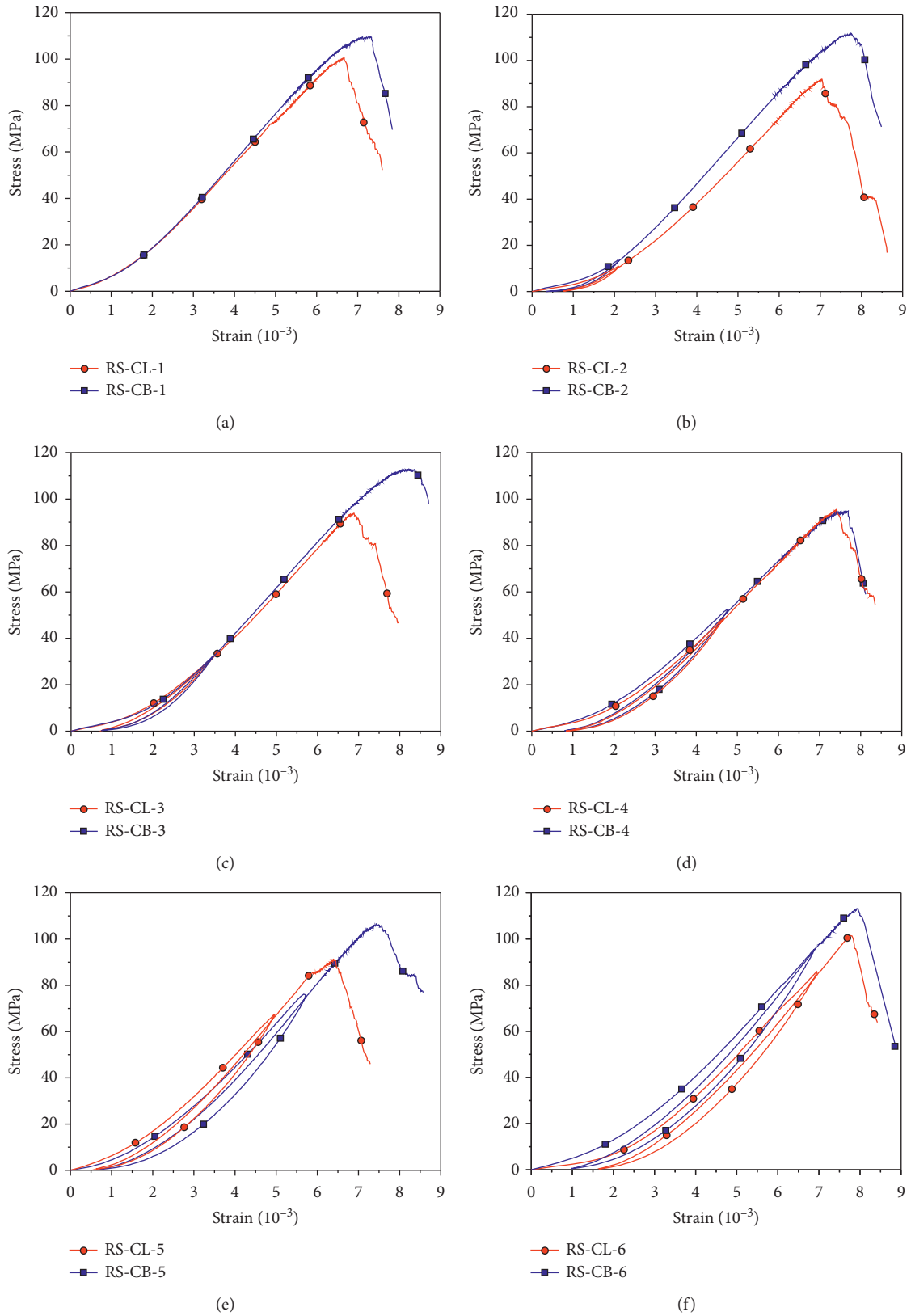


FIGURE 3: Stress-strain curves of cylindrical and cuboid specimens. (a) UC test. (b) $i = 0.1$. (c) $i = 0.3$. (d) $i = 0.5$. (e) $i = 0.7$. (f) $i = 0.9$.

TABLE 2: UCS of cylindrical and cuboid specimens.

Specimen shape	Specimen ID	Compressive strength (MPa)	Average (MPa)
Cylinder	RS-CL-1	100.66	95.76
	RS-CL-2	91.91	
	RS-CL-3	93.89	
	RS-CL-4	95.51	
	RS-CL-5	91.13	
	RS-CL-6	101.47	
Cuboid	RS-CB-1	108.77	107.68
	RS-CB-2	110.52	
	RS-CB-3	111.55	
	RS-CB-4	94.97	
	RS-CB-5	106.42	
	RS-CB-6	112.40	
	RS-CB-7	109.13	

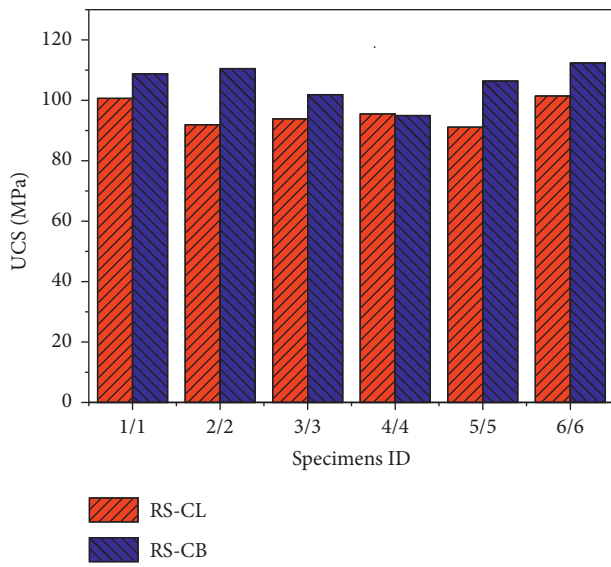


FIGURE 4: UCS of cylindrical and cuboid specimens.

capacities of the red sandstone. In other words, the linear energy storage and dissipation laws had no concern with the specimen shape and were the intrinsic nature of rock materials. Hence, according to the linear energy storage and dissipation laws, the EED and DED at each point can be calculated by using the IED at any corresponding point of the stress-strain curve. Especially, when the u_o^i denoted the peak IED, the EED and DED at the peak point (peak EED and peak DED) of each specimen can be calculated easily and accurately, namely,

$$U_e = AU_o + c, \quad (9)$$

$$U_d = BU_o - c, \quad (10)$$

where U_o , U_e , U_d are the peak IED, peak EED, and peak DED, respectively. These results of the peak EED and peak DED of cylindrical and cuboid specimens are shown in Table 5, as well as the results of the FED. For specimens with the same shape, the energy densities at the peak points were diverse. However, for the same kind of energy density at the specimen peak point, the energy density minimum of the

cuboid specimens was higher than the maximum of the cylindrical specimens. For example, the minimum EED for the cuboid specimens was $0.2344 \text{ mJ}\cdot\text{mm}^{-3}$, which was higher than the maximum of the cylindrical specimens that was $0.2221 \text{ mJ}\cdot\text{mm}^{-3}$.

The reason why the quadratic fitting curves of cuboid specimens are above to those of the cylindrical specimens (in Figure 5(a)) can be explained using the linear energy storage and dissipation laws. Because of the higher strength of the cuboid specimens than that of the cylindrical ones, whilst at the same unloading level, the unloading point of the cuboid specimens was higher than that of the cylindrical specimens. Therefore, according to the energy calculation method, the IED can be calculated in a larger area for cuboid specimens than cylindrical specimens, and the IED of cuboid specimens was larger than that of cylindrical specimens, so the IED curve of cuboid specimens was fitted higher than that of cylindrical specimens further. Meanwhile, due to the energy storage or dissipation coefficients of the two shaped specimens were almost equal, the EED or the DED of the cuboid specimens was larger than that of the cylindrical ones at the same unloading level, and the EED or the DED curve of the cuboid specimens was higher than the curves of cylindrical specimens further.

3.3. Failure Characteristics of Rock Specimens. Using a high-speed camera, the bursting moments of the specimens were recorded. The processes with the same unloading level are contrastively illustrated in Figure 6. The time interval between every two images was annotated as 8 ms for every specimen. Taking the results of the UC tests as examples to show the burst process (as shown in Figures 6(a) and 6(b)). For specimen RS-CL-1, before bursting, a microfracture occurred and a handful of rock fragments slid down near the specimen. Afterward, the specimen burst with a slight voice, and in the meantime, the microfracture expanded and the fragments as well as grains ejected to the ramp below at a slow velocity. For specimen RS-CB-1, the rock block had loosened from the specimen matrix before bursting. Soon, considerable amounts of rock blocks and fragments as well as grains quickly ejected in an approximately horizontal direction.

TABLE 3: Calculation results of energy density.

Specimen shape	Specimen ID	Unloading point (MPa)	Actual unloading level	At unloading point		
				IED ($\text{mJ}\cdot\text{mm}^{-3}$)	EED ($\text{mJ}\cdot\text{mm}^{-3}$)	DED ($\text{mJ}\cdot\text{mm}^{-3}$)
Cylinder	RS-CL-1	—	—	—	—	—
	RS-CL-2	11.03	0.12	0.0085	0.0048	0.0037
	RS-CL-3	30.98	0.33	0.0396	0.0301	0.0095
	RS-CL-4	47.76	0.50	0.0812	0.0608	0.0204
	RS-CL-5	66.52	0.73	0.1353	0.1020	0.0333
	RS-CL-6	86.25	0.85	0.2136	0.1617	0.0519
Cuboid	RS-CB-1	—	—	—	—	—
	RS-CB-2	13.26	0.12	0.0109	0.0065	0.0044
	RS-CB-3	31.23	0.28	0.0395	0.0281	0.0114
	RS-CB-4	52.02	0.55	0.0940	0.0696	0.0244
	RS-CB-5	76.62	0.72	0.1682	0.1268	0.0414
	RS-CB-6	94.42	0.84	0.2611	0.1979	0.0632
	RS-CB-7	103.67	0.95	0.3054	0.2247	0.0807

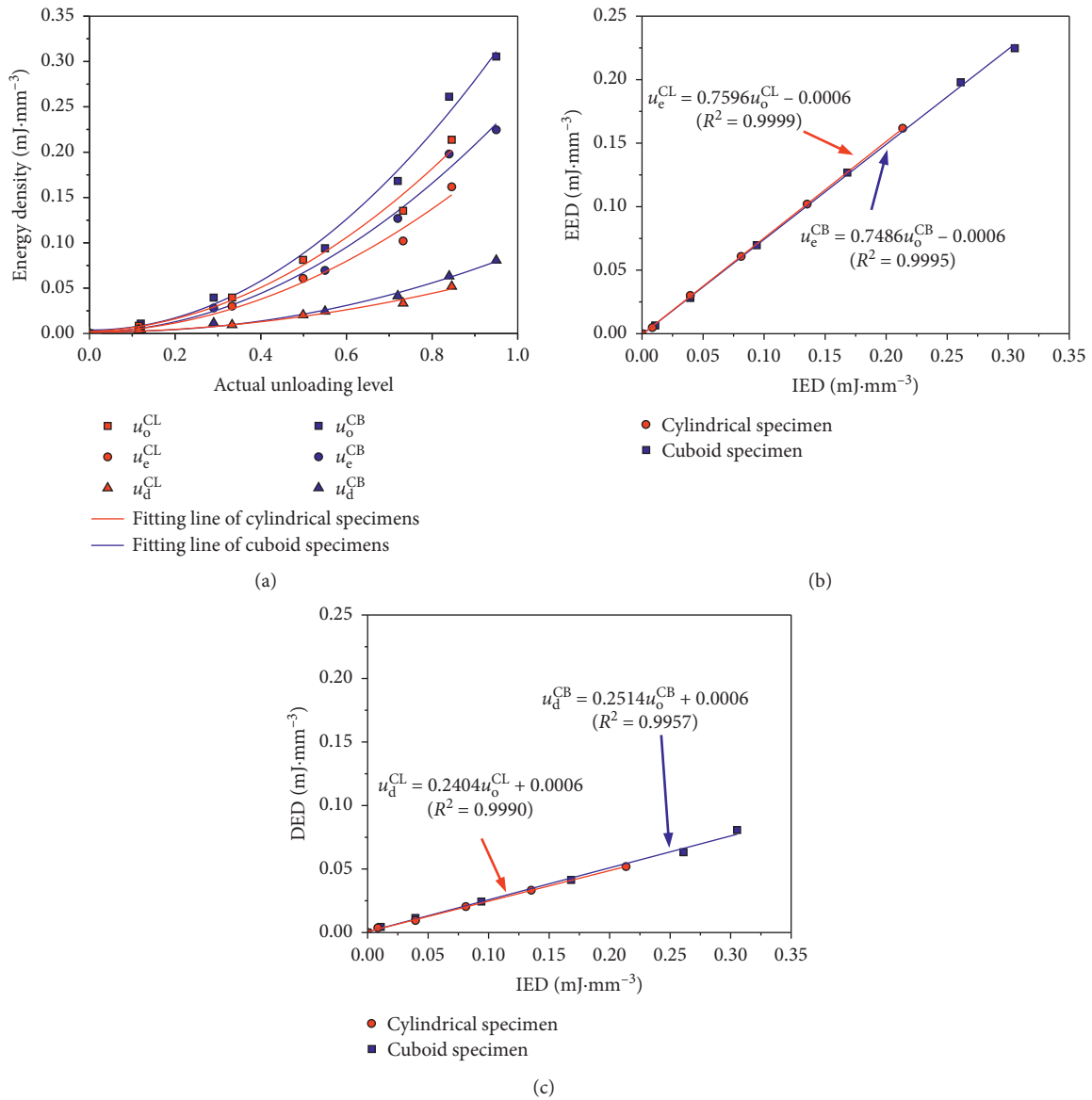


FIGURE 5: Comparison of energy characteristics inside cylindrical and cuboid specimens.

TABLE 4: Fitting functions among three types of energy densities and the actual unloading level.

Relationship	Cylindrical specimen	Cuboid specimen
u_o and i_a	$u_o^{CL} = 0.2582i_a^2 + 0.0178i_a + 0.0022$ ($R^2 = 0.9846$)	$u_o^{CB} = 0.3574i_a^2 - 0.0166i_a + 0.0048$ ($R^2 = 0.9924$)
u_e and i_a	$u_e^{CL} = 0.1970i_a^2 + 0.0128i_a + 0.0012$ ($R^2 = 0.9844$)	$u_e^{CB} = 0.2621i_a^2 - 0.0072i_a + 0.0023$ ($R^2 = 0.9905$)
u_d and i_a	$u_d^{CL} = 0.0612i_a^2 + 0.0051i_a + 0.0011$ ($R^2 = 0.9841$)	$u_d^{CB} = 0.0952i_a^2 - 0.0094i_a + 0.0025$ ($R^2 = 0.9926$)

TABLE 5: Calculations of the energy density.

Specimen shape	Specimen ID	At peak point			FED ($\text{mJ}\cdot\text{mm}^{-3}$)
		IED ($\text{mJ}\cdot\text{mm}^{-3}$)	EED ($\text{mJ}\cdot\text{mm}^{-3}$)	DED ($\text{mJ}\cdot\text{mm}^{-3}$)	
<i>Cylinder</i>	RS-CL-1	0.2932	0.2221	0.0711	0.0755
	RS-CL-2	0.2556	0.1936	0.0620	0.0942
	RS-CL-3	0.2605	0.1973	0.0632	0.0795
	RS-CL-4	0.2829	0.2143	0.0686	0.0697
	RS-CL-5	0.2506	0.1898	0.0608	0.0615
	RS-CL-6	0.2904	0.2200	0.0704	0.0536
<i>Cuboid</i>	RS-CB-1	0.3562	0.2661	0.0901	0.0696
	RS-CB-2	0.3680	0.2749	0.0931	0.0753
	RS-CB-3	0.3913	0.2923	0.0990	0.0657
	RS-CB-4	0.3139	0.2344	0.0795	0.0379
	RS-CB-5	0.3331	0.2488	0.0843	0.0969
	RS-CB-6	0.3707	0.2769	0.0938	0.0817
	RS-CB-7	0.3951	0.2952	0.0999	0.0549

Given the limited space available, the bursting processes of other specimens were not reported in detail here. In addition, the failure mode and burst characteristics of each rock specimen are shown in Figure 7 and Table 6. For failure mode, the cylindrical specimens showed a mainly tensile failure, while most cuboid specimens showed a shear failure. In the simulation conducted by Xu and Cai [28], the granite cylindrical and cuboid specimens both showed the shear failure, which were inconsistent with our test results of red sandstone specimens. The differences may be caused by the different composition, arrangement, and cementation of rock particles inside different lithological rocks. Besides, the specimens with the same shape showed the different failure modes in our study, for example, the specimen RS-CB-1 showed a shear failure, but the specimen RS-CB-4 showed a tensile failure, which was influenced by the anisotropy of specimens.

In fact, for the shear failure of specimens, the microcracks inside the rocks continued to grow and nucleate under the external loads and formed the macroscopic shear plane as approaching the peak strength, which eventually led to the rock failure; for the tensile failure, the axial compression was accompanied by lateral expansion, which was conducive to the development of longitudinal microcracks; after these microcracks reached a certain length, the microcrack propagation became unstable, resulting in axial splitting [37].

Moreover, for the tests with same specimen shape but at different unloading levels, or the tests at a constant unloading

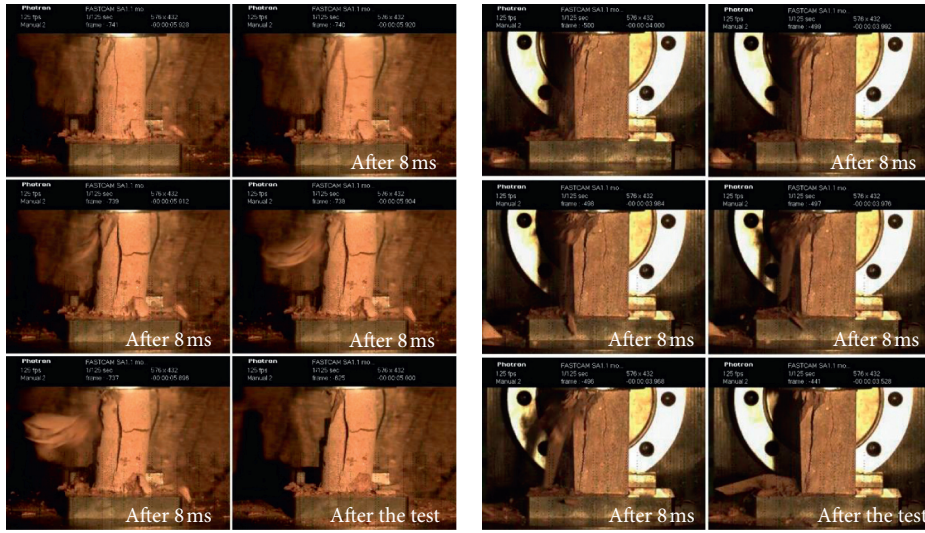
level but with different specimen shapes, the burst characteristics of specimens performed some differences. For example, specimen RS-CB-3 (the cuboid-shaped specimen at the unloading point of 0.3) exhibited the rock block flying out and a mass of fragments ejected at a fast velocity, while only a handful of fragments ejected at a relatively slow velocity for specimen RS-CB-6 (the cuboid-shaped specimen at the unloading point of 0.9); specimen RS-CL-2 (the cylindrical-shaped specimen at the unloading point of 0.1) just burst with fragments falling, while specimen RS-CB-2 (the cuboid-shaped specimen at the unloading point of 0.1) burst with fast fragments ejection. But on the whole, the cylindrical specimens emitted a slight sound at burst moment, and the minor quantity of fragments was ejected at a slow velocity, while the cuboid specimens emitted a louder sound, and a greater quantity of fragments was ejected with a faster velocity.

4. Rockburst Proneness Analysis

4.1. The Elastic Energy Index. The elastic energy index (W_{ET}) proposed by Kidybiński was extensively used in the rock mechanics field. The index is determined by the ratio of elastic energy to dissipated energy being at 80%~90% of peak strength. Accordingly, the values of W_{ET} for specimens RS-CL-6 and RS-CB-6 are 3.16 and 3.13, respectively. From the classification criteria as follows, the red sandstone specimens shaped as cylinder and cuboid performed the same burst proneness, i.e., the low rockburst proneness.



FIGURE 6: Continued.

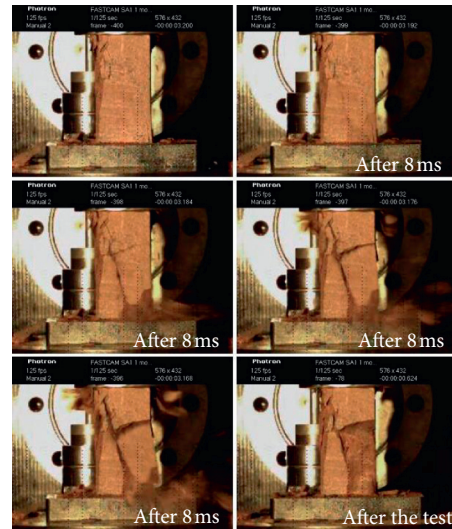


(g)

(h)



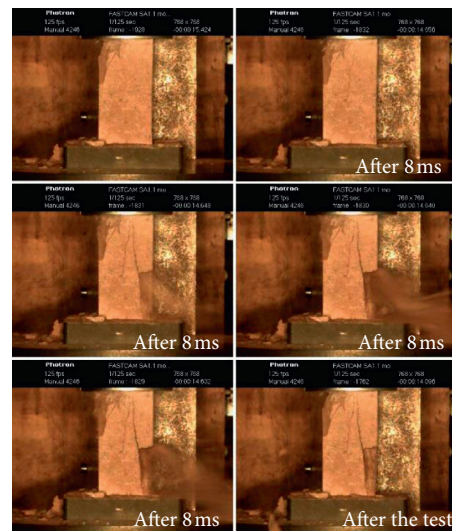
(i)



(j)



(k)



(l)

FIGURE 6: Failure process of specimens with uniaxial compression tests. (a) RS-CL-1. (b) RS-CB-1. (c) RS-CL-2. (d) RS-CB-2. (e) RS-CL-3. (f) RS-CB-3. (g) RS-CL-4. (h) RS-CB-4. (i) RS-CL-5. (j) RS-CB-5. (k) RS-CL-6. (l) RS-CB-6.

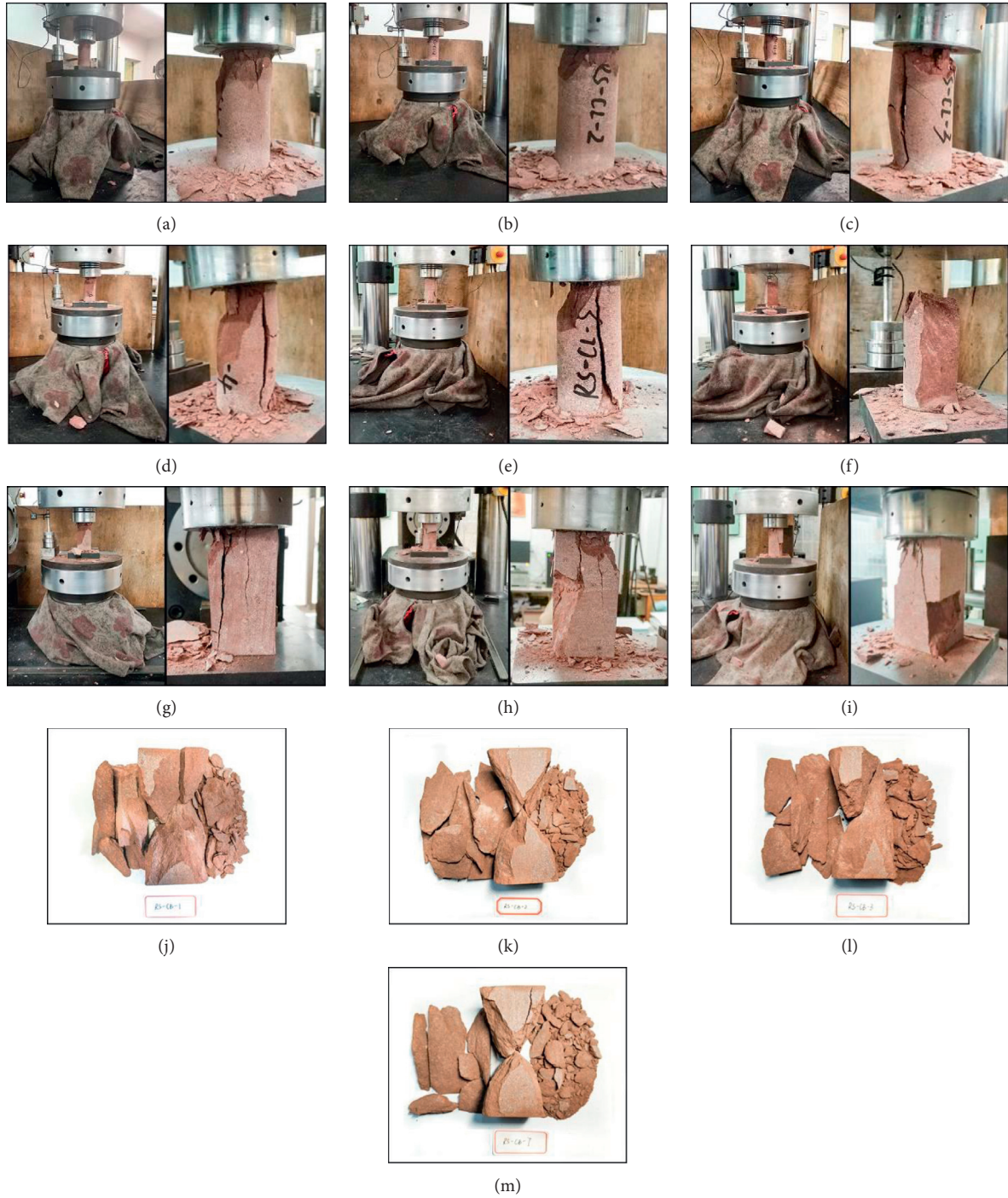


FIGURE 7: Failure characteristics of cylindrical and cuboid specimens. (a) RS-CL-1. (b) RS-CL-2. (c) RS-CL-3. (d) RS-CL-4. (e) RS-CL-5. (f) RS-CL-6. (g) RS-CB-4. (h) RS-CB-5. (i) RS-CB-6. (j) RS-CB-1. (k) RS-CB-2. (l) RS-CB-3. (m) RS-CB-7.

$$W_{ET} \begin{cases} < 2, & \text{no rockburst proneness,} \\ = 2 \sim 5, & \text{low rockburst proneness,} \\ > 5, & \text{high rockburst proneness.} \end{cases} \quad (11)$$

4.2. *The Residual Elastic Energy Index.* According to the obtained linear energy storage law of rock under uniaxial compression [16, 24, 35], Gong et al. [16] proposed the residual elastic energy index (A_{EF}), which was a novel

TABLE 6: Ejection characteristic information of specimens.

Specimen shape	Specimen ID	Failure mode	Burst sound	Fragments ejection velocity	Fragments ejection quantity
<i>Cylinder</i>	RS-CL-1	Tensile	Slight	Slow	Minor
	RS-CL-2	Tensile	Slight	—	—
	RS-CL-3	Tensile and shear	Slight	Slow	Minor
	RS-CL-4	Tensile and shear	Slight	Slow	Modest
	RS-CL-5	Tensile	Slight	Slow	Minor
	RS-CL-6	Tensile and shear	Slight	Slow	Modest
<i>Cuboid</i>	RS-CB-1	Shear	Loud	Fast	Great
	RS-CB-2	Shear	Loud	Medium	Modest
	RS-CB-3	Shear	Loud	Fast	Great
	RS-CB-4	Tensile	Moderate	Slow	Modest
	RS-CB-5	Shear and tensile	Moderate	Medium	Modest
	RS-CB-6	Tensile	Moderate	Medium	Modest
	RS-CB-7	Shear	Loud	Fast	Great

method to estimate rockburst proneness. The calculation method of A_{EF} is as follows:

$$A_{EF} = U_e - U_a, \quad (12)$$

where U_a can be calculated by equation (7), and U_e can be calculated by equation (9). Additionally, the classification criteria of A_{EF} are as follows:

$$A_{EF} \begin{cases} < 50 \frac{\text{kJ}}{\text{m}^3}, & \text{no rockburst proneness,} \\ = 50 \sim 150 \frac{\text{kJ}}{\text{m}^3}, & \text{light rockburst proneness,} \\ = 150 \sim 200 \frac{\text{kJ}}{\text{m}^3}, & \text{moderate rockburst proneness,} \\ > 200 \frac{\text{kJ}}{\text{m}^3}, & \text{strong rockburst proneness.} \end{cases} \quad (13)$$

The A_{EF} values of different shaped specimens are given in Table 7, and the comparative results are shown in Figure 8. According to the classification criteria, most of the cylindrical specimens showed light rockburst proneness, yet the cuboid specimens were moderate and strong in rockburst proneness. Meanwhile, on average for A_{EF} , the cylindrical specimens belonged to light rockburst proneness, yet the cuboid specimens reached to strong rockburst proneness, which indicated the rockburst proneness of cylindrical specimens was lighter than cuboid ones in general.

4.3. The Far-Field Ejection Mass Ratio. Rockburst in deep engineering is a dynamic failure phenomenon. Studying the kinetic energy of the rock fragments after the rock failure in a laboratory test was effective to analyze the rockburst proneness. If the accurate kinetic energy of the ejected rock fragment was required, the ideal was to obtain the mass and velocity of all rock fragments. However, in the UC test, the rock fragments will be ejected into various directions and

angles. We cannot accurately track the path of all rock fragments to measure their speed and mass.

Even so, the faster the speed of the rock fragments was, the farther the ejection distance will be, and the more the mass of the rock fragment ejected into a farther distance will be, the stronger rockburst proneness the specimen showed. Therefore, Gong et al. divided the inner and outer regions according to the boundary of the equipment indenter, and the fragment mass in the two regions was counted, respectively (shown as in Figure 9), and then the rockburst proneness index named far-field ejection mass ratio (M_F) was proposed [16]. The calculation method of M_F is as follows:

$$M_F = \frac{m_1}{(m_1 + m_2)}, \quad (14)$$

where m_1 denotes the fragment mass falling in the area that is outside the indenter and within the test platform; m_2 denotes the fragment mass on the indenter; and the sum of m_1 and m_2 is the fragment mass separated from the specimen matrix. Significantly, because the velocity and distance of the ejected rock fragments were considered, the M_F can manifest the kinetic energy of the fragments to some extent.

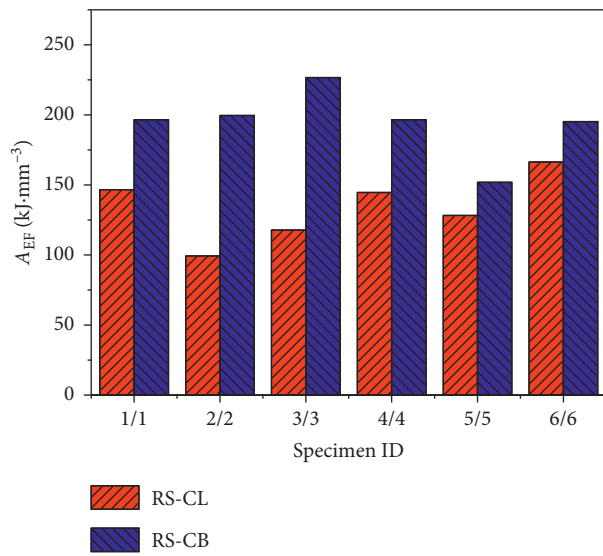
The classification criteria of M_F are as follows:

$$M_F = \begin{cases} = 0, & \text{no rockburst proneness,} \\ = 0 \sim 0.4, & \text{light rockburst proneness,} \\ = 0.4 \sim 0.6, & \text{moderate rockburst proneness,} \\ > 0.6, & \text{strong rockburst proneness.} \end{cases} \quad (15)$$

According to the definition and classification criteria of M_F , two extreme phenomena may exist: (1) when $m_1 = 0$, no fragment mass flies beyond the indenter, under this circumstance, $M_F = 0$, which corresponds to no rockburst proneness; (2) when $m_2 = 0$, all the fragments fly beyond the indenter; in this case, $M_F = 1$, which corresponds that the rock specimen tested is subject to strongest rockburst proneness. When $0 < M_F < 1$, the rockburst proneness degree was in the range from light rockburst proneness to strong rockburst proneness. Table 8 lists the calculations of M_F in this work.

TABLE 7: Calculations of the residual elastic energy index of specimens.

Specimen shape	Specimen ID	A_{EF} ($\text{kJ}\cdot\text{mm}^{-3}$)	Rockburst proneness	Average of A_{EF} ($\text{kJ}\cdot\text{mm}^{-3}$)
Cylinder	RS-CL-1	146.6	Light	133.83
	RS-CL-2	99.4	Light	
	RS-CL-3	117.8	Light	
	RS-CL-4	144.6	Light	
	RS-CL-5	128.3	Light	
	RS-CL-6	166.4	Moderate	
Cuboid	RS-CB-1	196.5	Moderate	200.94
	RS-CB-2	199.6	Moderate	
	RS-CB-3	226.6	Strong	
	RS-CB-4	196.5	Moderate	
	RS-CB-5	151.9	Moderate	
	RS-CB-6	195.2	Moderate	
	RS-CB-7	240.3	Strong	

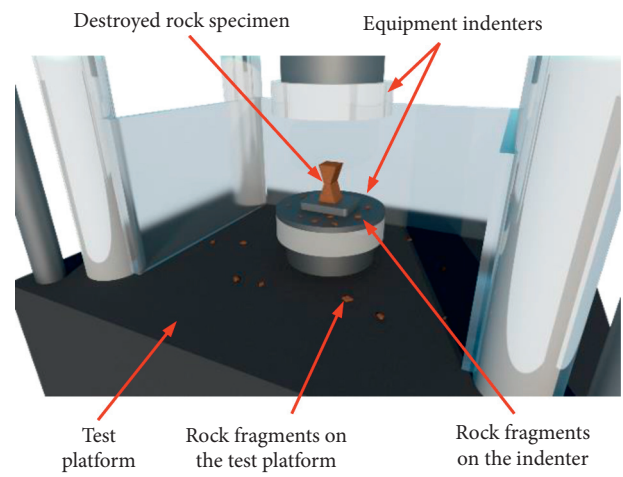
FIGURE 8: Comparative results of cylindrical and cuboid specimens with A_{EF} .

According to the results, the cylindrical specimens performed mainly light and moderate rockburst proneness, yet the cuboid specimens performed moderate and strong proneness on the whole. On average for M_F , the cylindrical specimens were light rockburst proneness, yet the cuboid specimens were strong rockburst proneness.

5. Discussions

In this paper, three indexes (the W_{ET} , A_{EF} , and M_F) were adopted to access the rockburst proneness of red sandstone specimens with two shapes, respectively. However, the discriminations of three indexes had some discrepancies: W_{ET} indicated that the cylindrical and cuboid specimens showed the same low rockburst proneness; A_{EF} and M_F indicated the cylindrical specimens showed the light rockburst proneness, yet the cuboid specimens showed the moderate and strong rockburst proneness in general.

To compare the accuracy of the discriminant results of two shaped specimens by the three rockburst proneness indexes, we analyzed the discriminant mechanism of them.

FIGURE 9: Calculation schematic of M_F .

At first, we took the maximal peak IED of two shaped specimens (in Table 5) as the maximal value (for example, the maximal peak IED of the cylindrical specimen was $0.2932 \text{ mJ}\cdot\text{mm}^{-3}$). By bringing the IED from 0 to $0.2932 \text{ mJ}\cdot\text{mm}^{-3}$ into the linear energy storage and dissipation laws of the cylindrical specimen, the EED and DED corresponding to the IED at each point in the pre-peak phase of the stress-strain curve can be calculated, and the ratio of EED to DED corresponding to the IED at each point can be calculated further. Hence, the variations of the ratio of EED to DED versus IED can be shown in Figure 10. Besides, the ratio results attained from the actual tests are also demonstrated as the discrete points in Figure 10 as well.

In Figure 10, the discrete points were well distributed near the variations of energy density ratio for specimens of each shape, and the discreteness of discrete points of the cuboid specimens was apparently smaller than that of the cylindrical specimens. Besides, as the IED increased, the energy density ratio tended to rise up sharply at first and then quickly became nearly steady. The ratio increased extremely slowly when the IED exceeded $0.20 \text{ mJ}\cdot\text{mm}^{-3}$. With the IEDs reaching to their maximums (i.e., at the peak strength), the energy density ratios for cylindrical and cuboid specimens are 3.12 and 2.95, respectively, which show

TABLE 8: Calculations of the far-field ejection mass ratio of specimens.

Specimen shape	Specimen ID	M_F	Rockburst proneness	Average of M_F
Cylinder	RS-CL-1	0.47	Moderate	0.30
	RS-CL-2	0.04	Light	
	RS-CL-3	0.15	Light	
	RS-CL-4	0.43	Moderate	
	RS-CL-5	0.14	Light	
	RS-CL-6	0.59	Moderate	
Cuboid	RS-CB-1	0.76	Strong	0.64
	RS-CB-2	0.48	Moderate	
	RS-CB-3	0.71	Strong	
	RS-CB-4	0.58	Moderate	
	RS-CB-5	0.55	Moderate	
	RS-CB-6	0.54	Moderate	
	RS-CB-7	0.86	Strong	

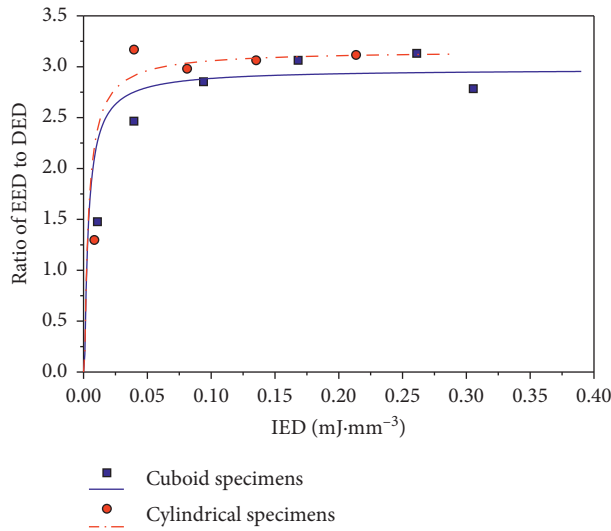


FIGURE 10: Relationship between IED and the ratio of EED to DED.

the rockburst proneness of the two shaped specimens being the low proneness and are consistent with the assessments by W_{ET} . From this viewpoint, W_{ET} had certain validity. Unexpectedly, according to the failure phenomena of the specimens accorded by a high-speed camera, the rockburst proneness of the cylindrical specimen was significantly lighter than that of the cuboid specimen.

In fact, the evaluation results of the W_{ET} (or the method which used the ratio of EED to DED at the peak strength in this paper) did not consider the post-peak phase, and it cannot reflect the energy dissipation required for the failure of the rock after the peak strength and the energy release after the rock failure. Moreover, the laboratory rockburst phenomenon of the rock specimen only occurred when the applied stress reaches the peak strength, which also indicated that the assessment of the rockburst proneness of the specimen via the W_{ET} had certain limitations.

Since the UCS of the cuboid specimen was greater than that of the cylindrical specimen in general, more energy needed to be input into the cuboid specimen to reach its peak point, so the peak IED of the cuboid specimen will be

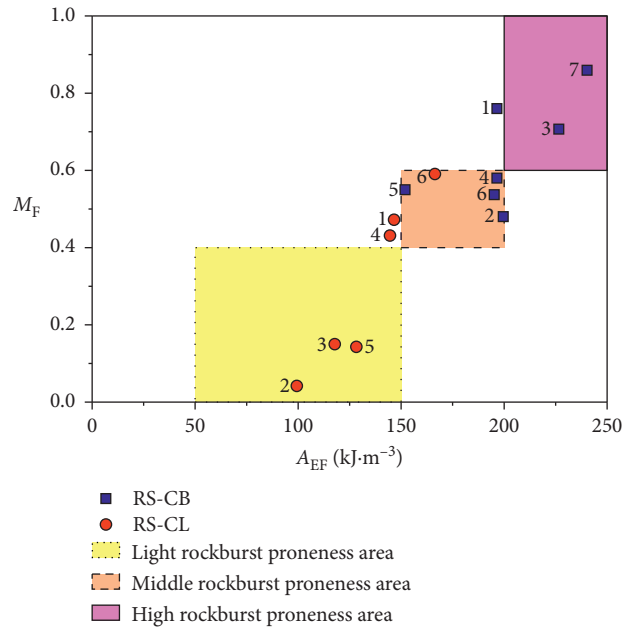


FIGURE 11: Matching relationship between the residual elastic energy index and far-field ejection mass ratio.

greater than that of the cylindrical specimen. Moreover, due to the energy storage coefficients for the cuboid and cylindrical specimens were roughly constant, the peak EED of the cuboid specimen was larger than that of the cylindrical specimen. Besides, Gong et al. [16] have found that no connection existed between the peak EED and FED. The residual EED was mainly determined by the peak EED. According to the calculations of the energy densities at the peak point (in Table 5), the peak EED of the cylindrical specimen was always smaller than that of the cuboid specimen, so the residual EED of the cylindrical specimen will be smaller than that of the cuboid specimen in general. Thus, the cylindrical specimen showed a lighter rockburst proneness than the cuboid specimen, which was in close accordance with the failure phenomena of both cylindrical and cuboid specimens. Namely, the A_{EF} was more suitable than the W_{ET} to assess the rockburst proneness of specimens.

Moreover, the rockburst proneness of the two shaped specimens was evaluated from the kinetic energy of ejected rock fragments through the M_F in this work, and the results also conform to the actual burst phenomena, namely, the cylindrical specimen showed the light rockburst proneness, and the cuboid specimen showed the moderate and strong rockburst proneness. Figure 11 illustrates the matching area of corresponding rockburst proneness degree between the A_{EF} and M_F . It shows that the rockburst proneness estimated results from cylindrical and cuboid specimens were at or near the same matching areas. In other words, the rockburst proneness estimated results calculated by the A_{EF} and M_F were in good accordance, and these two methods can accurately assess the rockburst proneness of specimens.

In fact, the A_{EF} assessed the rockburst proneness of rock materials via a qualitative method from the energy conversion perspective, and the M_F was a semiquantitative method that considered the failure characteristics. If A_{EF} and M_F are combined to evaluate the rockburst proneness, the evaluation results may be more accurate.

6. Conclusions

Based on the results attained from the UC and SCLUC tests with cylindrical and cuboid specimens, a comparison study of the specimen shape effect on rockburst proneness of the red sandstone was carried out. The following conclusions were drawn:

- (1) The development paths of the stress-strain curves change little with the changing specimen shapes. Meanwhile, the UCS of the cuboid specimens was approximately 12 MPa higher than that of the cylindrical specimens. Equalizing the stressed areas of the two shaped specimens would narrow the difference in UCS.
- (2) For either cylindrical or cuboid specimens, significant energy laws occur during the loading and unloading process. On the one hand, any of the IED, EED, or DED presents distinctly quadratic functional relationships with the increment of the actual unloading level. On the other hand, the prominent linear law occurs between the EED, DED, and IED. Moreover, the energy storage coefficient and energy dissipation coefficient are barely affected by the change in specimen shape.
- (3) For the failure mode, the cylindrical specimens show a principally tensile failure, and the cuboid specimens show a shear failure. Moreover, for the tests with same specimen shapes but at different unloading levels, or the tests at a constant unloading level but with different specimen shapes, the specimens show the different burst characteristics that are slight or strong. But on the whole, the cylindrical specimen emitted a slight sound, and its ejected fragments are slow and minor, while the cuboid specimen mostly performed a louder sound, and a

greater quantity of fragments was ejected at a faster velocity.

- (4) The rockburst proneness of every specimen is evaluated by the elastic energy index (W_{ET}), the residual elastic energy index (A_{EF}), and the far-field ejection mass ratio (M_F). Of these, the calculation results of the W_{ET} are different from the actual burst phenomena, yet the results of A_{EF} and M_F are in favourable agreement and in accordance with the burst phenomena that the cylindrical specimens show a light rockburst proneness, while the cuboid specimens show a moderate or strong rockburst proneness on the whole.

Nomenclature

m_1 :	Rock fragment mass that is outside the indenter and on the test platform (g)
m_2 :	Rock fragment mass on the indenter (g)
U_a :	Failure energy density after the peak point ($\text{mJ}\cdot\text{mm}^{-3}$)
u_d :	Dissipated energy density ($\text{mJ}\cdot\text{mm}^{-3}$)
u_d^{CL} and u_d^{CB} :	Dissipated energy density of cylindrical and cuboid specimens ($\text{mJ}\cdot\text{mm}^{-3}$)
u_e :	Elastic energy density ($\text{mJ}\cdot\text{mm}^{-3}$)
u_e^{CL} and u_e^{CB} :	Elastic energy density of cylindrical and cuboid specimens ($\text{mJ}\cdot\text{mm}^{-3}$)
u_e^i :	Elastic energy density at the unloading point ($\text{mJ}\cdot\text{mm}^{-3}$)
U_e :	Elastic energy density at the peak point ($\text{mJ}\cdot\text{mm}^{-3}$)
u_d^i :	Dissipated energy density at the unloading point ($\text{mJ}\cdot\text{mm}^{-3}$)
u_o :	Input energy density ($\text{mJ}\cdot\text{mm}^{-3}$)
u_o^{CL} and u_o^{CB} :	Input energy density of cylindrical and cuboid specimens ($\text{mJ}\cdot\text{mm}^{-3}$)
u_o^i :	Input energy density at the unloading point ($\text{mJ}\cdot\text{mm}^{-3}$)
U_o :	Input energy density at the peak point ($\text{mJ}\cdot\text{mm}^{-3}$)
$\sigma_c^{\text{CL}}, \sigma_c^{\text{CB}}$:	Uniaxial compressive strength of cylindrical and cuboid specimens in the UC test (MPa)
$\sigma_c^{i\text{CL}}, \sigma_c^{i\text{CB}}$:	Uniaxial compressive strength of cylindrical and cuboid specimens in the SCLUC test (MPa)
<i>Dimensionless</i>	
A_{EF} :	Residual elastic energy index
DED:	Dissipated energy density
EED:	Elastic energy density
FED:	Failure energy density
i :	Setting unloading level in the SCLUC test
i_a^{CL} and i_a^{CB} :	Actual unloading level of cylindrical and cuboid specimens in the SCLUC test
IED:	Input energy density
M_F :	Far-field ejection mass ratio
SCLUC:	Single-cycle loading-unloading uniaxial compression
UC:	Uniaxial compression
UCS:	Uniaxial compressive strength
W_{ET} :	Elastic energy index

W_p^{ET} : Peak-strength strain energy storage index.

Data Availability

All data generated or analyzed during this study are included within this article.

Conflicts of Interest

The authors declare that there are no conflicts of interest regarding the publication of this paper.

Acknowledgments

This work was supported by the National Natural Science Foundation of China (Grant no. 41877272) and the State Key Laboratory for GeoMechanics and Deep Underground Engineering, China University of Mining & Technology, Beijing (Grant no. SKLGDUEK1827).

References

- [1] W. D. Ortlepp and T. R. Stacey, "Rockburst mechanisms in tunnels and shafts," *Tunnelling and Underground Space Technology*, vol. 9, no. 1, pp. 59–65, 1994.
- [2] P. K. Kaiser and M. Cai, "Design of rock support system under rockburst condition," *Journal of Rock Mechanics and Geotechnical Engineering*, vol. 4, no. 3, pp. 215–227, 2012.
- [3] C. P. Lu, G. J. Liu, H. Y. Wang, and J. H. Xue, "Numerical investigation of rockburst effect of shock wave on underground roadway," *Shock and Vibration*, vol. 2015, Article ID 867582, 10 pages, 2015.
- [4] P. G. Ranjith, J. Zhao, M. Ju, R. V. S. De Silva, T. D. Rathnaweera, and A. K. M. S. Bandara, "Opportunities and challenges in deep mining: a brief review," *Engineering*, vol. 3, no. 4, pp. 546–551, 2017.
- [5] X. B. Li, F. Q. Gong, M. Tao et al., "Failure mechanism and coupled static-dynamic loading theory in deep hard rock mining: a review," *Journal of Rock Mechanics and Geotechnical Engineering*, vol. 9, no. 4, pp. 767–782, 2017.
- [6] C. P. Lu, Y. Liu, N. Zhang, T. B. Zhao, and H. Y. Wang, "In-situ and experimental investigations of rockburst precursor and prevention induced by fault slip," *International Journal of Rock Mechanics and Mining Sciences*, vol. 108, pp. 86–95, 2018.
- [7] X. T. Feng, Y. Y. Zhou, and Q. Jiang, "Rock mechanics contributions to recent hydroelectric developments in China," *Journal of Rock Mechanics and Geotechnical Engineering*, vol. 11, no. 3, pp. 511–526, 2019.
- [8] P. K. Kaiser and S. M. Maloney, "Scaling laws for the design of rock support," *Seismicity Associated with Mines, Reservoirs and Fluid Injections*, vol. 150, no. 3-4, pp. 415–434, 1997.
- [9] X. F. Si and F. Q. Gong, "Strength-weakening effect and shear-tension failure mode transformation mechanism of rockburst for fine-grained granite under triaxial unloading compression," *International Journal of Rock Mechanics and Mining Sciences*, vol. 131, Article ID 104347, 2020.
- [10] A. Manouchehrian and M. Cai, "Simulation of unstable rock failure under unloading conditions," *Canadian Geotechnical Journal*, vol. 53, no. 1, pp. 22–34, 2016.
- [11] F. q. Gong, Y. Luo, X. B. Li, X. F. Si, and M. Tao, "Experimental simulation investigation on rockburst induced by spalling failure in deep circular tunnels," *Tunnelling and Underground Space Technology*, vol. 81, pp. 413–427, 2018.
- [12] F. Q. Gong, X. F. Si, X. B. Li, and S. Y. Wang, "Experimental investigation of strain rockburst in circular caverns under deep three-dimensional high-stress conditions," *Rock Mechanics and Rock Engineering*, vol. 52, no. 5, pp. 1459–1474, 2019.
- [13] H. Wagner, "Deep mining: a rock engineering challenge," *Rock Mechanics and Rock Engineering*, vol. 52, no. 5, pp. 1417–1446, 2019.
- [14] M. He, L. Ribeiro e Sousa, T. Miranda, and G. Zhu, "Rockburst laboratory tests database—application of data mining techniques," *Engineering Geology*, vol. 185, pp. 116–130, 2015.
- [15] C. S. Ma, W. Z. Chen, X. J. Tan, H. M. Tian, J. P. Yang, and J. X. Yu, "Novel rockburst criterion based on the TBM tunnel construction of the Neelum–Jhelum (NJ) hydroelectric project in Pakistan," *Tunnelling and Underground Space Technology*, vol. 81, pp. 391–402, 2018.
- [16] F. Q. Gong, J. Y. Yan, and X. B. Li, "A new criterion of rock burst proneness based on the linear energy storage law and the residual elastic energy index," *Chinese Journal of Rock Mechanics and Engineering*, vol. 37, no. 9, pp. 1993–2014, 2018.
- [17] M. Cai and P. K. Kaiser, *Rockburst Support Reference Book—Volume I: Rockburst Phenomenon and Support Characteristics*, MIRARCO, Laurentian University, Greater Sudbury, Canada, 2018.
- [18] A. Kidybiński, "Bursting liability indices of coal," *International Journal of Rock Mechanics and Mining Sciences*, vol. 18, no. 4, pp. 295–304, 1981.
- [19] S. P. Singh, "Burst energy release index," *Rock Mechanics and Rock Engineering*, vol. 21, no. 2, pp. 149–155, 1988.
- [20] J. A. Wang and H. D. Park, "Comprehensive prediction of rockburst based on analysis of strain energy in rocks," *Tunnelling and Underground Space Technology*, vol. 16, no. 1, pp. 49–57, 2001.
- [21] A. Mazaira and P. Konicek, "Intense rockburst impacts in deep underground construction and their prevention," *Canadian Geotechnical Journal*, vol. 52, no. 10, pp. 1426–1439, 2015.
- [22] M. F. Cai, "Prediction and prevention of rockburst in metal mines—a case study of Sanshandao gold mine," *Journal of Rock Mechanics and Geotechnical Engineering*, vol. 8, no. 2, pp. 204–211, 2016.
- [23] W. Y. Guo, T. B. Zhao, Y. L. Tan, F. H. Yu, S. C. Hu, and F. Q. Yang, "Progressive mitigation method of rock bursts under complicated geological conditions," *International Journal of Rock Mechanics and Mining Sciences*, vol. 96, pp. 11–22, 2017.
- [24] F. Q. Gong, J. Y. Yan, X. B. Li, and S. Luo, "A peak-strength strain energy storage index for rock burst proneness of rock materials," *International Journal of Rock Mechanics and Mining Sciences*, vol. 117, pp. 76–89, 2019.
- [25] B. C. Haimson and C. Chang, "A new true triaxial cell for testing mechanical properties of rock, and its use to determine rock strength and deformability of westerly granite," *International Journal of Rock Mechanics and Mining Sciences*, vol. 37, no. 1-2, pp. 285–296, 2000.
- [26] C. D. Ma, X. B. Li, F. Chen, and J. C. Xu, "Fracturing behavior study of biaxial compression of rock subjected to dynamic disturbance load," *Chinese Journal of Rock Mechanics and Engineering*, vol. 29, no. 6, pp. 1238–1244, 2010.
- [27] X. G. Zhao, M. Cai, J. Wang, and P. F. Li, "Strength comparison between cylindrical and prism specimens of Beishan granite under uniaxial compression," *International Journal of Rock Mechanics and Mining Sciences*, vol. 76, pp. 10–17, 2015.
- [28] Y. H. Xu and M. Cai, "Numerical study on the influence of cross-sectional shape on strength and deformation behaviors

- of rocks under uniaxial compression," *Pure and Applied Geophysics*, vol. 84, pp. 129–137, 2017.
- [29] H. P. Xie, Y. Ju, and L. Y. Li, "Criteria for strength and structural failure of rocks based on energy dissipation and energy release principles," *Chinese Journal of Rock Mechanics and Engineering*, vol. 24, no. 17, pp. 3003–3010, 2005.
- [30] Z. T. Bieniawski, "Mechanism of brittle fracture of rock: part I—theory of the fracture process," *International Journal of Rock Mechanics and Mining Sciences & Geomechanics Abstracts*, vol. 4, no. 4, pp. 395–406, 1967.
- [31] R. W. Zimmerman, "The effect of microcracks on the elastic moduli of brittle materials," *Journal of Materials Science Letters*, vol. 4, no. 12, pp. 1457–1460, 1985.
- [32] J. C. Jaeger, N. G. W. Cook, and R. W. Zimmerman, *Fundamentals of Rock Mechanics*, Blackwell Publishing, Malden, MA, USA, 4th edition, 2007.
- [33] R. Peng, Y. Ju, J. G. Wang, H. Xie, F. Gao, and L. Mao, "Energy dissipation and release during coal failure under conventional triaxial compression," *Rock Mechanics and Rock Engineering*, vol. 48, no. 2, pp. 509–526, 2015.
- [34] B. G. Tarasov and T. R. Stacey, "Features of the energy balance and fragmentation mechanisms at spontaneous failure of class I and class II rocks," *Rock Mechanics and Rock Engineering*, vol. 50, no. 10, pp. 2563–2584, 2017.
- [35] F. Q. Gong, S. Luo, and J. Y. Yan, "Energy storage and dissipation evolution process and characteristics of marble in three tension-type failure tests," *Rock Mechanics and Rock Engineering*, vol. 51, no. 11, pp. 3613–3624, 2018.
- [36] F. Q. Gong, J. Y. Yan, S. Luo, and X. B. Li, "Investigation on the linear energy storage and dissipation laws of rock materials under uniaxial compression," *Rock Mechanics and Rock Engineering*, vol. 52, no. 12, pp. 4237–4255, 2019.
- [37] H. Munoz, A. Taheri, and E. K. Chanda, "Fracture energy-based brittleness index development and brittleness quantification by pre-peak strength parameters in rock uniaxial compression," *Rock Mechanics and Rock Engineering*, vol. 49, no. 12, pp. 4587–4606, 2016.

Research Article

Experimental Investigation of the Use of Expansive Materials to Increase Permeability in Coal Seams through Expansive Fracturing

Xiao Cui,^{1,2} Jiayong Zhang ^{1,2}, Liwen Guo,^{1,2} and Xuemin Gong³

¹College of Mining Engineering, North China University of Science and Technology, Tangshan, Hebei 063210, China

²Mining Development and Safety Technology Key Lab of Hebei Province, Tangshan, Hebei 063210, China

³College of Chemical Engineering, North China University of Science and Technology, Tangshan, Hebei 063210, China

Correspondence should be addressed to Jiayong Zhang; zjy815@ncst.edu.cn

Received 4 February 2020; Revised 16 June 2020; Accepted 10 July 2020; Published 31 July 2020

Academic Editor: Hongwei Yang

Copyright © 2020 Xiao Cui et al. This is an open access article distributed under the Creative Commons Attribution License, which permits unrestricted use, distribution, and reproduction in any medium, provided the original work is properly cited.

Hydration reactions of expansive materials are typically very safe, easy to induce, and low in cost, while the crushing of such materials is typically free from noise, dust, vibration, and toxic gases. In the present study, to realize the application of expansive materials in the prevention of coal seam gas disasters, the microstructure, heat release rate, and expansive pressure of expansive materials were investigated for different degrees of hydration based on temperature and pressure measurements and using a scanning electron microscope (SEM); fracture characteristics were determined based on fracture tests of coal-like materials. The results show that the expansive material with +30% water has the lowest hydration temperature (100°C). The expansive pressure of the steel tube was found to reach 57 MPa, which is deemed suitable for application in coal seams. The strain and displacement of coal-like materials were found to increase with time, with four main cracks appearing. Based on these results, it is feasible that hydration reactions of expansive materials could increase both gas drainage and permeability in coal seams, thus reducing the risk of rock burst around boreholes in coal seams.

1. Introduction

The permeability of coal seams decreases with increasing coal seam depth, leading to simultaneous increases in gas content and pressure. Such processes result in considerable threat to production safety [1, 2]. Drilling boreholes in low-permeability coal seams typically results in the discharge of gas; previous studies have shown that optimizing the drilling position and enlarging the extracting radius can help to improve coal bed permeability [3, 4]. Recent developments in pressure relief and permeability-increasing technology include hydraulic boreholes, hydraulic fracturing, intensive drilling, and concussion blasting [5, 6]. However, these technologies have disadvantages: they are often labor intensive and require long construction periods and considerable financial investment. Therefore, investigating new pressure relief and permeability-increasing technology is important.

In the context considered here, expansive materials are gel-like cement materials that react with water and crystallize into the solid phase, resulting in an increase in their volume. The crystallization process exerts pressure on borehole walls, resulting in rock burst around the borehole when the expansive pressure and vertical tensile stress exceed the tensile strength of the surrounding brittle materials [7, 8]. In an early study, expansive cement was produced by grinding ettringite and gypsum, calcining them at 1500°C, and adding a proportion of finely ground slag [9]. A subsequent study increased the calcination temperature of calcium oxide and obtained an expansive material containing calcium sulfate and calcium oxide [10]. Expansive materials have also been developed by mixing calcium oxide and water in a borehole; this *in situ* hydration of quicklime was found to double the volume of material in the borehole, resulting in fracturing due to expansive pressure [11]. Efforts to develop expansive materials in China were initiated in the

1950s. Early efforts investigated the sintering of high-aluminum cement with a rotary kiln and provided important guidance for future investigation of expansive materials [12], while a self-stressing silicate cement was developed successfully in 1957. A later study investigated the viability of using calcium oxide calcined at high temperature as an expansive source, based on analysis of the reaction mechanisms of the expansive material and on laboratory experiments and industrial testing, and developed an expansive crushing agent with a reaction pressure that can exceed 60 MPa [13]. Expansive materials have been used widely in non-coal mining and construction blasting, and the technology is well developed. However, owing to the complexity of the coal seam environment, hydration reactions of expansive materials used in construction technology may cause some stability issues; thus, their use requires further optimization, and this technology has not yet been used in coal production.

Although the pressure in the borehole will decrease when the coal body breaks, as the hydration reaction continues, the volume of the expansive material can increase by more than 2 times, and the width and length of the cracks produced by the coal seam will continue to develop. The expansive pressure generated by the hydration reaction of the expansive material has a slower reaction speed and a uniform pressure increase to cause the cracked object, so the whole crushing process is noise-free, dust-free, and vibration-free. After the hydration reaction, it does not produce any toxic and harmful substances, which is a safe and reliable way of fracturing. The main features of the expansive fracturing were compared with those of other methods, as shown in Table 1.

Traditional borehole drilling technology is one of the most common methods adopted for use in coal seams with low gas permeability; drilling in this manner has been shown to increase the exposed area and pressure release range of boreholes, thus both increasing gas drainage and reducing gas pressure. Here, a new technology that increases the permeability of coal seams is proposed; this method adopts recent advances in borehole technology and expansive materials rather than relying on traditional methods. According to existing knowledge regarding borehole gas drainage, the expansion of boreholes in coal seams can be achieved using either perfusive materials or expansive materials; the nature of this expansion depends on the expansive pressure exerted by drilling in the vicinity of coal fractures and on the physical and chemical changes that affect the gas state. The ability to increase coal seam permeability using these techniques could help address gas drainage issues associated with mining processes. Therefore, the production of an expansive material for use in coal seams would be of great theoretical and practical significance for coal mine production safety, gas resource development, and environmental protection.

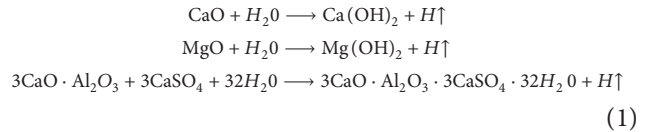
2. Materials and Methodology

2.1. Materials. The expansive materials were calcined at temperatures of 1350–1500°C and comprised primarily the

following components (in order of decreasing percentage content): calcium oxide (f-CaO), tricalcium silicate (C₃S), tetracalcium aluminoferrite (C₄AF), and tricalcium aluminate (C₃A). Based on mass balance calculations, calcium oxide reacts with silicon dioxide (SiO₂), aluminum oxide (Al₂O₃), and ferric oxide (Fe₂O₃), producing tricalcium silicate (C₃S), tetracalcium aluminoferrite (C₄AF), and tricalcium aluminate (C₃A), and transforms the remaining calcium oxide to f-CaO. The components of the expansive materials are presented in Table 2.

2.2. Reaction Temperature Measurement. Owing to the complexity of the coal seam environment and to ensure production safety, accurate reaction parameters must be recorded for expansive materials used in coal seams. In particular, reaction temperature and reaction rate are important factors determining the effects of expansive materials.

The use of expansive materials in coal seam drilling to induce expansive fracturing can result in exothermic hydration reactions and increase the volume of calcium oxide (CaO) [11, 14, 15], magnesium oxide (MgO), and anhydrous calcium sulfoaluminate (3CaO·Al₂O₃) [16, 17]. The main hydration reactions for the expansive material are as follows:



Physical parameters of each compound are shown in Table 3. Calcium oxide (CaO) reacts with water to produce calcium hydroxide (Ca(OH)₂). Magnesium oxide (MgO) reacts with water to produce magnesium hydroxide (Mg(OH)₂); calcium sulfate (CaSO₄) and anhydrous calcium sulfoaluminate (3CaO·Al₂O₃) react with water to produce calcium sulfoaluminate hydrates (3CaO·Al₂O₃·3CaSO₄·32H₂O). The solid volume growth rate after hydration is as follows [13]:

$$\begin{aligned} \Delta V_{\text{CaO}} &= \frac{33.18 - 16.79}{16.79} \times 100\% = 97\%, \\ \Delta V_{\text{MgO}} &= \frac{24.71 - 11.26}{11.26} \times 100\% = 119\%, \\ \Delta V_{\text{CA}} &= \frac{725 - 371}{371} \times 100\% = 95\%. \end{aligned} \quad (2)$$

The device used to test reaction temperature is shown in Figure 1. Temperature tests were conducted under ambient temperature conditions (~20°C). A sealing and heat preservation device (volume 1L) was adopted, a Pt100 temperature sensor (measurement range 0–200°C) was connected, and the MK-200E paperless recorder was used to monitor data. A balance (accurate to 0.01 g) was used to weigh out 500 g of the expansive material; then, the material was stirred evenly with varying proportions of water before being added to the insulation device. Changes in reaction temperature over time were recorded.

TABLE 1: Comparison of expansive fracturing with other methods of permeability improvement.

Method	Principle	Advantage	Limitation
Expansive fracturing	Solid expansion and exothermic desorption	Noise-free, dust-free, and vibration-free	Reaction exotherm
Concussion blasting	Gas volume expansion	Quick reaction and obvious effect	Vibration, noise, flying stone, toxic gas, and easy to induce gas outburst
Drilling	Pressurization-discharging	Traditional technology	Large amount of work, long construction period, and rapid drilling-induced coal and gas outburst
Hydraulic method	Liquid punching, fracturing, and displacement	The coal is adequately relieved of pressure	Fracture development has no direction and the process is complex
CO ₂ phase change fracturing	Gas volume expansion and displacement	Gas can be replaced to improve the recovery rate	The coal body with complex device, high sealing requirement of borehole and excessive crushing is easy to lead to pore blockage

TABLE 2: Components of expansive materials.

LOI (loss on ignition)	Chemical composition (%)							Liter weight (g/L)
	SiO ₂	Al ₂ O ₃	Fe ₂ O ₃	CaO	MgO	f-CaO	∑	
0.62	5.41	1.10	2.60	89.10	0.92	73.26	99.75	1320

TABLE 3: Physical parameters of each compound.

	CaO	MgO	CaO·Al ₂ O ₃	CaSO ₄	Ca (OH) ₂	Mg (OH) ₂	H ₂ O
Molecular weight (g)	56.08	40.30	101.96	172.17	74.08	58.32	18.02
Apparent density (g/cm ³)	3.34	3.58	3.90	2.61	2.24	2.36	1.00
Gram-molecular volume (cm ³)	16.79	11.26	26.14	65.97	33.08	24.71	18.02



FIGURE 1: Device used to test reaction temperature.

2.3. Expansive Pressure Measurement. The measurement of expansion pressure is made using thick-walled round steel tubes based on Building Materials Industry Standard of China (JC 506-1992). The basic principles underlying expansive pressure testing of expansive materials are as follows. The expansive material is poured into a thick-walled circular steel tube; when the expansive material in the tube undergoes a hydration reaction and expands in volume [18], the material will exert strain on the tube wall. This causes the tube to expand. The expansive pressure acting on the inner wall of the tube can be described by the thick-wall cylinder theory of elastic mechanics [19, 20]. The radial compressive stress and tangential tensile stress of the thick-walled tube under expansive pressure are as follows:

$$\sigma_r = (P_{ex} - P_0) \frac{R_i^2}{R_e^2 - R_i^2} \left[1 - \frac{R_e^2}{r^2} \right], \quad (3)$$

$$\sigma_\theta = (P_{ex} - P_0) \frac{R_i^2}{R_e^2 - R_i^2} \left[1 + \frac{R_e^2}{r^2} \right], \quad (4)$$

where σ_r and σ_θ are the radial compressive stress and tangential tensile stress, respectively, and P_{ex} and P_0 are the internal expansive and external pressures, respectively. Under the test conditions considered here, the steel tube is not subject to external pressures, such that $P_0 = 0$. R_i and R_e represent the internal radius and external radius, respectively, and r is the radial distance from the center to the cylinder. When $r = R_e$, equations (3) and (4) can be modified as follows:

$$\sigma_\theta = \frac{2P_{ex}R_i^2}{R_e^2 - R_i^2}. \quad (5)$$

According to the theory of elasticity, the tangential strain of a steel tube under radial and tangential stress is as follows:

$$\varepsilon_\theta = \frac{\sigma_\theta - \nu\sigma_r}{E} = \frac{2P_{ex}R_i^2}{E(R_e^2 - R_i^2)}, \quad (6)$$

where E is the elastic modulus of the steel tube. Then, the expansive pressure can be expressed as follows:

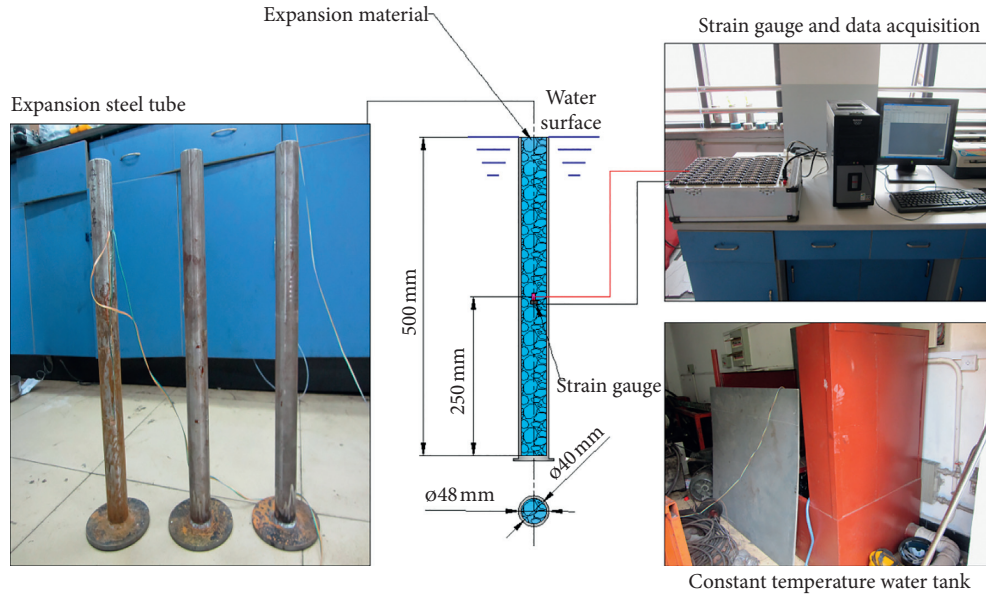


FIGURE 2: Determination of expansive pressure.

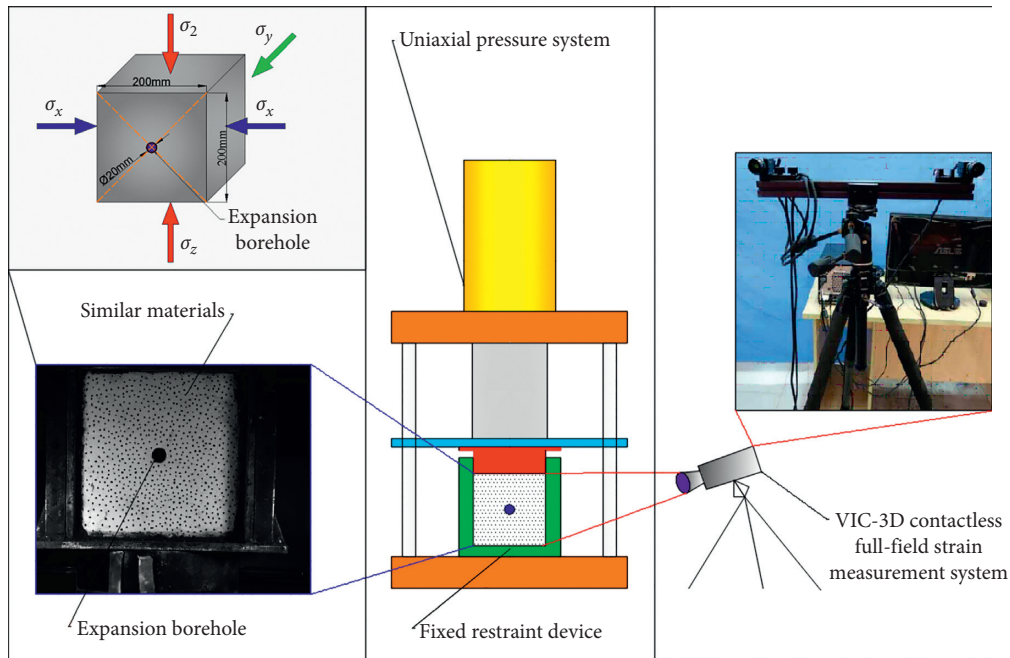


FIGURE 3: Experimental setup used to analyze fracturing of the expansive material.

$$P_{ex} = \frac{\varepsilon_{\theta} E (R_e^2 - R_i^2)}{2R_i^2}. \quad (7)$$

In this test, a Q235 cold-processed steel tube was used, with an elastic modulus of 200.06 GPa and an inner radius, outer radius, and length of 20 mm, 24 mm, and 500 mm, respectively [21]. One end of the steel tube was sealed by welding with a thick steel plate. The resistance strain gauge was glued to the adhesive strain gauge at the midpoint of the steel tube, 250 mm from the base of the tube. The strain gauge used was model BX120-20AA. The leading end of the

resistance strain gauge was connected to the strain gauge by a double-stranded wire [21, 22], and the steel tube was placed in a water bath with a constant temperature of 25°C. The device used to test expansive pressure is shown in Figure 2.

2.4. Microstructural Analysis of Expansive Material Using SEM. To further analyze the expansive pressure generated by the expansive material and investigate the structural changes and mechanical properties of the material, its microstructure before and after the hydration reaction was

studied using the JSM-IT100 scanning electron microscope (SEM) [23, 24]. Double-sided tape was pasted on the load tray to maintain a dry environment, and small samples of the expansive material were placed on the tape to ensure uniform distribution. Metal film was sprayed on the surface of the sample before the microstructural morphology of the expansive material was observed. The hydration reaction was induced by adding +30% water for 24 h; then, a specimen of the expansive material was observed to identify any changes in crystal structure following hydration.

2.5. Fracture Analysis of Expansive Material

2.5.1. Preparation of Coal-Like Materials. The compressive strengths of materials can be used as an index to measure their similarity to raw coal. Cement and gypsum were used to produce a material with similar strength to coal. The ratios of pulverized coal to cement, gypsum, and water in this material were determined to be 0.5 : 0.25 : 0.05 : 0.2 based on the results of uniaxial testing undertaken in previous studies [25]. This mixture was stirred evenly and placed into a self-made cube mold with dimensions of 200 × 200 × 200 mm; the mold was left to stand for 9–10 h to allow demodulation and was maintained at constant temperature in a drying oven for one week. Then, the center of the coal-like material was drilled using a coring drill with diameter of 20 mm.

2.5.2. VIC-3D System for Strain Measurement. The surface displacement and strain distribution of the coal-like material under expansive pressure and uniaxial stress were calculated by comparing image correlation points with the VIC-3D contactless full-field strain measurement system. This system requires only two image collectors. The surface of the tested material was coated with a random black and white pattern. During the deformation of the sample, the movement of individual pixels was recorded and translated into a vector; in this manner, the strain data before and after deformation can be determined based on a vector field generated by the surface deformation of the material. The coal-like material and the experimental setup used to analyze fracturing of the expansive material are shown in Figure 3. Coal seams are under static isotropic pressure due to the overlying and surrounding rocks, and this pressure increases with depth of a coal seam within the rock mass. Here, the distribution of coal seam stress was optimized by setting the boundary conditions in the x , $-x$, and $-y$ directions as fixed constraints, with the in situ stress $\sigma_z = 5$ MPa. The y direction indicates distance along the mining section, with the y axis set as the free surface.

3. Results and Discussion

3.1. Reaction Temperature. Temperature is one of the primary factors influencing the performance of the expansive material: when temperature is higher, the hydration rate of the expansive material is faster and the expansion pressure exerted is higher. Moreover, the response of expansive materials with different proportions of water added for the

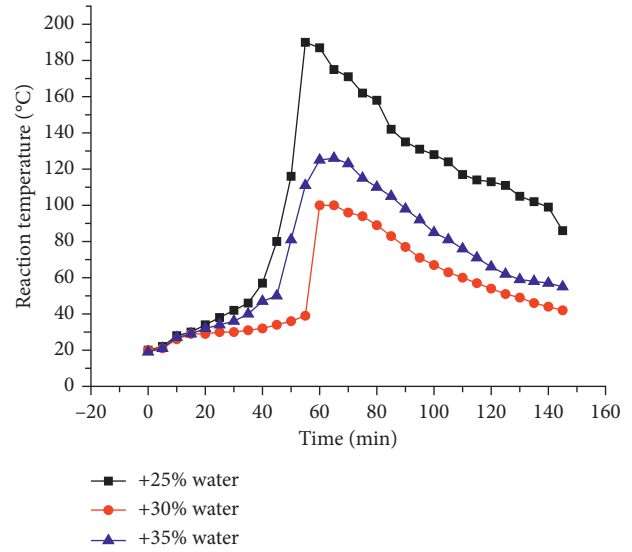


FIGURE 4: Variation in reaction temperature with time.

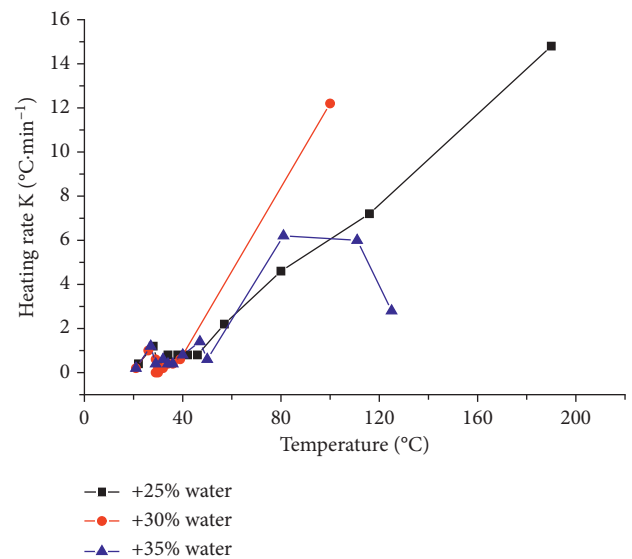


FIGURE 5: Heating rate curve for the expansive material.

hydration reaction (25%, 30%, and 35%) will vary depending on temperature. Reaction temperatures were measured during the laboratory experiments, as shown in Figure 4. The results show that changes in reaction temperature can be controlled effectively by controlling the water-cement ratio.

Changes in reaction temperature for expansive materials with different water-cement ratios can be summarized as follows. Initially, reaction temperature increases slowly over the range 20–40°C; when the temperature reaches 40°C, the reaction speeds up and there is a marked increase in temperature. Subsequently, reaction temperature peaks before declining slowly. These results demonstrate that temperature changes during the hydration reaction of the expansive material exhibit the same form regardless of water content. The maximum reaction temperatures reached for the +25%,

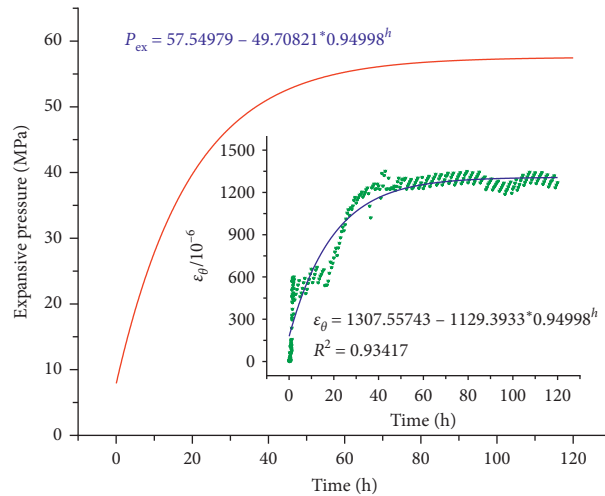


FIGURE 6: Changes in tangential strain for steel tube and expansive pressure of expansive material over time.

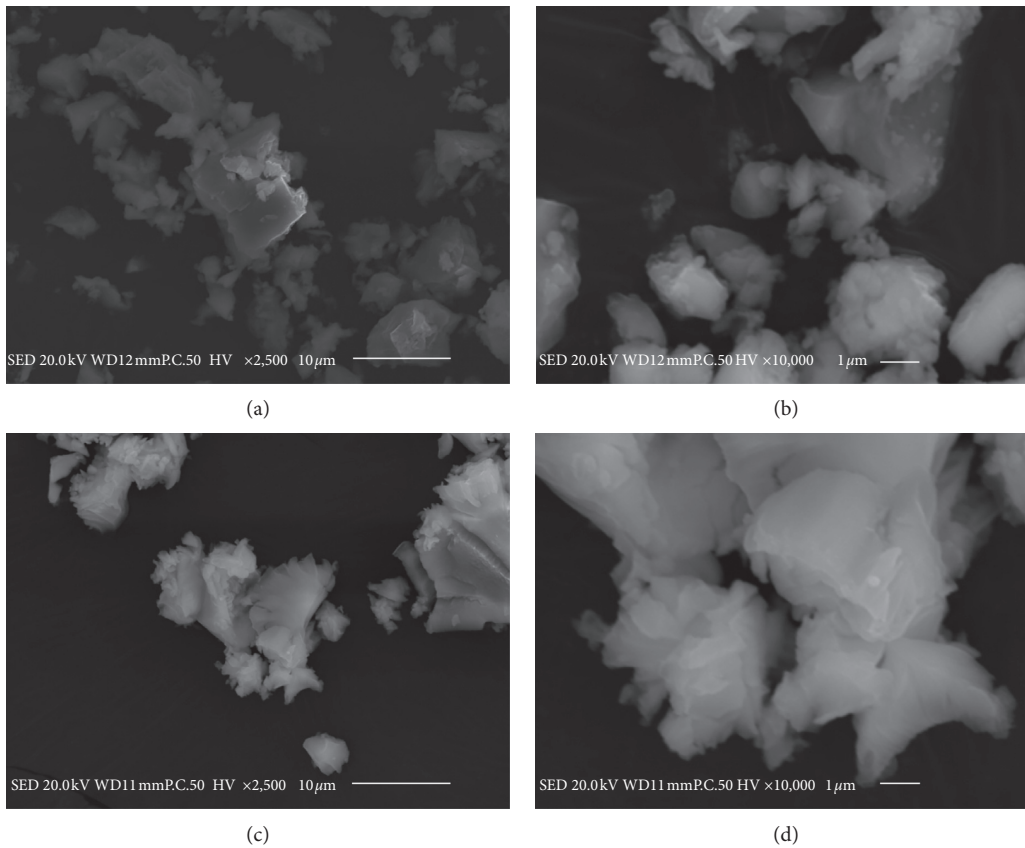


FIGURE 7: SEM images for expansive material. (a) Sample before hydration at 2,500x. (b) Sample before hydration at 10,000x. (c) Sample after hydration at 2,500x. (d) Sample after hydration at 10,000x.

+30%, and +35% mixtures were 190°C, 100°C, and 126°C, respectively; these temperatures were reached at 55, 60, and 65 min, respectively. These results demonstrate that the time required for the expansive material to reach the maximum reaction temperature increases with increasing water-cement ratio. However, the maximum reaction temperature was found to decrease considerably with increasing water content between +25% and +35%.

The temperature of the expansive material was measured every 5 min for each mixture and the temperature dependence of the heating rate K was investigated. This parameter is considered to represent the rate of change of reaction temperature for the expansive material, where $K = \Delta T/5$.

The heating rate curve for the expansive material with +25%, +30%, and +35% water is presented in Figure 5; this curve was developed based on fitting of the temperature

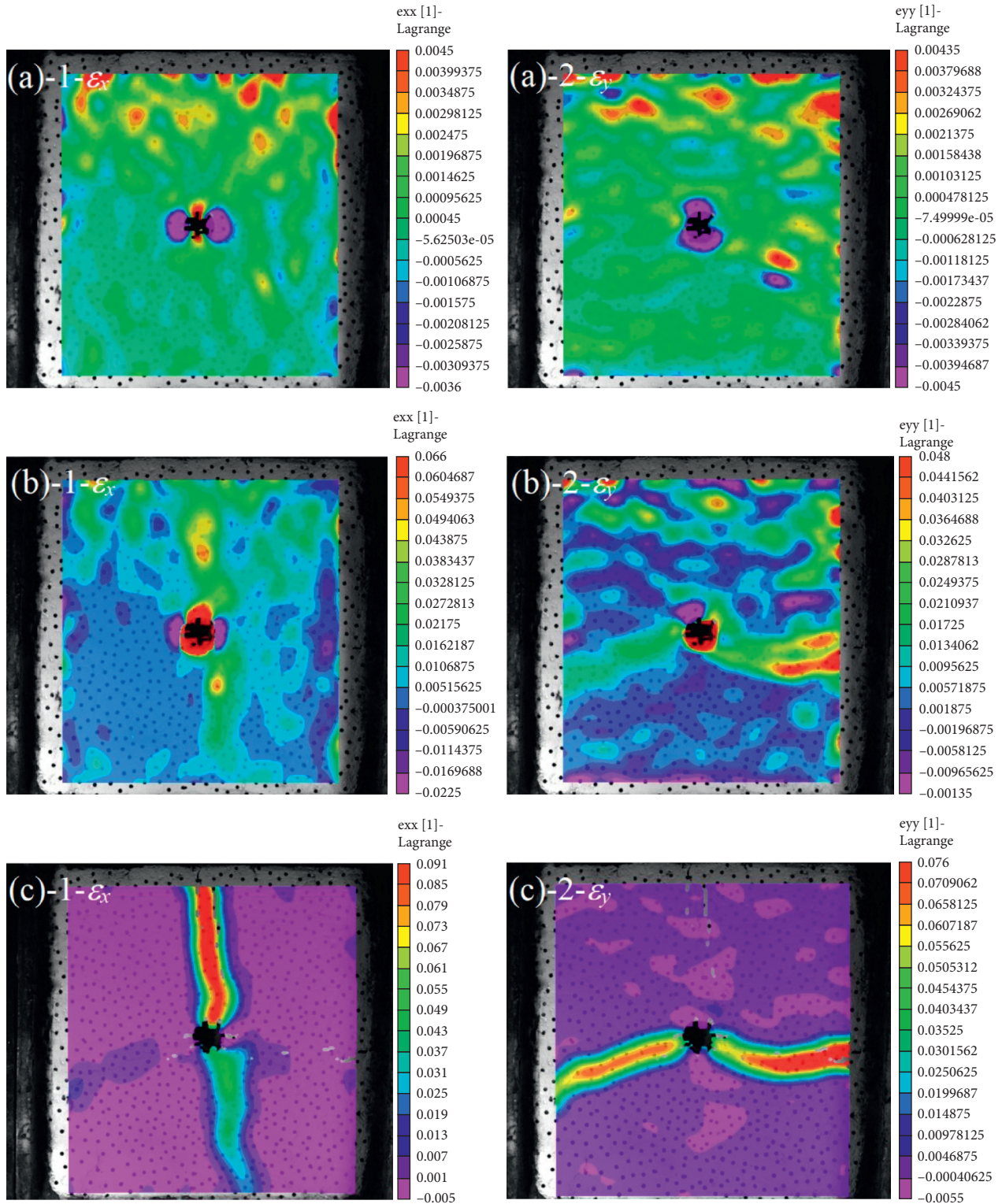


FIGURE 8: Variation in strain response for coal-like materials with reaction time similar to the expansive material considered here. (a)-1 Hydration reaction time 3 h (x direction strain). (a)-2 Hydration reaction time 3 h (y direction strain). (b)-1 Hydration reaction time 6 h (x direction strain). (b)-2 Hydration reaction time 6 h (y direction strain). (c)-1 Hydration reaction time 10 h (x direction strain). (c)-2 Hydration reaction time 10 h (y direction strain).

change curve in Figure 4. These results demonstrate that when the reaction temperature of the expansive material is less than 40°C , the heating rate is slow and is effectively the

same for all three types of expansive material. Conversely, when the reaction temperature exceeds 40°C , the heating rate increases rapidly for all three types, although heating

occurs much more rapidly for the material with +30% and +35% water than for the material with +25% water. This occurs because the heat of hydration reactions is released more rapidly with increasing moisture content; more complete reaction of the expansive material also occurs with increasing moisture content. However, when the moisture content is very high and the reaction temperature reaches 100°C (i.e., the boiling point of water), the water begins to evaporate, resulting in a reduction in the rate of heating. Conversely, when the moisture content is low, the influence of water on the expansive material leads to a continuous increase in the heating rate. Here, the maximum temperature reached for the expansive material with +30% water was 100°C; accordingly, it can be assumed that complete hydration of the expansive material occurred and that the moisture content effectively controlled the reaction temperature.

3.2. Expansive Pressure. Measurement of the expansive pressure of the expansive material based on tangential strain exerted on a thick-walled circular steel tube is presented here. Through the test of variation in reaction temperature with time, it is determined that the expansive material under the condition of +30% water is most suitable for coal seam, so only the expansive pressure under this specific condition is measured. Changes in tangential strain and expansive pressure with time are illustrated in Figure 6.

The test was conducted in a water bath with a constant temperature of 25°C. Initially, the reaction rate of the expansive material was rapid; this accelerated reaction increased the tangential strain significantly. As the test progressed, the reaction slowed down gradually, resulting in small changes in strain. However, as the expansive material was not fully developed when the reaction rate slowed, the tangential strain continued to increase slowly. Accordingly, the measured strain did not reach a stable level until ~120 h after the reaction was initiated. As the strain gauge used here is relatively sensitive, variation in strain with time (h) was further analyzed and fitted according to the following relationship:

$$\varepsilon_{\theta} = 1307.55743 - 1129.3933 \times 0.94998^h. \quad (8)$$

The expansive pressure can be obtained based on the strain acting on the steel tube as described in equation (4). As shown in Figure 6, comparative analysis has shown that expansive pressure varies with time in a manner similar to strain; in fact, the expansive pressure of the expansive material increases with time to a maximum of 57 MPa. These results suggest that the expansive pressure generated by the hydration reaction of the expansive material can be utilized to fracture coal seams by drilling.

3.3. Microstructural Analysis Using SEM. SEM micrographs of the expansive material before and after hydration are shown in Figure 7 and demonstrate clearly that hydration changes the microstructure and density of the expansive

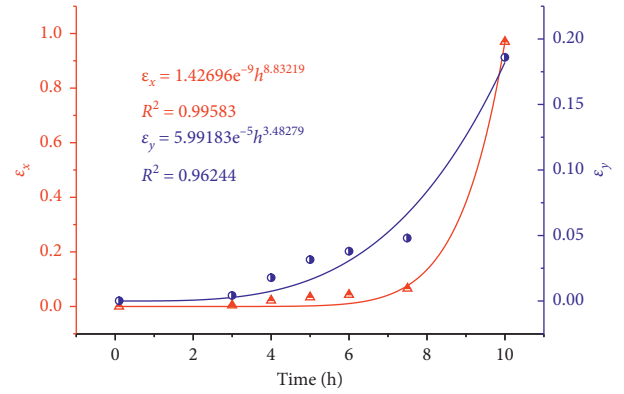


FIGURE 9: Variation in maximum stress variables with time in the x and y directions.

material. As shown in Figures 7(a) and 7(b), the expansive material was composed of particles with smooth, dense, and nonporous surfaces before hydration; the apparent density of these particles was relatively high. The main component of the expansive material is calcium oxide. Small and dispersed particles of calcium oxide facilitate hydration, forming calcium hydroxide crystal centers and a large number of fine crystals. As shown in Figures 7(c) and 7(d), the particle surfaces following hydration are relatively rough and microcracks and nanocracks are relatively well dispersed, forming many small voids and increasing porosity, although the volume of the hydrated particles is twice that of the original particles. These results demonstrate that changes in expansive pressure are a result of changes in crystal structure during hydration.

3.4. Analysis of Borehole Expansive Fracturing. Images taken by the VIC-3D contactless full-field strain measurement system can be used to explain the development of strain over time when expansive materials are used to fracture coal-like materials. Changes in the expansive pressure occur with increasing hydration time; this is reflected in changes in the mechanical properties of the expansive material. Changes in strain response for the materials with similar reaction times to the expansive material used here are shown in Figure 8.

In Figure 8, high-strain regions are shown in red and low-strain regions are shown in blue. For the coal-like materials, it is clear that, under uniaxial stress, the failure mechanism develops from widely distributed strain to highly localized strain with increasing hydration time. The wider distribution of strain results partly from the expansive pressure of the material after hydration and partly from the action of *in situ* stress. The figure also shows the fracture characteristics of the coal-like materials with fixed constraints; these conditions replicate the crushing mechanism that acts during the fracture process as a result of holes being drilled in the surrounding area during the reaction of expansive materials. With increasing hydration reaction time, the fracture effect is gradually increased. Fitting analysis was performed on the maximum stress variables at different times in the x and y directions; the results are presented in

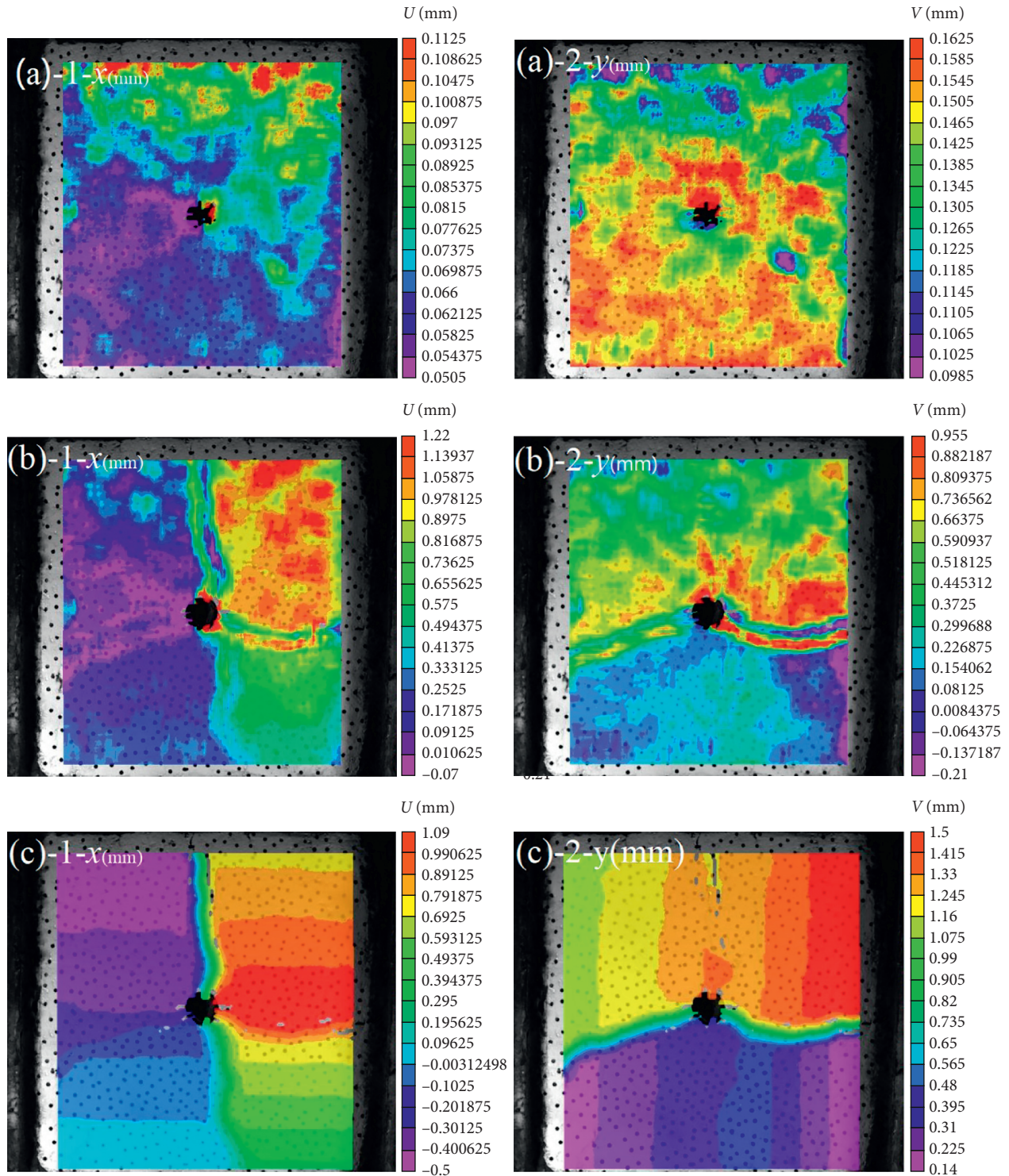


FIGURE 10: Variation in displacement of coal-like materials with reaction time of the expansive material. (a)-1 Hydration reaction time 3 h (x direction displacement). (a)-2 Hydration reaction time 3 h (y direction displacement). (b)-1 Hydration reaction time 6 h (x direction displacement). (b)-2 Hydration reaction time 6 h (y direction displacement). (c)-1 Hydration reaction time 10 h (x direction displacement). (c)-2 Hydration reaction time 10 h (y direction displacement).

Figure 9. The strain was found to increase significantly after a reaction time of 6 h, indicating that the coal-like material fractured; this can be considered to represent the formation of a gas migration channel in a coal seam.

Further analysis was conducted for the coal-like materials in the form of a displacement test (Figure 10). The number of macroscopic cracks on the surface of the coal-like material increased to 4, and cracks started to form in the

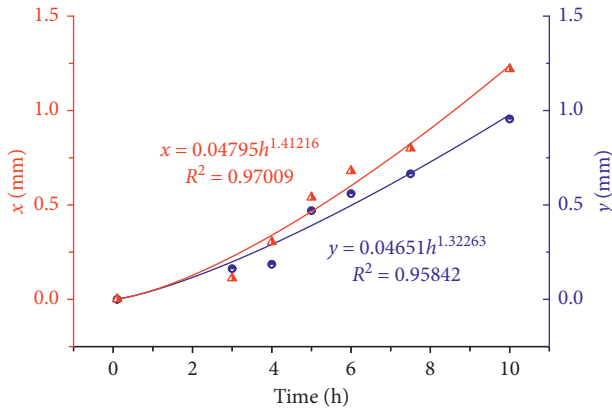


FIGURE 11: Changes in maximum displacement with time in the x and y directions.

outer wall of the expansion borehole and penetrate the entire specimen. In the expansive material, thermal stress was the dominant controlling factor at the start of the reaction, forming a temperature gradient around the borehole; this contributed to changes in the physical and mechanical properties of material in this area. In particular, elevated temperature resulted in thermal expansion and increases in *in situ* stress, focusing stress along the coal specimen boundary and forming fractures in the damaged area. As the reaction progressed, the expansive stress became the dominant controlling factor. Meanwhile, the constraint imposed by the borehole wall of the coal specimen was higher than that of the boundary. Under the action of the expansive force, cracks began to form in the damaged strip along the boundary, and these cracks expanded from the borehole to the boundary until the coal-like materials were connected. Changes in fracture displacement with time are shown in Figure 11. Four main cracks were generated during the test; the length and width of these cracks increased with the reaction time of the expansive material.

4. Conclusion

Based on a combination of theoretical research, basic testing, and fracture testing, the response characteristics of an expansive material and its effect on fracturing of coal-like materials have been studied. The following conclusions can be drawn.

Measurement of the basic parameters of the expansive material indicated that the hydration temperature of the expansive material was lowest (100°C) when +30% water was used. After the expansive material had reacted fully, it continued to exert pressure on the wall of the steel tube, controlling the expansive pressure effectively at 57 MPa.

Based on investigation of the mechanical properties and structural characteristics of coal, expansive fracture testing was conducted on materials with reaction times similar to that of the expansive material. Four main cracks were generated by fracturing of the test block.

Coal seam fracturing based on expansive materials is known to be safe, easy to undertake, low in cost, noise-free,

dust-free, vibration-free, and free from toxic gas products. This study represents an initial feasibility study for the practical application of this technology. The process of expansion is known to increase damage and exploit inherent weaknesses in coal seams. However, the slow development of fractures can ensure stability of the coal roof, effectively preventing coal and gas outburst, and may be suitable for application in gas prevention and control for low-permeability coal seams. Such application could greatly reduce construction quantity and operation time. Application of this new coal seam fracturing technology based on expansive materials may prove to be feasible in practice and merits further investigation.

Data Availability

The data used to support the findings of this study are available from the corresponding author upon request.

Conflicts of Interest

The authors declare that they have no conflicts of interest.

Acknowledgments

This research was supported by the National Natural Science Foundation Fund (51874012), the National Key Research and Development Plan (2018YFC0808100), the Hebei Natural Science Foundation Fund (E2016209249), and the Graduate Student Innovation Fund of North China University of Science Technology (2018B26).

References

- [1] W. Yang, B.-q. Lin, Y.-a. Qu et al., "Stress evolution with time and space during mining of a coal seam," *International Journal of Rock Mechanics and Mining Sciences*, vol. 48, no. 7, pp. 1145–1152, 2011.
- [2] Y.-P. Cheng, L. Wang, and X.-L. Zhang, "Environmental impact of coal mine methane emissions and responding strategies in China," *International Journal of Greenhouse Gas Control*, vol. 5, no. 1, pp. 157–166, 2011.
- [3] H. Zhou, J. Gao, K. Han, and Y. Cheng, "Permeability enhancements of borehole outburst cavitation in outburst-prone coal seams," *International Journal of Rock Mechanics and Mining Sciences*, vol. 111, pp. 12–20, 2018.
- [4] D. Li, "A new technology for the drilling of long boreholes for gas drainage in a soft coal seam," *Journal of Petroleum Science and Engineering*, vol. 137, pp. 107–112, 2016.
- [5] E. C. Dunlop, A. Salmachi, and P. J. McCabe, "Investigation of increasing hydraulic fracture conductivity within producing ultra-deep coal seams using time-lapse rate transient analysis: a long-term pilot experiment in the Cooper Basin, Australia," *International Journal of Coal Geology*, vol. 103, 2019.
- [6] Y. Lu, L. Wang, Z. Ge, Z. Zhou, K. Deng, and S. Zuo, "Fracture and pore structure dynamic evolution of coals during hydraulic fracturing," *Fuel*, vol. 259, p. 116272, 2020.
- [7] J. Xu, C. Zhai, L. Qin, and G. Yu, "Evaluation research of the fracturing capacity of non-explosive expansion material applied to coal-seam roof rock," *International Journal of Rock Mechanics and Mining Sciences*, vol. 94, pp. 103–111, 2017.

- [8] C. Zhai, J. Xu, S. Liu, and L. Qin, "Fracturing mechanism of coal-like rock specimens under the effect of non-explosive expansion," *International Journal of Rock Mechanics and Mining Sciences*, vol. 103, pp. 145–154, 2018.
- [9] W. Nocuń-Wczelik, Z. Konik, and A. Stok, "Blended systems with calcium aluminate and calcium sulphate expansive additives," *Construction and Building Materials*, vol. 25, no. 2, pp. 939–943, 011.
- [10] X. Li, Y. Zhang, X. Shen, Q. Wang, and Z. Pan, "Kinetics of calcium sulfoaluminate formation from tricalcium aluminate, calcium sulfate and calcium oxide," *Cement and Concrete Research*, vol. 55, pp. 79–87, 2014.
- [11] K. Goto, K. Kojima, and K. Watabe, "The mechanism of expansive pressure and blowout of static demolition agent," in *Proceedings of the Paper Presented at the Second International RILEM Symposium on Demolition and Reuse of Concrete and Masonry*, Tokyo, Japan, November 1988.
- [12] X. Liu, B. Ma, H. Tan et al., "Effect of aluminum sulfate on the hydration of Portland cement, tricalcium silicate and tricalcium aluminate," *Construction and Building Materials*, vol. 232, p. 117179, 2020.
- [13] B. You, *Static Blasting Technology: Silent Crushing Agent and its Application*, China Building Materials Industry Press, Taiyuan, China, 2008.
- [14] S. Arshadnejad, K. Goshtasbi, and J. Aghazadeh, "A model to determine hole spacing in the rock fracture process by non-explosive expansion material," *International Journal of Minerals, Metallurgy, and Materials*, vol. 18, no. 5, pp. 509–514, 2011.
- [15] A. S. Natanzi, D. F. Laefer, and L. Connolly, "Cold and moderate ambient temperatures effects on expansive pressure development in soundless chemical demolition agents," *Construction and Building Materials*, vol. 110, pp. 117–127, 2016.
- [16] W. Nocuń-Wczelik, A. Stok, and Z. Konik, "Heat evolution in hydrating expansive cement systems," *Journal of Thermal Analysis and Calorimetry*, vol. 101, pp. 527–532, 2010.
- [17] S. Arshadnejad, "Design of hole pattern in static rock fracture process due to expansion pressure," *International Journal of Rock Mechanics and Mining Sciences*, vol. 123, p. 104100, 2019.
- [18] V. R. S. De Silva, P. G. Ranjith, M. S. A. Perera, B. Wu, and T. D. Rathnaweera, "Investigation of the mechanical, microstructural and mineralogical morphology of soundless cracking demolition agents during the hydration process," *Materials Characterization*, vol. 130, pp. 9–24, 2017.
- [19] S. P. Timoshenko and J. N. Goodier, *Theory of Elasticity*, McGraw Book Company, New York, NY, USA, 1951.
- [20] A. Bentur and M. Ish-Shalom, "Properties of type K expansive cement of pure components II. Proposed mechanism of ettringite formation and expansion in unrestrained paste of pure expansive component," *Cement and Concrete Research*, vol. 4, no. 5, pp. 709–721, 1974.
- [21] R. W. Hertzberg, *Deformation and Fracture Mechanics of Engineering Materials*, John Wiley & Sons, New York, NY, USA, 1996.
- [22] J. Hinze and J. Brown, "Properties of soundless chemical demolition agents," *Journal of Construction Engineering and Management*, vol. 120, no. 4, pp. 816–827, 1994.
- [23] B. Kwiecińska, S. . Pusz, J. Brett, and Valentine, "Application of electron microscopy TEM and SEM for analysis of coals, organic-rich shales and carbonaceous matter," *International Journal of Coal Geology*, vol. 211, pp. 103–203, 2019.
- [24] S.-B. Song, J.-F. Liu, D.-S. Yang et al., "Pore structure characterization and permeability prediction of coal samples based on SEM images," *Journal of Natural Gas Science and Engineering*, vol. 67, pp. 160–171, 2019.
- [25] W. Zhang, *Influence of Borehole Expansion Agent on Development Law of Coal Seam Fissure*, North China University of Science and Technology, Habei, China, 2019.

Research Article

Discussions on the Complete Strain Energy Characteristics of Deep Granite and Assessment of Rockburst Tendency

Lu Chen and Lijie Guo 

Beijing General Research Institute of Mining and Metallurgy, Beijing 102628, China

Correspondence should be addressed to Lijie Guo; guolijie@bgrimm.com

Received 20 March 2020; Revised 15 June 2020; Accepted 10 July 2020; Published 26 July 2020

Academic Editor: Hongwei Yang

Copyright © 2020 Lu Chen and Lijie Guo. This is an open access article distributed under the Creative Commons Attribution License, which permits unrestricted use, distribution, and reproduction in any medium, provided the original work is properly cited.

In deep mining, the rockburst hazard has become a prominent problem. Rockburst is difficult to be predicted, and it gives a severe threat to mining safety. In this paper, the triaxial compressive tests with an acoustic emission (AE) device and full cyclic loading and unloading tests were carried out, respectively, to present characteristics of linear elastic strain energy and peak strain energy. Also, to consider the time-delay strain characteristics of granite found in the abovementioned tests, a new stage loading and unloading test with dual monitoring systems was designed and performed. Through 20 days' time-delay strain monitoring, the peak-strength strain energy was further modified. The results showed that the peak strain energy is approximate 1.2-1.3 times than linear elastic strain energy under the same confining pressure, and after considering the time-delay strain effect, the modified maximal strain energy value of the deep granite significantly increased. The peak strain energy values are further enhanced from $1.0 \times 10^4 \text{ J/m}^3$ to $1.8 \times 10^4 \text{ J/m}^3$, respectively. At last, by taking advantage of the strain energy index model of rockburst, the tendency and intensity of rockburst were assessed contrastively.

1. Introduction

With the depletion of shallow resources, deep mining is an inevitable trend of future mining work. Nowadays, the deepest mine in the world (Mponeng Gold Mine in South Africa) has exceeded 4000 m, and some scholars predicted that the mining extends at a rate of 10–25 m per year in depth. In the next 10 to 15 years, more than 50% iron ore mines will be over 1000 m deep in China [1]. In deep mining, due to the complex geological environment with high geostress, high pore water pressure, and high rock temperature, the rockburst hazard is becoming a prominent problem during the deep mining process. Also, as the mining depth increases, the rockburst will occur more frequently and intensively. The rockburst is defined as a sudden or violent damage during the host rock excavation [2]. Rockburst hazard is a long-standing problem and serious threat to mine safety, so many scholars try to predict rockburst employing various methods. Kornowski and Kurzeja [3] built an expert system of hazard

evaluation to predict rockburst probability. Hosseini [4] used the passive seismic velocity tomography and image subtraction technique to estimate the rockburst potential. Li et al. [5] adopted the microseismic monitoring data to analyze the frequent rockbursts. Faradonbeh and Taheri [6] used the three mining techniques to predict the rockburst hazard in deep underground. Faradonbeh et al. [7] studied the rockburst clustering problem by application of self-organizing map and fuzzy c-mean techniques. Ghasemi et al. [8] evaluated the rockburst occurrence and intensity with a decision tree approach. Rockburst is an extremely complex rock failure process, and many factors can affect the occurrence of rockburst disaster. Jiang et al. [9] proposed a combined early warning method, including the microseismic monitoring data, the electromagnetic emission monitoring data, and the drilling cutting data, to predict the rockburst. Jia et al. [10] used the optimized unascertained measure theory to build a comprehensive prediction model of rockburst tendency.

Although numerous researches have been conducted, because of the complicated process and multiple influencing factors, rockburst problem is not well solved and still a hot topic in rock mechanics and mining engineering. Also, it is hard to obtain accurate data to assess the rockburst mechanism and process from the unitary in situ monitoring activities. So, scholars designed and carried out extensive laboratory experiments to simulate the rockburst process or explore the rockburst mechanism, such as the bedding plane influence test [11], true-triaxial test [12, 13], size effect test [14], and loading and unloading test [15], to name a few. A large number of studies show that it is more scientific and effective for energy theory to analyze the rockburst problem [16–18]. Under the framework of the rock energy theory system, a large number of rock mass violent failures or rockburst problems have been studied. Khademian and Ozbay [19] researched the violent rock failures model in tunneling and shaft boring based on energy balance calculations. As the research continues, the whole energy process of rockburst is gradually refined, and the main considering energy during rock failure process is the initial elastic strain energy. Weng et al. [20] studied the rockburst characteristics using a strain energy density index in the numerical simulation process; using a strain energy density index in the numerical simulation process, Shou et al. [21] built a critical condition of the zonal disintegration in deep rock masses based on the strain energy density approach; Razavi et al. [22] obtained a mixed mode fracture load of granite rock with application of an average strain energy density criterion. Also, scholars studied other energy components, such as redistributed energy induced by mining or excavation [23–25], dissipative energy during rock failure [26, 27], and released energy accompanied by rockburst [28, 29]. Among these energy analysis models, the elastic strain energy stored in rock mass is the origin of all energy process, and it is also the main power source of rockburst disaster. As described in the abovementioned references' review, the existing researches mainly focus on linear elastic strain storage energy, and its value can be obtained by combining the AE monitoring test [30–32]. However, the linear elastic storage energy ignores the part of strain energy that is below the peak strength and above the elastic-plastic boundary point. In this part, although the rock has been damaged gradually, it still has a certain strain energy storage capacity.

In this paper, to discuss the complete strain energy characteristics of deep granite, firstly, the triaxial loading tests accompanied with an AE monitoring system of deep granite were carried out. The initial crack point of rocks could be visually obtained corresponding with AE data. Then, the linear elastic strain energy value could be calculated by the elastic modulus and stress value at the initial crack point. Secondly, to study the capacity of peak-strength strain energy storage of deep granite, a series of cyclic loading and unloading tests under typical confining pressures was carried out. After analyzing the elasticity modulus of peak unloading curve and peak stress, the peak-strength strain energy could also be presented. Thirdly, based on the time-delay strain characteristics of rock found in full loading and unloading tests, a novel step loading

and unloading test was designed and performed. Through time-delay strain monitoring, the peak-strength strain energy could be further modified. At last, using the values of strain energy and employing the typical rockburst prediction model, the tendency and intensity of rockburst were assessed contrastively.

2. Linear Elastic Strain Energy Confirmed by AE Monitoring

2.1. Granite Samples and Basic Parameters. In the tests, the rock specimen is granite, drilled from -895 level of San-shandao Gold Mine (Shandong Province, China), with the mineral composition of quartz, anorthose, biotite, and alkali feldspar. The density of rock samples is 2.72 g/cm^3 , and the porosity is 0.59%. To make sure of the uniformity, all the rock samples were cut form a whole block rockmass without any obvious cracks. According to the proposed approach of ISRM, the allowed deviation of roughness at the two ends for the specimen is $\pm 0.05 \text{ mm}$, and the allowed perpendicularity deviation is $\pm 0.25^\circ$. In the tests, 25 standard rock samples with 50 mm diameter and 100 mm height were obtained, as shown in Figure 1.

2.2. Triaxial Compressive Test with AE Monitoring. During the tests, the TAW-2000 microcomputer servo rock testing machine was adopted to carry out the granite triaxial compressive tests, and the SAEU2S digital AE instrument was used for AE monitoring. During the test, with the increasing loading, the rock samples would undergo crack closure, crack initial, crack connection, and peak stage. At each special point, there would be an obvious change of AE events, so the initial crack point of granite could be found by the AE monitoring data. The test devices are shown in Figure 2.

After 15 tests with different confining pressures (5 MPa, 10 MPa, 20 MPa, 30 MPa, and 40 MPa), the stress-strain curves with AE data from triaxial compressive tests were obtained, to display the part of AE events corresponding to the initial crack point, and to eliminate the display problem caused by overlarge AE events at the peak stage, the detailed diagram of AE events should be presented. The typical testing curves and their partial detailed diagram are shown in Figure 3.

As shown in Figure 3, for calculation of linear elastic strain energy of deep granite, the initial crack point of granite acquired acoustic emission monitoring was recognized as the turning point of rock from strain energy storage to energy dissipation.

2.3. Result of Linear Elastic Strain Energy. After analysis of 15 stress-strain curves with AE monitoring data, the elastic modulus and stress value at the initial crack point are confirmed to calculate linear elastic strain energy.

$$W_e = \frac{1}{2} E \sigma_{ci}^2, \quad (1)$$

where W_e is the linear elastic strain energy, E is the elastic modulus, and σ_{ci} is the value of initial crack stress.



FIGURE 1: The granite samples and their optical image.

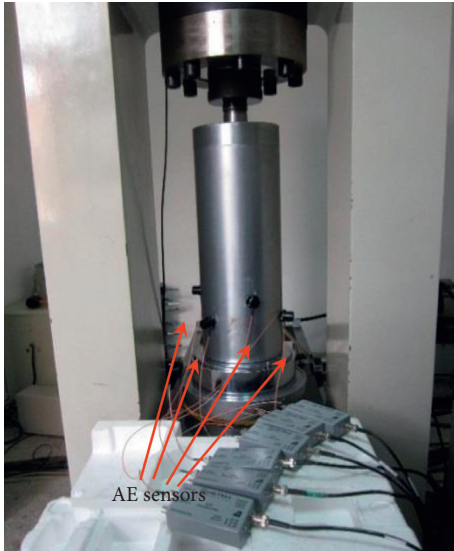


FIGURE 2: Triaxial compressive test of granite with AE monitoring.

Table 1 shows the initial crack stress, the elastic modulus, and Poisson's ratio corresponding to the initial crack point and the calculated linear elastic strain energy density of deep granite with 5 typical confining pressures. Based on the test data in Table 1, the linear elastic strain energy density curves of deep granite under different confining pressures can be fitted, as shown in Figure 4.

As shown in Figure 4, with increase of confining pressure, the linear elastic strain energy density value presents a linear growth law. When the confining pressure is 40 MPa, the linear elastic strain energy density value of granite is close to $1.4e^5 \text{ J/m}^3$.

3. Peak Strain Energy Confirmed by the Full Cyclic Loading and Unloading Test

In order to supplement the elastic strain energy storage capacity of granite in the stage after the initial crack point and before the peak strength, the elastic stress-strain curve of this stage needs to be acquired. However, after the initial crack point, the elastic deformation and plastic damage deformation under the loading path are mixed together and cannot be distinguished. If the unloading test is carried out at this stage, since the elastic strain can recover, while the plastic strain cannot recover, the unloading curve can present the loading elastic stress-strain curve. Based on this view, the full cyclic loading and unloading tests are conducted to research the peak strain energy of deep granite.

3.1. Full Cyclic Loading and Unloading Tests. In the tests, the instrument is a MTS815 rock testing machine. In the full cyclic loading and unloading tests on granite samples, also 5 groups of typical confining pressure (5 MPa, 10 MPa, 20 MPa, 30 MPa, and 40 MPa) were selected. Based on the peak-strength values obtained from triaxial compressive tests, to select a suitable initial value for the cyclic loading and avoid the effect of fatigue damage caused by multiple cycles, the number of loading and unloading cycles should be controlled strictly. After the preliminary testing, the first cyclic point was set at 150 MPa of the axial pressure level and cycled at every 50 MPa. When the stress-strain curve seemingly approached the peak strength of the triaxial compressive test under the same confining pressure, the cyclic step was set at every 5 MPa, and after the peak strength, the cyclic space was readjusted to every 50 MPa. The loading and unloading path diagrams are shown in Figure 5.

3.2. Testing Result and Peak Strain Energy Analysis. After the full cyclic loading and unloading testing, the full cyclic stress-strain curves of 5 groups of granite samples under different confining pressure were obtained, and the specific data of peak unloading curves were also determined. The typical testing data curves are shown in Figure 6.

As shown in Figure 6, it is easy to confirm the peak stress. To obtain the unloading elastic modulus value for calculating the peak strain energy, the unloading curve at the peak-strength point was selected. Because the unloading curve is not a straight line, the slope value of the tangent line at the peak-strength point (red line with arrow) was recognized as the unloading elastic modulus. According to the peak unloading curve data, the curve between confining pressure and peak strain energy density can be fitted in the same way as energy density. The comparing data with the linear elastic strain energy diagram are shown in Figure 7.

As shown in Figure 7, with the increase in confining pressure, the strain energy density obtained by these two methods presents the linear growth law. Also, the peak strain energy is about 1.2 times than the linear elastic strain energy under the same confining pressure.

4. Maximum Strain Energy Considering Time-Delay Strain Characteristics

4.1. Time-Delay Strain Characteristics of Deep Granite. In the abovementioned full cyclic loading and unloading studies, it is found that although the rock samples are in the linear elastic stage, there is still a certain difference between the loading curve and the unloading curve. Because there is no plastic effect, this strain difference must be the recoverable elastic strain and may recover in the next period of time. In view of this finding, 20% and 40% peak stress unloading tests were performed to verify the time-delay strain characteristic of granite. The testing curves with 10 MPa and 20 MPa confining pressure are shown in Figure 8.

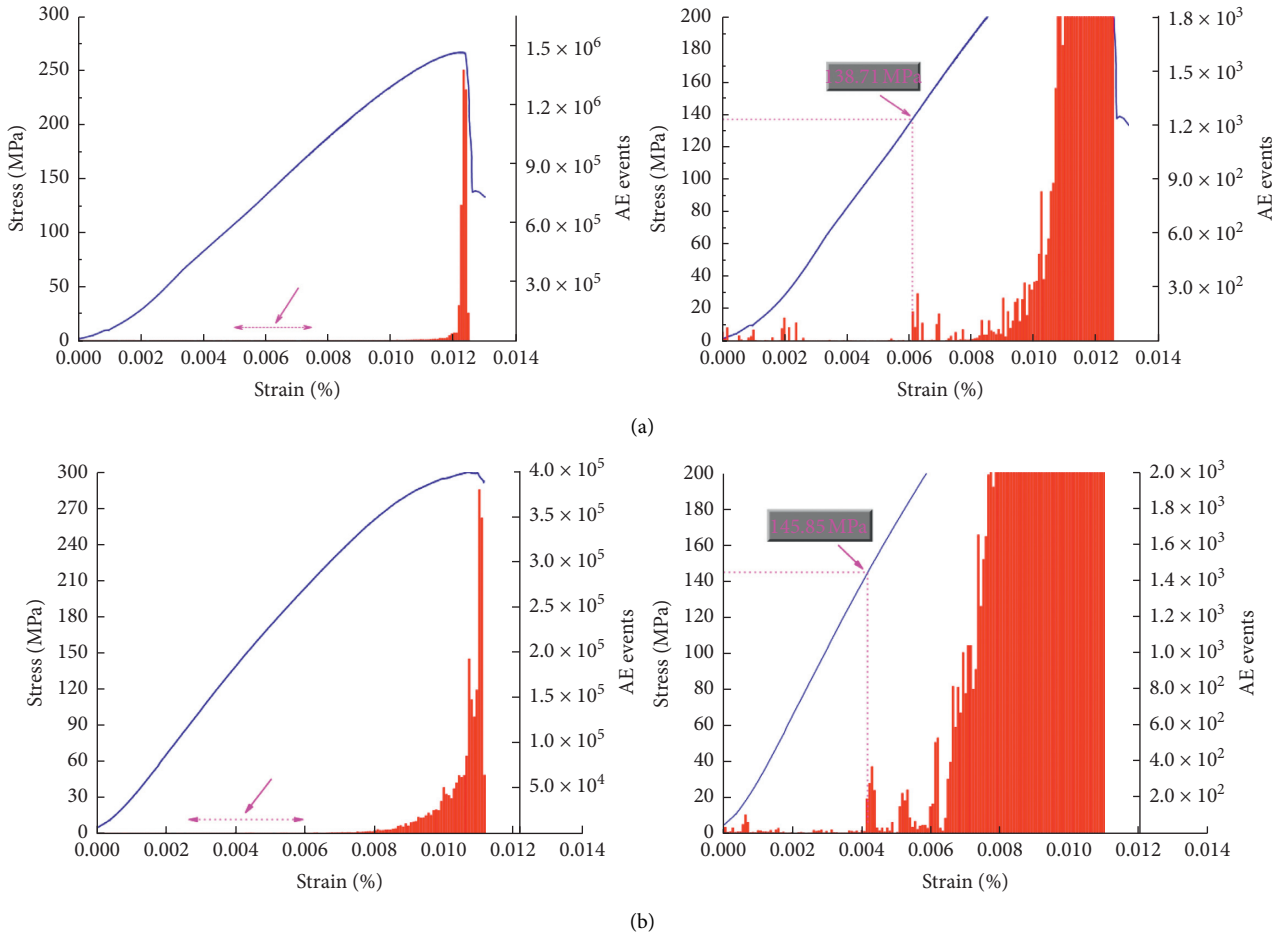


FIGURE 3: Typical stress-strain curve with AE events and its partial diagram of an initial crack point. (a) No. 1 testing specimen with 20 MPa confining pressure. (b) No. 2 testing specimen with 20 MPa confining pressure.

TABLE 1: The testing data and linear elastic strain energy.

Confining pressure (MPa)	Elasticity modulus (GPa)	Poisson's ratio	Initial crack stress (MPa)	Strain energy density ($J \cdot m^{-3}$)
5.0	60.30	0.21	93.50	$7.16E+04$
5.0	59.97	0.19	95.71	$6.78E+04$
5.0	61.16	0.21	110.47	$7.07E+04$
10.0	76.13	0.21	128.02	$7.82E+04$
10.0	74.56	0.23	137.19	$8.83E+04$
10.0	79.92	0.20	128.48	$7.89E+04$
20.0	85.27	0.23	138.71	$9.35E+04$
20.0	82.76	0.22	145.85	$1.03E+05$
20.0	78.01	0.23	164.03	$9.10E+04$
30.0	80.94	0.21	174.23	$1.26E+05$
30.0	91.86	0.23	194.00	$1.12E+05$
30.0	87.12	0.22	208.83	$1.19E+05$
40.0	86.24	0.24	214.94	$1.20E+05$
40.0	87.60	0.22	191.46	$1.34E+05$
40.0	83.90	0.23	249.61	$1.39E+05$

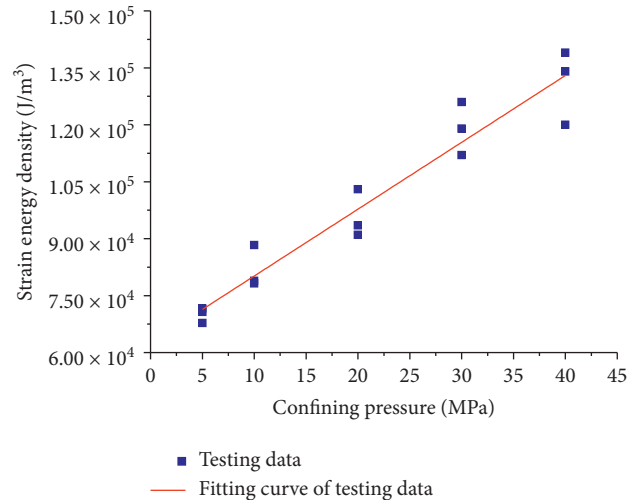


FIGURE 4: Linear elastic strain energy by the triaxial compressive test.

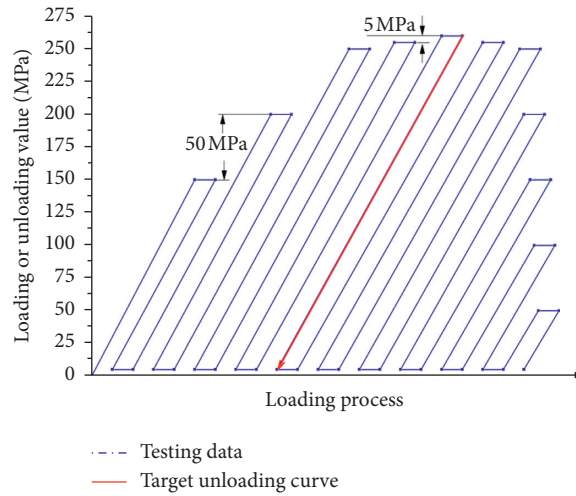


FIGURE 5: The loading and unloading path diagram.

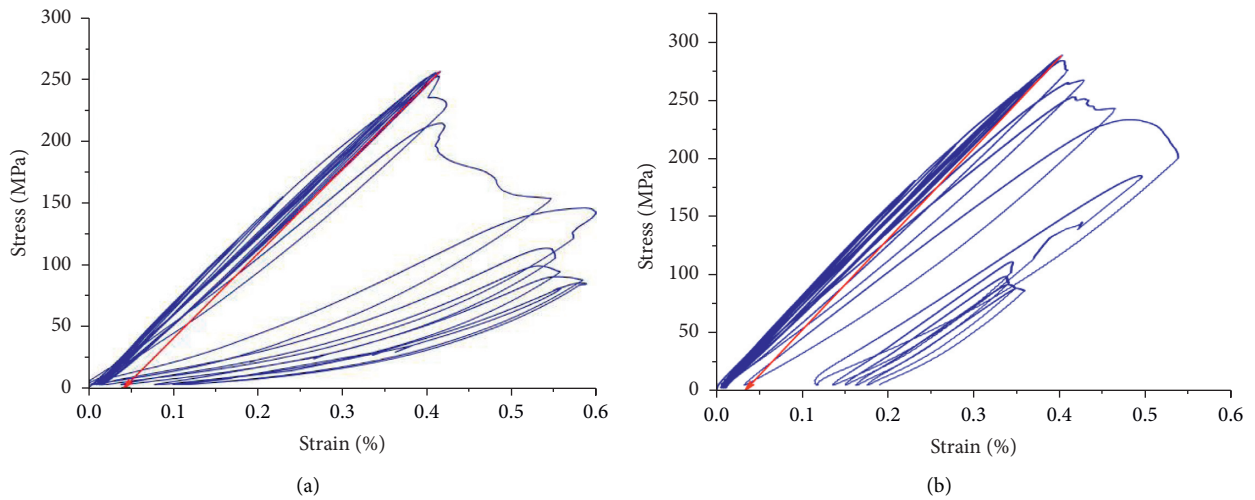


FIGURE 6: Typical stress-strain loading and unloading curves of granite. (a) 20 MPa. (b) 30 MPa.

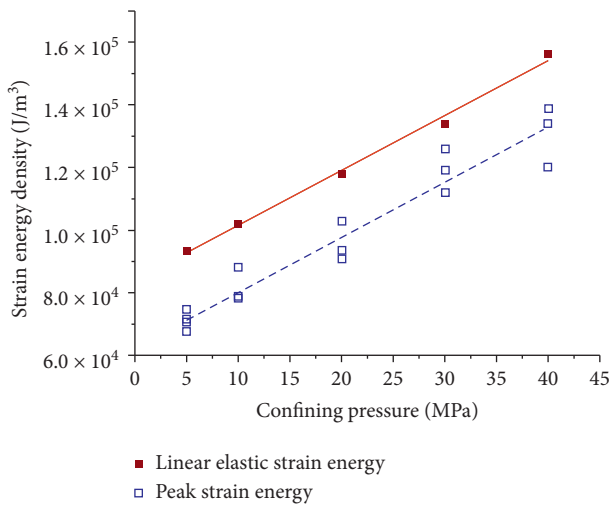


FIGURE 7: Strain energy density values of the peak unloading and crack initiation point method.

As shown in Figure 8, whether the loading is 20% or 40% peak stress, after 5 times loading and unloading, each unloading curve exactly coincides with the previous one. This also proves that a limited number of cycles do not cause fatigue damage. But, there is an obvious strain distance between the first loading curve and other curves, and the distance values are 0.01381 and 0.01577 corresponding to 20% and 40% peak stress under 10 MPa confining pressure. Under the 20 MPa confining pressure, the values are 0.01543 and 0.01846, respectively. From these strain distance values, two main conclusions can be reflected. Firstly, there is an obvious time-delay characteristic for the deep granite. Secondly, the time-delay strain mostly occurs in the early loading process (for $0.01577 - 0.01381 = 0.00196$, it is about 88% time-delay strain occurred in the previous 20% peak stress, and only 12% time-delay strain occurred in the next 20% peak stress under 10 MPa confining pressure. Also, the values are 84% and 16% for the time-delay strain occurred in the previous 20% and the next 20% peak stress under 20 MPa confining pressure).

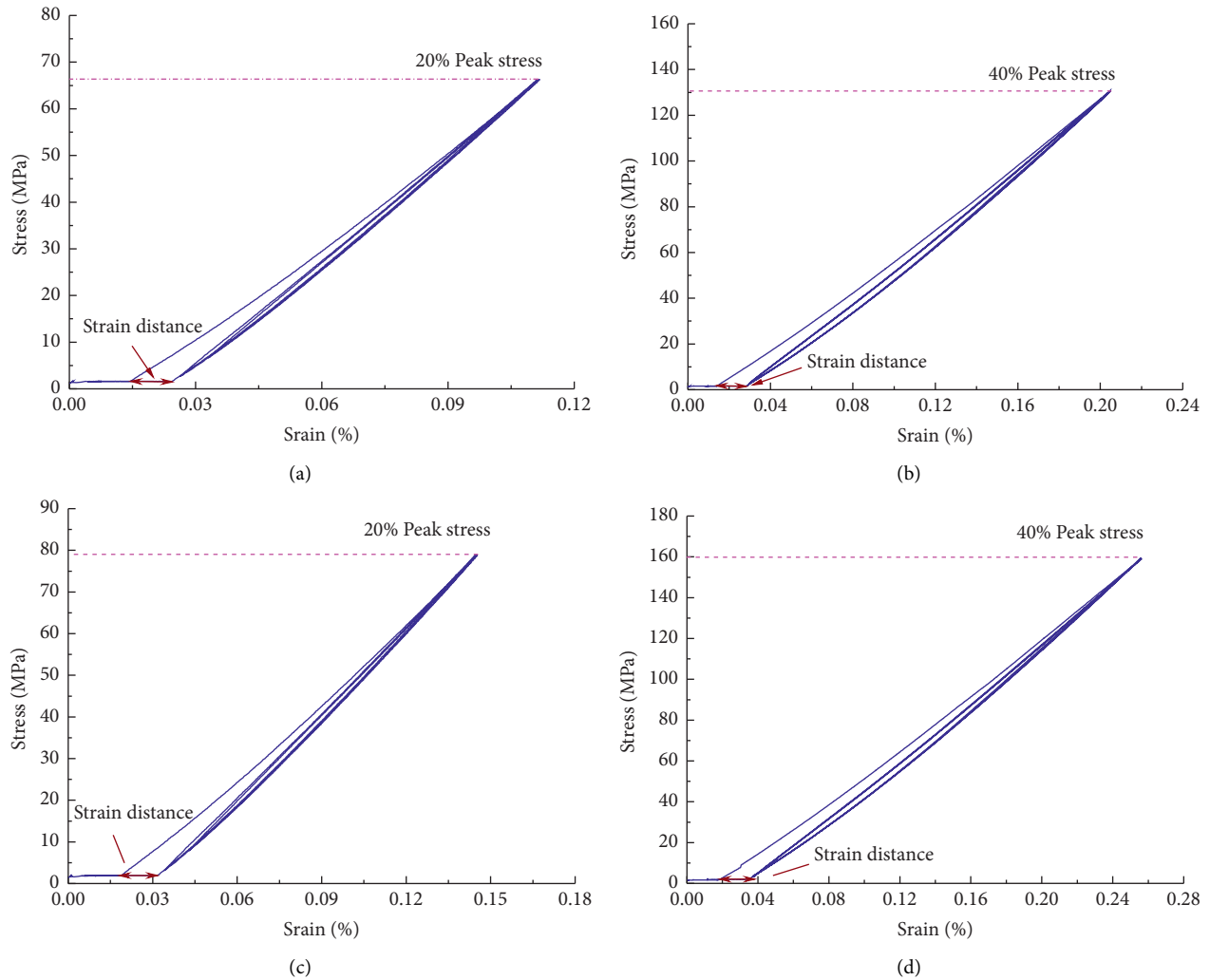


FIGURE 8: Time-delay characteristic verification test of granite. (a) 20% peak stress under 10 MPa. (b) 40% peak stress under 10 MPa. (c) 20% peak stress under 20 MPa. (d) 40% peak stress under 20 MPa.

4.2. Stage Cyclic Loading and Unloading Test with Dual Monitoring Systems. In order to quantify the time-delay strain characteristics of deep granite more accurately, stage cyclic loading and unloading tests with dual monitoring systems (extensometer system and strain rosette) were carried out. The dual monitoring systems are shown in Figure 9.

To obtain the most comprehensive time-delay strain value and ensure the rock sample does not develop obvious macroscopic cracks which can affect the next strain rebound monitoring, the largest loading value is set as the long-term strength of deep granite. After 3 groups of testing, the typical stage loading and unloading testing curves are as shown in Figure 10.

As shown in Figure 10, after the stage loading and unloading test, the axial and lateral strain both have the certain noninstantaneous rebound strain. In order to acquire the noninstantaneous rebound strain value and confirm the

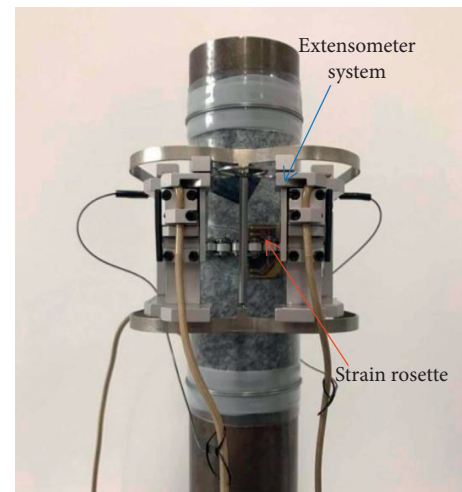


FIGURE 9: Extensometer and the strain monitoring system during the test.

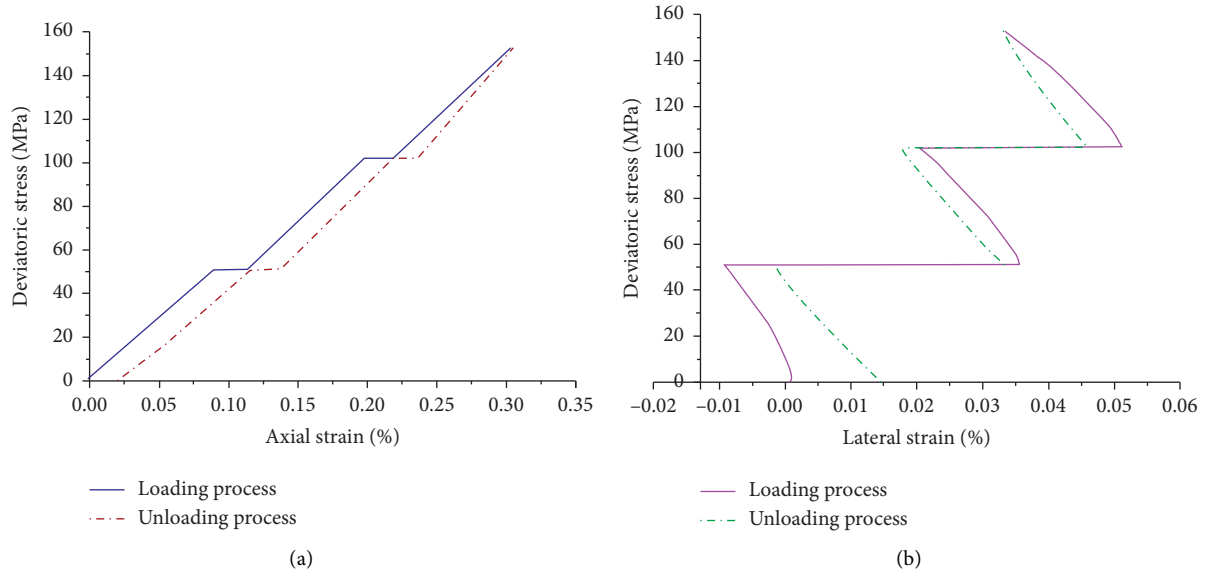


FIGURE 10: Typical stage loading and unloading testing curve. (a) Axial time-delay strain. (b) Lateral time-delay strain.

time of strain recovery, the prepaste strain gauges on the granite sample were connected to the strain collector and put into the incubator to eliminate the influence of temperature on the strain. The strain rebound value was collected for 2 hours every day with a sampling interval of 5 minutes. After 20 days of continuous monitoring, the monitoring data are as shown in Figure 11.

As shown in Figure 11, the axial strain rebound microstrain value is 132, and the lateral strain rebound microstrain value is 82, accounting for 5.6% and 22.7% of the corresponding total strain, respectively. Hence, for the maximal strain energy of deep granite, the value should consider the extra 5.6% addition in the vertical direction and 22.7% in the lateral direction.

4.3. Rockburst Tendency Prediction Based on Strain Energy.

In rockburst tendency analysis, the elastic strain energy model is often taken as the index. According to the elastic strain energy model, rockburst intensity can be divided into four grades:

$$W_e < 40 \text{ kJ/m}^3, \quad \text{I: Weak}, \quad (2)$$

$$40 \text{ kJ/m}^3 \leq W_e < 100 \text{ kJ/m}^3, \quad \text{II: Medium}, \quad (3)$$

$$100 \text{ kJ/m}^3 \leq W_e < 200 \text{ kJ/m}^3, \quad \text{III: Strong}, \quad (4)$$

$$200 \text{ kJ/m}^3 < W_e, \quad \text{IV: Intensity}. \quad (5)$$

The abovementioned research introduced different methods to obtain the strain energy of deep granite and calculated the corresponding strain energy density. Here, based on the calculated strain energy values, the rockburst strength grades are provided, the results are shown in Table 2, and the fitted curve are shown in Figure 12.

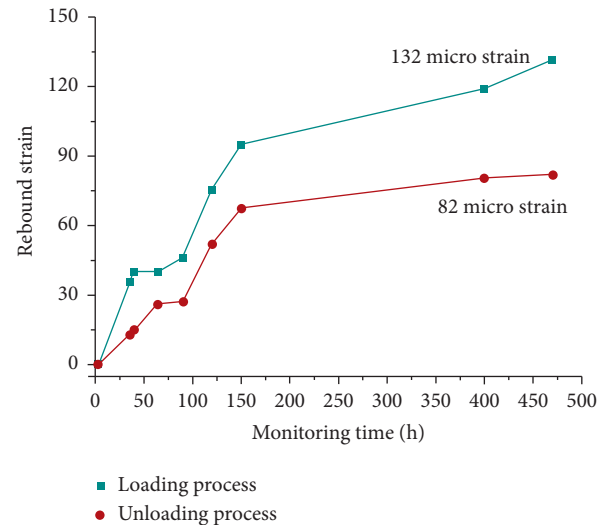


FIGURE 11: Elastic time-delay strain rebound monitoring data.

From Table 2 and Figure 12, it is easily found that the rockburst grades present an obvious increasing trend after considering the peak strain energy and time-delay strain energy. When the testing granite were located in a lower geostress condition (less than 20 MPa), the rockburst grades present as the “Weak” with the linear strain energy approach, and the rockburst grades will improve to the “medium” using the maximal strain energy approach. Also, even under the 40 MPa confining pressure, the strain energy density is increased by $4.3e^4 \text{ J/m}^3$. Therefore, scientifically measuring the strain energy storage capacity of deep granite can provide accurate data support for defining the magnitude of rockburst and other dynamic disasters.

TABLE 2: Rockburst tendency under different confining pressures.

Confining pressure (MPa)	Linear strain energy density	Rockburst grades	Peak strain energy density	Rockburst grades	Maximal strain energy density	Rockburst grades
5	$7.0E+04$	Weak	$9.31E+04$	Weak	$1.04E+05$	Medium
10	$8.2E+04$	Weak	$1.02E+05$	Medium	$1.14E+05$	Medium
20	$9.6E+04$	Weak	$1.18E+05$	Medium	$1.32E+05$	Medium
30	$1.2E+05$	Medium	$1.34E+05$	Medium	$1.49E+05$	Medium
40	$1.31E+05$	Medium	$1.56E+05$	Medium	$1.74E+05$	Medium

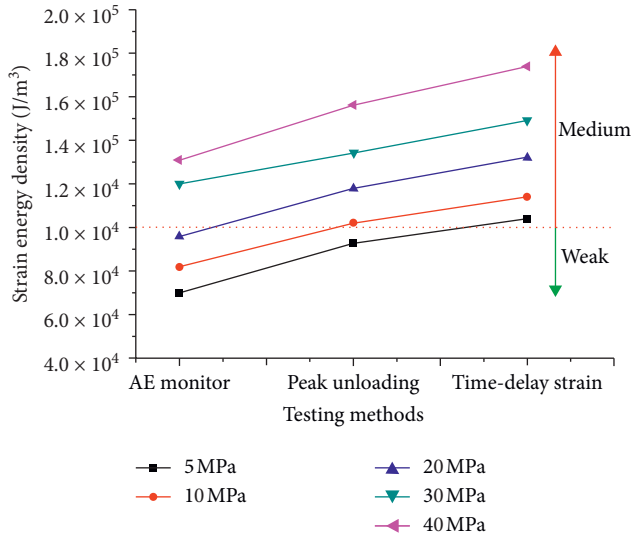


FIGURE 12: Strain energy and rockburst tendency analysis.

5. Conclusions

In this article, three different testing methods were adopted to present the storage capacity of strain energy, and the main conclusions are as follows:

- (1) In this study, based on the AE monitoring data, the initial stress point under different confining pressures were confirmed, and the linear elastic strain energy of deep granite was calculated. The testing results showed that, with the increase in confining pressure, the linear elastic strain energy density value presents a linear growth law. Also, when the confining pressure is 40 MPa, the linear elastic strain energy density value of granite is close to $1.4e^5 \text{ J/m}^3$.
- (2) To supplement the elastic strain energy storage capacity of granite in the stage after the initial crack point and before the peak strength, the full cyclic loading and unloading tests are designed and carried out to assess the peak strain energy. After testing, the peak strain energy also presents the linear growth law. Also, the peak strain energy is about 1.2 times than linear elastic strain energy under the same confining pressure.
- (3) During the full cyclic loading and unloading studies, the deep granite presents obvious time-delay characteristics, so the 20% and 40% peak stress unloading

tests were performed to testify the time-delay characteristics. The stage loading and unloading tests with a dual monitoring system were carried out to acquire time-delay value and recovery time. The testing data indicated that there are 132 microstrains in the axial direction, and the 82 microstrains in the lateral direction can recover in 20 days.

- (4) At last, the rockburst tendency was analyzed by employing the elastic strain energy index model. After investigating, it is easily found that the rockburst grades present an obvious increasing trend after considering the peak strain energy and time-delay strain energy. Under the 40 MPa confining pressure, the strain energy density is increased by $4.3e^4 \text{ J/m}^3$. A precise strain energy characterization method can provide accurate data support for rockburst evaluation.

Data Availability

All data used to support the findings of this study are available from the corresponding author upon request.

Conflicts of Interest

All the authors declare that there are no conflicts of interest regarding the publication of this paper.

Acknowledgments

The authors acknowledge the financial supports from the State Key Research Development Program of China (No. 2018YFE0123000).

References

- [1] H. Xie, H. Konietzky, and H. W. Zhou, "Special issue "deep mining"," *Rock Mechanics and Rock Engineering*, vol. 52, no. 5, pp. 1415-1416, 2019.
- [2] P. K. Kaiser, D. D. Tannant, and D. R. McCreath, *Canadian Rockburst Support Handbook*, Geomechanics Research Centre/Laurentian University, Sudbury, Canada, 1996.
- [3] J. Kornowski and J. Kurzeja, "Prediction of rockburst probability given seismic energy and factors defined by the expert method of hazard evaluation (MRG)," *Acta Geophysica*, vol. 60, no. 2, pp. 472-486, 2012.
- [4] N. Hosseini, "Evaluation of the rockburst potential in longwall coal mining using passive seismic velocity tomography and image subtraction technique," *Journal of Seismology*, vol. 21, no. 5, pp. 1101-1110, 2017.

- [5] Z.-L. Li, X.-Q. He, L.-M. Dou, and G.-F. Wang, "Rockburst occurrences and microseismicity in a longwall panel experiencing frequent rockbursts," *Geosciences Journal*, vol. 22, no. 4, pp. 623–639, 2018.
- [6] R. S. Faradonbeh and A. Taheri, "Long-term prediction of rockburst hazard in deep underground openings using three robust data mining techniques," *Engineering with Computers*, vol. 35, no. 2, pp. 659–675, 2019.
- [7] R. S. Faradonbeh, S. S. Haghshenas, A. Taheri, and R. Mikaeil, "Application of self-organizing map and fuzzy c-mean techniques for rockburst clustering in deep underground projects," *Neural Computing and Applications*, vol. 32, no. 12, pp. 8545–8559, 2019.
- [8] E. Ghasemi, H. Gholizadeh, and A. C. Adoko, "Evaluation of rockburst occurrence and intensity in underground structures using decision tree approach," *Engineering with Computers*, vol. 36, no. 1, pp. 213–225, 2020.
- [9] B. Y. Jiang, L. G. Wang, Y. L. Lu, C. Q. Wang, and D. Ma, "Combined early warning method for rockburst in a Deep Island, fully mechanized caving face," *Arabian Journal of Geosciences*, vol. 9, no. 20, p. 743, 2016.
- [10] Q. J. Jia, L. Wu, B. Li, C. H. Chen, and Y. X. Peng, "The comprehensive prediction model of rockburst tendency in tunnel based on optimized unascertained measure theory," *Geotechnical and Geological Engineering*, vol. 37, no. 4, pp. 3399–3411, 2019.
- [11] M. C. He, W. Nie, Z. Y. Zhao, and W. Guo, "Experimental investigation of bedding plane orientation on the rockburst behavior of sandstone," *Rock Mechanics and Rock Engineering*, vol. 45, no. 3, pp. 311–326, 2012.
- [12] K. Du, M. Tao, X.-B. Li, and J. Zhou, "Experimental study of slabbing and rockburst induced by true-triaxial unloading and local dynamic disturbance," *Rock Mechanics and Rock Engineering*, vol. 49, no. 9, pp. 3437–3453, 2016.
- [13] G. S. Su, X. T. Feng, J. H. Wang, J. Q. Jiang, and L. H. Hu, "Experimental study of remotely triggered rockburst induced by a tunnel axial dynamic disturbance under true-triaxial conditions," *Rock Mechanics and Rock Engineering*, vol. 50, no. 8, pp. 2207–2226, 2017.
- [14] F. Zhao and M. C. He, "Size effects on granite behavior under unloading rockburst test," *Bulletin of Engineering Geology and the Environment*, vol. 76, no. 3, pp. 1183–1197, 2017.
- [15] F.-Q. Gong, C. Wu, S. Luo, and J.-Y. Yan, "Load-unload response ratio characteristics of rock materials and their application in prediction of rockburst proneness," *Bulletin of Engineering Geology and the Environment*, vol. 78, no. 7, pp. 5445–5466, 2019.
- [16] G. N. Feit, O. N. Malinnikova, V. S. Zykov, and V. A. Rudakov, "Prediction of rockburst and sudden outburst hazard on the basis of estimate of rock-mass energy," *Journal of Mining Science*, vol. 38, no. 1, pp. 61–63, 2002.
- [17] D. Y. Li, Z. Sun, T. Xie, X. B. Li, and P. G. Ranjith, "Energy evolution characteristics of hard rock during triaxial failure with different loading and unloading paths," *Engineering Geology*, vol. 228, pp. 270–281, 2017.
- [18] J. Xu, J. D. Jiang, N. Xu, Q. S. Liu, and Y. F. Gao, "A new energy index for evaluating the tendency of rockburst and its engineering application," *Engineering Geology*, vol. 230, pp. 46–54, 2017.
- [19] Z. Khademian and U. Ozbay, "Modeling violent rock failures in tunneling and shaft boring based on energy balance calculations," *Tunnelling and Underground Space Technology*, vol. 90, pp. 62–75, 2019.
- [20] L. Weng, L. Q. Huang, A. Taheri, and X. B. Li, "Rockburst characteristics and numerical simulation based on a strain energy density index: a case study of a roadway in Linglong gold mine, China," *Tunnelling and Underground Space Technology*, vol. 69, pp. 223–232, 2017.
- [21] Y. D. Shou, X. P. Zhou, and Q. H. Qian, "A critical condition of the zonal disintegration in deep rock masses: strain energy density approach," *Theoretical and Applied Fracture Mechanics*, vol. 97, pp. 322–332, 2018.
- [22] S. M. J. Razavi, M. R. M. Aliha, and F. Berto, "Application of an average strain energy density criterion to obtain the mixed mode fracture load of granite rock tested with the cracked asymmetric four-point bend specimens," *Theoretical and Applied Fracture Mechanics*, vol. 97, pp. 419–425, 2018.
- [23] X. J. Dong, A. Karrech, H. Basarir, M. Elchalakani, and C. C. Qi, "Analytical solution of energy redistribution in rectangular openings upon insitu rock mass alteration," *International Journal of Rock Mechanics and Mining Sciences*, vol. 106, pp. 74–83, 2018.
- [24] M. Sepehri, D. B. Apel, S. Adeebe, P. Leveille, and R. A. Hall, "Evaluation of mining-induced energy and rockburst prediction at a diamond mine in Canada using a full 3D elastoplastic finite element model," *Engineering Geology*, vol. 266, Article ID 105457, 2020.
- [25] G. F. Wang, S. Y. Gong, L. M. Dou, H. Wang, W. Cai, and A. Y. Cao, "Rockburst characteristics in syncline regions and microseismic precursors based on energy density clouds," *Tunnelling and Underground Space Technology*, vol. 81, pp. 83–93, 2018.
- [26] Z. Y. Chen, G. S. Su, J. W. Ju, and J. Q. Jiang, "Experimental study on energy dissipation of fragments during rockburst," *Bulletin of Engineering Geology and the Environment*, vol. 78, no. 7, pp. 5369–5386, 2019.
- [27] N. Li, Y. S. Zou, S. C. Zhang et al., "Rock brittleness evaluation based on energy dissipation under triaxial compression," *Journal of Petroleum Science and Engineering*, vol. 183, Article ID 106349, 2019.
- [28] F. Wang and R. Kaunda, "Assessment of rockburst hazard by quantifying the consequence with plastic strain work and released energy in numerical models," *International Journal of Mining Science and Technology*, vol. 29, no. 1, pp. 93–97, 2019.
- [29] P. Ying, Z. M. Zhu, F. Wang, M. Wang, C. Y. Niu, and L. Zhou, "The characteristics of dynamic fracture toughness and energy release rate of rock under impact," *Measurement*, vol. 147, Article ID 106884, 2019.
- [30] X. C. Hu, G. S. Su, G. Y. Chen et al., "Experiment on rockburst process of borehole and its acoustic emission characteristics," *Rock Mechanics and Rock Engineering*, vol. 52, no. 3, pp. 783–802, 2019.
- [31] G. S. Su, Y. J. Shi, X. T. Feng, J. Q. Jiang, J. Zhang, and Q. Jiang, "True-triaxial experimental study of the evolutionary features of the acoustic emissions and sounds of rockburst processes," *Rock Mechanics and Rock Engineering*, vol. 51, no. 2, pp. 375–389, 2018.
- [32] X. M. Sun, H. C. Xu, L. G. Zheng, M. C. He, and W. L. Gong, "An experimental investigation on acoustic emission characteristics of sandstone rockburst with different moisture contents," *Science China Technological Sciences*, vol. 59, no. 10, pp. 1549–1558, 2016.

Research Article

A New Method for Predicting Coal and Gas Outbursts

Guowei Dong ^{1,2,3}, Xuanming Liang^{1,3} and Qixiang Wang^{4,5}

¹School of Energy Engineering, Xi'an University of Science and Technology, Xi'an 710054, China

²The State Key Laboratory of Coal Resources and Safe Mining (CUMT), Xuzhou 221116, China

³Key Laboratory of Western Mine Exploitation and Hazard Prevention of the Ministry of Education, Xi'an 710054, China

⁴China Coal Technology and Engineering Group Corp Chongqing Research Institute, Chongqing 400039, China

⁵National Key Laboratory of Gas Disaster Monitoring, Preventing and Emergency Controlling, Chongqing 400039, China

Correspondence should be addressed to Guowei Dong; leng285@xust.edu.cn

Received 4 April 2020; Revised 18 May 2020; Accepted 4 June 2020; Published 24 June 2020

Academic Editor: Hongwei Yang

Copyright © 2020 Guowei Dong et al. This is an open access article distributed under the Creative Commons Attribution License, which permits unrestricted use, distribution, and reproduction in any medium, provided the original work is properly cited.

In view of the fact that coal and gas outbursts are difficult to predict, a new method for predicting coal and gas outbursts was proposed based on occurrence mechanisms of coal and gas outbursts relating to coal mass strength, gas pressure, and *in situ* stress. The method revealed that the rate of occurrence of coal and gas outbursts in mines was 5% to 10% and gas pressures for coal and gas outbursts in shallow and deep mines in China were greater than 0.74 and 0.6 MPa, respectively. The prediction index for coal and gas outbursts based on the gas factor was the gas desorption index of drilling cuttings (K_1), which is referred to the gas content desorbed from the coal mass in the first minute of drilling. The prediction index for coal and gas outbursts based on coal mass strength was the thickness of a soft layer that could be twisted into powder by hand. Based on many cases of coal and gas outbursts, the critical thickness of the soft layer was found to have been 0.2 m. The prediction index for coal and gas outbursts based on *in situ* stress was the weight of drilling cuttings, which represented the mass of drilling cuttings per linear metre of boreholes with diameters of 42 or 75 mm. Finally, the new prediction method and prediction index critical values for coal and gas outbursts were verified based on industrial application tests. This method has been widely applied on-site and obtained good prediction results.

1. Introduction

From the perspective of energy demand, the dominance of coal in the energy structure will not change in the near future in China. The proportion of coal consumption will remain at about 50% for a long time and about 80% of this coal is mined in underground wells. In recent years, with the large-scale exploitation of coal, mining depth of mines in the central and eastern China has rapidly increased and extends to the deep parts at the rate of nearly 20 m per year. Western resources have also been developed in a large area, with coal production increasing in these regions, such as Shaanxi Province, the Inner Mongolia Autonomous Region, and the Xinjiang Uygur Autonomous Region. This leads to an increasingly serious threat posed by dynamic disasters, such as coal and gas outbursts, to safe production in coal mines. Statistical data in recent years show that although a series of effective measures have been taken to prevent disasters and

accidents in coal mines, the number of outburst-prone mines still increases by hundreds every year [1], and the number of outburst accidents and deaths has not decreased significantly. Therefore, effectively preventing gas accidents in coal mines, especially coal and gas dynamic disasters represented by coal and gas outbursts, has been the primary task of engineers working in the field of coal mine safety.

The mechanism of occurrence of coal and gas outbursts refers to the cause, condition, and process of initiation, excitation, development, and termination of coal and gas outbursts. The comprehensive theory of action is generally accepted in terms of occurrence mechanism and prediction of coal and gas outbursts. The representative theories include energy theory, theory of crushing wave, theory of uneven stress distribution, theory of initiation centre, the rheological hypothesis of Zhou and He [2], the spherical shell destabilisation concept of Jiang and Yu [3], instability theory of flow fixation coupling of Liang et al. [4], and the catastrophe

theory of Wang and Yu [5]. In addition, the stick-slip mechanism of Guo and Han [6], dimensional analysis method of Zheng [7], mechanical theory of Hu et al. [8], deductive method of Xian et al. [9], hierarchical control theory of geological structure of Zhang [10], main controlling geological body theory of the authors [11], and key structure body theory of Shu et al. [12] are also included. Other scholars have done physical simulation experiments of coal and gas outbursts [13–25], Xu et al. [13] have obtained that the exposed area of coal seam has some effect on coal and gas outburst; Tang et al. [14] have obtained that high-pressure gas is not only outbursting power but also damage power for powdered coal; Zhang et al. [15] have investigated the distribution and characteristics of gas pressure and stress ahead of the crosscut uncovering the closed type tectonic fracture zone; Lei et al. [16] have acquired the frequency characteristics in the four stages; Zhao et al. [17] have designed the simulation test system of coal and gas outburst including single gas pressure test machine and gas pressure and ground stress comprehensive test machine; Nie et al. [18] have conducted an artificial outburst with absorption equilibrium pressure of 0.30 MPa and inducing pressure of 0.53 MPa; Li et al. [19] have studied the judgment criterion of the comprehensive effect for coal body stress and gas pressure; Wang et al. [20] have studied the influences of gas adsorption on coal and gas outburst; Wang et al. [21] have established a model of energy conditions and a model of intensity assessment for outburst and have verified the model with real cases; Li et al. [22] have established the prediction models of outburst energy and taken Pingdingshan mining area as an example; Xu et al. [23] have analyzed the evolution process of temperature-pressure-stress during outburst; Wen et al. [24] have analyzed the theoretical requirements of the over-kilometer deep mining environment on the indexing requirements of the outburst simulation system loading capacity, system stiffness, gas pressure, and temperature and have proposed its critical indicators; and the outburst simulation tests have verified theories of relevant mechanisms of occurrence. Hu et al. [25] used the drilling cuttings index to predict coal and gas outbursts; Dong [26] used the drilling cuttings index and acoustic emission index to predict coal and gas outbursts; Li et al. [27] predicted coal and gas outbursts based on spatial chaos theory using gas desorption index of drill cuttings; Tang et al. [28] used the expansion energy of the initially released gases to predict coal and gas outbursts; Chen et al. [29] studied an FDA-based multiple indicators discriminant model of coal and gas outburst and applied the discriminant model to predict coal and gas outbursts; Qiu et al. [30] used electromagnetic signals to predict coal and gas outbursts; Li et al. [31] used the acoustic emission index to predict coal and gas outbursts; Dong et al. [32] used the gas concentration extraction indices to provide an early warning of atypical outbursts. Wang et al. [33] used the microseismic index to predict coal and gas outbursts; Lu et al. [34–36] have studied the microseismic location method and multiparameter characteristics of microseismic events. Current predictions of coal and gas outburst mainly depend on indices related to drilling cuttings, initial velocity of gas

emission from a borehole, thickness of the soft layer, coal temperature, gas concentration extraction, acoustic emissions, and microseismic event counts. Research results have been adopted in relevant laws and regulations, such as Coal Mine Gas Grade Appraisal Method, Detailed Rules and Regulations for Prevention, and Control of Coal and Gas Outburst and Coal Mine Safety Regulation.

Although much research has been conducted on the mechanism of occurrence and prediction of coal and gas outbursts, how to use indices of gas pressure, drilling cuttings index, initial velocity of gas emission from borehole, thickness of soft layer, precursor signals, and so on to predict coal and gas outbursts is rarely reported. Aiming at this scientific problem, a new method for predicting coal and gas outbursts based on the mechanism of occurrence thereof was proposed in terms of coal mass strength, gas pressure, and *in situ* stress. By means of theoretical analysis, laboratory experiments, mathematical treatment, and industrial testing, coal and gas outbursts were predicted. Moreover, the method has been verified on-site.

2. A New Method for Predicting Coal and Gas Outbursts

For the new method for predicting coal and gas outbursts, many approaches such as theoretical analysis, laboratory experiments, mathematical treatment, and industrial testing were used to predict coal and gas outbursts. The method revealed that the rate of occurrence of coal and gas outbursts in mines was between 5% and 10% and gas pressures for coal and gas outbursts in shallow and deep mines separately were above 0.74 and 0.6 MPa in China [37]. During field measurement in a mining roadway, the prediction indices for coal and gas outbursts in the mine were determined according to geologic tectonic region, presence or absence of precursor areas of outbursts, changes before and after taking measures for preventing outbursts, and percentages of indices (i.e., normalised values thereof). The generally used prediction indices included gas desorption of drilling cuttings (K_1), weight of drilling cuttings (S), initial velocity of gas emission (q), and thickness of a soft layer.

The prediction index for coal and gas outbursts based on gas factor was gas desorption index K_1 of drilling cuttings, which denoted the gas content desorbed from the coal mass in the first minute of drilling. Firstly, the relationship between K_1 and gas pressure P was established through adsorption and desorption experiments in the laboratory and the initial prediction index critical value of K_1 was determined at gas pressures of 0.6 and 0.74 MPa during outbursts in the mine. Secondly, K_1 data were collected through *in situ* testing. When the proportion of a certain value among the collected data was 30% (considering a triple safety factor) [26], the value was taken as the initial prediction index critical value of K_1 . Thirdly, in accordance with that value of K_1 corresponding to outburst precursors collected *in situ*, the initial prediction index critical value was determined. The smallest value of the three was taken as the prediction index critical value of coal and gas outbursts in the coal seam. The prediction index for coal and gas outbursts based

on coal mass strength was the thickness of the soft layer that could be twisted into powder by hand. Based on many cases of coal and gas outbursts, the prediction index critical value of the thickness of the soft layer was 0.2 m [37]. Furthermore, the prediction index for coal and gas outbursts based on *in situ* stress was the weight of drilling cuttings, which indicated the weight of drilling cuttings per linear metre of boreholes with diameters of 42 or 75 mm. Firstly, through the industrial test conducted on-site, the data pertaining to the weight of drilling cuttings were collected. If the proportion of a certain value accounted for 30% of the collected data [26] (considering a triple safety factor), the value was adopted as the initial prediction index critical value of the index. Secondly, according to the weight of drilling cuttings corresponding to outburst precursors collected *in situ*, the initial prediction index critical value was determined. The smaller one of the two was the critical value of prediction index of coal and gas outbursts in the coal seam. Finally, the new method for predicting coal and gas outbursts and critical values were verified based on industrial application.

Compared with other methods, the new method is simple and practical.

3. Case Study: A New Method for Predicting Coal and Gas Outbursts

3.1. Overview of the Mine. The No. 2 well in Enhong Coal Mine, Yunnan Province, China, has been in production since 1958, with a designed production capacity of 6×10^5 t/a and the actual production capacity of about 4×10^5 t/a. It is a coal and gas outburst mine.

The mine is mainly controlled by the Cathaysian tectonic system. Primary structures in the mine including fault from Fuyuan County to Mile City, fault from Yingshang Township to A'gang Township, and Enhong compound syncline control the occurrence, metamorphism, and failure of coal-bearing strata.

The coal seams in the mine belong to the Late Permian Longtan Formation. The coal seams in the mine field extend about 6 km from southwest to northeast, while they dip about 3 km from the northwest to the southeast. The dip angle of the coal seams ranges from 5° to 12° . Of them, the C9 coal seam, containing low ash, low sulphur, and high calorific value coking coal, is mainly mined.

Inclined shaft development was used in the No. 2 well of Enhong Coal Mine. Two mining levels were set, that is, the levels at elevations of +1940 m and +1800 m. There were two mining areas, namely, the north wing and south wing. The stopping face in the south wing at the level of +1800 m was under active mining, while the mining in the north wing at the same level was about to be completed. About nine tunnelling faces were arranged in the mine. The stopping face was subject to longwall retreating mining along the strike and the coal blasting process, and the roof was controlled through the total subsidence method: blasting tunnelling technology and I-shaped steel supports were used in the tunnelling faces.

In the No. 2 well in Enhong Coal Mine, 23 coal and gas outbursts have occurred since 1980, with the maximum amount of outburst coal of 235 t and average amount of

16.55 t. The maximum amount of gas emitted was 8.3×10^4 m³. The outburst sites showed elevation of +1932 to 1874 m at vertical distances of 120 to 416 m from the surface (Table 1).

The gas desorption index of drilling cuttings and critical values recommended by the Detailed Rules and Regulations for Prevention and Control of Coal and Gas Outbursts were adopted as the current prediction indices and critical values for the test working face of the mine. They are as follows: the thickness of the soft layer was 0.2 m, $K_1 = 0.5$ mL/g.min^{1/2}, and $S = 6$ kg/m (in a borehole with a diameter of 42 mm) or 18 kg/m (in a borehole with a diameter of 75 mm).

3.2. Determination of Parameters for Coal and Gas Outbursts in the C9 Coal Seam. By using the channel sampling method on-site, four samples were taken from the C9 coal seam: one from all levels and three from the soft layer. The gas parameters including proximate analysis of coal, initial velocity of gas emission, and Protodyakonov coefficient were determined in the laboratory (Tables 2 and 3).

The method for measuring pressure in boreholes was used on-site to determine gas pressures in the coal seam and other gas parameters (Table 4).

3.3. Determination of Sensitive Indices for Coal and Gas Outbursts in the C9 Coal Seam. In the process of field measurement of the mining roadway, based on the index indicating the presence or absence of precursor areas of outbursts and change therein before and after taking measures for preventing outbursts, the sensitivities of index K_1 of drilling cuttings desorption, S , and initial velocity q of gas emission were investigated. Finally, the gas desorption index K_1 of drilling cuttings was selected as the main prediction index. Considering the increase of burial depth and geologic tectonic zone, the weight S of drilling cuttings was regarded as a reference index (Tables 5 and 6 and Figures 1 and 2).

According to Table 5 and Figure 1, the gas desorption index K_1 of drilling cuttings decreased to a significant extent (33% reduction); when the thickness of the coal seam changed likewise, the value of precursor areas of outbursts was large and measures for preventing outbursts were taken; namely, the index was sensitive to coal and gas outbursts.

Based on Table 6 and Figure 2, the index S of the weight of drilling cuttings reduced slightly when the thickness of the coal seam changed and values of precursor areas of outbursts were small after taking measures for preventing outbursts (e.g., drilling holes). This implied that the index was not sensitive to coal and gas outbursts; however, by taking the increase of burial depth and geological structural zone into account, the index S of the weight of drilling cuttings was considered as a reference index.

During the test, several tests were conducted for determining initial velocity q of gas emission: however, due to softness of coal seam, collapses in boreholes, and lack of a tight seal to such boreholes, test indices were generally small and the initial velocity of gas emission from boreholes could not be determined at most points; therefore, it was not used

TABLE 1: Statistics pertaining to times and intensity of outbursts in the mine.

Grade of outburst intensity (t)	Times of outburst		Outburst intensity		
	Times	Proportion (%)	Maximum amount of coal burst (t)	Average amount of coal burst (t)	Maximum amount of gas emitted (10^4 m^3)
Submassive outburst (100 to 499 t)	2	8.7	235	186	3.3
Medium outburst (50 to 99 t)	2	8.7	94	72	3.4
Small outburst (<50 t)	19	82.6	39	12.4	8.3
Total	23	—	235	32.7	8.3

TABLE 2: Parameters including gas adsorption constant and proximate analysis of the C9 coal seam.

Coal seam	Sampling site	Proximate analysis (%)			True density, TRD	Apparent density, ARD	Porosity, F (%)	Gas adsorption constant	
		M_{ad}	A_d	V_{daf}				a	b
C9	Transportation roadway in the 121901 working face at the 1800 m level	0.43	8.74	22.31	1.37	1.20	12.41	20.5147	0.8480

Note: adsorption experiments were conducted at $t_s = 30^\circ\text{C}$.

TABLE 3: Failure type in the C9 coal seam, initial velocity of gas emission, and firmness coefficient.

Coal seam	Sampling site	Outburst parameter		
		Failure type of coal seam	Initial velocity of gas emission, ΔP	Protodyakonov coefficient, f
C9	Return air roadway in the 121901 working face	V	21	0.19
	Transportation roadway in the 121901 working face	V	23	0.18
	2# connection roadway in the 121901 working face	V	19	0.19

TABLE 4: Gas pressures in the C9 coal seam and other gas parameters.

Coal seam	Testing site	Gas pressure, P (MPa)	Gas content, Q (m^3/t)	Permeability coefficient, λ ($\text{m}^2/\text{MPa}^2 \cdot \text{d}$)	Attenuation coefficient of flow in borehole, α (d^{-1})
C9	Floor drainage roadway at the 1800 m level	1.02	10.81	0.1341	0.111

as a predictive index for coal and gas outbursts and the test values are listed in Table 7.

During field investigation, the thickness of the soft layer was not obvious, so it was not used as a predictive index for coal and gas outbursts.

3.4. Determination of Critical Values of Sensitive Indices for Coal and Gas Outbursts in the C9 Coal Seam

3.4.1. Determination of Critical Value of Gas Desorption Index K_1 of Drilling Cuttings

- (1) Preliminarily determining critical value of gas desorption index K_1 of drilling cuttings based on the modelled K_1 - P relationship

The experimental process of assessing the K_1 - P relationship model is as follows: coal samples with particle sizes between 1 and 3 mm were taken and degassed for 2 h using a vacuum pump. After that, the coal samples were pressurised to the predetermined gas pressure for adsorption, to allow the coal samples to absorb gas for 24 h. The gas pressure under equilibrium was recorded. After exposing the coal samples to the atmosphere for 1 to 2 min, the value of K_1 was determined. At least five experiments were conducted on each coal sample. By fitting these data, the K_1 - P relationship model could be obtained. Figures 3–5 show the experimental results pertaining to the K_1 - P relationship model for coal samples from different sites in the C9 coal seam in Enhong Coal Mine.

TABLE 5: Gas desorption index K_1 of drilling cuttings based on geological structure and precursor areas of outbursts.

Area	Failure type of the coal seam	$K_{1\max}$ index	Geological structure	Outburst precursor
Return air roadway in the 121901 working face	III, IV	0.56	Thinning of coal seam	—
Return air roadway in the 121901 working face	III, IV	0.83	Thinning of coal seam	—
Return air roadway in the 121901 working face	III, IV	0.89	Thinning of coal seam	—
Transportation roadway in the 121901 working face	III, IV	0.82	Thinning of coal seam	—
Transportation roadway in the 121901 working face	III, IV	0.95	Thinning of coal seam	—
Transportation roadway in the 121901 working face	III, IV	0.69	Thinning of coal seam	—
Transportation roadway in the 121901 working face	III, IV	0.80	Thinning of coal seam	—
Transportation roadway in the 121901 working face	III, IV	0.57	Thickening of coal seam	—
Transportation roadway in the 121901 working face	III, IV	0.83	Thinning of coal seam	—
Transportation roadway in the 121901 working face	III, IV	0.70	Thinning of coal seam	—
Transportation roadway in the 121901 working face	III, IV	0.85	Thinning of coal seam	—
Transportation roadway in the 121901 working face	III, IV	0.74	Thinning of coal seam	—
2# connection roadway in the 121901 working face	III, IV	1.01	Thinning of coal seam	—
2# connection roadway in the 121901 working face	III, IV	1.04	Thinning of coal seam	—
South return air roadway at 1800 m level	III, IV	0.72	Thinning of coal seam	Coal burst
Transportation roadway in the 121901 working face	III, IV	0.78	Thinning of coal seam	Emission after pulling the drill pipe out
2# connection roadway in the 121901 working face	III, IV	0.88	Thinning of coal seam	Emission after pulling the drill pipe out
2# connection roadway in the 121901 working face	III, IV	0.88	Thickening of coal seam	Emission after pulling the drill pipe out

Based on the K_1 - P relationship model, the critical value of gas desorption index K_1 of drilling cuttings was preliminarily determined as $0.62 \text{ mL/g} \cdot \text{min}^{1/2}$ (gas pressure $P = 0.74 \text{ MPa}$), as presented in Table 8.

- (2) Preliminarily determining the critical value of gas desorption index K_1 of drilling cuttings based on percentages of data collected on-site

By cycling samples 109 times to collect prediction index K_1 on-site, the index and its percentages are shown in Figure 6 and Table 9; accordingly, when $K_{1\max} \geq 0.7 \text{ mL/g} \cdot \text{min}^{1/2}$, the percentage was 29%.

- (3) Determining initial critical value according to the K_1 value corresponding to outburst precursors collected during field testing

In accordance with Table 5, the minimum K_1 value corresponding to outburst precursors including coal burst and emission after pulling the drill pipe out collected during field testing was $0.72 \text{ mL/g} \cdot \text{min}^{1/2}$, so the value was used as the initial critical value of K_1 .

By combining the initial critical values (0.62, 0.70, and $0.72 \text{ mL/g} \cdot \text{min}^{1/2}$ (occurrence of coal and gas outburst)) as separately determined from the K_1 - P relationship model, data percentages, and outburst precursors, $0.60 \text{ mL/g} \cdot \text{min}^{1/2}$ was selected as the critical value of gas desorption index K_1 of drilling cuttings after numerical rounding of the data.

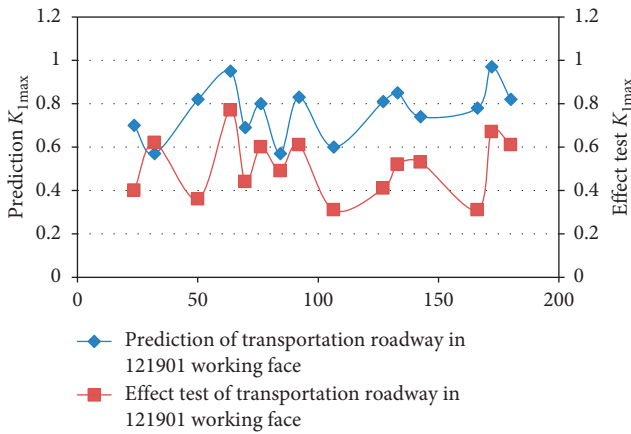
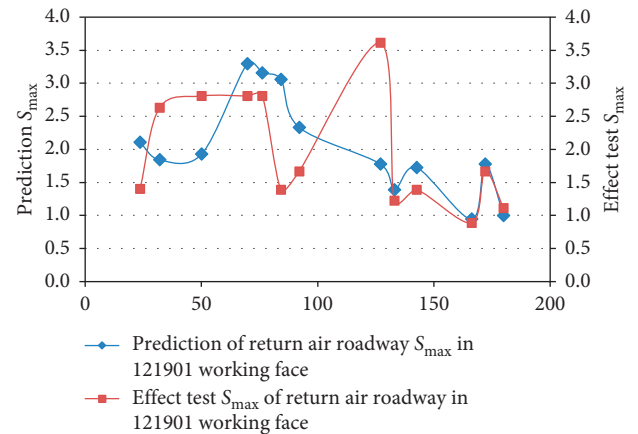
3.4.2. Determining the Critical Value of Index S of the Weight of Drilling Cuttings

- (1) Preliminarily determining the critical value of index S of the weight of drilling cuttings according to percentages of data collected on-site

A total of 68 cycles were conducted *in situ* to collect values for S as a prediction index. The index and its percentages are demonstrated in Figures 7 and 8 and Tables 10 and 11: when $S_{\max} \geq 3 \text{ kg/m}$ (in a borehole with a diameter of 42 mm), the percentage was 38%; for $S_{\max} \geq 14 \text{ kg/m}$ (in a borehole with a diameter of

TABLE 6: Index S of the weight of drilling cuttings based on geological structure and precursor areas of outbursts.

Area	Failure type of coal seam	S_{\max} index	Geological structure	Outburst precursor
Return air roadway in the 121901 working face	III, IV	1.4 ($\Phi 42$)	Thinning of coal seam	—
Return air roadway in the 121901 working face	III, IV	4.5 ($\Phi 42$)	Thinning of coal seam	—
Transportation roadway in the 121901 working face	III, IV	11 ($\Phi 75$)	Thinning of coal seam	—
Transportation roadway in the 121901 working face	III, IV	18.8 ($\Phi 75$)	Thinning of coal seam	—
Transportation roadway in the 121901 working face	III, IV	18 ($\Phi 75$)	Thinning of coal seam	—
Transportation roadway in the 121901 working face	III, IV	5.5 ($\Phi 42$)	Thickening of coal seam	—
Transportation roadway in the 121901 working face	III, IV	4.2 ($\Phi 42$)	Thinning of coal seam	—
Transportation roadway in the 121901 working face	III, IV	3.6 ($\Phi 42$)	Thinning of coal seam	—
Transportation roadway in the 121901 working face	III, IV	2.5 ($\Phi 42$)	Thinning of coal seam	—
Transportation roadway in the 121901 working face	III, IV	3.1 ($\Phi 42$)	Thinning of coal seam	—
2# connection roadway in the 121901 working face	III, IV	2 ($\Phi 42$)	Thinning of coal seam	—
South return air roadway at the 1800 m level	III, IV	2.2 ($\Phi 42$)	Thinning of coal seam	Coal burst
Transportation roadway in the 121901 working face	III, IV	2.5 ($\Phi 42$)	Thinning of coal seam	Emission after pulling the drill pipe out
2# connection roadway in the 121901 working face	III, IV	1.5 ($\Phi 42$)	Thinning of coal seam	Emission after pulling the drill pipe out
2# connection roadway in the 121901 working face	III, IV	2.7 ($\Phi 42$)	Thickening of coal seam	Emission after pulling the drill pipe out

FIGURE 1: Changes of $K_{1\max}$ index before and after taking preventative measures in the transportation roadway in the 121901 working face.FIGURE 2: Changes of the index of S_{\max} before and after taking preventative measures in the transportation roadway in the 121901 working face.

75 mm), the percentage was 39%. The initial critical values of the index S of the weight of drilling cuttings were determined as $S_{\max} = 3 \text{ kg/m}$ (in a borehole with a diameter of 42 mm) or $S_{\max} = 14 \text{ kg/m}$ (in a borehole with a diameter of 75 mm); however, the indices of the weight of drilling cuttings were generally small.

- (2) Determining the initial critical value of S in accordance with data corresponding to outburst precursors collected during field testing

As listed in Table 6, the minimum S value corresponding to outburst precursors including coal burst and emission after pulling the drill pipe out collected

TABLE 7: Test of initial velocity q of gas emission.

Site	2	3	4	5	6	7	8	9	10
3# connection roadway at the 1800 m level	3.2	2.3	0.1	0.2	0.2	0	0.1	0	—
3# connection roadway at the 1800 m level	0.2	0.2	2	1.2	0.2	0.2	—	—	—
3# connection roadway at the 1800 m level	1.2	3.2	—	—	—	—	—	—	—
3# connection roadway at the 1800 m level	2.6	0.8	1.2	1	1	2	—	—	—
Transportation roadway in the 121901 working face	—	1.2	—	—	3.4	—	—	—	—
Transportation roadway in the 121901 working face	0.2	1	—	—	—	—	—	—	—

TABLE 8: Initial critical value of gas desorption index K_1 of drilling cuttings.

Coal samples	Sampling site	Initial critical value of gas desorption index K_1 of drilling cuttings (mL/g.min ^{1/2})	K_1 - P relationship $K_1 = AP^B$	
			A	B
1	Return air roadway in the 121901 working face	0.62	0.7222	0.4948
2	Transportation roadway in the 121901 working face	0.69	0.8038	0.5122
3	2# connection roadway in the 121901 working face	0.67	0.7729	0.4961

TABLE 9: Distribution of percentages of prediction index K_{1max} during the test.

K_{1max} (mL/g.min ^{1/2})	Total times (109)	Percentage
≥0.1	109	100
≥0.2	107	98
≥0.3	96	88
≥0.4	70	64
≥0.5	61	56
≥0.6	44	40
≥0.7	32	29
≥0.8	20	18
≥0.9	7	6
≥1.0	4	4

TABLE 10: Distribution of percentages of prediction index S_{max} (Φ42 mm) during the test.

S_{max} (kg/m)	Total times (45)	Percentage
≥1	45	100
≥2	31	69
≥3	17	38
≥4	4	9
≥5	2	4
≥6	0	0

during field testing was 1.5 kg/m (in a borehole with a diameter of 42 mm). As no outburst precursors were observed for boreholes with a diameter of 75 mm, 1.5 kg/m (Φ42 mm) was regarded as the initial critical value of S .

TABLE 11: Distribution of percentages of prediction index S_{max} (Φ75 mm) during the test.

S_{max} (kg/m)	Total times (23)	Percentage
≥10	23	100
≥12	19	83
≥14	9	39
≥16	4	17
≥18	2	9

TABLE 12: Distribution of percentages of gas desorption index K_{1max} of drilling cuttings predicted during the field testing.

K_{1max} (mL/g min ^{1/2})	Total times (157)	Percentage
≥0.1	157	100
≥0.2	157	100
≥0.3	154	98
≥0.4	147	94
≥0.5	136	87
≥0.6	114	73
≥0.7	97	62
≥0.8	83	53
≥0.9	67	43
≥1.0	49	31

The initial critical values determined by combining with data percentages and outburst precursors and the S index were not sensitive to coal and gas outbursts in the C9 coal seam in this mine. Meanwhile, considering the increase of burial depth and the prevailing geological

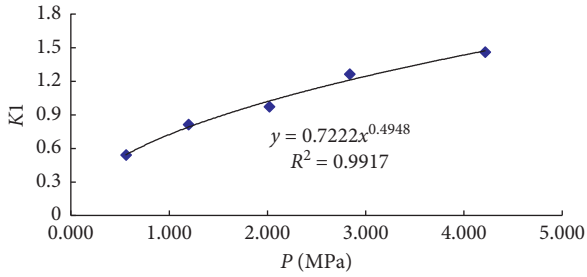


FIGURE 3: K_1 - P relationship model in the return air roadway in the 121901 working face.

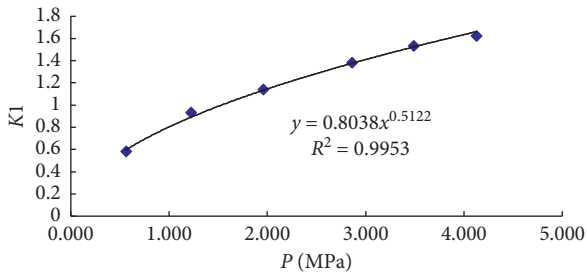


FIGURE 4: K_1 - P relationship model in the transportation roadway in the 121901 working face.

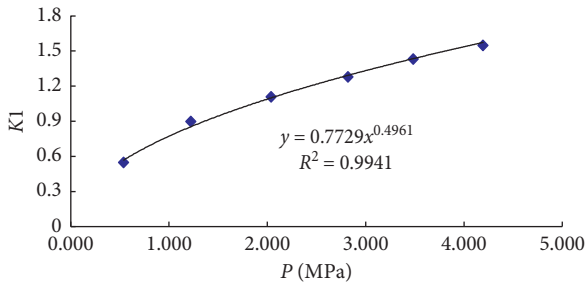


FIGURE 5: K_1 - P relationship model in the 2# connection roadway in the 121901 working face.

structural belt, $S = 6 \text{ kg/m}$ (in a borehole with a diameter of 42 mm) or $S = 18 \text{ kg/m}$ (in a borehole with a diameter of 75 mm) could be selected as critical values.

3.4.3. Situation during Application of Indices K_1 and S for Coal and Gas Outbursts. Based on the aforementioned research, gas desorption index K_1 of drilling cuttings was used as the main predictive index for coal and gas outbursts in the C9 coal seam in Enhong Coal Mine and its critical value was $0.6 \text{ mL/g}\cdot\text{min}^{1/2}$. The auxiliary index was the index S of the weight of drilling cuttings, and its critical values were 6 kg/m (in a borehole with a diameter of 42 mm) or 18 kg/m (in a borehole with a diameter of 75 mm).

During field testing, 157 cycles were applied to collect values of K_1 and the percentages of the index are shown in Table 12 and Figure 9. It can be seen from the figure and the table that the percentage was 73% for $K_{1\text{max}} \geq 0.6 \text{ mL/g}\cdot\text{min}^{1/2}$. Later, it was found that there was a large fault with

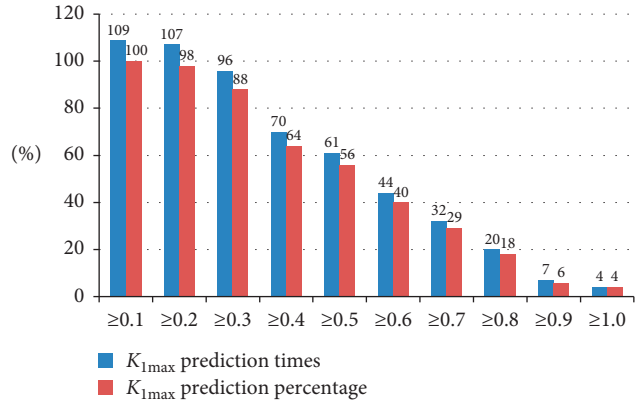


FIGURE 6: Distribution of $K_{1\text{max}}$ during the test.

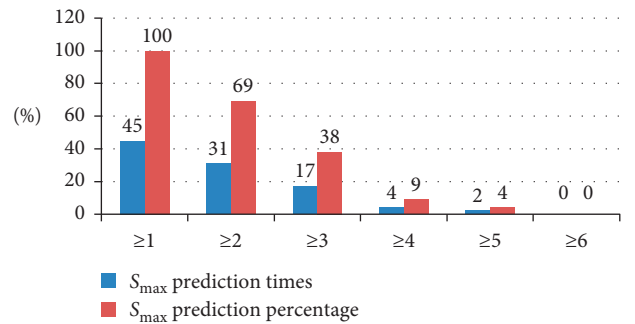


FIGURE 7: Distribution of S_{max} ($\Phi 42 \text{ mm}$) during the test.

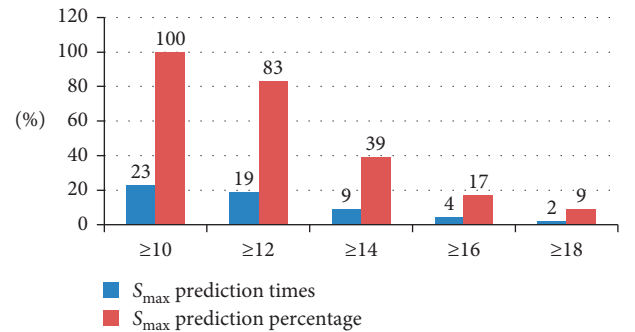


FIGURE 8: Distribution of S_{max} ($\Phi 75 \text{ mm}$) during the test.

the drowthrow of 20 m near the 121901 working face, increasing the risk of an outburst. This further proved the sensitivity of the prediction index K_1 and the accuracy of its critical value.

During field testing, a total of 135 cycles were applied to collect the weight of drilling cuttings S . Percentages of the index are shown in Table 13 and Figure 10. The number of cycles exceeding the critical value was zero when $S_{\text{max}} \geq 6 \text{ kg/m}$.

During application, the roadway was safely tunnelled for about 1000 m according to the determined prediction indices for coal and gas outbursts, without a coal and gas outburst occurring.

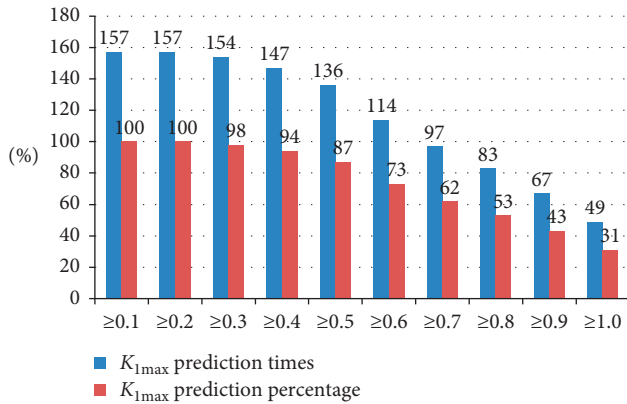


FIGURE 9: Distribution of range of gas desorption index $K_{1\max}$ of drilling cuttings predicted during field testing.

TABLE 13: Distribution of percentages of the index S_{\max} ($\Phi 42$ mm) of weight of drilling cuttings predicted during field testing.

S_{\max} (kg/m)	Total times (135)	Percentage
≥ 1	135	100
≥ 2	119	88
≥ 3	24	18
≥ 4	4	3
≥ 5	0	0
≥ 6	0	0

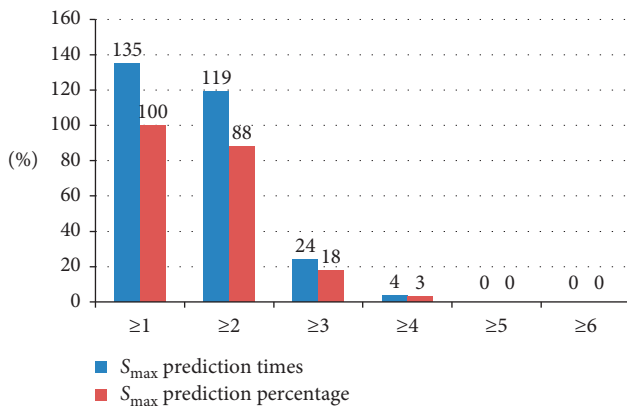


FIGURE 10: Distribution of range of the index S_{\max} ($\Phi 42$ mm) of the weight of drilling cuttings predicted during field testing.

4. Conclusion

- (1) Based on the mechanism of occurrence of a coal and gas outburst relating to coal mass strength, gas pressure, and *in situ* stress, a method for predicting coal and gas outbursts was proposed.
- (2) During *in situ* measurement of the mining roadway, the specific prediction indices for coal and gas outbursts were determined according to indices including geological tectonic region, presence or absence of outburst precursors, changes before and after taking measures for preventing outbursts, and

percentages of indices. The indices generally used were the gas desorption index K_1 of drilling cuttings, the weight of drilling cuttings, initial velocity q of gas emission, and thickness of the soft layer.

- (3) By using the new method for predicting coal and gas outbursts, the main prediction index for coal and gas outbursts in the C9 coal seam in Enhong Coal Mine was the gas desorption index K_1 of drilling cuttings and its critical value was $0.6 \text{ mL/g min}^{1/2}$. The index S of the weight of drilling cuttings was used as the auxiliary index and its critical values were 6 kg/m (in a borehole with a diameter of 42 mm) or 18 kg/m (in a borehole with a diameter of 75 mm).
- (4) The new method of coal and gas outbursts can greatly improve the technical level of coal and gas outburst personnel and the prediction accuracy of coal and gas outbursts.

Data Availability

The data supporting the conclusion of the article are shown in the relevant figures and tables in the article.

Conflicts of Interest

The authors declare no conflicts of interest.

Authors' Contributions

Guowei Dong conceived and designed the experiments and wrote the paper; Xuanming Liang analyzed the data; Qixiang Wang performed the theoretical analysis.

Acknowledgments

This work was funded by the National Key Research and Development Programme of China (Grant no. 2016YFC0801402), National Science and Technology Major Project of the Ministry of Science and Technology of China in the 13th Five-Year Period (Grant no. 2016ZX05045-004), One Hundred Youth Talents Project of Shaanxi Province of China, Shaanxi Natural Science Foundation of China (Grant no. 2020JM-519), and the Research Fund of the State Key Laboratory of Coal Resources and Safe Mining, CUMT (SKLCRSM18KF017).

References

- [1] Q. T. Hu and G. C. Wen, *Mechanical Mechanism of Coal and Gas Outburst*, Science Press, Beijing, China, 2013.
- [2] S. N. Zhou and X. Q. He, "Rheological hypothesis of coal and methane outburst mechanism," *Journal of China University of Mining & Technology*, vol. 19, no. 2, pp. 1–8, 1990.
- [3] C. L. Jiang and Q. X. Yu, "The hypothesis of spherical shell destabilization of coal and gas outburst," *Safety in Coal Mines*, no. 2, pp. 17–25, 1995.
- [4] B. Liang, M. T. Zhang, Y. S. Pan et al., "Theory of instability of flow fixation coupling for coal and gas outburst," *Journal of China Coal Society*, vol. 20, no. 5, pp. 492–496, 1995.

- [5] K. Wang and Q. X. Yu, "Study on catastrophe theory of the starting process of coal and gas outburst," *China Safety Science Journal*, vol. 8, no. 6, pp. 10–15, 1998.
- [6] D. Y. Guo and D. X. Han, "The stick-slip mechanism of coal and gas outburst," *Journal of China Coal Society*, vol. 28, no. 6, pp. 598–602, 2003.
- [7] Z. M. Zheng, *The Mechanism of Coal and Gas Outburst from the View of Quantity and Dimensional Analysis Collected Works of Zheng Zhemin*, Peking University Press, Beijing, China, 2003.
- [8] Q. T. Hu, S. N. Zhou, and X. Q. Zhou, "Mechanical mechanism of coal and gas outburst," *Journal of China Coal Society*, vol. 33, no. 12, pp. 1368–1372, 2008.
- [9] X. F. Xian, M. Gu, and X. H. Li, "Excitation and occurrence conditions for coal and gas outburst," *Rock and Soil Mechanics*, vol. 30, no. 3, pp. 577–581, 2008.
- [10] Z. M. Zhang, *Mining Gas-Geology*, pp. 167–284, University of Mining and Technology Press, Xuzhou, China, 2009.
- [11] G. W. Dong and Q. T. Hu, "Main controlling geological body theory and geological effect mechanisms of coal and gas dynamic disaster," *Journal of Xi'an University of Science and Technology*, vol. 37, no. 1, pp. 7–14, 2017.
- [12] L. Y. Shu, K. Wang, Q. X. Qi et al., "Key structural body theory of coal and Gas outburst," *Chinese Journal of Rock Mechanics and Engineering*, vol. 36, no. 2, pp. 347–356, 2017.
- [13] J. Xu, D. Liu, S. J. Peng et al., "Coal and gas outburst analogous test under the different diameter of exposed coal seam surface," *Journal of China Coal Society*, vol. 38, no. 1, pp. 9–14, 2013.
- [14] J. P. Tang, Y. S. Pan, and S. L. Yang, "Experimental study of coal and gas outburst under tridimensional stresses," *Chinese Journal of Rock Mechanics and Engineering*, vol. 32, no. 5, pp. 960–965, 2013.
- [15] C. H. Zhang, Z. G. Liu, J. Liu et al., "Physical scale modeling of mechanical characteristics of outburst induced by closed geological structure," *Journal of China University of Mining & Technology*, vol. 42, no. 4, pp. 554–559, 2013.
- [16] W. J. Lei, S. Q. Li, P. Shang et al., "Coal and gas outburst simulation experiment reacted by microseismic monitoring," *Journal of Mining and Safety Engineering*, vol. 31, no. 1, pp. 161–166, 2014.
- [17] Z. G. Zhao, Q. T. Hu, and Y. H. Geng, "Design of simulation test system of coal and gas outburst," *Mining Safety and Environmental Protection*, vol. 36, no. 5, pp. 9–12, 2009.
- [18] B. S. Nie, Y. K. Ma, J. Q. Meng et al., "Middle scale simulation system of coal and gas outburst," *Chinese Journal of Rock Mechanics and Engineering*, vol. 37, no. 5, pp. 1218–1225, 2018.
- [19] H. Li, Z. C. Feng, and D. Zhao, "Simulation experiments and mechanism analysis of coal and gas outbursts under 3d stresses," *Journal of Mining & Safety Engineering*, vol. 35, no. 2, pp. 422–428, 2018.
- [20] D. K. Wang, P. Zhang, Q. C. Fu et al., "Experimental study on outburst of gas-containing coal under static and dynamic loads," *Journal of Henan Poly Technic University (Natural Science)*, vol. 37, no. 5, pp. 27–32, 2018.
- [21] G. Wang, M. M. Wu, H. Y. Wang et al., "Sensitivity analysis of factors affecting coal and gas outburst based on energy equilibrium model," *Chinese Journal of Rock Mechanics and Engineering*, vol. 34, no. 2, pp. 1–11, 2015.
- [22] C. W. Li, S. Fu, B. J. Xie et al., "Establishment of the prediction model of coal and gas outburst energy and its application in Pingdingshan mining area," *Journal of China University of Mining & Technology*, vol. 47, no. 2, pp. 231–239, 2018.
- [23] J. Xu, B. Zhou, S. J. Peng et al., "Coal and gas outburst analogous test under the different diameter of exposed coal seam surface," *Journal of China Coal Society*, vol. 45, no. 1, pp. 213–222, 2020.
- [24] G. C. Wen, H. T. Sun, J. Cao et al., "Simulation experiment system of coal and gas dynamic disaster in deep mine and its application in accident analysis," *Journal of China Coal Society*, vol. 45, no. 1, pp. 223–231, 2020.
- [25] Q. T. Hu, G. C. Wen, and S. M. Xu, "Sensitive index and critical value of outburst prediction in working face," *Coal Engineer Supplementary*, no. S1, pp. 8–10, 1998.
- [26] G. W. Dong, "Study on predicted indexes of coal and outburst disaster in donglin mine," *Coal Science and Technology*, vol. 8, pp. 40–42, 2012.
- [27] D. Li, Y. Cheng, L. Wang, H. Wang, L. Wang, and H. Zhou, "Prediction method for risks of coal and gas outbursts based on spatial chaos theory using gas desorption index of drill cuttings," *Mining Science and Technology (China)*, vol. 21, no. 3, pp. 439–443, 2011.
- [28] J. Tang, C. Jiang, Y. Chen, X. Li, G. Wang, and D. Yang, "Line prediction technology for forecasting coal and gas outbursts during coal roadway tunneling," *Journal of Natural Gas Science and Engineering*, vol. 34, pp. 412–418, 2016.
- [29] L. Chen, E. Y. Wang, J. J. Feng et al., "Hazard prediction of coal and gas outburst based on fisher discriminant analysis," *Geomechanics and Engineering*, vol. 13, no. 5, pp. 861–879, 2017.
- [30] L. Qiu, Z. Li, E. Wang et al., "Characteristics and precursor information of electromagnetic signals of mining-induced coal and gas outburst," *Journal of Loss Prevention in the Process Industries*, vol. 54, pp. 206–215, 2018.
- [31] J. Li, Q. Hu, M. Yu, X. Li, J. Hu, and H. Yang, "Acoustic emission monitoring technology for coal and gas outburst," *Energy Science & Engineering*, vol. 7, no. 2, pp. 443–456, 2019.
- [32] G. W. Dong, X. L. Ren, and Z. Wang, "A novel early warning method for atypical outbursts disasters in mines: extraction of indexes from gas concentration data for the early warning of atypical outbursts," *Arabian Journal of Geosciences*, vol. 12, p. 796, 2019.
- [33] A. H. Wang, D. Z. Song, X. Q. He et al., "Investigation of coal and gas outburst risk by microseismic monitoring," *PLoS One*, vol. 14, no. 5, Article ID e0216464, 2019.
- [34] C.-P. Lu, G.-J. Liu, Y. Liu, N. Zhang, J.-H. Xue, and L. Zhang, "Microseismic multi-parameter characteristics of rockburst hazard induced by hard roof fall and high stress concentration," *International Journal of Rock Mechanics and Mining Sciences*, vol. 76, pp. 18–32, 2015.
- [35] H. Barthwal and M. van der Baan, "Microseismicity observed in an underground mine: source mechanisms and possible causes," *Geomechanics for Energy and the Environment*, vol. 22, 2020.
- [36] K. H. Palgunadi, N. Poiata, J. Kinscher, P. Bernard, F. De Santis, and I. Contrucci, "Methodology for full waveform near real-time automatic detection and localization of microseismic events using high (8 kHz) sampling rate records in mines: application to the garpenberg mine (Sweden)," *Seismological Research Letters*, vol. 91, no. 1, pp. 399–414, 2020.
- [37] State Administration of Coal Mine Safety, *Detailed Rules for Prevention and Control of Coal and Gas Outburst*, Coal Industry Press, Beijing, China, 2019.

Research Article

Dynamic Splitting Experimental Study on Sandstone at Actual High Temperatures under Different Loading Rates

Qi Ping ^{1,2,3} Mingjing Wu,^{2,3} Pu Yuan,^{1,2,3,4} Haipeng Su,^{2,3} and Huan Zhang^{2,3}

¹State Key Laboratory of Mining Response and Disaster Prevention and Control in Deep Coal Mines, Anhui University of Science and Technology, Huainan, Anhui 232001, China

²Engineering Research Center of Mine Underground Projects, Ministry of Education, Anhui University of Science and Technology, Huainan, Anhui 232001, China

³School of Civil Engineering and Architecture, Anhui University of Science and Technology, Huainan, Anhui 232001, China

⁴Department of Civil, Construction, and Environmental Engineering, The University of Alabama, Tuscaloosa, AL 35487, USA

Correspondence should be addressed to Qi Ping; ahpingqi@163.com

Received 17 April 2020; Revised 29 May 2020; Accepted 6 June 2020; Published 22 June 2020

Academic Editor: Hongwei Yang

Copyright © 2020 Qi Ping et al. This is an open access article distributed under the Creative Commons Attribution License, which permits unrestricted use, distribution, and reproduction in any medium, provided the original work is properly cited.

The tensile failure of rocks is a common failure mode in rock engineering. Many studies have been conducted on the tensile strength and failure mode of rocks after high-temperature treatment under dynamic loading. However, research on the effects of high temperature on the dynamic splitting tensile characteristics of sandstone at actual high temperatures is lacking. To investigate the dynamic tensile characteristics of rocks at actual high temperatures, split Hopkinson pressure bar (SHPB) test apparatus and high-temperature environment box were used to perform dynamic splitting tensile tests under six striker velocities for sandstone specimens at 25°C–800°C. The dynamic splitting tensile strength, radial strain, average strain rate, and failure mode of sandstone under different test conditions were investigated. Test results revealed that the brittleness of sandstone specimens is enhanced at 200°C and 400°C, but slight ductility is observed at 600°C and 800°C. The strain rate effect of dynamic tensile strength is closely related to temperature. When the striker velocity exceeds 2.3 m/s, the dynamic radial strain first decreases and then increases with rising temperature. A quadratic polynomial relationship between the dynamic radial strain and temperature was observed. The temperature effect on the average strain rate is strong at low striker velocity and weak at high striker velocity. In the dynamic splitting tensile tests, high-temperature sandstone specimens are split into two semicylinders along the radial loading direction.

1. Introduction

In rock engineering, rock mass lies in a certain hydrogeological environment. Rock engineering under unfavorable hydrogeological condition may lead to some engineering geology disaster, such as rockburst hazard [1–3], large deformation, and water inrush hazard [4, 5]. The temperature of rock mass rises with increasing depth, and secondary disasters may be induced in rock mass due to high geothermal situation [6]. Rock mass in deep engineering, such as superdeep mining, deep disposal of high-level radioactive nuclear wastes, geothermal resource exploitation, and underground coal gasification, always suffers from high geothermal effect [7, 8]. The influence of high geotherm on

rock mechanical characteristics has become a research hotspot in rock mechanics [9, 10].

Tensile strength is a significant parameter in the design of geotechnical engineering [11, 12]. Given that rock is a quasibrittle material, directly measuring its tensile strength is very difficult. In 1978, the International Society for Rock Mechanics and Rock Engineering suggested Brazilian disc test, an indirect measuring method, as a method for determining the tensile strength of rock material [13]. As tensile strength of rocks is only approximately one-tenth less than its compressive strength, the deformation and failure mode of rock mass mainly depend on its tensile characteristics [14]. Research on the quasistatic or dynamic splitting tensile tests of rocks is mainly conducted at room

temperature or after heat treatment. These achievements contribute to understanding the tensile strength and deformation properties of rocks under test conditions. However, studies on dynamic splitting tensile tests at real-time high temperature are rarely reported [15, 16]. As rock mass exists in a coupled high-temperature and dynamic-stress environment, high geothermal condition and dynamic-stress disturbance increase the possibility of engineering hazards. Hence, studying the dynamic tensile strength of rocks under coupled high temperature and high loading rate can provide experimental references for the stability analysis of surrounding rocks in blasting excavation process.

The results of several studies indicate that temperature has a significant influence on the physical and mechanical properties of rocks [17–19]. Much literature has recently emerged and offers contradictory findings about the compressive and tensile strengths of rocks after temperature treatment. The action mechanism of temperature on the internal structure of rocks has also been investigated. Studies reveal that, in high-temperature situations, thermal cracking occurs and leads to the deterioration of the properties of rocks, such as porosity, Young's modulus, and mechanical strength [17]. By using MTS815 servo-controlled rock mechanics testing system, Chen et al. [17] conducted Brazilian splitting tests for sandstone specimens, which were heated to six kinds of temperatures ranging from 25°C to 1000°C and then cooled down to room temperature naturally, to investigate the damage evolution caused by high temperature. By varying temperatures and duration of thermal treatment, Sirdesai et al. [16] performed indirect tensile test by using a Brazilian cage. The tensile strength and the physical characteristics of the rocks underwent a substantial and irreversible change upon heating. After heat treatment from 100°C to 600°C, Liang et al. [19] compared the physical properties and longitudinal wave velocities of two cooling ways, natural and water cooling. They also studied the Brazilian splitting characteristics. The above experiments were conducted under static or quasistatic load, and the effects of temperature and rock type on static tensile strength were investigated. However, strain rate effect was not considered.

The deformation and failure of rocks under dynamic loads, such as blasting load, are closely related to loading rate, which shows a distinct strain rate effect [20, 21]. Spalling test based on Hopkinson bar apparatus is a method for determining the tensile strength of concrete at high strain rates. Klepaczko and Brara [22] conducted dynamic tensile test for concrete, and the dynamic tensile strength was determined by spalling caused by reflected tensile wave. Using a Hopkinson bar apparatus, Schuler et al. [23] investigated the dynamic tensile and fracture energy of concrete at high strain rates by measuring the free surface velocity at the end of the specimen. For the complexity of the time and space of the transient loading in spalling tests, Erzar and Forquin [24] put forward several advances to improve the process of spalling tests. Given its simple test design and operation process, the Brazilian splitting test in static state is performed to measure the dynamic tensile strength in the split Hopkinson pressure bar (SHPB) test [25, 26]. The

Brazilian splitting test has become a handy and effective test method for studies on dynamic tensile strength [27–29]. By conducting dynamic Brazilian splitting tests for coal specimens, Zhao et al. [30] discussed the influence of impact velocity and stratification dip angle on dynamic tensile strength, failure strain, and strain rate. Moreover, primary analyses on dynamic splitting and surface strain field evolution were conducted using high-speed camera and speckle image correlation digital technique. Through the dynamic Brazilian splitting test, Du et al. [31] investigated the influence of wetting-drying cycle and strain rate on the dynamic tensile strength of red sandstone and developed a calculation formula for dynamic tensile strength. Wen et al. [32] performed dynamic splitting tensile tests for sandstone specimens in various moisture contents. Li et al. [33] conducted high-strain-rate dynamic splitting tests for intact granite specimens and prefabricated single-jointed granite specimens with a height-to-diameter ratio of 0.5. However, as all the experiments were conducted at room temperature, the major problem of this kind of test is that temperature effect is not considered.

In recent years, SHPB test with high temperature has been attempted [34–36]. Using an SHPB test system, Yin et al. [35] performed dynamic fracture tests on a cracked straight-through Brazilian disc to investigate the dynamic fracture toughness of granite after heat treatment at 25°C to 600°C. Liu et al. [36] conducted dynamic tensile tests for marble Brazilian disc specimens after heat treatment at 25°C to 1000°C. They also analyzed the influence of loading rate and temperature on dynamic tensile strength and failure modes by using an SHPB test system with large diameter. Most studies on the effect of temperature on the dynamic mechanical properties of rocks focus on the test conditions after temperature treatment. However, only little attention has been paid to the dynamic tensile characteristics of rocks at real-time temperatures.

In this study, dynamic splitting tensile tests under six striker velocities were conducted for sandstone specimens under five kinds of real-time temperature conditions (25°C, 200°C, 400°C, 600°C, and 800°C) by using $\phi 50$ mm SHPB test apparatus and high-temperature environment box. And dynamic tensile stress-strain curves were obtained based on acquired incident wave, reflected wave, and transmitted wave. Then, the influence of high temperature on dynamic splitting tensile characteristics of sandstone was analyzed from dynamic tensile strength, dynamic radial strain, average strain rate, and failure modes. The strain rate effect of high-temperature sandstone was also studied.

2. Methodology

2.1. Preparation of High-Temperature Sandstone Specimens. Sandstone samples were obtained from the Panyidong coal mine of Huainan Mining Group. Raw rock cores were obtained by ZS-100 vertical drilling machine with drilling direction perpendicular to the bedding plane. Then, DQ-4 cutting machine and SHM-200 double-end grinding machine were applied to process raw rock cores into disc specimens with the size of $\phi 50$ mm \times 25 mm. Both ends of

the sandstone specimens were flat within 0.02 mm, and irregularities across the thickness of the disc specimen were within 0.025 mm. To reduce the difference between the rock structure and rock composition, tested sandstone specimens were obtained from one rock sample and had similar longitudinal wave velocity.

As presented in Figure 1, box-type resistance furnace with automatic temperature control system was used to heat the sandstone specimens. Its heating part is composed of silicon carbide, and its highest heating temperature is 1200°C.

According to Wang et al. [37], the time constant to achieve a uniform temperature distribution state is r^2/d , where r is the radius of rock sample and d is the thermal diffusivity of the rock. In this study, the radius of sandstone specimen was 25 mm (namely, 0.025 m), and the thermal diffusivity of sandstone ranged from $0.75 \times 10^{-6} \text{ m}^2/\text{s}$ to $1.27 \times 10^{-6} \text{ m}^2/\text{s}$. Then, the time constant for temperature equilibrium in sandstone specimens ranges from 492 s (8.2 min) to 833.3 s (about 13.9 min). Hence, the temperature gradients in sandstone specimens are modest during heating. Sandstone specimens were heat treated at a rate of $10^\circ\text{C}/\text{min}$; then sandstone specimens were kept in the box-type resistance furnace for 4 h to make the temperature effect more sufficient.

2.2. Real-Time High-Temperature SHPB Test System. As illustrated in Figure 2, real-time high-temperature SHPB test system consists of a $\phi 50$ mm variable cross-section SHPB test apparatus and a high-temperature environment box.

All bars in the SHPB test apparatus are made of high-strength alloy steel with a density of $7580 \text{ kg}/\text{m}^3$, Young's modulus of 210 GPa, and longitudinal wave velocity of 5190 m/s. The lengths of the striker, input bar, output bar, and absorbing bar are 800, 2400, 1200, and 1000 mm, respectively. The impact end of the input bar is a 200 mm variable cross-section part with its diameter gradually varying from 37 mm to 50 mm.

Figure 3 presents the acquired incident stress $\sigma_I(t)$, reflected stress $\sigma_R(t)$, and transmitted stress $\sigma_T(t)$ for 800°C sandstone specimen. To estimate stress equilibrium, the stress at the end contacting with the input bar is also calculated by $\sigma_I(t) + \sigma_R(t)$.

As presented in Figure 3, the stress-time histories at the end contacting with input bar $\sigma_I(t) + \sigma_R(t)$ are basically consistent with the end contacting with output bar $\sigma_T(t)$, which denotes that the dynamic splitting tests results are valid and reliable. Moreover, due to the variable cross-section part in the front of the input bar, P-C oscillations were eliminated, and the increasing time of incident stress wave was retarded, which could prevent the premature failure of rock-like materials and improve the stress uniformity in the specimen [38–40].

As shown in Figure 4, a high-temperature environment box was designed and manufactured for the SHPB test apparatus. The box can provide a high-temperature environment ranging from room temperature to 1200°C . It can compensate for the heat loss during the transfer and



FIGURE 1: Sandstone specimens heated using box-type resistance furnace.

placement of high-temperature sandstone specimen and maintain the temperature during dynamic splitting tensile tests. The high-temperature box can also prevent the fragments from flying out and ensure safety during dynamic splitting tensile tests.

High-temperature environment box was equipped with a temperature controller, which can monitor the temperature with a temperature sensor and heat the sandstone specimen to the designed temperature. As shown in Figure 4, the high-temperature environment box consists of two parts, the upper and the lower parts. The lower part was set up on the girder of the SHPB test apparatus and could slide along the girder. Hinge and buckle were applied to connect and fix these two parts. When the buckle was opened, the upper part could be turned up, and high-temperature sandstone specimens could be placed and removed.

2.3. Experimental Procedure of Dynamic Splitting Tensile Tests. Experimental procedure of dynamic splitting tensile tests for high-temperature environment box is shown as follows:

First, place the processed sandstone specimen into the box-type resistance furnace to elevate the specimen to the designed high temperature.

Second, heat the high-temperature environment box at the designed high temperature.

Third, place the striker in a settled position in a launching chamber, and set the air pressure to drive the striker.

Fourth, take the sandstone specimen from the box-type resistance furnace to the high-temperature environment box and immediately place the sandstone between the input and output bars, as illustrated in Figure 5. The axis of the sandstone specimen should be coaxial with the input and output bars.

Fifth, lock the high-temperature environment box and immediately fill the gap between the bars and the box with fire retardant cotton.

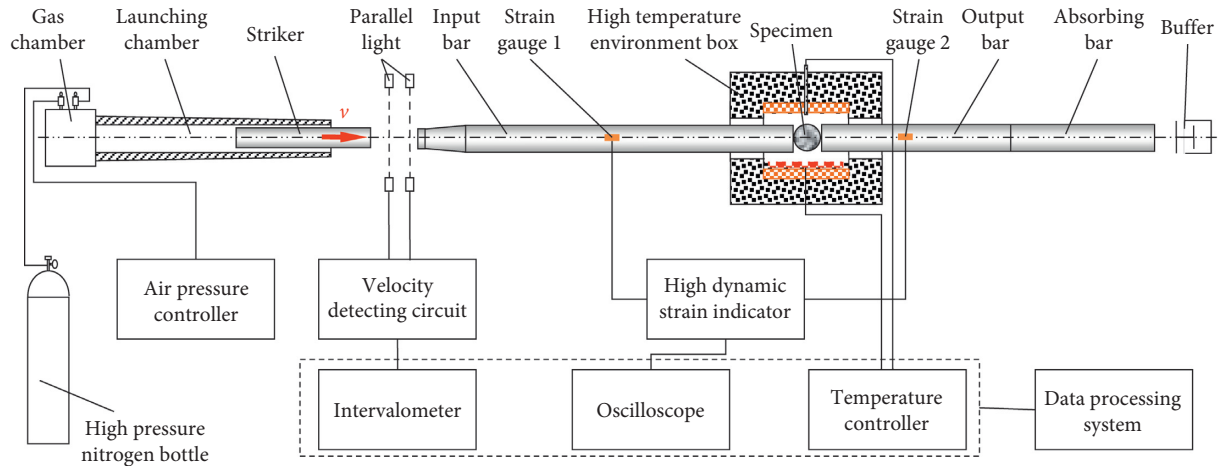


FIGURE 2: Schematic of real-time high-temperature SHPB test system.

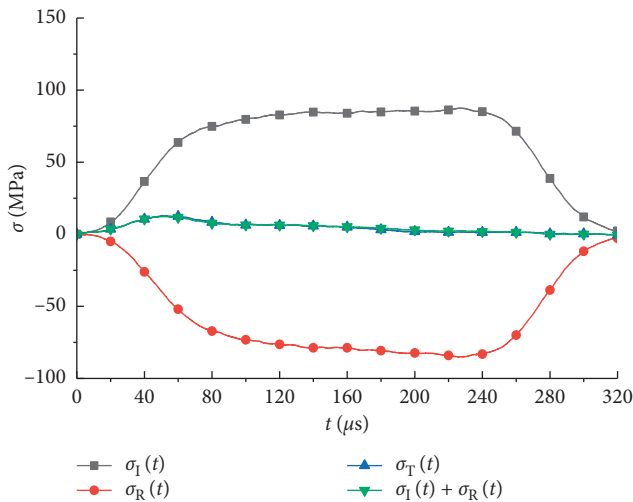


FIGURE 3: Acquired stress-time histories in dynamic splitting tensile tests (800°C , $v = 5.4 \text{ m/s}$).



FIGURE 5: Placement of high-temperature sandstone specimen in the dynamic splitting tensile test.

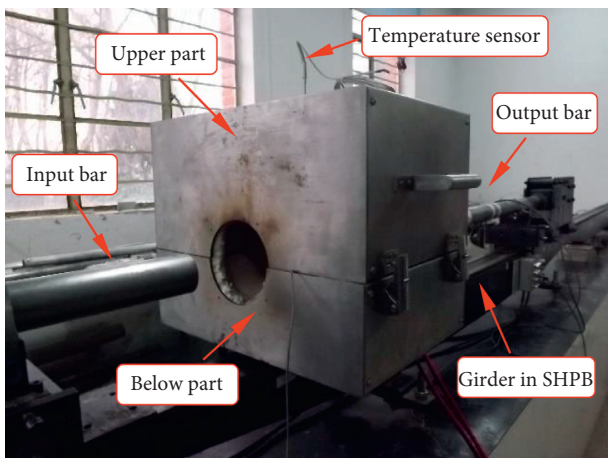


FIGURE 4: High-temperature environment box for SHPB test apparatus.

Sixth, maintain the high temperature for 5 min to compensate for the heat lost during transfer and placement. Finally, launch the striker and load the dynamic stress wave to the high-temperature sandstone specimen.

According to Xia et al. [41], the shape of the incident wave is basically unchanged when it propagates through a gradient temperature field. The uncorrected incident and transmitted wave exhibit little difference from the amplitude of the original wave at approximately 10%. To eliminate the influence of high temperature on the acquired signals from the input and output bars, three countermeasures were adopted. First, the temperature of the high-temperature environment box was quickly elevated to the designed value. For example, the time for elevating to 800°C was not longer than 15 min. Second, the gap between the bars and the box was filled with fire retardant cotton to avoid thermal radiation. Third, a towel soaked in cold water was twisted around the input and output bars near the high-temperature environment box to cool down and reduce heat conduction. In

the dynamic splitting tensile test, the surface temperature on both bars was cooled down to room temperature (25°C) at 320 mm away from the outlet of the high-temperature environment box. Hence, the strain gauges were mounted 400 mm away from the high-temperature environment box to eliminate the high-temperature effect.

2.4. Basic Principle of Dynamic Splitting Tensile Tests. During the dynamic splitting tensile test, the high-temperature sandstone specimen was placed between the input and output bars, as shown in Figure 6.

When launching, the striker impacts the input bar with a certain velocity v ; then an incident wave $\varepsilon_I(t)$ is generated in the input bar. When the incident wave propagates to the contact interface with the high-temperature sandstone specimen, some of incident waves reflect to the input bar, while the other incident waves transmit into high-temperature sandstone specimens. Reflection and transmission also occur in the contact interface between the high-temperature sandstone specimen and the output bar. The wave reflected to the input bar is called reflected wave $\varepsilon_R(t)$, and the wave propagating into the output bar is called transmitted wave $\varepsilon_T(t)$. Incident wave $\varepsilon_I(t)$, reflected wave $\varepsilon_R(t)$, and transmitted wave $\varepsilon_T(t)$ can be collected by the strain gauges mounted on the input and output bars.

According to the two basic assumptions of SHPB tests, the dynamic force, dynamic radial strain, and strain rate of high-temperature sandstone specimen can be calculated using the following three wave methods [26]:

$$\begin{aligned} P(t) &= \frac{EA}{2} [\varepsilon_I(t) + \varepsilon_R(t) + \varepsilon_T(t)], \\ \varepsilon(t) &= \frac{C}{D} \int_0^t [\varepsilon_I(t) - \varepsilon_R(t) - \varepsilon_T(t)] dt, \\ \dot{\varepsilon}(t) &= \frac{C}{D} [\varepsilon_I(t) - \varepsilon_R(t) - \varepsilon_T(t)], \end{aligned} \quad (1)$$

where E and A are Young's modulus and cross section of bar, C is longitudinal wave velocity of bar, and D is diameter of high-temperature sandstone specimen.

The issue on the validity of dynamic splitting tensile test is whether the tensile crack is parallel to the loading direction or not [42]. To validate the dynamic splitting tensile test, Gomez et al. [43] performed photoelastic dynamic splitting tensile tests. Photoelastic results show that the specimen quickly reaches stress equilibrium and remains in stress equilibrium until fracture occurs. Therefore, the assumption of elastic behavior is reasonable for dynamic splitting tensile test. Hence, the calculation formula in static splitting tensile test can also be used for dynamic splitting tensile test. When dynamic splitting failure occurs, the maximum dynamic tensile stress is its dynamic tensile strength. According to elastic mechanics, the dynamic tensile stress can be calculated using the following equation:

$$\sigma_t^d(t) = \frac{2P(t)}{\pi DH} = \frac{EA}{\pi DH} [\varepsilon_I(t) + \varepsilon_R(t) + \varepsilon_T(t)], \quad (2)$$

where H is the height of disc specimen.

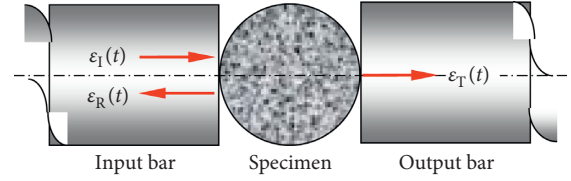


FIGURE 6: Principle of dynamic splitting tensile tests.

3. Result Analysis and Discussion

3.1. Dynamic Tensile Stress-Strain Curve. The typical dynamic tensile stress-strain curves of high-temperature sandstone specimens at temperatures ranging from 25°C to 800°C are shown in Figure 7.

As illustrated in Figure 7, when the heating temperature ranges from 25°C to 800°C, the dynamic tensile stress-strain curves at various striker velocities are similar to one another at the same temperature. In addition, the peak tensile stress increases as the growth of striker velocity increases. When the temperature is 25°C, the dynamic tensile stress-strain curves gently increase before the peak points. When the temperature is 200°C, the dynamic tensile stress-strain curves exhibit a steep increase before the peak points, and a relatively small peak radial strain is presented. Moreover, the brittle failure characteristics of the sandstone at 200°C and 400°C are more evident than those at other temperatures. When temperature rises from 200°C to 800°C, the peak radial strain shows a right shift tendency, which indicates weak brittleness. At 600°C and 800°C, the sandstone specimens exhibit reduced brittleness and demonstrate slight ductility. The peak radial strains at 800°C remain larger than those at 25°C.

3.2. Strain Rate Effect of High-Temperature Sandstone. The variation of the strain rate of high-temperature sandstone specimens with striker velocity is shown in Figure 8.

As shown in Figure 8, the strain rate increases in a quadratic polynomial function as striker velocity increases:

$$\dot{\varepsilon} = f v^2 + g v + h, \quad (3)$$

where f , g , and h are fitting parameters and their values are listed in Table 1.

The relation between the dynamic tensile strength and average strain rate of high-temperature sandstone specimens at 25°C to 800°C is presented in Figure 9.

As illustrated in Figure 9, the dynamic tensile strength increases as the growth of average strain rate increases under the same temperature. Hence, a distinct strain rate effect is observed. The dynamic tensile strength-average strain rate curve at 200°C and 400°C is higher than that at 25°C. Therefore, a temperature strengthening effect is observed for dynamic tensile strength. On the contrary, dynamic tensile strength-average strain rate curve at 600°C and 800°C is lower than that at 25°C. Hence, a temperature weakening effect is found. An approximate power relation exists between dynamic tensile strength and average strain rate, and the fitting formula is shown as follows:

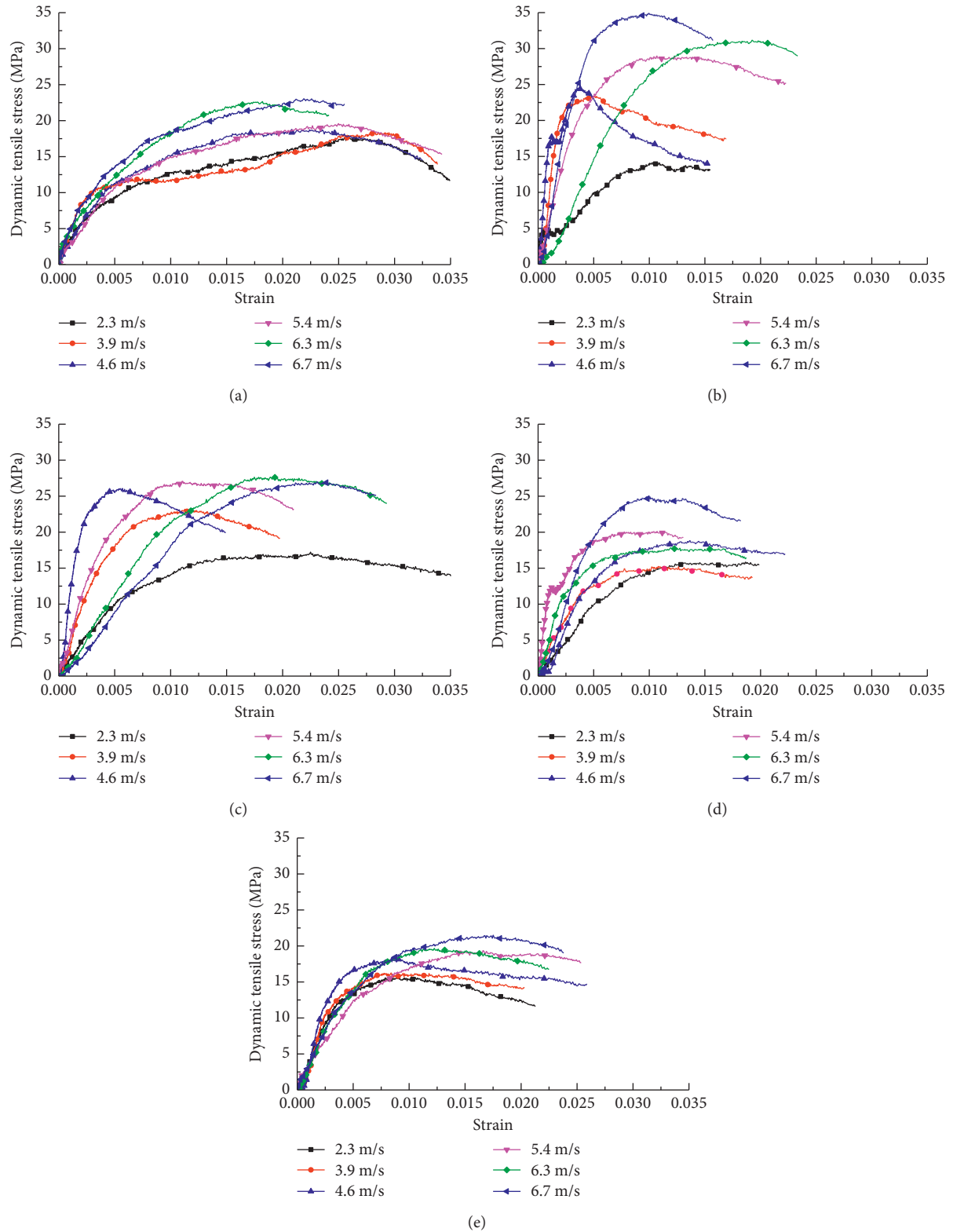


FIGURE 7: Dynamic tensile stress-strain curves of sandstone at various temperatures. (a) 25°C. (b) 200°C. (c) 400°C. (d) 600°C. (e) 800°C.

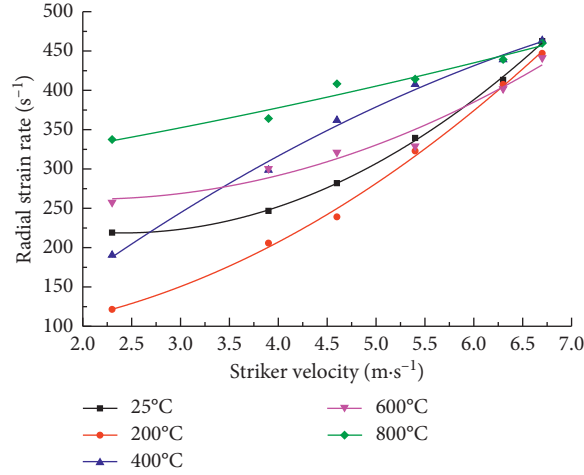


FIGURE 8: Variation of strain rate with striker velocity.

TABLE 1: Fitting parameters for strain rate and striker velocity.

Temperature (°C)	f	g	h	Correlation coefficient (R^2)
25	13.092 0	-62.927 0	294.270	0.999 2
200	8.984 4	-6.310 3	88.581	0.997 5
400	-4.943 6	106.780 0	-31.475	0.995 0
600	7.862 4	-32.059 0	294.230	0.966 9
800	1.042 2	18.123 0	288.660	0.965 2

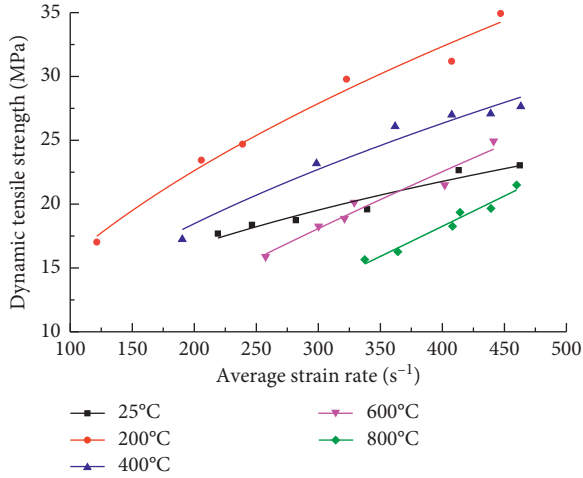


FIGURE 9: Relation between dynamic tensile strength and average strain rate.

$$\sigma_t^d = a \cdot \dot{\epsilon}^b, \quad (4)$$

where σ_t^d is the dynamic tensile strength, $\dot{\epsilon}$ is the average strain rate, and a and b are the fitting parameters. Their values are listed in Table 2.

As presented in Table 2, the minimum correlation coefficient is 0.9438, which indicates a remarkable correlation. The variation of fitting parameters with heating temperature is shown in Figure 10.

TABLE 2: Fitting parameters for dynamic tensile strength and average strain rate.

Temperature (°C)	a	b	Correlation coefficient (R^2)
25	2.369 6	0.369 9	0.943 8
200	1.386 4	0.526 2	0.986 9
400	1.046 4	0.538 7	0.969 3
600	0.229 5	0.765 5	0.958 2
800	0.041 1	1.017 5	0.964 2

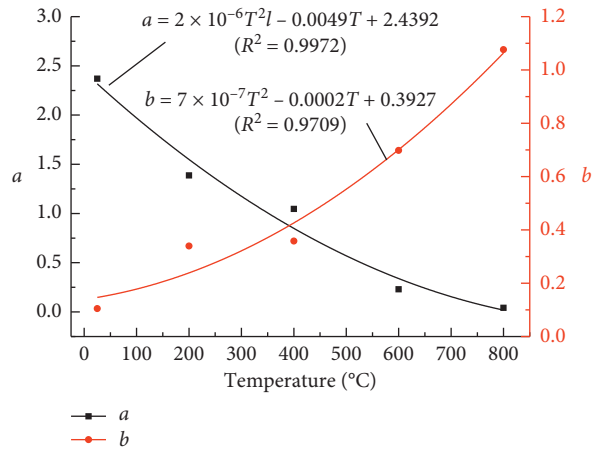


FIGURE 10: Variation of fitting parameters for dynamic tensile strength and strain rate with heating temperature.

As displayed in Figure 10, fitting parameter a decreases as temperature increases, whereas fitting parameter b increases as temperature increases. A quadratic polynomial relation exists between fitting parameters a and b and heating temperature. Therefore, the strain rate effect of dynamic tensile strength is closely related to temperature.

3.3. Temperature Effect on the Dynamic Tensile Strength of High-Temperature Sandstone. The variation of the dynamic tensile strength of high-temperature sandstone specimens with heating temperature is illustrated in Figure 11.

As displayed in Figure 11, the dynamic tensile strength exhibits a decreasing tendency with the increase in heating temperature under various striker velocities. When the striker velocity is 2.3 m/s, the dynamic tensile strength at 800°C is approximately 12% less than that at 25°C. When the striker velocity exceeds 2.3 m/s, the dynamic tensile strength first increases and then decreases as the heating temperature increases. The dynamic tensile strength at 200°C and 400°C is greater than that at 25°C. Compared with the dynamic tensile strength at 25°C, that at 200°C increases by approximately 28%, 32%, 52%, 38%, and 52% at striker velocities of 3.9, 4.6, 5.4, 6.3, and 6.7 m/s, respectively. The dynamic tensile strength at 600°C is basically equal to that at 25°C. However, the dynamic tensile strength at 800°C reduces by approximately 11%, 3%, 1%, 13%, and 7% at striker velocities of 3.9, 4.6, 5.4, 6.3, and 6.7 m/s, respectively. Hence, the temperature strengthening effect is observed from 200°C to 400°C, whereas the weakening effect is observed from 600°C to 800°C. The minimum and maximum temperatures of the dynamic tensile strength are 200°C and 800°C, respectively.

3.4. Temperature Effect on the Dynamic Radial Strain of High-Temperature Sandstone. The variation of the peak dynamic radial strain of the high-temperature sandstone specimens with heating temperature is shown in Figure 12.

As displayed in Figure 12, the peak dynamic radial strain exhibits a decreasing tendency as the heating temperature increases at various striker velocities. When the striker velocity is 2.3 m/s, the peak dynamic radial strain decreases as the heating temperature increases:

$$\varepsilon = -0.0011T^2 + 0.0031T + 0.0235, (R^2 = 0.9930). \quad (5)$$

However, when the striker velocity exceeds 2.3 m/s, the peak dynamic radial strain first decreases and then increases as the heating temperature increases. The peak dynamic radial strain rapidly reduces when the temperature rises from 25°C to 200°C. It reduced by 83%, 80%, 57%, 40%, and 18% at striker velocities of 3.9, 4.6, 5.4, 6.3, and 6.7 m/s, respectively. Peak dynamic radial strain gradually increased when the temperature rose from 200°C to 800°C, thereby indicating a transition from brittleness to ductility. A quadratic polynomial relation exists between peak dynamic radial strain and temperature, which is expressed as follows:

$$\varepsilon = cT^2 + dT + e (200^\circ\text{C} \leq T \leq 800^\circ\text{C}), \quad (6)$$

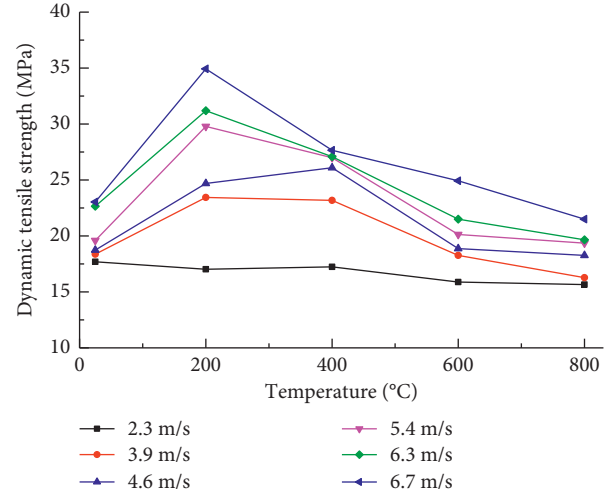


FIGURE 11: Variation of dynamic tensile strength with heating temperature.

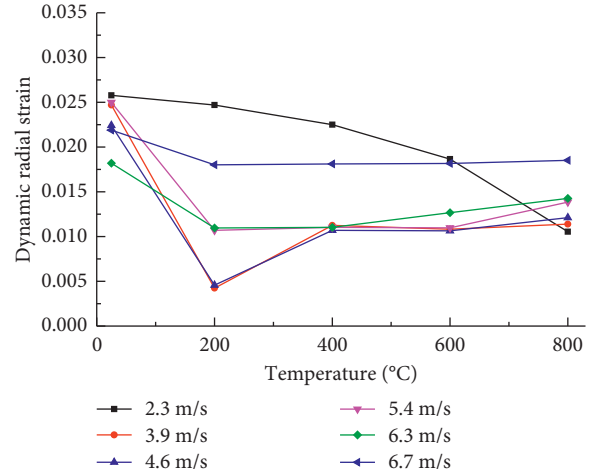


FIGURE 12: Variation of peak dynamic radial strain with heating temperature.

where c , d , and e are the fitting parameters and their values are listed in Table 3.

3.5. Temperature Effect on the Strain Rate of High-Temperature Sandstone. The variation of the average strain rate of high-temperature sandstone specimens with heating temperature is shown in Figure 13.

Figure 13 illustrates that the average strain rate first decreases and then increases as heating temperature increases and reaches its minimum value at 200°C. Moreover, the average strain rate-temperature curves exhibit a shift tendency as the striker velocity increases. When the striker velocity is 2.3 m/s, the average strain rate at 25°C, 200°C, 400°C, 600°C, and 800°C is 219.1 s⁻¹, 121.4 s⁻¹, 190.4 s⁻¹, 257.5 s⁻¹, and 337.4 s⁻¹, respectively. When the striker velocity is 6.7 m/s, the average strain rate at 25°C, 200°C, 400°C, 600°C, and 800°C is 462.5 s⁻¹, 447 s⁻¹, 463.3 s⁻¹, 441.3 s⁻¹, and 459.9 s⁻¹, respectively. The variation range of the average

TABLE 3: Fitting parameters for peak dynamic radial strain and temperature.

Striker velocity ($\text{m}\cdot\text{s}^{-1}$)	C	d	e	Correlation coefficient (R^2)
3.9	-1.6×10^{-3}	0.010 2	0.003 9	0.901 2
4.6	-1.2×10^{-3}	0.008 1	0.002 0	0.912 0
5.4	6.0×10^{-4}	0.002 2	0.012 5	0.915 8
6.3	4.0×10^{-4}	0.000 8	0.011 3	0.982 8
6.7	6.0×10^{-5}	0.000 2	0.018 1	0.965 0

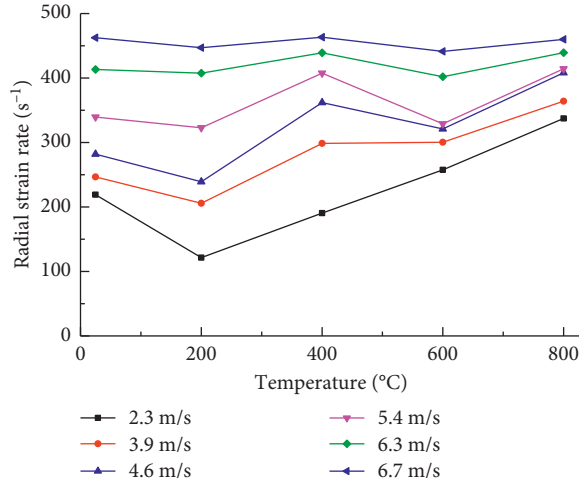


FIGURE 13: Variation of average strain rate with heating temperature.

strain rate is approximately $\pm 48\%$ at a striker velocity of 2.3 m/s and approximately $\pm 3\%$ at a striker velocity of 6.7 m/s. Therefore, temperature has a large effect on the average strain rate at low striker velocity and a small effect on the average strain rate at high striker velocity. Therefore, the influence of temperature on average strain rate is weakened as the striker velocity increases.

3.6. Failure Modes of High-Temperature Sandstone Specimens in Dynamic Splitting Tensile Tests. Under the six kinds of striker velocities, the failure modes of high-temperature sandstone specimens at 25°C–800°C are presented in Table 4. The left side of the sandstone specimen is in contact with the input bar, whereas the right side is in contact with the output bar.

As presented in Table 4, under six kinds of striker velocities, the high-temperature sandstone specimens are split into two roughly equal semicylinders along the radial loading direction. Meanwhile, two local crushing zones emerge in the sandstone specimens at the contact positions with the input and output bars. Moreover, the local crushing zone near the input bar is slightly larger than that near the output bar.

At the same temperature, striker velocity influences the failure modes. When the striker velocity is small, the sandstone specimens are split into two approximately complete semicylinders with very small local crushing zones. As the striker velocity increases, the size of the local crushing zone gradually increases. Additional fractures appear on one

of the two semicylinders, which lead to the high breakage degree and formation of small fragments.

Under the same striker velocity, the breakage degree of two semicylinders varies as the heating temperature increases. When the striker velocity is 2.3 m/s, the sandstone specimens are split into two approximately complete semicylinders, and the temperature shows little influence on the splitting failure mode. However, when the striker velocity exceeds 2.3 m/s and the temperature ranges from 200°C to 800°C, the breakage degree of sandstone specimens increases with the growth of heating temperature. The breakage degrees at 200°C and 400°C are less than that at 25°C, whereas those at 600°C and 800°C are higher than that at 25°C.

The dynamic splitting failure mode of high-temperature sandstone specimens is relatively complex due to the coupling effect of high temperature and impact load. Under impact load, disordered microcracks in sandstones propagate in an orderly manner, and those in the center of the sandstone specimen initiate and grow quickly along the loading direction. Subsequently, the main crack along the radial direction is formed through the sandstone specimens. As the striker velocity increases, the force applied on the sandstone specimens sharply increases. Before the main crack is formed through high-temperature sandstone specimens, local crushing zones occur at its contact positions with the input and output bars due to the greater compressive stress than the compressive strength. Given that the impact loading rate is considerably higher than the propagation speed of the splitting crack, two semicylinders can still contact with the input and output bars. Hence, continuous loading leads to compression crushing at the two ends of the semicylinders.

When the temperature rises from 25°C to 200°C, the water in the sandstone specimens evaporates, micropores close, and the microstructure becomes dense due to thermal expansion. When the temperature rises from 400°C to 800°C, physical and chemical changes occur in the minerals in the sandstone. The size of the micropores in the sandstone specimens increases, and some cracks appear. As the heating temperature increases, the damage in the sandstone increases due to the growth and coalescence of internal microcracks. Hence, the bearing capacity and tensile strength are decreased, and brittleness is also weakened.

As presented in Table 4, the color of the sandstone specimens changes at high temperature. At 25°C, the sandstone specimens are gray. At 200°C and 400°C, the gray color of the sandstone specimens is deeper than that at 25°C, whereas at 600°C and 800°C, it turns gray white. The color of the high-temperature sandstone specimens is the lightest at 800°C.

TABLE 4: Failure modes of sandstone specimens in dynamic splitting tensile tests.

Temperature (°C)	Striker velocity (m·s ⁻¹)					
	2.3	3.9	4.6	5.4	6.3	6.7
25						
200						
400						
600						
800						

4. Conclusions

To investigate the dynamic splitting tensile characteristics of sandstones at actual high temperatures, dynamic splitting tensile tests were conducted on sandstone specimens at different actual high temperatures and loading rates by using SHPB device and high-temperature environment box. The effects of loading rate and high temperature on the dynamic stress-strain curves, tensile strength, deformation, and failure mode were also discussed. The major conclusions are as follows:

- (1) Before the peak points, dynamic tensile stress-strain curves gently increase at 25°C, when the heating temperature is higher than 200°C. The brittleness of sandstone specimens is enhanced at 200°C and 400°C, but slight ductility is observed at 600°C and 800°C.
- (2) Dynamic tensile strength increases in a power function with average strain rate, and the strain rate effect of dynamic tensile strength is closely related to temperature. When the striker velocity exceeds 2.3 m/s, the dynamic radial strain first decreases and then increases with the rising temperature. A quadratic polynomial relation exists between dynamic radial strain and heating temperature.
- (3) The average strain rate first decreases and then increases with the rising temperature. The temperature effect on the average strain rate is strong at low striker velocity and weak at high striker velocity. Under the same temperature, the strain rate increases in a quadratic polynomial function with the growth of the striker velocity.
- (4) In dynamic splitting tensile tests, high-temperature sandstone specimens are split into two semicylinders along the radial loading direction. Moreover, two local crushing zones appear at the contact positions with the input and output bars; the local crushing zone near the input bar is slightly larger than that near the output bar. The temperature effect on failure mode is weak at low striker velocity and strong at high striker velocity.

In this study, the dynamic tensile characteristics of rocks at actual high temperatures are investigated using the SHPB test device. This research provides references for the stability analysis of surrounding rocks in the blasting excavation process. Given the limited types of rock samples used, the dissolution law of other types of rock will be studied in future works.

Data Availability

The datasets generated and analyzed in the current study may be obtained from the corresponding author upon reasonable request.

Conflicts of Interest

The authors declare no conflicts of interest regarding the publication of this paper.

Acknowledgments

This research was funded by the National Natural Science Foundation of China (no. 51674008), Anhui Natural Science Foundation (nos. 1808085ME134, 1808085QE148, and 2008085QE220), project funded by China Postdoctoral Science Foundation (no. 2018M642504), Anhui Postdoctoral Science Foundation (no. 2015B058), and Quality Engineering Project of Anhui Province (no. 2016jyxm0283).

References

- [1] C.-P. Lu, L.-M. Dou, N. Zhang et al., "Microseismic frequency-spectrum evolutionary rule of rockburst triggered by roof fall," *International Journal of Rock Mechanics and Mining Sciences*, vol. 64, pp. 6–16, 2013.
- [2] C.-P. Lu, G.-J. Liu, Y. Liu, N. Zhang, J.-H. Xue, and L. Zhang, "Microseismic multi-parameter characteristics of rockburst hazard induced by hard roof fall and high stress concentration," *International Journal of Rock Mechanics and Mining Sciences*, vol. 76, pp. 18–32, 2015.
- [3] C.-P. Lu, Y. Liu, H.-Y. Wang, and P.-F. Liu, "Microseismic signals of double-layer hard and thick igneous strata separation and fracturing," *International Journal of Coal Geology*, vol. 160–161, pp. 28–41, 2016.
- [4] D. Ma, J. Wang, and Z. Li, "Effect of particle erosion on mining-induced water inrush hazard of karst collapse pillar," *Environmental Science and Pollution Research*, vol. 26, no. 19, pp. 19719–19728, 2019.
- [5] D. Ma, H. Y. Duan, W. T. Liu, X. T. Ma, and M. Tao, "Water-sediment two-phase flow inrush hazard in rock fractures of overburden strata during coal mining," *Mine Water and the Environment*, vol. 39, pp. 308–319, 2020.
- [6] M. C. He and P. Y. Guo, "Deep rock mass thermodynamic effect and temperature control measures," *Chinese Journal of Rock Mechanics and Engineering*, vol. 32, no. 12, pp. 2377–2393, 2013.
- [7] W. R. Alexander, H. M. Reijonen, and I. G. McKinley, "Natural analogues: studies of geological processes relevant to radioactive waste disposal in deep geological repositories," *Swiss Journal of Geosciences*, vol. 108, no. 1, pp. 75–100, 2015.
- [8] S. Cloetingh, J.-D. Van Wees, and V. Wesztergom, "Thermo-mechanical controls on geothermal energy resources: case studies in the Pannonian Basin and other natural laboratories," *Acta Geodaetica et Geophysica*, vol. 52, no. 2, pp. 157–160, 2017.
- [9] L. X. Xiong and L. J. Yu, "Advances of mechanical properties of rock under high temperature and after high temperature," *Journal of Geological Hazards and Environment Preservation*, vol. 29, no. 1, pp. 76–82, 2018.
- [10] H. Tian, T. Kempka, S. Yu, and M. Ziegler, "Mechanical properties of sandstones exposed to high temperature," *Rock Mechanics and Rock Engineering*, vol. 49, no. 1, pp. 321–327, 2016.
- [11] D. Ma, J. J. Wang, X. Cai et al., "Effects of height/diameter ratio on failure and damage properties of granite under coupled bending and splitting deformation," *Engineering Fracture Mechanics*, vol. 220, Article ID 106640, 14 pages, 2019.
- [12] J. Shang, S. R. Hencher, and L. J. West, "Tensile strength of geological discontinuities including incipient bedding, rock joints and mineral veins," *Rock Mechanics and Rock Engineering*, vol. 49, no. 11, pp. 4213–4225, 2016.

- [13] Z. T. Bieniawski and I. Hawkes, "Suggested methods for determining tensile strength of rock materials," *International Journal of Rock Mechanics and Mining Sciences*, vol. 15, no. 3, pp. 99–103, 1978.
- [14] S. Kahraman, M. Fener, and E. Kozman, "Predicting the compressive and tensile strength of rocks from indentation hardness index," *Journal of the Southern African Institute of Mining and Metallurgy*, vol. 112, pp. 331–339, 2012.
- [15] P. A. Siratovich, M. C. Villeneuve, J. W. Cole, B. M. Kennedy, and F. Bégué, "Saturated heating and quenching of three crustal rocks and implications for thermal stimulation of permeability in geothermal reservoirs," *International Journal of Rock Mechanics and Mining Sciences*, vol. 80, pp. 265–280, 2015.
- [16] N. N. Sirdesai, T. N. Singh, P. G. Ranjith, and R. Singh, "Effect of varied durations of thermal treatment on the tensile strength of red sandstone," *Rock Mechanics and Rock Engineering*, vol. 50, no. 1, pp. 205–213, 2017.
- [17] Y. B. Chen, Y. Wang, and H. Luo, "Study on the Brazil split test of sandstone under different temperatures," *Mining Research and Development*, vol. 38, no. 8, pp. 45–50, 2018.
- [18] T. Yin, P. Wang, X. Li, B. Wu, M. Tao, and R. Shu, "Determination of dynamic flexural tensile strength of thermally treated laurentian granite using semi-circular specimens," *Rock Mechanics and Rock Engineering*, vol. 49, no. 10, pp. 3887–3898, 2016.
- [19] M. Liang, S. H. Zhang, and B. Shu, "Effect of different cooling ways on Brazilian tension characteristics of heat-treated granite," *Journal of Water Resources and Water Engineering*, vol. 29, no. 2, pp. 186–193, 2018.
- [20] Z. Zhou, X. Cai, X. Li, W. Cao, and X. Du, "Dynamic response and energy evolution of sandstone under coupled static-dynamic compression: insights from experimental study into deep rock engineering applications," *Rock Mechanics and Rock Engineering*, vol. 53, no. 3, pp. 1305–1331, 2020.
- [21] F.-Q. Gong, X.-F. Si, X.-B. Li, and S.-Y. Wang, "Dynamic triaxial compression tests on sandstone at high strain rates and low confining pressures with split Hopkinson pressure bar," *International Journal of Rock Mechanics and Mining Sciences*, vol. 113, pp. 211–219, 2019.
- [22] J. R. Klepaczko and A. Brara, "An experimental method for dynamic tensile testing of concrete by spalling," *International Journal of Impact Engineering*, vol. 25, no. 4, pp. 387–409, 2001.
- [23] H. Schuler, C. Mayrhofer, and K. Thoma, "Spall experiments for the measurement of the tensile strength and fracture energy of concrete at high strain rates," *International Journal of Impact Engineering*, vol. 32, no. 10, pp. 1635–1650, 2006.
- [24] B. Erzar and P. Forquin, "An experimental method to determine the tensile strength of concrete at high rates of strain," *Experimental Mechanics*, vol. 50, no. 7, pp. 941–955, 2010.
- [25] F.-Q. Gong and G.-F. Zhao, "Dynamic indirect tensile strength of sandstone under different loading rates," *Rock Mechanics and Rock Engineering*, vol. 47, no. 6, pp. 2271–2278, 2014.
- [26] Y. X. Zhou, K. Xia, X. B. Li et al., "Suggested methods for determining the dynamic strength parameters and mode-I fracture toughness of rock materials," *International Journal of Rock Mechanics and Mining Sciences*, vol. 49, pp. 105–112, 2012.
- [27] F. Dai, S. Huang, K. Xia, and Z. Tan, "Some fundamental issues in dynamic compression and tension tests of rocks using split Hopkinson pressure bar," *Rock Mechanics and Rock Engineering*, vol. 43, no. 6, pp. 657–666, 2010.
- [28] Q. Ping, Q. Y. Ma, and P. Yuan, "Energy dissipation analysis of stone specimens in SHPB tensile test," *Journal of Mining and Safety Engineering*, vol. 30, no. 3, pp. 401–407, 2013.
- [29] F. Gong and J. Hu, "Energy dissipation characteristic of red sandstone in the dynamic brazilian disc test with SHPB setup," *Advances in Civil Engineering*, vol. 2020, Article ID 7160937, 10 pages, 2020.
- [30] Y. Zhao, H. Xiao, and Y. Huang, "Dynamic split tensile test of Brazilian disc of coal with split Hopkinson pressure bar loading," *Journal of China Coal Society*, vol. 39, no. 2, pp. 286–291, 2014.
- [31] B. Du, H. Bai, Z. Ma, L. Ming, and G. Wu, "Experimental study on the dynamic tensile properties of red-sandstone after cyclic wetting and drying," *Chinese Journal of Rock Mechanics and Engineering*, vol. 37, no. 7, pp. 1671–1679, 2018.
- [32] M. Wen, Z. Chen, J. Xu, W. Peng, and S. Lin, "Static-dynamic split tensile tests and micro analysis on red-sandstone with different moisture contents," *Chinese Journal of Underground Space and Engineering*, vol. 3, no. 1, pp. 86–92, 2017.
- [33] M. Li, L. Qiao, and Q. Wen, "Energy dissipation of rock specimens under high strain rate with single joint in SHPB tensile tests," *Chinese Journal of Geotechnical Engineering*, vol. 19, no. 7, pp. 1336–1343, 2017.
- [34] A. Mardoukhi, Y. Mardoukhi, M. Hokka, and V.-T. Kuokkala, "Effects of heat shock on the dynamic tensile behavior of granitic rocks," *Rock Mechanics and Rock Engineering*, vol. 50, no. 5, pp. 1171–1182, 2017.
- [35] T. Yin, L. Bai, X. Li, X. Li, and S. Zhang, "Effect of thermal treatment on the mode I fracture toughness of granite under dynamic and static coupling load," *Engineering Fracture Mechanics*, vol. 199, pp. 143–158, 2018.
- [36] S. Liu, J. Y. Xu, E. L. Bai, L. ZHI, and T. CHEN, "Experimental study of dynamic tensile behaviors of marble after high temperature," *Rock and Soil Mechanics*, vol. 34, no. 12, pp. 3500–3504, 2013.
- [37] X.-Q. Wang, A. Schubnel, J. Fortin, Y. Guéguen, and H.-K. Ge, "Physical properties and brittle strength of thermally cracked granite under confinement," *Journal of Geophysical Research: Solid Earth*, vol. 118, no. 12, pp. 6099–6112, 2013.
- [38] Q. Ping, Q. Y. Ma, and P. Yuan, "Sensitivity of time for stress equilibrium to wave impedance ratio with different rising times in SHPB tests," *Chinese Journal of Rock Mechanics and Engineering*, vol. 32, no. 10, pp. 2128–2134, 2013.
- [39] P. Yuan, Q.-y. Ma, and D.-d. Ma, "Stress uniformity analyses on nonparallel end-surface rock specimen during loading process in SHPB tests," *Advances in Civil Engineering*, vol. 2018, Article ID 5406931, 12 pages, 2018.
- [40] Q. Ping, Q. Y. Ma, and P. Yuan, "Stress equilibrium in rock specimen during the loading process of SHPB experiment," *Explosion and Shock Waves*, vol. 33, no. 6, pp. 655–661, 2013.
- [41] K. Xia, J. Cheng, and S. Hu, "Application of SHPB apparatus to the measurement of high temperature dynamical mechanical behavior of materials," *Journal of Experimental Mechanics*, vol. 13, no. 3, pp. 307–313, 1998.
- [42] K. Xia and W. Yao, "Dynamic rock tests using split Hopkinson (Kolsky) bar system—a review," *Journal of Rock Mechanics and Geotechnical Engineering*, vol. 7, no. 1, pp. 27–59, 2015.
- [43] J. T. Gomez, A. Shukla, and A. Sharma, "Static and dynamic behavior of concrete and granite in tension with damage," *Theoretical and Applied Fracture Mechanics*, vol. 36, no. 1, pp. 37–49, 2001.

Research Article

Linkage Analysis between Solid-Fluid Coupling and the Strength Reduction Method for Karst Cave Water Inrush in Mines

Yanlin Zhao , Jian Liao, Qiang Liu, Yang Li, and Jianchao Cheng

*Hunan Provincial Key Laboratory of Safe Mining Techniques of Coal Mines,
Work Safety Key Lab on Prevention and Control of Gas and Roof Disasters for Southern Coal Mines,
Hunan University of Science and Technology, Xiangtan, Hunan, China*

Correspondence should be addressed to Yanlin Zhao; yanlin_8@163.com

Received 15 January 2020; Accepted 3 February 2020; Published 4 June 2020

Academic Editor: Longjun Dong

Copyright © 2020 Yanlin Zhao et al. This is an open access article distributed under the Creative Commons Attribution License, which permits unrestricted use, distribution, and reproduction in any medium, provided the original work is properly cited.

The present paper aims to study the mechanical mechanism and characteristics of water irruption from Karst cave. Combining the nonlinear seepage-pipe coupling model with the strength reduction method, the linkage analysis of fluid solid coupling and strength reduction method are constructed to study the whole process of confined Karst cave water inrush. Taking the water inrush accident of Shibaijing of the Qiyi mine in south China as an example, the instability mechanism of the water-proof rock pillar and evolution of water inrush are discussed. It is suggested that water discharge on the working face augments with the increase in the reduction factor of the water-proof rock pillar before the rock pillar loses its stability. Once the rock pillar becomes unstable, Karst water bursts from confined Karst cave in a pipe flow shape, and the water irruption quantity reaches the peak value in a short time by adopting the pipe flow to simulate and then decreases slowly. The hydraulic rough flow at the initial stage changes into pipe laminar flow finally in the process of Karst water inrush, due to the constraint of Karst cave water reserve. The conception for the safety factor of the water-proof rock pillar introduced, the relation of the safety factor, Karst cave water pressure, and thickness of the water-proof rock pillar are studied. It is proposed that thickness of the water-proof rock pillar whose safety factor equals 1.5 is regarded as the calculating safety thickness of the water-proof rock pillar, and the safety thickness of the water-proof rock pillar setting in mining engineering should be equal to the sum of the blasthole depth, blasting disturbance depth, and the calculating safety thickness. The reason leading to Karst water inrush of Qiyi Mine is that without advanced boreholes, the water-proof rock pillar is set so small that it could not possess safety margin, so the confined Karst cave water breaks the water-proof rock pillar and bursts out. Combining the solid fluid coupling theory, pipe flow theory, and strength reduction method, the nonlinear mechanical response of confined Karst cave water inrush is studied, which provides a new study method for the whole process of confined Karst cave water inrush.

1. Introduction

China owns many types of coal-bearing basins and has large amounts of coal resources. The stress and hydrogeological conditions are extremely complex during deep mining, and especially, one of the main challenges associated to deep mining is the increased water pressure. The coal production reached 3,700 million tons in 2012. Water inrush into coal mines is regarded as a serious detriment to mining safety. In China, there have been thousands of casualties in groundwater-related coal mine accidents since 2000. Among underground engineering accidents, including water rush

[1–4], gas explosion [5], rock burst [6–8], and time-dependent large deformation [8–10], the groundwater inrush in coal mines is second only to gas explosion in causing catastrophic accidents according to government statistics (State Administration of Coal Mine Safety 2008). Mining depths and mining intensity have increased, causing the encountered hydrogeological conditions to become more complicated. Water inrush threatens mine safety and coal mine productivity [11, 12]. Geological settings and hydrogeological conditions of the coalfields in China are very complicated. The coalfields in north China are typical permian-Carboniferous coalfields. Many coal seams lie

above the Ordovician limestone which is a highly permeable confined aquifer. Because of the potential impacts of the confined water in the Ordovician limestone on the mining activities, the coal seams, accounting for 37% of the total reserve, are listed as prospective reserves in north China [11, 12].

The coalfields in south China locally occurred in late permian. Figure 1 shows the representative stratigraphic column of the region [13]. The main minable coal layer lies in the late permian Longtan Formation. The overall coal products of this region account for a small part of the national total coal production. Hydrogeologically, south China is in humid region and dominated by modern Karst terrains. Coal excavation from late permian Longtan formation is seriously threatened by lower Maokou Karst aquifer and upper Changxing Karst aquifer. All the times, the key issue in south China is to prevent late permian Karst water bursting.

The Karst groundwater is mainly of the dissolved-cavern type and Karst-fissure type and usually forms the complicated systems of Karst fissures, dissolved cavern pipes, and Karst caves in south district [14]. The distribution and structure of underground water system are obviously of inhomogeneity, and this brings the anisotropism that the underground hydrodynamic force is connected. Although the Ordovician limestone in north and the Maokou limestone in south are both aquifers, there exist great differences between them. In north, its Karst underground is mainly of the Karst-fissure water-bearing type. Its hydraulic slope is rather soft, belonging to unified confined water-logged strata, and once the water is exposed, serious water inrush accidents happen, giving rise to the decline of water level of aquifer [15]. As for the southern area, particularly in the Songzao Mine Area in Chongqing city, Doulishan Mine Area in Hunan province, and the north area of Guizhou province, water filling Karst caves generally exist in the Maokou limestone; moreover, the horizontal hydraulic relation among Karst caves is weak and relative independence, which cannot form unified aquifer system [16–19]. With regard to the Maokou limestone of the basement in southern coalfield, its inhomogeneity of karst development in space distribution is found. When Karst is least developed, Maokou limestone strata can be seen as a relative impermeable layer. So, Maokou limestone strata can be fully utilized by adopting a scientific method. At present, development roadways are arranged in Maokou limestone strata in many southern coalfields, such as Xingwujing mine of Nantong Company in Guizhou province, Shipingyi mine of South Sichuan Coal Industry, Meitanba mine in Hunan Province, Huayingshan mine of Chongqing city, and so on [14, 18, 19]. While the Karst cave development area is the major hidden trouble for mine water inrush, Karst cave water inrush is seen as one of the coal mine flood accidents in south China, which generated to a large amount of economic loss, such as the “4-16” accident happened in the Qiyi mine of Hunan Province in 2003 (17 people died), “9.28” Karst cave water inrush accident happened in the Xinmao mine of Hunan Province in 2010, and “12.12” Karst cave water bursting in the Tianchi mine of Guizhou Province

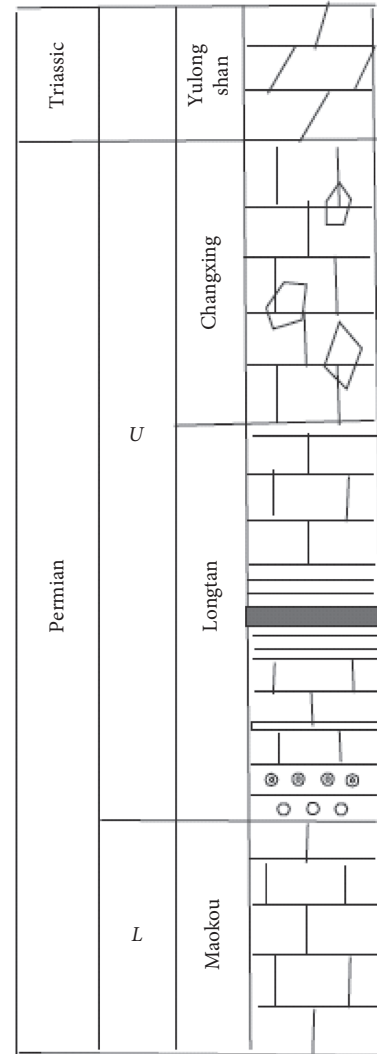


FIGURE 1: The representative stratigraphic column of the coalfields in south China.

in 2004 (21 deaths and 15 missing), which were typical Karst cave water inrush accidents in late Permian Maokou limestone.

The rock strata between the working face and Karst cave act as a geological barrier that prevents Karst cave water from invading into the roadways. The effectiveness of the geological barrier depends on its thickness, lithology, and integrity [20, 21]. Water inrushes are likely to occur when the geological barrier is too thin to withhold the pressure of Karst cave water. In a Karst mine, the main technique for controlling water inrush is to leave a sufficient thickness of the water-proof rock pillar. While the calculating method about safety thickness of rock pillar setting for confined Karst cave is not given in regulations of mine water control of China [22], a study on stability of the water-proof rock pillar and its safety thickness is of great significance for controlling Karst water inrush in a mine. In order to do so, it is of vital importance to study strata failure characteristics and hydraulic conductivity changes due to mining and thereafter find a way to predict and prevent water inrushes.

Various research studies have been conducted in this area [23–26]; however, the mechanism of water inrushes is still not well-understood. In this paper, linkage analysis between solid-fluid coupling and the strength reduction method based on flow state conversion theory is adopted to discuss the stability of the water-proof rock pillar. Meanwhile, the concept of safety factor of the water-proof rock pillar introduced, and the safety thickness of the water-proof rock pillar setting in mining engineering is proposed.

2. Solid-Fluid Coupling Mechanism of Confined Karst Water Inrush

When a confined Karst cave is concealed before a roadway, disturbance stress evokes the sharp change of stress field and seepage field of surrounding rocks. There would be strong coupling effect in the surrounding rock mass between the Karst cave and working face. This kind of coupling effect is shown as follows: (1) the action of a high hydraulic gradient (high seepage stress) on the surrounding rocks results in the change of stress field; (2) also, due to mining-induced fissures in the surrounding rocks under high hydraulic pressure and disturbance stress field, the hydraulic conductivity of the surrounding rocks augments greatly. The schematic diagram for a water-proof rock pillar is shown in Figure 2. From the angle of rock mass fluid mechanics, under disturbance stress and high hydraulic pressure, confined Karst cave water inrush can be considered as a catastrophic instability of the water-proof rock pillar between the Karst cave and working face, accompanying with Karst cave water inrush.

2.1. Elastic-Plastic Analysis for a Water-Proof Rock Pillar of a Confined Karst Cave. Constitutive relation of elastic-plastic mechanics for rock mass under coupling effect of stress field and seepage field can be denoted as

$$\sigma_{ij,j} + F_i + (\alpha p)_{,j} = 0, \quad (1)$$

where $(\alpha p)_{,j}$ is equivalent volumetric stress acting on the water-proof rock pillar, which reflects the coupling effect of seepage field on stress field.

Yield criterion is the Mohr–Coulomb Criterion, and the shear failure criterion is represented as

$$f^s = \sigma_1 - \sigma_3 \frac{1 + \sin \phi}{1 - \sin \phi} + 2c \sqrt{\frac{1 + \sin \phi}{1 - \sin \phi}} = 0. \quad (2)$$

The tensile failure criterion is that

$$f^t = \sigma_t - \sigma_3 = 0, \quad (3)$$

where σ_1 is the first effective principal stress, σ_3 is the third effective principal stress, ϕ is the internal friction angle of the rock mass, c is the cohesion, and σ_t is the tensile strength.

2.2. Nonlinear Seepage-Pipe Flow Coupling Based on Flow State Conversion Theory. The essence of Karst cave water inrush is the instability of the water-proof rock pillar. When the rock pillar is unstable, the flow discharge of working face

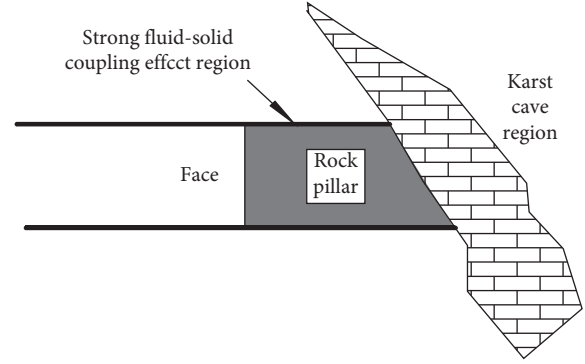


FIGURE 2: The schematic diagram for a water-proof rock pillar.

is in the form of seepage and small-scale water flow. Once the water-proof rock pillar becomes unstable, the water in the confined Karst cave bursts in the form of pipe flow.

2.2.1. Water-Proof Rock Pillar Instability. When the elastic-plastic calculation for the water-proof rock pillar is convergence, the water inflow form is hydraulic seepage, and the differential control equation for seepage analysis of the surrounding rocks is represented as

$$\frac{\partial p}{\partial t} = -u_s \frac{\partial}{\partial x_i} \left(k(\Theta, p) \frac{\partial p}{\partial x_j} \right), \quad (4)$$

where p is the seepage pressure, $k(\Theta, p)$ is the hydraulic conductivity, and u_s is the storage coefficient.

The influence of seepage pressure and stress field on the hydraulic conductivity can be presented as [27, 28]

$$k(\Theta, p) = \xi k_0 e^{-(\Theta/3 - \beta p)}, \quad (5)$$

where k_0 is the initial value of the hydraulic conductivity, $k(\Theta, p)$ is the hydraulic conductivity by means of coupling analysis, $\Theta = \sigma_1 + \sigma_2 + \sigma_3$ is the volumetric stress, ξ is the sudden jump coefficient of the hydraulic conductivity, and β is the coefficient.

In coupling analysis, for elastic units, the hydraulic conductivity is looked as the negative exponential function of the volumetric stress. In equation (5), ξ is 1.0 and β is 0.5.

For plastic yielding units, the hydraulic conductivity enhances greatly. The sudden jump coefficient of the hydraulic conductivity enhances obviously. In equation (5), ξ is 1000 and β is 1.0.

Equation (5) reflects the coupling effect of rock mass stress field on seepage field. Particularly, the strong coupling effect of plastic units on seepage field is reflected.

2.2.2. Water-Proof Rock Pillar Instability. When the elastic-plastic calculation has no convergence, the water-proof rock pillar is unstable, and Karst cave water bursts out to the roadway; the governing law for water inrush was studied by using the pipe flow model.

Nonlinear pipe flow is a complex problem educed from the Darcy–Weisbach equation:

$$\Delta H = f \frac{l}{d} \frac{u^2}{2g}, \quad (6)$$

where ΔH is the head loss, f is the friction factor of head loss, l is the length of the pipe, d is the inside diameter of the pipe, u is the mean flow velocity in the pipe, and g is the acceleration due to gravity.

The Reynolds number, Re , in the process of water inrush is represented as

$$Re = \frac{\rho v d}{\mu}, \quad (7)$$

where ρ is the density of water, v is water velocity in the water inrush channel, and μ is the dynamic viscosity of water.

Based on Nikuradse's experimental curves, when $Re > 100000$, f is related to relative roughness of the pipe wall, but it is independent of Re ; under this situation, head loss ΔH has direct ratio relations with u^2 , namely, "the hydraulic rough region", and the following equation can be attained by using the Von Karman equation:

$$f = \frac{1}{[1.74 + 2\lg(2\Delta/d)]^2}, \quad (8)$$

where Δ is the roughness of the roadway.

When $Re < 2300$, the friction factor of head loss can be obtained by the Hagen–poiseuille equation:

$$f = \frac{64}{Re}. \quad (9)$$

In this case, ΔH has a direct ratio relation with u , belonging to "the laminar region".

When $2300 \leq Re \leq 100000$, the friction factor of head loss can be obtained by the Blasius equation:

$$f = \frac{0.326}{Re^{0.25}}. \quad (10)$$

In this case, ΔH has a direct ratio relation with $u^{1.75}$, belonging to "the hydraulic smooth region".

During the process of Karst water inrush, flow velocity is fast at the initial water inrush, the diameter of water-burst channel is big, and the Reynolds number, Re , is much more than 100000 in the process of initial water inrush. So, the initial water inrush belongs to the hydraulic rough region. With the development of water inrush, the Karst cave water pressure drops off due to the limit of aquifers reserve in the Karst cave, and flow velocity in the roadway will become slower, the water flow in the roadway will transform from "the hydraulic rough region" into "the hydraulic smooth region" or even "the laminar region".

With regard to a noncircular roadway, the equivalent diameter of the roadway is used which can be denoted as

$$d = \frac{4S}{U}, \quad (11)$$

where S is water-carrying section areas and U is the wetted perimeter.

If T = the porosity of pipe flow $n = 1$, then $V = u$ equation (6) can be expressed as follows [25, 26]:

$$V = \frac{2gd}{fV} J = \frac{8gS}{fVU} J. \quad (12)$$

Comparing equation (12) with the Darcy law, the equivalent hydraulic conductivity of pipe flow is defined as follows:

$$K_L = \frac{8gS}{fVU}. \quad (13)$$

When the pipe flow is in the turbulent state, the flow law of pipe flow can be expressed to the nonlinear Darcy's law by substituting the equivalent hydraulic conductivity K_L for $k(\Theta, p)$ in equation (4).

If water flow is in the laminar state, the equivalent hydraulic conductivity K_L transforms into the true hydraulic conductivity K_{L1} by submitting equations (9) into (13):

$$K_{L1} = \frac{d^2 \rho g}{32\mu} = \frac{S^2 \rho g}{2U^2 \mu}. \quad (14)$$

The conception of equivalent hydraulic conductivity K_L is introduced to equation (4), and laminar region and turbulent region in the roadway are expressed with a unified law:

$$\frac{\partial p}{\partial t} = -u_s \frac{\partial}{\partial x_i} \left(k \frac{\partial p}{\partial x_j} \right), \quad (15)$$

where the hydraulic conductivity of water-proof rock pillar instability is $k = \xi k_0 e^{-(\Theta/3 - \beta p)}$, while for an unstable water-proof rock pillar, equivalent hydraulic conductivity K_L which is considered to the hydraulic conductivity k in equation (15) is adopted to describe pipe flow in the roadway.

2.3. Solid-Fluid Coupling Program Designing. The solid-fluid coupling analysis for confined Karst water inrush in a mine is conducted by the indirect coupling method. Firstly, the elastic-plastic stress field is calculated when time is t_i , then the hydraulic conductivity of surrounding rocks is obtained by using equations (5)–(14), which is delivered to seepage field calculation module, and then the coupling of stress field to seepage field is implemented. Secondly, the seepage volumetric stress obtained in seepage field acts on elastic-plastic stress calculation units, and then the coupling of seepage field to stress field can be implemented. The calculation does not stop until reaching desired calculation time.

If the calculation has no convergence, Karst cave water inrush occurs and forms pipe flow, and the equivalent hydraulic conductivity K_L of pipe flow is gained by FISH in FLAC^{3D} based on equations (13) and (14).

Based on the thought of program development given above, combining nonlinear seepage flow and pipe flow, the solid-fluid coupling analysis program is successfully conducted in FLAC^{3D}. This program is composed of three parts: an elastic-plastic stress calculation module, seepage calculation module, and coupling analysis module. The program flow chart is shown in Figure 2.

The indirect coupling analysis method developed by FLAC^{3D}, of which merits are the fact that the coupling parameters (for example, the hydraulic conductivity and seepage volumetric stress) evolve with the time steps, the coupling message of every subcoupling system (subseepage system and elastic-plastic stress system) can be delivered accurately with time steps.

As for pipe flow, the corresponding equation is selected to calculate equivalent hydraulic conductivity K_L , based on the Reynolds number, Re . From the analysis mentioned above, pipe flow of water inrush is not only considered to have great “permeability” but also its equivalent hydraulic conductivity varies with the Reynolds number, Re , and it is not a constant. However, node flow rates are unknown numbers in the first time step; thus, the solving has to be carried out by an iterative method. Owing to the fact that initial Karst cave water inrush belongs to the turbulent rough region, K_L is assumed to be the equivalent hydraulic conductivity of the hydraulic rough region. Through the given initial velocity of fluid flow V_{in} , roughness Δ of water inrush channel (roadway), water-carrying section areas S , and wetted perimeter U of the roadway, the equivalent hydraulic conductivity K_L is firstly gained. Water pressure p and flow velocity V of calculating elements are obtained by FLAC^{3D}. Then, the Reynolds number, Re , dependent of velocity V obtained by FLAC^{3D} is used to judge the laminar region or turbulent region. The friction factor of head loss f is calculated based on Reynolds number, Re . Then, the equivalent hydraulic conductivity K_L for the next step is determined by using equation (13). By the method given above, the equivalent hydraulic conductivity K_L evolves with the calculation time step as shown in Figure 3.

2.4. Linkage Analysis Between Solid-Fluid Coupling and the Strength Reduction Method. The basic principle of the strength reduction method is that shear parameters c and $\tan \varphi$ are divided by reduction factor F_i , and a new group of value c' , φ' is obtained, which is served as new calculation parameters [29, 30]:

$$c' = \frac{c}{F_i}, \quad (16)$$

$$\varphi' = \arctan(\tan \varphi / F_i). \quad (17)$$

In the strength reduction method for stability of a water-proof rock pillar, the shear parameters c and $\tan \varphi$ of the rock pillar do not reduce continuously until critical state.

Combing the solid-fluid coupling model and strength reduction method, the linkage analysis model between solid-fluid coupling and strength reduction method for confined Karst cave water inrush was established. The process of realization is illustrated in Figure 4.

It is noted that although the instability of water-proof rock pillar is also related with the time-dependent failure, tensile failure, and crack coalescence process of water-proof rock pillar [31–34], in this study, the plastic coalescence failure of the water-proof rock pillar is considered based on the strength reduction method.

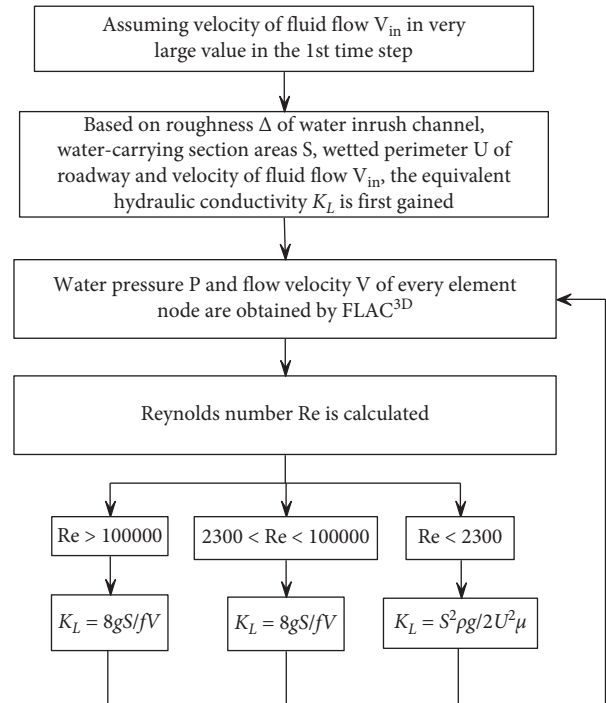


FIGURE 3: The equivalent hydraulic conductivity K_L evolved with calculation time step.

3. Case Analysis

3.1. Water Inrush Accident. An example of the accident of confined Karst cave water inrush in the Qiyi mine in Hunan Province was studied in this paper. Karst cave water inrush happened on the heading face in the Qiyi mine with -160 m level, which was a typical example of water bursting from confined Karst cave. The hydrological condition of the mine is very complex. Maokou limestone strata which is a confined aquifer under lies in coalseam 2. Karst caves in Maokou limestone strata always exist in the shape of moniliform structures, whose volumes are in state of half filling or full filling. However, water flow in Maokou limestone strata is less, and the Maokou limestone is a hard substance where Karst structures are less developed. The heading face with -160 m level is in No.23 mining area located in Maokou limestone strata. On 16th April 2003, at 8 am~19 pm, Karst cave water poured into the heading face. On 16th April at 8 am, the water-proof rock pillar between the working face and confined Karst cave could not withstand the water pressure in the Karst cave, and so the water-proof rock pillar was broken at the length. A loud sound that was heard when the water inrush occurred indicated a sudden fracturing of the rock pillar and a sudden releasing of deep groundwater pressure with abundant of water burst from Karst cave all of sudden. The inflow occurred at an estimated rate of $3,670 \text{ m}^3/\text{h}$ at the very beginning. After about 2 hours, water raised as much as 2.5 m, and flooded about 2 km of the roadway. The water flow was turbid along with small pieces of limestone, rock flour, and Karst breccias. In an accident, 17 people died. About $22,500 \text{ m}^3$ water in total burst out within nearly 11 h. A Karst cave with volume about

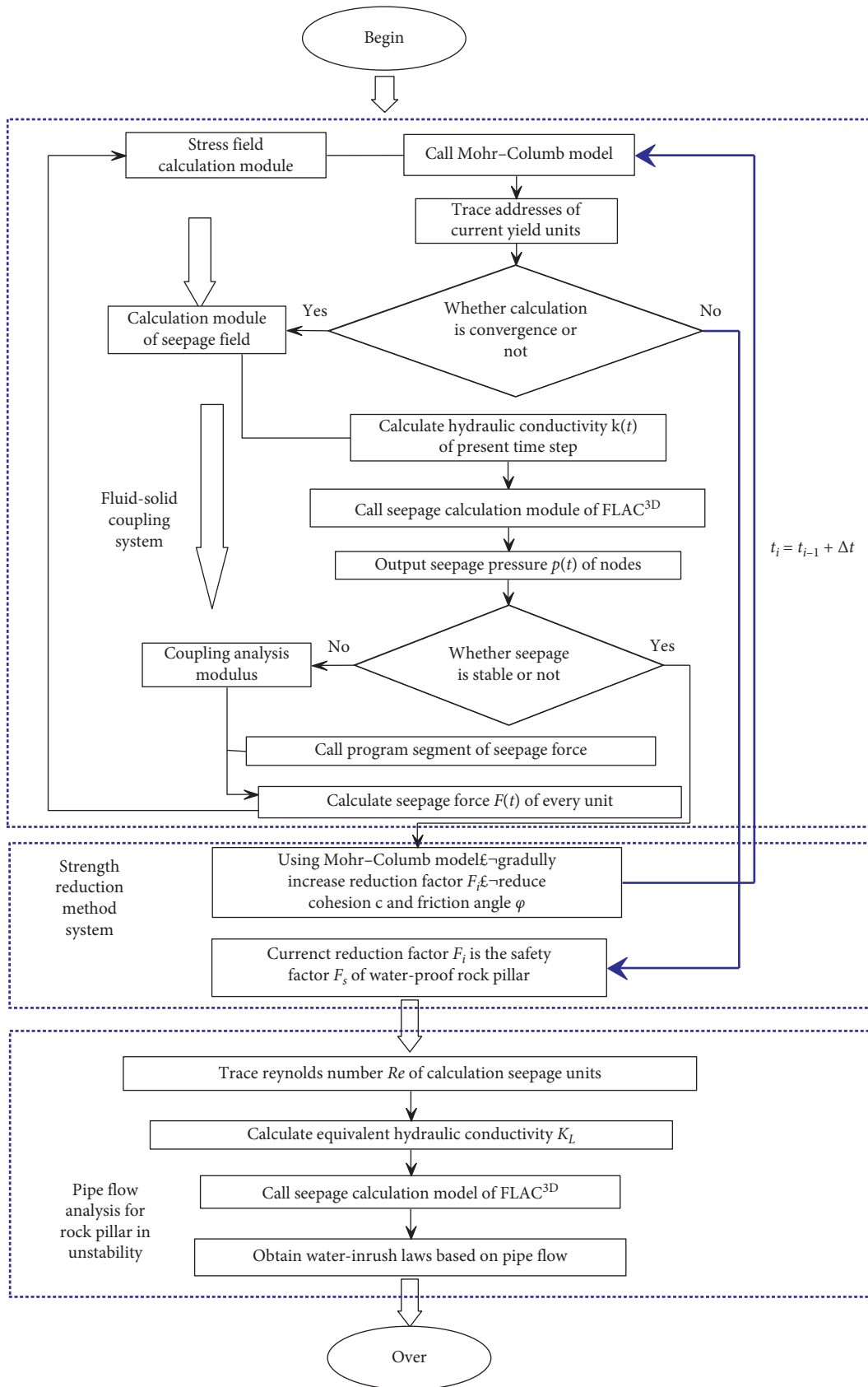


FIGURE 4: Flow diagram of linkage analysis between solid-fluid coupling and the strength reduction method based on flow state conversion theory.

20 m × 6 m × 20 m was exposed about 3~4 m before working face after slag clearing. The geological survey indicated that there were some major fractures and well-developed Karst caves around the roadway where water inrush took place, the deep confined Karst cave system exists in Maokou limestone strata in synclinal shaft of Doulishan coal mine area. The buried depth of roadway excavation is 450 m more or less. The hydrostatic pressure head is about 400 m, the water pressure in the confined Karst cave in Maokou limestone strata is about 4.0 MPa.

Figure 5 illustrates the picture of water discharge of the roadway 8 h after water inrush. By means of spot investigation after slag clearing, it was found that the Karst cave was strongly dissolved, whose walls were smooth as shown in Figure 6, the Karst water was supplied by Karst pipelines, and the Karst cave was filled with a large amount of water and yellow mud. Figure 7 is the vertical plane projection of Karst cave development.

Maokou limestone specimens were sampled from the water inrush Karst cave. It was discovered that abundant Karst fissure and pores exist in the limestone near the confined Karst cave. As the surrounding rocks near the Karst cave were deeply dissolved, its integrity and continuity were poor with high porosity and developed fissures, while the mechanical properties of Maokou limestone far away from Karst cave are good.

Laboratory tests were performed on rock samples extracted from surrounding rocks near the Karst cave. The tests included the compressive strength and permeability of Maokou limestone. Combining the laboratory test results, field investigation, and Hoek and Diederichs's research advances in deformation modulus of rock mass, Hoek-Brown strength theory was applied to obtain the mechanical parameters of rock mass by using Roclab software [35–37]. The rock mass calculation parameters of the Maokou limestone were obtained as shown in Table 1.

3.2. Calculation Model. The numerical model is established based on the in situ condition at the Qiyi coal mine in the south China. As shown in Figure 8, the simulation domain is 50 m long, 20 m wide, and 30 m deep, in which an excavation roadway in a semicircular arched shape is situated in the middle of the model, and confined Karst cave on the right edge of the model has a closely simplified ellipsoidal shape.

The left and right boundaries in this model are allowed to move along the vertical direction but are restrained in the horizontal direction. The bottom of the model is fixed. $\sigma_1 = 12.5$ MPa is applied on the upper surface of model to simulate crustal stress.

The boundary condition of seepage field is as follows: Karst cave hydraulic pressure is assumed to 1 MPa, 2 MPa, 3 MPa, 4 MPa, and 5 MPa, respectively, and the hydraulic pressure of the heading face is 0.1 MPa. No. 1~5 marked in Figure 5 simulates the driving by step. Footage by every step in the numerical simulation is 5 m. When the water-proof rock pillar between the working face and Karst cave is less than 10 m, for the purpose of studying the stability of the water-proof rock pillar with different thicknesses, footage by every step is 1 m in numerical simulation.



FIGURE 5: The picture of water discharge of the roadway in 8 h after water inrush.



FIGURE 6: The scene photographs of the inside of the Karst cave.

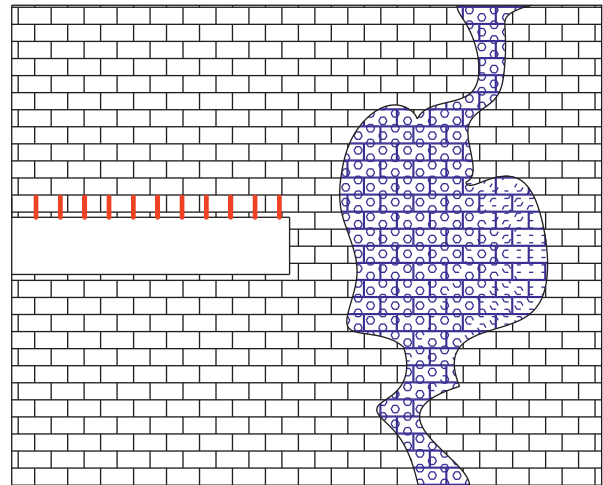


FIGURE 7: Vertical plane projection of Karst cave development.

As for an unstable water-proof rock pillar, water inrush from the Karst cave takes place. Considering that the supply of Karst water is not inexhaustible, it is assumed that the hydraulic pressure in the Karst cave attenuates dynamically in the course of water inrush, and the hydraulic pressure can be denoted as

$$p = p_0 \left(1 - \frac{t}{T} \right), \quad (18)$$

where p_0 is the initial cave hydraulic pressure, T is the whole duration of Karst water inrush (it is assumed that $T = 10$ h in this simulation), and t is the different water inrush time.

TABLE 1: The rock mass calculation parameters of the Maokou limestone.

Density (Kg/m ³)	Water absorption	Saturated coefficient	Softening coefficient	Uniaxial compression (MPa)	Tensile strength (MPa)	Young modulus (GPa)	Poisson ratio	Porosity	Cohesion (MPa)	Internal friction angle (°)	Hydraulic conductivity 10 ⁻¹⁰ m · s ⁻¹
26.2	0.22	0.56	0.68	12.7	0.82	12.6	0.35	0.25	1.5	29.7	0.85

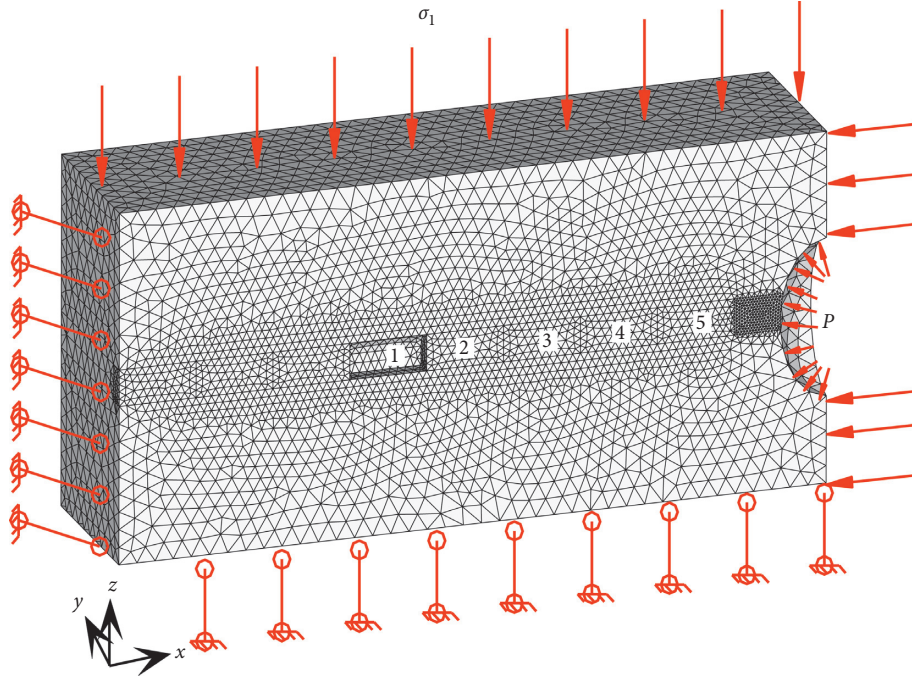


FIGURE 8: Numerical calculation model.

The roughness Δ of water inrush channel is assumed to 0.1 m [26]. Water-carrying section areas S of the roadway is 10.6 m², and the wetted perimeter U is 10.4 m. Suppose that the initial velocity of fluid flow V_{in} is 0.1 m/s, which is a large value. It indicates that water flows in a hydraulic rough region at the very beginning. Using linkage analysis between solid-fluid coupling and the strength reduction method, the paper analyzes the stability of the water-proof rock pillar. Taking the hydraulic pressure $p = 4$ MPa and the thickness $h = 8$ m of rock pillar as an example, the seepage properties of rock pillar and the evolution from stability to instability of the rock pillar are studied when the reduction factor gradually increases.

4. Results

4.1. Water-Proof Rock Pillar Instability. With gradually increase of the reduction factor, the strength parameters of the water-proof rock pillar gradually decrease. The hydraulic conductivity which is dependent of volumetric stress, hydraulic pressure, and plastic zones increases significantly under the action of disturbance stress and high hydraulic pressure.

The strength parameters of the water-proof rock pillar are $c = 1.36$ MPa and $\tan \varphi = 0.52$ when $F_i = 1.10$. Under the

strength, the plastic region of rock pillar is less; the hydraulic conductivity of the rock pillar is influenced mostly by volumetric stress and seepage pressure. The region which is nearly 1.5 m away from the working face is the enhanced hydraulic conductivity zone, which is about $3.25 \times 10^{-10} \sim 15.21 \times 10^{-10}$ m/s. The hydraulic conductivity for an undisturbed region in the middle of the rock pillar is about $0.70 \times 10^{-10} \sim 1.79 \times 10^{-10}$ m/s. The region near the Karst cave is also an enhanced hydraulic conductivity zone where the hydraulic conductivity is nearly $2.79 \times 10^{-10} \sim 5.68 \times 10^{-10}$ m/s. The hydraulic conductivity distribution map when reduction factor $F_i = 1.10$ is shown in Figure 9.

When $F_i = 1.54$, the strength parameters of the rock pillar are $c = 0.97$ MPa, $\tan \varphi = 0.39$. Under the strength, about 85% of units in the water-proof rock pillar are in the plastic state, and the hydraulic conductivity of rock pillar increases at the speed of magnitude in comparison with when $F_i = 1.54$ and it fluctuates between $1.47 \times 10^{-6} \sim 2.80 \times 10^{-6}$ m/s. The hydraulic conductivity distribution map when the reduction factor $F_i = 1.54$ is shown in Figure 10.

When the reduction factor $F_i = 1.10$, the seepage field distribution is calculated as shown in Figure 11. The seepage field of the surrounding rocks was disturbed because of

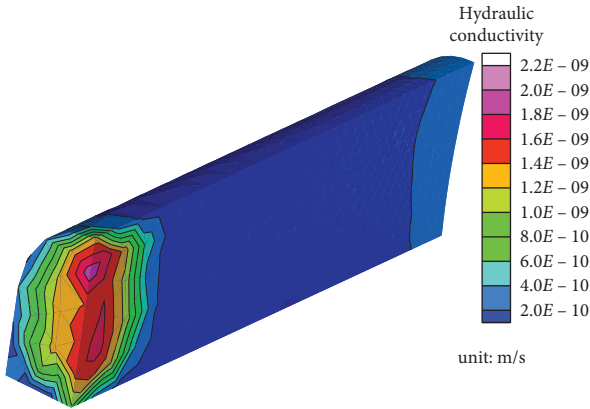


FIGURE 9: The hydraulic conductivity distribution map when the reduction factor $F_i = 1.10$.

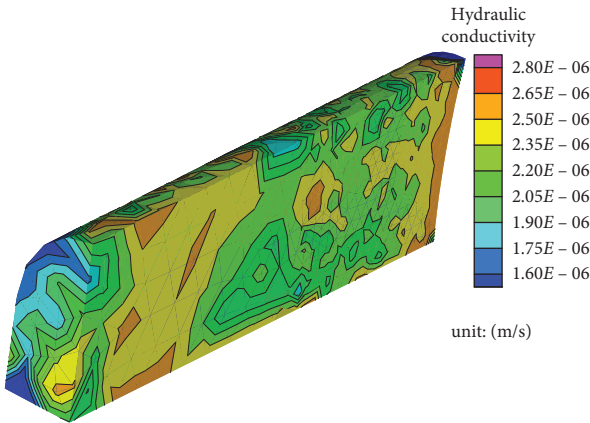


FIGURE 10: The hydraulic conductivity distribution map when the reduction factor $F_i = 1.54$.

excavation. The seepage field adjusts continuously for the purpose of eliminating the high potential water pressure in the Karst cave. As Karst cave water discharges to the working face, seepage pressure progressively decreases from the Karst cave to working face. The mean seepage pressure gradient of the water-proof rock pillar is 0.5 MPa/m, which brings the horizontal volumetric stress with the direction from Karst cave to working face, which is a driving force of instability of the water-proof rock pillar.

Based on linkage analysis on solid-fluid coupling and the strength reduction method, water discharges on the working face are achieved in the different reduction factors by FLAC^{3D}. Figure 12 illustrates that water discharge on the working face evolves from a low flow rate to a massive flow rate with the increase of the reduction factor. When $F_i = 1.10 \sim 1.53$, the flow rate of the working face fluctuates from 2.05×10^{-5} m/s (when $F_i = 1.1$) to 7.47×10^{-3} m/s (when $F_i = 1.53$). This implies that when the reduction factor $F_i = 1.10 \sim 1.53$, the water-proof rock pillar is stable, and water discharge on the working face is more seepage than water inrush. While the reduction factor $F_i = 1.54 \sim 1.58$, water discharge on the working face increases abruptly and fluctuates from 0.025 m³/s (when $F_i = 1.54$) to 0.027 m³/s (when $F_i = 1.58$), due to nonlinear extension of the plastic

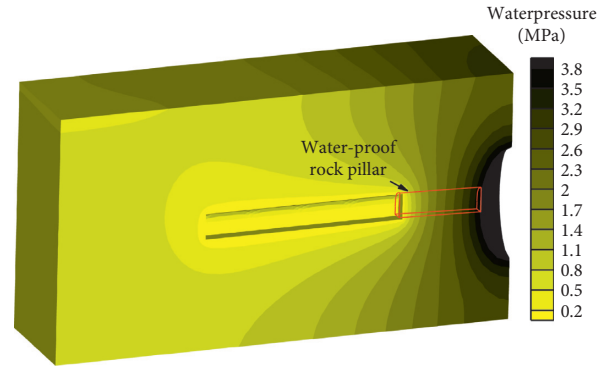


FIGURE 11: Distribution of seepage field of the surrounding rocks when the reduction factor $F_i = 1.10$.

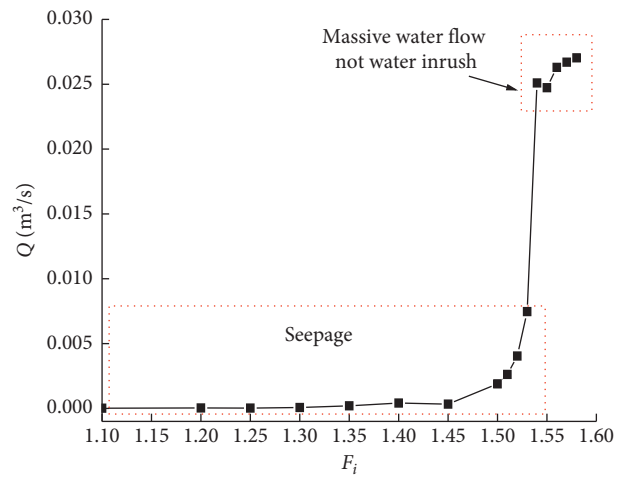


FIGURE 12: Water discharge of the working face evolves with the increase of reduction factor.

zone of rock pillar. Under the action of disturbance stress and high seepage volumetric stress, the displacement of the working face is about 15 cm by coupling calculation, when the reduction factor $F_i = 1.54$, which is shown in Figure 13.

4.2. Water-Proof Rock Pillar Instability. The evolution of the percentage of plastic units in the water-proof rock pillar with the reduction factor is visualized in Figure 14. The plastic units in the water-proof rock pillar nonlinearly increase with the increment of reduction factor. When $F_i \geq 1.54$, the percentage of plastic units in the rock pillar mutates. The percentage of plastic units in the rock pillar is about 85%~87% when $F_i = 1.54 \sim 1.58$. When $F_i = 1.59$, the whole rock pillar is in the plastic state, the calculation has no convergence, rock pillar is in the instability stage, and water inrush from the confined Karst cave in a pipe flow form happens. It indicates that when the Karst cave internal pressure $p = 4$ MPa and water-proof rock pillar thickness $h = 8$ m, the safety factor of the water-proof rock pillar is 1.59.

Karst cave water inbursts into the roadway in a pipe flow form, when the water-proof rock pillar is in the instability stage. Water irruption quantity increases rapidly in the initial phase of water inrush. Thereafter, with the passage of

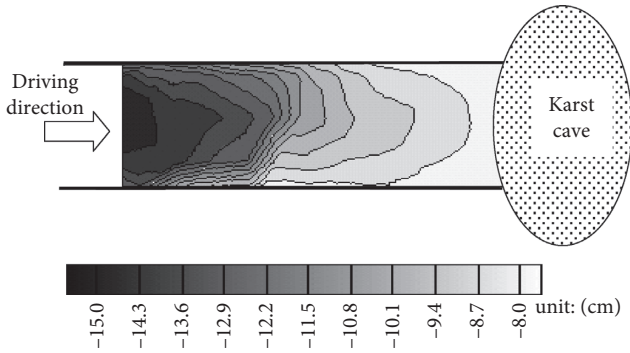


FIGURE 13: Horizontal displacement of the water-proof rock pillar when the reduction factor $F_i = 1.54$.

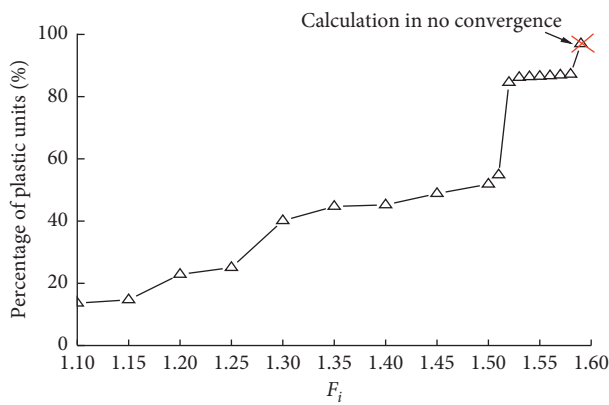


FIGURE 14: The evolution of the percentage of plastic units in the water-proof rock pillar with reduction factor.

time, the water irruption quantity attenuates unceasingly due to decrease of the supply of Karst water. In the calculation program, the evolution law of flow rate in the roadway during the process of water inrush is gained by pipe flow analysis illustrated in Figure 15. Water irruption quantity reaches the peak ($Q_{max} = 1.27m^3/s$) in short time ($t = 2.64 h$). Thereafter, water irruption quantity decreases rapidly. The results of numerical simulation agree well with practical flow law of confined Karst cave water inrush [38–40].

The evolution law of water pressure on roadway transverse sections where is 3 m, 8 m, 13 m, and 18 m away from the karst cave is visualized in Figure 16. With the increase in water inrush time, the water pressure in the roadway quickly increases and then attenuates after reaching the peak. Owing to hydraulic losses in the roadway, the water pressure in the roadway becomes smaller and smaller, when the distance from the Karst cave is longer and longer.

The water pressure distribution in the roadway is obtained by pipe analysis as shown in Figure 17. Due to the instability of the water-proof rock pillar, Karst water pours into the roadway with an dramatic increase in the water pressure in the roadway. With the development of water inrush time, hydraulic gradient in the roadway declines continuously, for example, when $t = 3.53 h$, the mean hydraulic gradient in the roadway is 5.6 much as that when

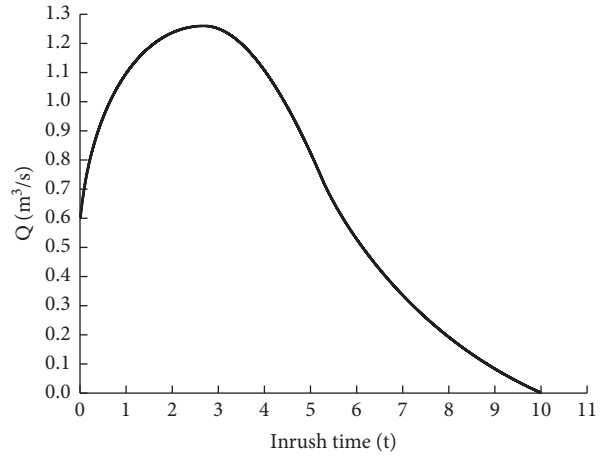


FIGURE 15: The evolution law of water discharge in the roadway during the process of water inrush.

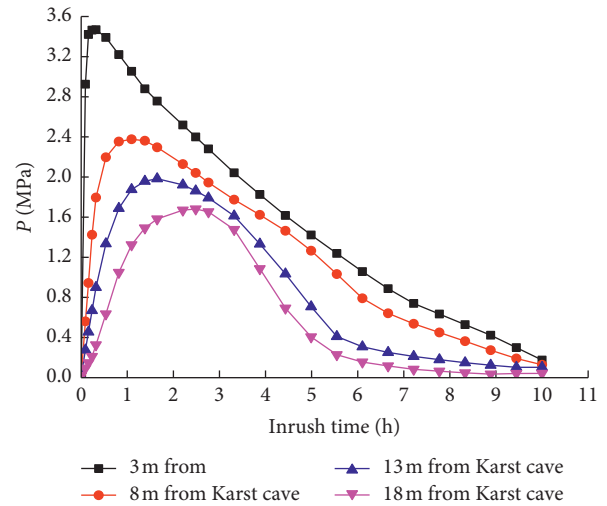


FIGURE 16: The evolution law of water pressure on roadway transverse sections which are 3 m, 8 m, 13 m, and 18 m away from karst cave.

$t = 9.44 h$. Owing to the hydraulic gradient decaying rapidly with the passage of time, resulting in the slowing down of water flow in the roadway, the hydraulic rough flow at the initial water inrush process changes into pipe laminar low finally.

4.3. Safety Factor of the Water-Proof Rock Pillar. By the linkage analysis of solid-fluid coupling theory and the strength reduction method adopted, the safety factor of the water-proof rock pillar is gained when karst cave hydraulic pressure p in the Karst cave and calculation thickness h of the water-proof rock pillar are different. In Figure 14, when the Karst cave hydraulic pressures are 1 MPa, 2 MPa, 3 MPa, 4 MPa, and 5 MPa, respectively, and the calculation thickness of the rock pillar is 3 m, 4 m, 5 m, 6 m, 7 m, 8 m, 9 m, and 10 m separately, and the relationship curves of safety factor F_S and karst cave hydraulic pressure p and calculation thickness h of the rock pillar are achieved.

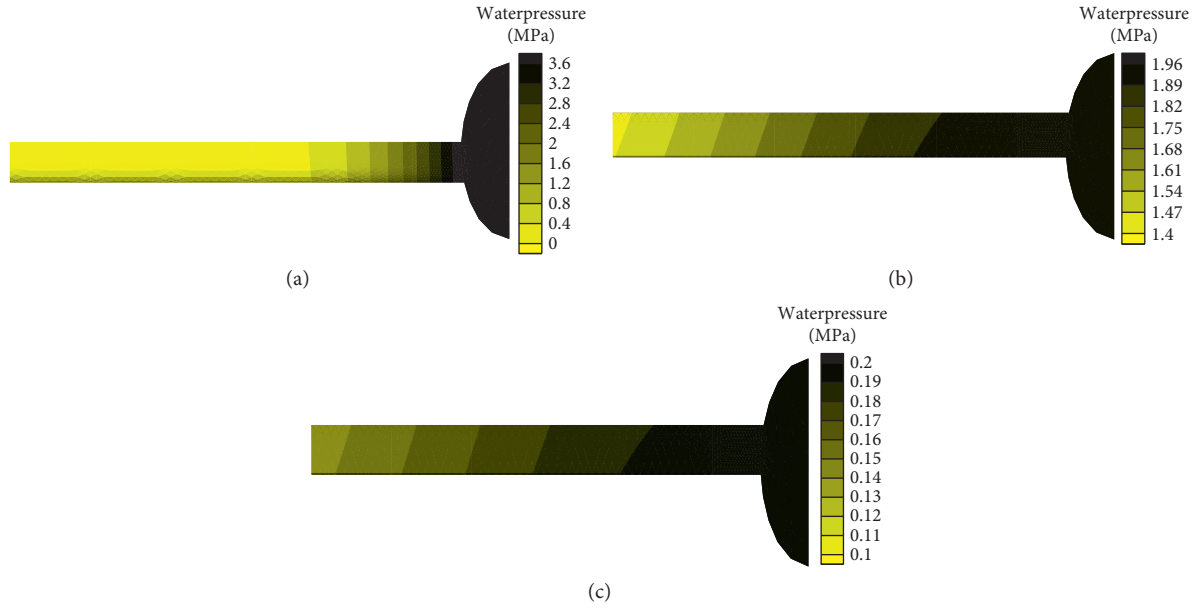


FIGURE 17: The water pressure distributions in the roadway by pipe analysis analysis in different times. (a) $t = 0.14$ h. (b) $t = 3.53$ h. (c) $t = 9.44$ h.

Figure 18 displays that the safety factor F_S increases gradually with the increase of calculation safety thickness h of the rock pillar, which is fitted by the exponential function:

$$F_S = a + b \exp(ch), \quad (19)$$

where F_S is the safety factor of the water-proof rock pillar; h is the calculation safety thickness of the water-proof rock pillar; and a , b , and c are undetermined coefficients.

The relation between safety factor F_S of the water-proof rock pillar and calculation safety thickness h of the water-proof rock pillar under different Karst cave water pressures p is obtained by using equation (19), which is demonstrated in Table 2. If $F_S = 1.5$ is considered as the yardstick of stability of the water-proof rock pillar, some yardsticks are educed:

When $F_S \geq 1.5$, the water-proof rock pillar is stable.

When $F_S < 1.5$, the water-proof rock pillar is unstable.

Conclusions can be drawn from Table 2 that the calculation safety thickness of the water-proof rock pillar should be thickened with the increment of Karst hydraulic pressure, such as when the Karst cave hydraulic pressures are 1 MPa and 5 MPa, respectively, and the calculation safety thickness of the water-proof rock pillar is 5.18 m and 9.32 m, respectively. The calculation safety thickness of the water-proof rock pillar is 4.14 m more when the hydraulic pressure $p = 5$ MPa than when the hydraulic pressure $p = 1$ MPa. This is because with the increase of Karst hydraulic pressure, the seepage volumetric stress in the water-proof rock pillar increases, which directly leads to the enhancement of lateral thrust along the direction of the working face, and the calculation thickness should be thickened.

4.4. Safety Thickness of Water-Proof Rock Pillar Setting. Drilling and blasting is mostly applied in mines in southern China, and the coupling analysis model is used without

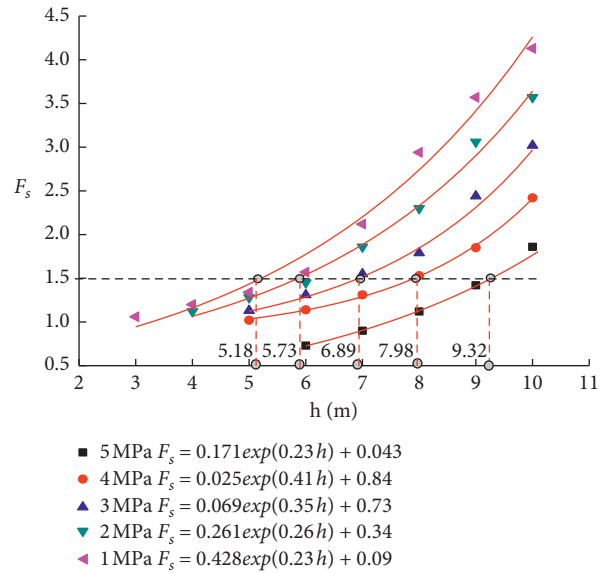


FIGURE 18: Variation relation curves between safe factor and calculation safety thickness of the water-proof rock pillar.

considering the disturbance of blasting to the surrounding rocks before the working face. Based on the experimental research and numerical analysis results [41–43], the disturbance depth of ordinary blasting, smooth blasting, and presplitting blasting to the surrounding rocks is about 1.5 m; meanwhile, disturbance depth increases with the increment of a single segment explosive dosage. So, safety thickness of water-proof rock pillar setting in mining engineering is the sum of the blasthole depth h_1 , blasting disturbance depth h_2 , and safety calculation thickness h_3 of the water-proof rock pillar, which can be denoted as follows:

TABLE 2: The relation between safety factor F_S and thickness h of the water-proof rock pillar under different karst cave water pressures.

Karst cave water pressure (MPa)	The relation between safety factor F_S and thickness of water-proof rock pillar h	The calculation safety thickness of water-proof rock pillar when safety factor $F_S = 1.5$ (m)
1	$F_S = 0.428 \exp(0.23 h) + 0.09$	5.18
2	$F_S = 0.261 \exp(0.26 h) + 0.34$	5.73
3	$F_S = 0.069 \exp(0.35 h) + 0.73$	6.89
4	$F_S = 0.025 \exp(0.41 h) + 0.84$	7.98
5	$F_S = 0.171 \exp(0.23 h) + 0.043$	9.32

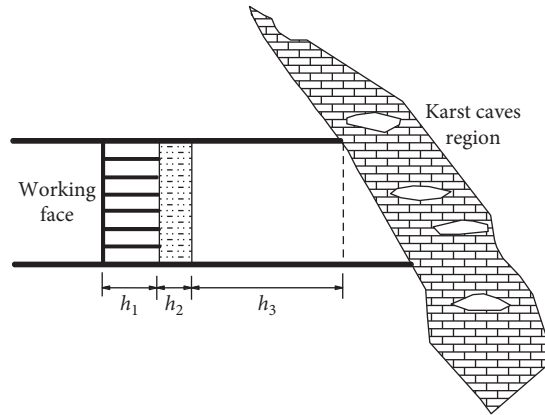


FIGURE 19: Schematic diagram of safety thickness of water-proof rock pillar setting in mining engineering.

TABLE 3: Safety thickness of water-proof rock pillar setting in the Maokou limestone for the Qiyi coal mine.

Kars water pressure (MPa)	Blasthole depth h_1 (m)	Blasting disturbance depth h_2 (m)	Calculation safety thickness of rock pillar h_3 (m)	Safety thickness of water-proof rock pillar setting (H/m)
1.0	2.5	1.5	5.18	9.18
2.0	2.5	1.5	5.73	9.73
3.0	2.5	1.5	6.89	10.89
4.0	2.5	1.5	7.98	11.98
5.0	2.5	1.5	7.98	13.32

$$H = h_1 + h_2 + h_3, \quad (20)$$

where H is the safety thickness of water-proof rock pillar setting in mining engineering; h_1 is the blasthole depth; h_2 is the blasting disturbance depth; and h_3 is the calculation safety thickness h of water-proof rock pillar based on equation (19).

The schematic diagram of safety thickness of water-proof rock pillar setting of a confined Karst cave before a roadway is visualized in Figure 19. The calculation safety thickness h_3 of the rock pillar is gained by the way proposed in this paper. Table 3 illustrates safety thickness of water-proof rock pillar setting for confined the Karst cave in the Qiyi mine based on equation (20). Based on Table 3, when hydraulic pressures of the Karst cave are from 1.0 MPa to 5.0 MPa, the safety thickness of water-proof rock pillar setting is from 9.2 m to 13.4 m. According to regulations of mine water control, when the hydraulic pressure is less than 1.0 MPa, the advanced horizontal distance of the pilot hole for detecting water should not be less than 10 m, and the length of water stop casing is more than 5 m for a rock roadway; with the

increase of hydraulic pressure, the advanced horizontal distance and the length of water stop casing must increase correspondingly; when the hydraulic pressure is more than 3.0 MPa, the advanced horizontal distance is more than 25 m and the length of water stop casing is more than 20 m. Base on the research results of this paper, if regulations of mine water control are strictly executed, especially regulations about exploring water and drilling advanced distance and the length of water stop casing, the chance for occurrence of water inrush would be extremely small because the advanced distance of pilot hole for detecting water and the length of water stop casing regulated in regulations of mine water control are more than the safety thickness of the water-proof rock pillar setting proposed in this paper. In a Karst coal mine, when hydrogeology condition is complicated or even extremely complicated, the rule of exploring before mining should be obeyed.

Water inrush accident induced by confined water breaking rock pillar happened on the heading face with -160 m level of the Qiyi mine. The investigation suggested that the Karst cave with a volume of $20 \text{ m} \times 6 \text{ m} \times 20 \text{ m}$ was

some 3~4 m away from the face. That is to say, the water-proof rock pillar between the Karst cave and working face was about 3~4 m. Even worse, as the surface water connected well with the Karst cave water, the hydraulic pressure in the Karst cave was about 3.5~4.0 MPa. Based on Table 3, the safety thickness of water-proof rock pillar setting should be 11~12 m. The water-proof rock pillar with a thickness of 3~4 m did not have the ability of preventing water inrush, let alone safety margins.

5. Conclusions

- (1) The linkage analysis of solid-fluid coupling and the strength reduction method to study the Karst cave water inrush is proposed. The interaction of disturbance stress and high seepage volumetric stress to the water-proof rock pillar gives rise to instability of the water-proof rock pillar. Accompanying with mechanical instability of water-proof rock, Karst cave water inrush is deemed a conversion process of the "seepage to pipe flow."
- (2) Equivalent hydraulic conductivity of pipe flow for confined Karst cave water inrush is introduced, and a nonlinear seepage-pipe coupling model of confined Karst cave water inrush is established. Combining the nonlinear seepage-pipe coupling model with the strength reduction method, the linkage analysis of fluid solid coupling and the strength reduction method is constructed to study the whole process of water inrush
- (3) Taking the water inrush accident of Shibaijing of the Qiyi mine as an example, it is proposed that the thickness of the water-proof rock pillar whose safety factor equals 1.5 is regarded as the calculating safety thickness of the water-proof rock pillar, and safety thickness of water-proof rock pillar setting in mining engineering is equal to the sum of the blasthole depth, blasting disturbance depth, and the calculating safety thickness of the water-proof rock pillar.
- (4) The reason leading to Karst water inrush of the Qiyi mine is that due to the absence of advanced boreholes, the water-proof rock pillar is set so small that it cannot possess a safety margin, and the confined Karst cave water breaks the water-proof rock pillar and bursts out.

Data Availability

The data used to support the findings of this study are included within the article.

Conflicts of Interest

The authors declare that they have no conflicts of interest.

Acknowledgments

This research was supported by the National Natural Science Foundation of China (nos. 51774131 and 51274097) and the CRSRI Open Research Program (CKWV2017508/KY).

References

- [1] Q. Wu and M. Wang, "Characterization of water bursting and discharge into underground mines with multilayered groundwater flow systems in the North China coal basin," *Hydrogeology Journal*, vol. 14, no. 6, pp. 882–893, 2006.
- [2] Q. Wu, M. Wang, and X. Wu, "Investigations of groundwater bursting into coal mine seam floors from fault zones," *International Journal of Rock Mechanics and Mining Sciences*, vol. 41, no. 4, pp. 557–571, 2004.
- [3] B. Yu, W. Zhu, and J. Xu, "Numerical simulation of surface subsidence characteristics during deep mining," *Journal of Mining and Safety Engineering*, vol. 24, no. 4, pp. 422–426, 2007.
- [4] Y. Zhao, L. Zhang, W. Wang, J. Tang, H. Lin, and W. Wan, "Transient pulse test and morphological analysis of single rock fractures," *International Journal of Rock Mechanics and Mining Sciences*, vol. 91, pp. 139–154, 2017.
- [5] Y. X. Wang, S. Y. Wang, Y. L. Zhao, P. P. Guo, Y. Liu, and P. Cao, "Blast Induced Crack Propagation and Damage Accumulation in Rock Mass Containing Initial Damage," *Shock and Vibration*, vol. 2018, pp. 1–18, 2018.
- [6] L. Dong, D. Sun, X. Li, J. Ma, L. Zhang, and X. Tong, "Interval non-probabilistic reliability of surrounding jointed rockmass considering microseismic loads in mining tunnels," *Tunneling and Underground Space Technology*, vol. 81, pp. 326–335, 2018.
- [7] L. J. Dong, W. Zou, D. Y. Sun, and X. J. Tong, "Some Developments and New Insights for Microseismic/Acoustic Emission Source Localization," *Shock and Vibration*, vol. 2019, pp. 1–15, 2019.
- [8] Y. Zhao, Y. Wang, W. Wang, W. Wan, and J. Tang, "Modeling of non-linear rheological behavior of hard rock using triaxial rheological experiment," *International Journal of Rock Mechanics and Mining Sciences*, vol. 93, pp. 66–75, 2017.
- [9] Y. L. Zhao, L. Y. Zhang, W. J. Wang, W. Wan, and W. H. Ma, "Separation of elastoviscoplastic strains of rock and a non-linear creep model," *International Journal of Geomechanics*, vol. 18, no. 1, 2018.
- [10] K. Peng, J. Zhou, Q. Zou, and X. Song, "Effect of loading frequency on the deformation behaviours of sandstones subjected to cyclic loads and its underlying mechanism," *International Journal of Fatigue*, vol. 131, Article ID 105349, 2020.
- [11] J. Zhang and B. Shen, "Coal mining under aquifers in China: a case study," *International Journal of Rock Mechanics and Mining Sciences*, vol. 41, no. 4, pp. 629–639, 2004.
- [12] Y. L. Gong and F. Z. Wan, "Impact of karst water on coal mining in North China," *Environmental Geology*, vol. 49, pp. 449–457, 2006.
- [13] C. S. Wang, H. B. Bai, and S. C. Liu, "Mine water issues in China," in *Proceedings of the IMWA 2010 Symposium Sydney*, vol. 445–448, Mine Water and Innovative Thinking, Nova Scotia, Canada, 2010.
- [14] H. Keqiang, Y. Jia, F. Wang, and Y. Lu, "Overview of karst geo-environments and karst water resources in north and south China," *Environmental Earth Sciences*, vol. 64, no. 7, pp. 1865–1873, 2011.
- [15] X. X. Miao, A. Wang, Y. J. Sun et al., "Research on theory of mining with water resources protection and its application to arid and semi-arid mining region," *Chinese Journal of Rock Mechanics and Engineering*, vol. 28, no. 2, pp. 217–227, 2009.
- [16] K. Q. He, R. L. Wang, and W. F. Jiang, "Groundwater inrush channel detection and curtain grouting of the Gaoyang iron

- ore mine, China,” *Mine Water and the Environment*, vol. 31, no. 4, pp. 297–306, 2012.
- [17] W. J. Wang, Y. L. Zhao, Q. F. Li et al., “Disaster mechanism of karst water bursting in mine,” *Journal of China Coal Society*, vol. 35, no. 3, pp. 443–448, 2010.
- [18] G. J. Wang, “The discussion of karst water dam age prevention in Huayingshan mine area,” *Journal of North China Institute of Science and Technology*, vol. 6, no. 4, pp. 96–100, 2009.
- [19] S. H. Zhou, “Maokou limestone karstic water flooding and harnessing in Songzao coalmine, chongqing,” *Coal Geology of China*, vol. 17, no. 5, pp. 65–77, 2005.
- [20] Y. L. Zhao, J. Z. Tang, Y. Chen, L. Y. Zhang, W. J. Wang, and J. P. Liao, “Hydromechanical coupling tests for mechanical and permeability characteristics of fractured limestone in complete stress–strain process,” *Environmental Earth Sciences*, vol. 76, no. 1, pp. 1–18, 2017.
- [21] C. L. Wang, L. Pan, Y. Zhao, Y. Zhang, and W. Shen, “Analysis of the pressure pulse propagation in rock: a new approach to simultaneously determine permeability, porosity, and adsorption capacity,” *Rock Mechanics and Rock Engineering*, vol. 52, no. 11, pp. 4301–4317, 2019.
- [22] Ministry of Coal Industry, *Regulations for Mine Water Prevention and Control*, Coal Industry Publication Press, Beijing, China, 2009.
- [23] H. Q. Zhang, Y. N. He, C. A. Tang, B. Ahmad, and L. J. Han, “Application of an improved flow–stress–damage model to the criticality assessment of water Inrush in a mine: a case study,” *Rock Mechanics and Rock Engineering*, vol. 42, no. 6, pp. 911–930, 2009.
- [24] Y. Wang, Q. Chen, and Y. Y. Wei, “Application of infrared acquisition technology to prediction of water inrush in Yuanliangshan tunnel,” *Chinese Journal of Rock Mechanics and Engineering*, vol. 22, no. 5, pp. 855–857, 2003.
- [25] C. X. Chen, “Groundwater flow model and simulation method in triple media of karst tube–fissure–pore,” *Earth Sciences*, vol. 20, no. 4, pp. 361–366, 1995.
- [26] S. H. Liu and S. C. Yu, “Effect of turbulent boundary layer to a small step change in wall roughness,” *Journal of Hydrodynamics*, vol. 13, no. 1, pp. 35–40, 1998.
- [27] Y. L. Zhao, Y. Wang, and L. Tang, “The compressive–shear fracture strength of rock containing water based on Drucker–Prager failure criterion,” *Arabian Journal of Geosciences*, vol. 12, p. 452, 2019.
- [28] Y. Zhao, P. He, Y. Zhang, and C. Wang, “A new criterion for a toughness-dominated hydraulic fracture crossing a natural frictional interface,” *Rock Mechanics and Rock Engineering*, vol. 52, no. 8, pp. 2617–2629, 2019.
- [29] J. J. Meng, Y. X. Wang, Y. L. Zhao, H. Ruan, and Y. Liu, “Stability analysis of earth slope using combined numerical analysis method based on DEM and LEM,” *Tehnički Vjesnik*, vol. 25, no. 5, pp. 1265–1273, 2018.
- [30] Y. Zhao, L. Zhang, W. Wang, C. Pu, W. Wan, and J. Tang, “Cracking and stress–strain behavior of rock-like material containing two flaws under uniaxial compression,” *Rock Mechanics and Rock Engineering*, vol. 49, no. 7, pp. 2665–2687, 2016.
- [31] C. Wang, Y. Zhao, Y. L. Zhao, and W. Wan, “Study on the interaction of collinear cracks and wing cracks and cracking behavior of rock under uniaxial compression,” *Advances in Civil Engineering*, vol. 2018, pp. 1–10, 2018.
- [32] Y. X. Wang, H. Zhang, H. Lin, Y. Zhao, and Y. Liu, “Fracture behaviour of central-flawed rock plate under uniaxial compression,” *Theoretical and Applied Fracture Mechanics*, vol. 106, 2020.
- [33] Y. Zhao, Y. Wang, W. Wang, L. Tang, Q. Liu, and G. Cheng, “Modeling of rheological fracture behavior of rock cracks subjected to hydraulic pressure and far field stresses,” *Theoretical and Applied Fracture Mechanics*, vol. 101, pp. 59–66, 2019.
- [34] L. J. Dong, W. W. Shu, X. B. Li, Z. Zhou, F. Gong, and X. Liu, “Quantitative evaluation and case study of risk degree for underground goafs with multiple indexes considering uncertain factors in mines,” *Geofluids*, vol. 2017, pp. 1–15, 2017.
- [35] Q. Wu, L. Chen, B. Shen, B. Dlamini, S. Li, and Y. Zhu, “Experimental investigation on rockbolt performance under the tension load,” *Rock Mechanics and Rock Engineering*, vol. 52, no. 11, pp. 4605–4618, 2019.
- [36] Y. L. Zhao, L. Y. Zhang, W. J. Wang et al., “Creep behavior of intact and cracked limestone under multi-level loading and unloading cycles,” *Rock Mechanics and Rock Engineering*, vol. 50, no. 6, pp. 1–16, 2017.
- [37] J. Chen, H. Peng, J. Fan, X. Zhang, W. Liu, and D. Jiang, “Microscopic investigations on the healing and softening of damaged salt by uniaxial deformation from CT, SEM and NMR: effect of fluids (brine and oil),” *RSC Advances*, vol. 10, no. 5, pp. 2877–2886, 2020.
- [38] X. R. Liu, X. D. Zhang, and M. Huang, “Delay characteristics and risk mitigation of karst water burst flood of tunnels,” *Chinese Journal of Geotechnical Engineering*, vol. 33, no. 9, pp. 1326–1332, 2011.
- [39] L. Zhang and J. A. Franklin, “Prediction of water flow into rock tunnels: an analytical solution assuming an hydraulic conductivity gradient,” *International Journal of Rock Mechanics and Mining Sciences & Geomechanics Abstracts*, vol. 30, no. 1, pp. 37–46, 1993.
- [40] T. Li, T. Mei, X. Sun, Y. Lv, J. Sheng, and M. Cai, “A study on a water-inrush incident at Laohutai coalmine,” *International Journal of Rock Mechanics and Mining Sciences*, vol. 59, pp. 151–159, 2013.
- [41] J. Y. Qi, “The Influence of tunnel blasting method for surrounding,” *Railway Engineering*, vol. 7, pp. 4–7, 1979.
- [42] G. Wang, Y. Luo, X. Li, T. Liu, R. Ma, and D. Qu, “Study on dynamic mechanical properties and meso-damage mechanism of jointed rock under impact load,” *European Journal of Environmental and Civil Engineering*, vol. 45, pp. 1–17, 2019.
- [43] W. X. Zheng, Y. L. Zhao, and Q. W. Bu, “The coupled control of floor heave based on a composite structure consisting of bolts and concrete antiarches,” *Mathematical Problems Engineering*, vol. 2018, pp. 1–14, 2018.